Imperial College of Science, Technology and Medicine

Royal School of Mines

Department of Earth Science and Engineering

Monitoring and Modelling of Microseismicity Associated with Rock Burst and Gas Outburst Hazards in Coal Mines

by

Wenzhuo Cao

A thesis submitted for the degree of
Doctor of Philosophy of Imperial College London
May 2019

Dedicated to my parents

Jiaxin Cao and Ying Shao

Abstract

This thesis aimed at establishing a better understanding of the mechanisms involved and methods for forecasting, prevention and control of rock bursts and gas outbursts in underground coal mining.

After a comprehensive review of relevant literature, the thesis first presents experimental investigations into the seismic response of coal blocks to stress and fracturing under true-triaxial stress conditions. The dynamic response of coal seams to longwall face advance has been investigated through continuous microseismic monitoring of several longwall panels over the research period. A conceptual model has been developed to interpret the recorded microseismicity based on the fracture slip seismicity-generation mechanism. Based upon the monitoring results and the conceptual model, a statistical short-term forecasting methodology was developed to estimate the probability of hazardous microseismicity during longwall coal mining. In addition, a discrete fracture network (DFN) based microseismic modelling methodology was developed to simulate Longwall Top Coal Caving (LTCC) mining induced microseismicity in a probabilistic framework through the combination of deterministic stress and failure analysis and stochastic fracture slip evaluation. The modelling methodology was further employed to investigate the impact of lithological heterogeneity on microseismic characteristics.

Further on, rock bursts and coal and gas outbursts are generalised as problems of dynamic instability under excavation unloading conditions. The role of excavation unloading as a source of dynamic stress perturbations in contributing to rock bursts was quantified. A coal and gas outburst model based on fracture mechanics and gas dynamics was formulated and further numerically implemented to simulate coal and gas outbursts during roadway developments. Key factors affecting outburst initiation and its temporal evolution were also identified.

Affirmation

The work submitted in this thesis is my own, and has not been submitted previously for any other degree. Results obtained in the course of this research have been presented in the following publications, corresponding to different chapters of this thesis.

Chapter 3

- Yildirim, B.*, **Cao, W**., Durucan, S., Korre, A., Wolf, K.H., Bakker, R., Barnhoorn, A., 2018. The effect of natural fracture heterogeneity on hydraulic fracture performance and seismic response in shale and coal formations. In 52nd US Rock Mechanics/Geomechanics Symposium. American Rock Mechanics Association.
- **Cao, W**.*, Yildirim, B., Durucan, S., Wolf, K.H., Cai, W., Agrawal, H., Korre, A. Active acoustic monitoring of hydraulic fracturing in naturally fractured coal under true triaxial stresses (*submitted to the Journal of Geophysical Research: Solid Earth*).

Chapter 4

- **Cao, W**.*, Durucan, S., Si, G., Cai, W., Shi, J.Q., Korre, A., Jamnikar, S., Lurka, A. Monitoring and forecasting of microseismicity associated with longwall coal mining: *In situ* monitoring and a conceptual seismic-generation model (*submitted to the International Journal of Coal Geology*).

Chapter 5

- **Cao, W**.*, Durucan, S., Cai, W., Shi, J.Q., Korre, A. Monitoring and forecasting of microseismicity associated with longwall coal mining: A statistical forecasting methodology (*submitted to the International Journal of Coal Geology*).
- **Cao, W.***, Durucan, S., Cai, W., Shi, J.Q., Korre, A. Multiple-panel Longwall Top Coal Caving induced microseismicity: Monitoring and development of a statistical forecasting model for hazardous microseismicity (*submitted to the 53rd US Rock*

Mechanics/Geomechanics Symposium to be held in New York, June 2019. American Rock Mechanics Association).

Chapter 6

- **Cao, W**.*, Shi, J.Q., Si, G., Durucan, S., Korre, A., 2018. Numerical modelling of microseismicity associated with longwall coal mining. International Journal of Coal Geology, 193, 30-45.

Chapter 7

- **Cao, W**.*, Shi, J.Q., Durucan, S., Si, G., Korre, A., 2017. Modelling the Influence of heterogeneity on microseismic characteristics in longwall coal mining. In 51st US Rock Mechanics/Geomechanics Symposium. American Rock Mechanics Association.
- **Cao, W**.*, Shi, J.Q., Durucan, S., Si, G., Korre, A. Numerical modelling of anomalous microseismicity influenced by lithological heterogeneity in longwall coal mining (*submitted to the International Journal of Coal Geology*).

Chapter 8

- Zhou, Z., Zhao, Y., **Cao, W**.*, Chen, L., Zhou, J., 2018. Dynamic response of pillar workings induced by sudden pillar recovery. Rock Mechanics and Rock Engineering, 51(10), 3075-3090.
- Li, X., **Cao, W**.*, Tao, M., Zhou, Z., Chen, Z., 2016. Influence of unloading disturbance on adjacent tunnels. International Journal of Rock Mechanics and Mining Sciences, 84, 10-24.

Chapter 9

- **Cao, W**.*, Shi, J.Q., Durucan, S., Si, G., Korre, A., 2018. Gas-driven rapid fracture propagation and gas outbursts under unloading conditions in coal seams. In 52nd US Rock Mechanics/Geomechanics Symposium. American Rock Mechanics Association.
- **Cao, W**.*, Shi, J.Q., Durucan, S., Si, G., Korre, A. Gas-driven rapid fracture propagation under unloading conditions in coal and gas outbursts (*submitted to the International Journal of Rock Mechanics and Mining Sciences*).

(Note: corresponding authors are marked with *)

Copyright Declaration

The copyright of this thesis rests with the author and is made available under a Creative Commons Attribution Non-Commercial No Derivatives licence. Researchers are free to copy, distribute or transmit the thesis on the condition that they attribute it, that they do not use it for commercial purposes and that they do not alter, transform or build upon it. For any reuse or redistribution, researchers must make clear to others the licence terms of this work.

Acknowledgements

I would like to express my sincerest gratitude to my supervisor, Prof. Sevket Durucan, for his guidance and support to make my adventurous journey towards the PhD an enjoyable one. He taught me coal mining, rock mechanics and skills of academic writing. He creates an intellectually stimulating and relaxed atmosphere for research and discussions, and continuously encourages me to take every chance to learn and improve. I admire his positive values, rigorous attitude, analytical mind and organised work style, and treasure what I learnt from him for a lifetime.

I am extremely grateful to my second supervisor, Dr. Ji-Quan Shi, who has always been willing to discuss and advise, and made a distinguished contribution to the quality of this work. His insights and rigorous thinking helped me obtain a better understanding of rock mechanics and reservoir engineering. I appreciate the assistance and support from Prof. Anna Korre, who taught me geostatistics and gave me opportunities to get prepared for a future career. I would also like to thank the UK Engineering and Physical Sciences Research Council (EPSRC) PhD scholarship awarded by the Faculty of Engineering at Imperial College London.

I greatly appreciate the help from my colleagues in the Minerals, Energy and Environmental Engineering Research Group: Dr. Guangyao Si, Dr. Mojgan Hadi Mosleh, Dr. Wu Cai, Dr. Rajesh Govindan, Betul Yildirim, and Harshit Agrawal. I also thank other colleagues: Dr. Zhenggang Nie, Dr. Maria Lathouri, Dr Saba Manzoor, Dr. Nondas Andrianopoulos, Ernesto Santibanez Borda, Muhammad Ashan, Yu Zhang, etc. I cherish our friendship and shall never forget the time we spent together.

Parts of research presented in this thesis was carried out as part of the European Commission Research Fund for Coal and Steel (RFCS) funded project “Monitoring, Assessment, Prevention and Mitigation of Rock Burst and Gas Outburst Hazards in Coal Mines - MapROC”, Grant No: RFCR-CT-2015-00005. I would like to express

my gratitude to Dr. Sergej Jamnikar from Coal Mine Velenje in Slovenia, and Dr. Adam Lurka and Mr Robert Siata from the Central Mining Institute of Poland, who undertook the field microseismic monitoring work and shared mine production schedule and field monitoring data with me. I would like to thank Prof. Karl-Heinz Wolf, Mr Marc Friebel, Mr Karel Heller, Dr. Richard Baker, Dr. Auke Barnhoorn of the Geoscience and Engineering Laboratory at Delft University of Technology, and Mr Graham Nash and Mr Gary Jones of the Geomechanics Laboratory at Imperial College London for their contributions to the laboratory experiments. Many thanks to the Itasca Education Partnership (IEP) program and the mentor Mr Jon Haycox, which provided me with a PFC license for my early modelling work.

I am grateful to Dr. John-Paul Latham and Prof. Yanghua Wang for their valuable comments on my research and careful reviews of my progress during the PhD. I thank Dr. Ming Tao and Dr. Qinghua Lei, who greatly extended my knowledge on rock mechanics and scientific programming, and most importantly, guided and inspired me in generating a flow of new ideas and conducting interdisciplinary research.

I appreciate the help from Chinese friends at Imperial College London past and present: Dr. Qinghua Lei, Dr. Dunhui Xiao, Dr. Pan Yang, Dr. Shuai Li, Dr. Xue Wan, Dr. Xiaoguang Wang, Bowen Song, Ying Gao, Peipei Wang, Rong Hu, Xinhuan Zhou, Wei Pan, Yuhua Xia, Jiashun Yao, Mengzheng Ouyang, Hao Wang, etc.

Special thanks to my former supervisors, Prof. Xibing Li and Prof. Zilong Zhou at Central South University, who guided me to the world of mining geomechanics and rock dynamics which laid a solid foundation for my future research. I would not have had the opportunity to continue my PhD study at Imperial College London without their strong support and help.

Finally, I would like to thank my parents for their support, encouragement and love throughout the years.

Table of Contents

ABSTRACT ……i

AFFIRMATION iii

COPYRIGHT DECLARATION v

ACKNOWLEDGEMENTS vii

TABLE OF CONTENTS ix

LIST OF FIGURES xv

LIST OF TABLES xxiii

NOMENCLATURE xxv

CHAPTER 1 INTRODUCTION AND OBJECTIVES 1

1.1 RESEARCH OBJECTIVES 1

1.2 THESIS OVERVIEW 4

CHAPTER 2 PREVIOUS RESEARCH ON UNDERGROUND HAZARDS IN COAL MINING 7

2.1 INTRODUCTION 7

2.2 COAL AS A POROUS GAS RESERVOIR 7

2.2.1 Coal structure 7

2.2.2 Gas sorption and desorption behaviour 8

2.2.3 Coal permeability 10

2.2.4 Gas flow in coal seams 12

2.3 CHARACTERISTICS OF ROCK BURST HAZARDS 13

2.3.1 Influencing factors and mechanisms of rock bursts 13

2.3.2 Coupled static and dynamic theory 16

2.3.3 Strain energy release, migration and dissipation in mining 17

2.3.4 The influence of stress release rate on excavation response 19

2.4 CHARACTERISTICS OF COAL AND GAS OUTBURST HAZARDS 21

2.4.1 Factors influencing the outburst potential *21*
2.4.2 Mechanisms of coal and gas outbursts *25*
2.4.3 Advances in modelling coal and gas outbursts *27*
2.5 ROCK BURSTS AND GAS OUTBURSTS AS DYNAMIC UNSTABLE FAILURE PROBLEMS 29
2.5.1 Similarities and differences between rock bursts and gas outbursts *29*
2.5.2 Unstable failure problems *31*
2.5.3 Dynamic unloading problems *33*
2.5.4 Rapid fracture propagation in dynamic problems *34*
2.6 MICROSEISMICITY ASSOCIATED WITH ROCK BURSTS AND GAS OUTBURSTS 36
2.6.1 Definition and background *36*
2.6.2 Field monitoring of mining-induced microseismicity *37*
2.6.3 Fracture-slip seismicity-generation mechanism *39*
2.6.4 Correlation between microseismicity and rock bursts and gas outbursts *40*
2.6.5 Evaluation and forecasting of underground hazards using microseismic monitoring *41*
2.6.6 Advances in modelling of seismic activities in rock formations *43*
2.6.7 Effect of heterogeneity on microseismic characteristics *46*
2.7 SUMMARY 48

CHAPTER 3 SEISMIC RESPONSE AND FRACTURING BEHAVIOUR OF COAL UNDER TRUE TRIAXIAL STRESS CONDITIONS 51

3.1 INTRODUCTION 51
3.2 EFFECTIVE DETECTION OF FRACTURING BEHAVIOUR 51
3.3 EQUIPMENT AND EXPERIMENTAL PROCEDURE 53
3.3.1 Experimental set-up *53*
3.3.2 Sample preparation *57*
3.3.3 Laboratory characterisation of mechanical and hydraulic properties of coal *58*
3.3.4 Experimental procedure for the true triaxial tests *63*
3.4 RESULTS AND ANALYSIS 65
3.4.1 Stress and hydraulic fracturing response *65*
3.4.2 Geometry of hydraulic and natural fractures *68*
3.4.3 Seismograms under different confining stresses *71*
3.4.4 Seismic and frequency spectrograms *74*
3.4.5 Seismic velocity tomography *81*
3.5 DISCUSSION 83
3.6 CONCLUSIONS 84

CHAPTER 4 FIELD MONITORING AND ANALYSIS OF MICROSEISMICITY ASSOCIATED WITH LONGWALL TOP COAL CAVING MINING 87

4.1 INTRODUCTION 87
4.2 THE FIELD MONITORING SITE 88
4.2.1 Geological conditions 88
4.2.2 Mining method and mine production schedule 88
4.2.3 Stress states assessed by numerical modelling 91
4.3 FIELD IMPLEMENTATION OF THE SEISMIC MONITORING TECHNIQUE 96
4.3.1 Field seismic monitoring at longwall panel K.-50/C in 2011 96
4.3.2 Field seismic monitoring around multiple longwall panels in 2016-2018 99
4.4 ANALYSIS OF MINING-INDUCED MICROSEISMICITY IN 2011 101
4.4.1 Active time-lapse seismic tomography measurements 101
4.4.2 Continuous microseismic monitoring measurements 101
4.5 ANALYSIS OF MINING-INDUCED MICROSEISMICITY DURING 2016-2018 106
4.5.1 Spatial distribution 107
4.5.2 Energy magnitude and scaling 112
4.5.3 Evolutional characteristics 114
4.6 DISCUSSIONS 119
4.6.1 Microseismic characteristics influenced by LTCC mining 119
4.6.2 A conceptual model for mining-induced microseismicity 121
4.7 CONCLUSIONS 124

CHAPTER 5 DEVELOPMENT OF A SHORT-TERM STATISTICAL METHOD TO FORECAST MICROSEISMICITY ASSOCIATED WITH LONGWALL COAL MINING 127

5.1 INTRODUCTION 127
5.2 A STATISTICAL MODEL TO FORECAST HAZARDOUS MICROSEISMICITY 127
5.2.1 Spatial, temporal and magnitude distribution 130
5.2.2 Parameter estimation 134
5.2.3 Risk assessment of hazardous events 136
5.3 APPLICATION OF THE FORECASTING METHODOLOGY AT COAL MINE VELENJE 137
5.4 RESULTS AND ANALYSIS 138
5.5 DISCUSSION 147
5.6 CONCLUSIONS 150

CHAPTER 6 A DFN-BASED MODEL TO SIMULATE MICROSEISMICITY ASSOCIATED WITH LONGWALL MINING 151

6.1 INTRODUCTION 151

6.2 METHODOLOGY DEVELOPMENT FOR MICROSEISMICITY MODELLING IN LONGWALL COAL MINES 152

6.2.1 DFN in FLAC^{3D} 153

6.2.2 Strain-softening post-failure constitutive model for coal 156

6.2.3 Fracture slip evaluation 157

6.2.4 Microseismic energy release 160

6.3 NUMERICAL MODELLING OF MICROSEISMIC EVENTS AT PANEL K. -50/C AT COAL MINE VELENJE 162

6.3.1 Model set-up and generation of a discrete fracture network 162

6.3.2 Modelling of longwall top coal caving mining 166

6.4 MODEL RESULTS AND ANALYSIS 166

6.4.1 Stress and failure responses to mining activities 166

6.4.2 Spatial distributions of simulated microseismicity 167

6.4.3 Frequency-magnitude distribution and released energy 169

6.4.4 Stress drop frequency 171

6.5 DISCUSSION 172

6.6 CONCLUSIONS 174

CHAPTER 7 MICROSEISMIC ANOMALY INFLUENCED BY LITHOLOGICAL HETEROGENEITY IN LONGWALL COAL MINING 175

7.1 INTRODUCTION 175

7.2 NUMERICAL SIMULATION OF LONGWALL COAL MINING-INDUCED MICROSEISMICITY 176

7.2.1 Numerical model description 176

7.2.2 Modelling scenarios 176

7.3 RESULTS: EFFECT OF ROCK STRENGTH ON SEISMIC RESPONSE 178

7.3.1 Stress and failure zone distribution 178

7.3.2 Frequency-magnitude distribution 180

7.3.3 Logarithmic released energy 181

7.3.4 Average stress drop 182

7.4 RESULTS: EFFECT OF FRACTURE ATTRIBUTES ON SEISMIC RESPONSE 183

7.4.1 Frequency-magnitude distribution 183

7.4.2 Logarithmic released energy 185

7.4.3 Average slipped fracture size 186

7.5 DISCUSSION 188
7.6 CONCLUSIONS 189

CHAPTER 8 UNLOADING INDUCED DYNAMIC STRESS PERTURBATIONS CONTRIBUTING TO ROCK BURSTS 191

8.1 INTRODUCTION 191
8.2 DYNAMIC STRESS DISTURBANCE INDUCED BY PILLAR RECOVERY 192
8.2.1 Problem definition 192
8.2.2 Dynamic instability criterion for pillar workings 194
8.2.3 Initial and transferred vertical pillar loads 194
8.2.4 Pillar recovery-induced dynamic stress 197
8.3 DYNAMIC STRESS DISTURBANCE INDUCED BY EXCAVATION UNLOADING 200
8.3.1 Problem definition 200
8.3.2 Dynamic responses of an existing excavation under transient wave incidence 201
8.3.3 Results and analysis 203
8.4 CONCLUSIONS 206

CHAPTER 9 UNLOADING INDUCED GAS-DRIVEN RAPID FRACTURE PROPAGATION IN COAL AND GAS OUTBURSTS 209

9.1 INTRODUCTION 209
9.2 A COAL AND GAS OUTBURST MODEL BASED ON FRACTURE MECHANICS AND GAS DYNAMICS 209
9.2.1 Conceptual model 209
9.2.2 Fracture behaviour subjected to intra-fracture effective stress 210
9.2.3 Estimation of outburst threshold limits 215
9.3 NUMERICAL IMPLEMENTATION OF THE OUTBURST MODEL 216
9.3.1 Evaluation of fracture behaviour 218
9.4 MODEL SET-UP FOR UNLOADING-INDUCED COAL AND GAS OUTBURSTS 219
9.5 RESULTS AND ANALYSIS 223
9.5.1 Coal outburst behaviour of the baseline model 223
9.5.2 Parametric investigations on coal outburst behaviour 229
9.6 DISCUSSION 231
9.7 CONCLUSIONS 233

CHAPTER 10 CONCLUSIONS AND RECOMMENDATIONS FOR FUTURE RESEARCH 235

10.1 SUMMARY OF THE PRESENT RESEARCH 235

10.2 MAIN CONCLUSIONS 236
10.3 RECOMMENDATIONS FOR FUTURE RESEARCH 239

REFERENCES 243

APPENDICES 1

APPENDIX 1 ANALYSIS OF RECORDED MICROSEISMICITY AT COAL MINE VELENJE IN 2016-2018 2
APPENDIX 2 MODELLED AGAINST RECORDED MICROSEISMICITY AT COAL MINE VELENJE IN 2011 22

List of Figures

Figure 1.1. Thesis structure and inter-relationships between individual chapters. 5

Figure 2.1. The cleat system in coal: (a) an image showing face and butt cleats in coal, and (b) the idealised bundled matchstick geometry (after Seidle *et al*., 1992). 8

Figure 2.2. Langmuir 3 parameter fitted high pressure isotherms of (a) seam 411 samples, (b) seam 412, (c) seam 413 from the Zofiowka Colliery Poland, and (d) from the #8 seam from the Monsacro Colleiry, Spain. Samples from each coal seam were grouped by particle size. All isotherms were measured in dry conditions and at a temperature of 45°C (after RWTH Aachen, 2016). 9

Figure 2.3. Schematic of loading system stiffness for rocks in compression (after Manouchehrian and Cai, 2015). 18

Figure 2.4. Schematic of dynamic instability (after Zubelewicz and Mroz, 1983). 19

Figure 2.5. Mining-induced energy change during excavations by steps (after Mitri *et al*., 1999; Sirait *et al*., 2013). 20

Figure 2.6. Work face conditions in an outburst zone (after Beamish and Crosdale, 1998; Williams and Weissmann, 1995)..... 24

Figure 2.7. Microseismic activities and gas flow rate during the week of increased gas emissions from 11 to 17 July 2011 (after Si *et al*., 2015a)..... 41

Figure 3.1. (a) True triaxial rock testing set-up equipped with loading, injection and acoustic systems, and (b) external view of the true triaxial rock testing unit..... 54

Figure 3.2. (a) Transducer configuration used during ultrasonic monitoring of the true triaxial experiment, and (b) trace types including straight transmission, oblique transmission and diffraction (XD: door normal to the x direction, YD: door normal to the y direction, ZC: cylinder normal to the z direction)..... 56

Figure 3.3. Cubic coal blocks used in the experiments: (a) coal block 1, and (b) coal block 2. 57

Figure 3.4. Permeability values for two coal samples measured using a Hassler cell (Each reading represents a different differential pressure across the sample also showing the Klinkenberg Effect). 59

Figure 3.5. (a) A schematic of the triaxial testing system, (b) 38 mm diameter core triaxial cell and stress-permeability testing components. 60

Figure 3.6. Axial stress-strain-permeability behaviour of coal determined through multi-stage triaxial testing: stress-strain curve and permeability values for (a) a coal sample cored parallel to bedding planes, and (b) and (c) two coal samples cored perpendicular to bedding planes. 61

Figure 3.7. (a) A schematic of the Brazilian testing system, (b) six 38 mm diameter coal disks prepared for Brazilian tests. 62

Figure 3.8. Stress-strain curves of the Brazilian tests for the six coal samples. 63

Figure 3.9. Stress, displacement and injection histories during the true triaxial experiments: (i) coal block 1, and (ii) coal block 2. 67

Figure 3.10. Interior fracture distribution in the split coal block 1 after hydraulic fracturing (only the hydraulic fracture and main natural fractures intruded by injected fluid are marked). 68

Figure 3.11. CT-scanned images before and after hydraulic fracturing for coal block 2: (a) surfaces, and (b) slice views (ONF: oil-intruded natural fractures; NNF: non-intruded natural fractures). 69

Figure 3.12. Reconstructed natural and hydraulic fracture networks from CT scan images: (a) 3D view for coal block 1, (b) front view for coal block 1, (c) 3D view for coal block 2, and (d) side view for coal block 2 (HF: hydraulic fractures; ONF: oil-intruded natural fractures; NNF: non-intruded natural fractures). 70

Figure 3.13. Examples of seismograms and Fourier spectrums under five hydrostatic confining stress conditions for coal black 1. The raypaths are classified to (a) S wave straight transmission (stS, pair ZC4-ZD4), (b) S wave oblique transmission (otS, pair YC14-YD9), and (c) S wave diffraction (dS, pair XC14-YC14). 72

Figure 3.14. Examples of seismograms and Fourier spectrums under five hydrostatic confining stress conditions for coal block 2. The raypaths are classified to (a) S wave straight transmission (stS, pair ZC14-ZD14), (b) S wave oblique transmission (otS, pair ZC19-ZD14), and (c) S wave diffraction (dS, pair ZC14-XD10). 73

Figure 3.15. S wave velocity as a function of hydrostatic confining stress. 74

Figure 3.16. Examples of seismic and frequency spectrograms for S wave straight transmission (stS, i: pair ZC4-ZD4 for coal block 1; ii: pair YC4-YD4 for coal block 2): (a) original seismograms, (b) processed seismograms (by subtracting the first scan from each subsequent scan), (c) seismic spectrogram, and (d) frequency spectrogram. 76

Figure 3.17. Examples of seismic and frequency spectrograms for S wave oblique transmission (otS, i: pair ZC19-ZD20 for coal block 1; ii: pair XC9-XD4 for coal block 2): (a) original seismograms, (b) processed seismograms (by subtracting the first scan from each subsequent scan), (c) seismic spectrogram, and (d) frequency spectrogram. 77

Figure 3.18. Examples of seismic and frequency spectrograms for S wave diffraction (dS, i: pair XC14-ZD5 for coal block 1, ii: pair YD14-ZD10 for coal block 2): (a) original seismograms, (b) processed seismograms (by subtracting the first scan from each subsequent scan), (c) seismic spectrogram, and (d) frequency spectrogram. 79

Figure 3.19. Examples of seismic and frequency spectrograms for P wave diffraction (dP, i: pair YD15-ZD10 for coal block 1; ii: pair XD20-YD20 for coal block 2): (a) original seismograms, (b) processed seismograms (by subtracting the first scan from each subsequent scan), (c) seismic spectrogram, and (d) frequency spectrogram. 80

Figure 3.20. S-wave velocity tomograms for coal blocks 1 (i) and 2 (ii): (a) before hydraulic fracturing, (b) after hydraulic fracturing, and (c) the difference induced by hydraulic fracturing. 82

Figure 3.21. Interpretation of seismograms in response to injection to naturally fractured blocks. 84

Figure 4.1. Schematic SW–NE trending geological cross-section of the Velenje coalfield (after Markič and Sachsenhofer, 2010). 88

Figure 4.2. (a) Schematic of the multi-level longwall top coal caving mining method implemented at the ultra-thick coal deposit of Coal Mine Velenje; (b) schematic of the multi-level longwall layout (after Jeromel *et al*., 2010; Si *et al*., 2015). 89

Figure 4.3. Mine production layout at -80 and -95 m production levels during 2016-2018 at Coal Mine Velenje, and the distribution of installed seismic stations of the microseismic monitoring system. The grey zone indicates the approximate shape of the central coal pillar protecting the main infrastructure in the production district. 90

Figure 4.4. Geometry of the geomechanical model containing the central coal pillar and surrounding longwall panels: (a) overview, and (b) cross-sections showing three geological structures. 92

Figure 4.5. Vertical stress field around the central coal pillar before the start of coal extraction at -80 m depth at Coal Mine Velenje (in October 2015): (a) 3D view, and (b) plan view. 93

Figure 4.6. Coal extraction simulated following the production schedule at K.-80/E and K.-80/B LTCC panels at Coal Mine Velenje 93

Figure 4.7. Stress variation in the central coal pillar affected by coal mining at K.-80/E and K.-80/B LTCC panels at Coal Mine Velenje. 94

Figure 4.8. Horizontal stress changes (monitor points) induced by the approaching LTCC face. 95

Figure 4.9. Vertical stress changes (monitor lines) induced by the approaching LTCC face. 95

Figure 4.10. The seismic monitoring data transmission system at Coal Mine Velenje (after Si *et al*., 2015) 97

Figure 4.11. Schematic of seismic sensor probe installation (after Si *et al*., 2015). 97

Figure 4.12. The time-lapse seismic tomography zone and the configuration of sensors used for microseismic monitoring and ventilation measurements at LTCC panel K.-50/C. 99

Figure 4.13. An example of recorded raw microseismic signals and the pickup of arrival time for P and S waves (the seismic event occurred at 19:35:23 on 26/09/2016, with a seismic energy of 10^4 J). 100

Figure 4.14. LTCC face K. -50/C P-wave velocity tomograms in X-component for the (a) 1st tomography campaign and (b) 2nd tomography campaign (after Si *et al*., 2015a). 101

Figure 4.15. Recorded microseismic events within 100 m ahead of the face-line at the K. -50/C LTCC panel level (after Si *et al*., 2015a) 102

Figure 4.16. Recorded weekly average released energy from microseismic events and event counts against face advance. 102

Figure 4.17. Frequency-magnitude plots of the recorded seismic events around LTCC panel K. -50/C during the study period. 104

Figure 4.18. Fitted *b* values at a two-week interval over a 12-week period showing a notable reduction in *b* as the longwall panel K. -50/C face-line reached the xylite-rich heterogeneous zone. 104

Figure 4.19. Recorded seismic energy released in two consecutive production weeks around LTCC panel K. -50/C at Coal Mine Velenje. 105

Figure 4.20. Fitted Gaussian distribution parameters for the microseismic event energy recorded during each production week of the study period at LTCC panel K. -50/C, Coal Mine Velenje. 106

Figure 4.21. Spatial distribution of weekly recorded microseismic events around six longwall panels at Coal Mine Velenje. 109

Figure 4.22. Spatial distribution of microseismicity associated with: (a) panel K.-80/E, (b) panel K.-80/B, (c) panel K.-80/D, (d) panel K.-80/C, (e) panel CD2, and (f) panel K.-95/E. 111

Figure 4.23. Microseismicity intensive regions associated with different longwall panels: (a) event count intensive regions (>30% of the maximum seismicity density), and (b) seismic energy intensive regions (>10^3 J/m^2) 112

Figure 4.24. Histograms of released energy of microseismic events recorded around: (a) all panels, (b) panel K.-80/B, and (c) panel K.-80/C. 113

Figure 4.25. Frequency-magnitude relationship of the recorded microseismicity around: (a) all panels, and (b) each panel. 114

Figure 4.26. Evolutional characteristics of LTCC mining-induced microseismicity on a daily basis around: (a) panel K.-80/B, and (b) panel K.-80/C. 116

Figure 4.27. Evolutional characteristics of LTCC mining-induced microseismicity on a weekly basis around: (a) panel K.-80/B, and (b) panel K.-80/C 117

Figure 4.28. The relationship between the daily event counts, average seismic energy released, average distance to the nearest operating longwall face and mining intensity. 120

Figure 4.29. Schematic illustrating longwall coal mining-induced microseismicity as a result of fracture slippage subjected to stress perturbations. 122

Figure 5.1 Schematic diagram illustrating the physical basis of the statistical forecasting method for hazardous microseismicity. 128

Figure 5.2. Flow chart of the forecasting procedure using longwall mining-induced microseismic sequence datasets with concurrent face advance records around a LTCC panel. 130

Figure 5.3. Frequency of daily microseismic event counts associated with longwall coal mining at three LTCC panels at the -80 m level at Coal Mine Velenje (the connecting lines are only guides for the eye). 131

Figure 5.4. Examples of recorded and fitted energy magnitude distribution for mining-induced microseismic events around different LTCC panels at Coal Mine Velenje: (a) histograms, and (b) cumulative distribution. 133

Figure 5.5. Examples of recorded and fitted spatial distribution with respect to the face-line for microseismic events around different LTCC panels at Coal Mine Velenje: (a) histograms, and (b) cumulative distribution. 135

Figure 5.6. Independence between the daily seismic event rate, average seismic energy released, and spatial distribution of recorded microseismicity around three longwall panels at Coal Mine Velenje. 139

Figure 5.7. Temporal, magnitude and spatial distributions of field monitored microseismicity within the time window around K.-80/D panel: (a) daily event counts frequency (the connecting lines are only guides for the eye), (b) energy magnitude distribution, and (c) spatial distribution with respect to the nearest longwall face in operation. 140

Figure 5.8. Time-varying temporal, magnitude and spatial seismic indicators decoupled from mining activities for microseismicity around panel K.-80/B. (Scaled daily event number under the average face advance rate represents the density of underlying fractures; the probability of a single microseismic event being a large event reflects the size distribution of underlying fractures; the probability of a single microseismic event being close to the longwall face reveals the spatial distribution of underlying fractures.)..... 141

Figure 5.9. Time-varying temporal, magnitude and spatial seismic indicators decoupled from mining activities for microseismicity around panel K.-80/D. (Scaled daily event number under the average face advance rate represents the density of underlying fractures; the probability of a single microseismic event being a large event reflects the size distribution of underlying fractures; the probability of a single microseismic event being close to the longwall face reveals the spatial distribution of underlying fractures.)..... 142

Figure 5.10. Time-varying temporal, magnitude and spatial seismic indicators decoupled from mining activities for microseismicity around panel K.-80/C. (Scaled daily event number under the average face advance rate represents the density of underlying fractures; the probability of a single microseismic event being a large event reflects the size distribution of underlying fractures; the probability of a single microseismic event being close to the longwall face reveals the spatial distribution of underlying fractures.)..... 143

Figure 5.11. Time-varying forecasted daily event number, and forecasted probability that at least one large microseismic event, a microseismic event close to the face-line, and a hazardous microseismic event occurs on the day of forecasting around panel K.-80/B. 144

Figure 5.12. Time-varying forecasted daily event number, and forecasted probability that at least one large microseismic event, a microseismic event close to the face-line, and a hazardous microseismic event occurs on the day of forecasting around panel K.-80/D. 145

Figure 5.13. Time-varying forecasted daily event number, and forecasted probability that at least one large microseismic event, a microseismic event close to the face-line, and a hazardous microseismic event occurs on the day of forecasting around panel K.-80/C. 146

Figure 5.14. Recommended upper limits of daily face advance given probability thresholds of hazardous events for (a) panel K.-80/B, (b) panel K.-80/D, and (c) panel K.-80/C. 149

Figure 6.1. Flow chart for the modelling procedure. 153

Figure 6.2. (a) Spatial distribution and (b) histogram of released energy of microseismic events recorded around LTCC panel K. -50/C at Coal Mine Velenje during 6 to 12 June 2011..... 155

Figure 6.3. Cumulative distribution function of the power law distribution. 156

Figure 6.4. (a) Strain-softening post-failure behaviour; and (b) Mohr-Coulomb failure criterion for intact and failed coal under confinement. 157

Figure 6.5. Slip test points on the periphery and centre of a circular fracture in local coordinates. 159

Figure 6.6. Flow diagram for the evaluation of a shear slip leading to microseismicity. 159

Figure 6.7. Failure criterion for fracture slip and associated stress drop after the fracture slips. 161

Figure 6.8. Mining geometry and geological implementation: (a) 3D model geometry, and (b) a cross-section of the model along the face advance direction at LTCC panel K.-50/C. 163

Figure 6.9. Estimation of the range of fracture sizes through the energy released from microseismic events during an eight-week coal production period from 23 May to 17 July 2011 around LTCC panel K.-50/C at Coal Mine Velenje..... 165

Figure 6.10. Spatial distribution of DFN following a power law relationship of fracture size in the model domain constructed. 165

Figure 6.11. Mining-induced failure zone (in either shear or tensile mode) in the advancing LTCC panel K.-50/C during the period 30 May to 5 June, 2011. 167

Figure 6.12. Major and minor principal stress profiles ahead of the LTCC panel K.-50/C face-line in the horizontal central cross-section of the LTCC face..... 167

Figure 6.13. Three-dimensional distribution of mining-induced microseismicity and the released energy at LTCC panel K.-50/C during coal production from 6 to 12 June 2011 (the colour legend is in log scale). 168

Figure 6.14. Simulated weekly microseismic events ahead of the longwall face located within the depth interval [-325m, -355m], and up to 100 m ahead of the longwall face as the LTCC face at panel K.-50/C advances..... 169

Figure 6.15. Frequency-magnitude plots of the recorded and modelled seismic events for the LTCC panel K.-50/C at Coal Mine Velenje. 170

Figure 6.16. Bi-weekly variation of *b* values for recorded and modelled microseismic events. 170

Figure 6.17. Comparison of the recorded and modelled seismic energy released in the first two production weeks at LTCC panel K.-50/C. 171

Figure 6.18. Fitted weekly Gaussian parameters for recorded and modelled microseismic events: (a) mean value μ, and (b) standard deviation σ. 171

Figure 6.19. Histogram of stress drops for microseismic events during each production week at LTCC panel K.-50/C..... 172

Figure 7.1. Mining geometry and geological implementation of the xylite-rich zone: (a) 3D model geometry, and (b) the central cross-section of the model along the face advance direction. 177

Figure 7.2. Distribution of DFNs located at the panel level [-330 m, -350 m] following power law relationship with $a_c = 2.7$, $a_h = 1.8$, $\alpha_h = 0.7\alpha_c$. 178

Figure 7.3. Failure zone distribution around the working longwall face for the scenario $\sigma_{ch} = 2\sigma_{cc}$, $\sigma_{th} = 2\sigma_{tc}$: (a) during Week 30 May to 5 June, and (b) during Week 11 to 17 July. 179

Figure 7.4. Major and minor principal stress profiles ahead of the longwall face in the central cross-section of the model domain for the scenario $\sigma_{ch} = 2\sigma_{cc}$, $\sigma_{th} = 2\sigma_{tc}$. 179

Figure 7.5. The bi-weekly *b* values for frequency-magnitude distribution of the recorded and simulated microseismic events over the monitoring period..... 180

Figure 7.6. Examples of b values obtained through regression fitting for the recorded and simulated microseismic events during 1 to 14 August 2011. 181

Figure 7.7. Example of weekly histograms of the logarithmic event energy for the recorded seismicity and simulated seismicity for the scenario $\sigma_{ch} = 2\sigma_{cc}$, $\sigma_{fh} = 2\sigma_{fc}$: (a) during Week 23 to 29 May 2011, and (b) during Week 1 to 7 August 2011. 182

Figure 7.8. The fitted Gaussian distribution parameters to the logarithmic event energy for the recorded and simulated seismicity over the monitoring period: (a) mean value μ, and (b) standard deviation σ. 182

Figure 7.9. Simulated average stress drops over the twelve-week monitoring period. ... 183

Figure 7.10. Histograms of stress drops for the scenario $\sigma_{ch} = 2\sigma_{cc}$, $\sigma_{fh} = 2\sigma_{fc}$: (a) during Week 30 May to 5 June 2011, and (b) during Week 1 to 7 August 2011. 184

Figure 7.11. The bi-weekly b values for frequency-magnitude distribution of the recorded and simulated microseismic events over the monitoring period. 184

Figure 7.12. Examples of b values obtained through regression fitting for the recorded and simulated microseismic events during 1 to 14 August 2011. 185

Figure 7.13. Examples of weekly histograms of the logarithmic event energy for the recorded seismicity and simulated seismicity for the scenario $a_h = 1.8$, $\alpha_h = 0.7\alpha_c$: (a) during Week 23 to 29 May 2011, and (b) during Week 1 to 7 August 2011. 186

Figure 7.14. The fitted Gaussian distribution parameters to the logarithmic event energy for the recorded and simulated seismicity over the monitoring period: (a) mean value μ, and (b) standard deviation σ. 186

Figure 7.15. Average slipped fracture sizes over the monitoring period. 187

Figure 7.16. Histograms of average slipped fracture sizes for the scenario $a_h = 1.8$, $\alpha_h = 0.7\alpha_c$: (a) during Week 30 May to 5 June 2011, and (b) during Week 1 to 7 August 2011. 188

Figure 8.1. Schematic of instantaneous pillar recovery and induced dynamic response of adjacent pillar workings: (a) before pillar recovery, and (b) after pillar recovery. 193

Figure 8.2. Pillar geometry and the zone of influence used in the PAT-based method... 196

Figure 8.3 Dynamic response of a pre-stressed pillar subjected to a suddenly applied loading. 197

Figure 8.4. Loading history of a transferred pillar load. 198

Figure 8.5. Dynamic amplification coefficients of a pillar for different extraction time ($n = t_0/T$). 200

Figure 8.6. Schematic illustration showing the superposition principle applied to the stress analysis of a pre-stressed excavation opening subjected to dynamic disturbance. 201

Figure 8.7. A schematic diagram showing the dynamic response of the existing excavation subjected to cylindrical wave excitation..... 202

Figure 8.8. Numerical results of the DSCF at the pre-existing excavation boundary. 204

Figure 9.1. Schematic representation of fracture opening in relation to effective stress changes ahead of a working face (modified after Feldman *et al.*, 2017)..... 210

Figure 9.2. Stress intensity factors K_I as a function of fracture radius a_0 and effective stress p-σ_{min}. Fractures are deemed to propagate if $K_I \geqslant K_{Ic}$. 215

Figure 9.3. Intra-fracture gas pressure p_{lim} as a function of fracture toughness K_{Ic} and fracture radius a_0 for fractures located close to a working face. Fractures are deemed to propagate if $p_{lim} \leqslant p_{equ}$. 216

Figure 9.4. Flow chart for the modelling procedure. 217

Figure 9.5. Flow diagram for the calculation of the fracture expansion and propagation in a model element at time t. 220

Figure 9.6. General stratigraphy and model geometry of roadway development in the modelled coal seam. 222

Figure 9.7. Intra-fracture gas pressure distribution caused by gas desorption after each roadway development step (Unit: Pa). 224

Figure 9.8. Extension of the coal outburst zone over time: (a) 60 s, (b) 120 s, (c) 180 s, (d) 240 s, (e) 300 s and (f) 360 s after reaching the outburst prone zone. 224

Figure 9.9. Time since fracture expansion begins and gas desorption from coal elements is initiated (only the left half of the outburst prone zone is shown). 225

Figure 9.10. Minor principal stress contours as the development face reaches the outburst prone zone (only the left half of the outburst prone zone is shown). 226

Figure 9.11. Evolution of intra-fracture gas pressure and associated fracture behaviour at monitoring point 1. 226

Figure 9.12. Minor principal stress, intra-fracture gas pressure and effective stress profiles along the central trace line at different times after the onset of the outburst. 227

Figure 9.13. Minor principal stresses and intra-fracture gas pressures over time at different monitoring points after the onset of the outburst. 228

Figure 9.14. Fracture radius profile along the central trace line in the outburst prone zone. 228

Figure 9.15. Fracture radius growth at different monitoring points over time. 229

Figure 9.16. Fracture propagation velocity variation over time. 229

Figure 9.17. Influences of (a) K_{Ic}, (b) a_0, (c) p_0, and (d) σ_v on variations in intra-fracture gas pressure and fracture radius close to a development face. 230

Figure 9.18. Influences of (a) K_{Ic}, (b) a_0, (c) p_0, and (d) σ_v on the ejected volume of coal over time. 231

List of Tables

Table 2.1. Empirical thresholds and theoretical criteria for rock bursts. 15
Table 2.2. Factors affecting coal and gas outburst risk in coal mining. 22
Table 2.3. Empirical thresholds and theoretical criteria for coal and gas outbursts. 25
Table 3.1. Physical, mechanical and hydraulic properties for coal samples tested. 61
Table 3.2. Tensile strength and fracture toughness for the coal samples tested. 63
Table 3.3. Experimental operations in sequential stages of the true triaxial experiment. 66
Table 4.1. Longwall panel operational sequence and the associated recorded microseismicity during the monitoring period (29/02/2016-20/05/2018) at Coal Mine Velenje. 91
Table 6.1. Rock mechanical properties used in the K.-50/C LTCC model (after Si *et al*., 2015c; Zavšek, 1993). 164
Table 8.1. Dynamic effects of the existing excavation subjected to instantaneous unloading disturbance. 206
Table 9.1. Model parameters used in the baseline model. 222
Table 9.2. Parameter magnitude ranges used in the parametric investigations. 223

Nomenclature

Alphabet

Symbol	Description	Units
A	Content of gas contained in the coal	m^3
	Cross-sectional area	m^2
a	Power law scaling exponent	dimensionless
	Radius of the existing excavation	m
	Radius of a penny-shaped fracture	m
$\overline{a}$	Radius of the new excavation	m
b	A measure of the scaling of seismicity magnitude distribution	dimensionless
C	Gas concentration	dimensionless
C_f	Cleat volume compressibility	MPa^{-1}
c	Cohesion	MPa
	Half of the fracture length	mm
c_f	Cohesion along the fracture plane	MPa
c_p	Peak cohesion for intact coal	MPa
c_r	Residual cohesion for failed coal	MPa
D	Diffusion coefficient	m^2/s
	Diameter of the test specimen	mm
d	Distance from microseismicity to the longwall face in operation	m
	Average fracture spacing	m
	Thickness of a penny-shaped fracture	m
E	Young's modulus	GPa
	Seismic energy released	J
E_k	Released kinetic energy	J
E_{min}	Minimum seismic energy released	J
e	Extraction ratio	%
G	Shear modulus	GPa
g	Gravity acceleration	m/s^2
H	Mining depth	m
h	Thickness of the loosened surficial microlayer	m
K	Bulk modulus	GPa
	Elastic stiffness	N/m
K_I	Stress intensity factor	$MPa \cdot m^{1/2}$
K_{Ic}	Fracture toughness	$MPa \cdot m^{1/2}$
k	Permeability	m^2
	Shape parameter of Weibull distribution	dimensionless
k_0	Initial permeability	m^2
L	Length of coal	m
l	Fracture size	m

	Scale parameter of Weibull distribution	dimensionless
M_L	Richter magnitude of seismicity	dimensionless
M_{min}	Minimum energy magnitude	dimensionless
M_0	Seismic moment	N·m
m	Number of time intervals within the time window	dimensionless
	Mass of the pillar	kg
N	Cumulative number of seismic events	dimensionless
	Total number of fractures	dimensionless
n	A constant related to coal type	dimensionless
	Seismic event counts over each time interval	dimensionless
$n(l)$	Number of fractures with size l per unit volume	dimensionless
P	Gas pressure	MPa
	Load at failure	N
∇P	Pressure gradient	MPa/m
P_L	Langmuir pressure	MPa
P_ε	Pressure at which the swelling strain $\varepsilon_s = 0.5\varepsilon_{smax}$	MPa
P_1	Inlet gas pressure	MPa
P_2	Outlet gas pressure	MPa
p	Pore pressure	MPa
p_{atm}	Atmospheric pressure	MPa
p_{equ}	Intra-fracture gas pressure at adsorption/desorption equilibrium	MPa
p_0	Initial pore pressure	MPa
Q	Gas flow rate	m^3/s
R	Disc radius	mm
	Fracture radius	m
	Dynamic amplification coefficient	%
R_{max}	Maximum dynamic amplification coefficient	%
r	Distance from the diffusion source	m
	Distance between the source and receiver	m
	Face advance rate	m/day
	Distance from a point to the centre of the existing excavation	m
$\bar{r}$	Average face advance rate during the previous monitoring period	m/day
	Distance from a point to the centre of the new excavation	m
r_0	Excavation spacing	m
T	Natural vibration period of the pillar	s
ΔT	Period of a time window	day
t	Time of gas molecule diffusion	s
	Thickness of the specimen measured at the centre	mm
	Time to forecast hazardous seismicity potential	day
	Elapsed time since excavation unloading	s
	Gas desorption time	s
Δt	Period of a time interval	day
t_0	A time constant associated with coal particle size	s
	Duration of pillar load transfer	s
t_1	Starting time for bounding a group of P and S waves	s
t_2	End time for bounding a group of P and S waves	s
U	Total released energy in the extraction	J
U_C	Increased strain energy	J
U_d	External energy from the dynamic disturbance	J
U_f	Energy needed to be consumed in fracturing rock/coals	J

U_m	Stored strain energy in mined-out rock	J
U_s	Strain energy stored in the rock/coal to be extracted	J
$u_P(t)$	Time-integrated values of particle vibration velocities of P waves	m
$u_S(t)$	Time-integrated values of particle vibration velocities of S waves	m
V	Adsorbed gas volume per unit mass of coal	m^3/kg
	Volume of the 3D model domain	m^3
V_c	Volume of a penny-shaped fracture	m^3
V_{coal}	Volume of surficial microlayers on both sides of the fracture	m^3
V_g	Volume of desorbed gas	m^3
V_i	Adsorbed volume for the i^{th} gas component per unit mass of coal	m^3/kg
V_L	Langmuir volume per unit mass of coal	m^3/kg
V_{Li}	Langmuir volume for the i^{th} gas component per unit mass of coal	m^3/kg
V_{total}	Initial volume of adsorbed gas	m^3
$V(t)$	Desorbed gas volume after time t	m^3
v_P	P wave velocities travelling through the medium	m/s
v_S	S wave velocities travelling through the medium	m/s
W	Work done by external forces	J
	Total work done to form a disk-shaped fracture	J
W_E	Elastic strain energy accumulated before rock failure	J
W_P	Dissipated energy in the post-failure stage	J
W_r	Released energy	J
W_S	Work done on mining support	J
W_{sp}	Energy dissipated by plastic deformation during unloading process	J
W_{st}	Stored energy in rock	J
w_e	Effective width for non-square pillars	m
y_s	Increment in pillar deformation	m

Greek symbol

Symbol	Description	Units
α	Half of the arc distance where the load is distributed radially	mm
	Density term	dimensionless
	Compressional wave number	dimensionless
β	Strength reduction factor	dimensionless
	Shear wave number	dimensionless
ε	Strain	%
ε_e	Elastic strain	%
ε_p	Plastic strain	%
ε_s	Volumetric swelling strain	%
ε_{smax}	Maximum volumetric swelling strain	%
η	Ratio of current over previous face advance rates	%
	Dynamic effect coefficient	%
θ	Angle at the centre of the existing excavation	°
$\bar{\theta}$	Angle at the centre of the new excavation	°
κ	Ratio of P to S wave velocities	%
	Diffusivity of coal	min^{-1}
λ	Average seismic event count	dimensionless
μ	Gas viscosity	Pa·s
	Coefficient of friction	dimensionless

	Mean value of a Gaussian distribution	dimensionless
μ_{df}	Dynamic friction coefficient along the fracture	dimensionless
μ_{sf}	Static friction coefficient along the fracture	dimensionless
υ	Poisson' ratio	dimensionless
ρ	Density of medium	kg/m^3
σ	Effective hydrostatic stress	MPa
	Normal stress on the fracture plane	MPa
	Standard deviation of a Gaussian distribution	dimensionless
$\Delta\sigma$	Change in the effective horizontal stress	MPa
σ_0	Initial effective hydrostatic stress	MPa
σ_c	Uniaxial compressive strength	MPa
σ_{cri}	Pillar load under the critical equilibrium state	MPa
σ_d	Dynamic pillar load	MPa
$\Delta\sigma_d$	Maximum dynamic pillar load	MPa
σ_{eff}	Effective stress	MPa
σ_H	Maximum horizontal *in situ* stress	MPa
σ_h	Minimum horizontal *in situ* stress	MPa
σ_L	Radial stress of cross section in disturbed zone	MPa
σ_{max}	Maximum horizontal stress on the boundary of an opening	MPa
σ_{min}	Minor principal stress	MPa
$\Delta\sigma_n$	Stress change normal to the fracture plane	MPa
σ_p	Peak stress	MPa
σ_r	Residual stress	MPa
σ_{rm}	Triaxial rockmass strength	MPa
σ_s	Static pillar load	MPa
$\Delta\sigma_s$	Increment in vertical pillar load	MPa
σ_t	Tensile strength	MPa
σ_{tc}	Residual tensile strength	MPa
σ_v	Vertical pillar load	MPa
	Vertical *in situ* stress	MPa
$\Delta\sigma_v$	Incremental vertical stress	MPa
$\sigma_{\theta max}$	Maximum tangential stress of cross section in disturbed zone	MPa
$\bar{\sigma}_{\theta\theta}$	Steady-state dimensionless tangential stress	dimensionless
σ_1	Maximum principal stress	MPa
σ_3	Minimum principal stress	MPa
τ	Shear stress	MPa
$\bar{\tau}$	Normalised elapsed time since excavation unloading	dimensionless
$\Delta\tau$	Shear stress drop	MPa
τ_{df}	Dynamic strength of the fracture surface	MPa
τ_s	Shear strength of intact rock	MPa
τ_{sf}	Resistance prior to fracture slip	MPa
Φ	A stress intensity factor coefficient	dimensionless
ϕ	Porosity	%
ϕ_0	Initial porosity	%
φ	Frictional angle	°
φ_d	Dynamic frictional angle	°
φ_s	Static frictional angle	°
ω	Circular frequency	rad/s

Chapter 1 Introduction and objectives

1.1 Research objectives

The advancement of mining technology allows coal mines to go deeper with ever increasing stress and gas emission conditions. The deep coal seams or rock masses are subjected to severe conditions compared to shallow ones, such as rock burst and gas outburst hazards. As the mining depth increases, these hazards become one of the urgent issues which are closely related to the effective and safe exploitation of underground resources and the stability of surrounding rock around the excavations.

Being one of the violent failure modes of rock mass, rock burst is a dynamic mechanical phenomenon in which the rock mass or geological structure under high stress or equilibrium state is perturbed by excavation to suddenly release the stored strain energy, inducing part of the surrounding rock to dramatically extrude or eject (Ortlepp and Stacey, 1994). Coal and gas outbursts experienced during coal mining are a violent dislodgement and ejection of coal as a consequence of internal gas energy and strain energy release, usually accompanied with a powerful discharge of large amounts of gas in a very short period of time (Farmer and Pooley, 1967; Hargraves, 1980; Jackson, 1984; Shepherd *et al*., 1981). In some outbursts, as much as hundreds of tonnes of fragmented coal mass, and thousands of cubic meters of methane or carbon dioxide are emitted from a working face over a period of several seconds (Khristianovich and Salganik, 1983). As a consequence, these hazards usually bring about disastrous outcomes, for instance casualties, equipment damage, and even the abandonment of underground structures (Jackson, 1984; Mazaira and Konicek, 2015). Furthermore, this can lead to huge economic loss and severely delay the production schedule.

Since the first rock burst event in the 18th century (Linkov, 1996) and the first recorded coal and gas outburst in the Issac Colliery, France, in 1843 (Cao *et al*., 2001), tens of

thousands of rock bursts and gas outbursts have been experienced in underground mines all over the world. Beamish and Crosdale (1998) summarised the global outburst-prone areas and major incidents in most coal-producing countries. In South Africa, gold was discovered near present-day Johannesburg in 1886, and earth tremors and rock bursts were already a cause of concern to mining communities as early as the first decade of the 20th century (Durrheim *et al*., 2011). A great deal of rock mechanics and seismological research has been conducted since 1964. Large seismic events causing serious damage to surface and/or mine infrastructure first occurred in the Free State region in the 1970s. Mining-induced seismicity and rock bursts in China have been reported at 102 coal mines and 20 metallic mines. About 83.6% of the seismic activities occur in coal mines and the disasters are more serious in coal mines than in others. In general, a majority of deep mines have experienced rock burst and gas outburst problems and suffered seismic damage to various degrees.

Rock bursts and coal/gas outbursts have affected coal production at Coal Mine Velenje in Slovenia since the early days of mine production. The mine experienced a rock burst event at a longwall face on 02 September 1994, when one miner died and a further two miners were injured. Another major coal and gas outburst in the mine took place in 2003, when two miners lost their lives, and the longwall district in question lost one month's worth of production. Besides such major incidents, Coal Mine Velenje experiences at least one uncontrolled gas emission related stoppage each year, losing 5 days' worth of production (35,000 tonnes of coal) per event on average. After 2012, the intensity of rock bursts and gas outbursts at the mine increased and culminated in a stronger event on 15 October 2013, when 7 miners were injured. Later on, two rock bursts were reported at the mine on 19 March and 17 April 2018 respectively, the latter of which caused severe damage of floor in an around 25 m-long section of a gateroad.

In Spain, the underground operations at S.A. Hullera Vasco-Leonesa often experienced gas outburst and sudden emissions during roadway development. In 2009, a coal and gas outburst affected a 40 metres length of a development heading in the virgin section of the coal seam. In October 2013 six miners lost their lives in one of the biggest mine disasters in Spain in recent years, and the gas outburst experienced released around 12,000 m^3 of methane in a few seconds.

Mining districts H, D and G at Zofiówka coal mine of JSW have been identified as the areas most prone to rock bursts as well as coal and gas outburst hazards in the Zofiówka-Borynia complex. In the years 2003-2018, there have been a number of incidents of seismic events in districts H and D. In particular, the coal and gas outburst which occurred during the drivage of district D transportation incline in seam 409/4 killed 3 miners in 2005. More recently, 5 miners lost their lives as a result of a large rock burst event that occurred in district H, seam 409/4 on 5 May 2018.

It is generally recognised that dynamic hazards manifest themselves in different ways depending on variations in rock types and conditions of gas pressure and stress. In this respect, both dynamic phenomena in coal mining are considered as dynamic unstable failure problems as a consequence of the combined effects of rock/coal properties, stress and gas pressure conditions, geological structures and mining activities, with the ejected materials ranging from massive rock fragments to fine particles of coal accompanied with gas. Both underground seismic hazards, therefore, were investigated in this research in order to gain a better and more comprehensive understanding.

In recent years, extensive investigations have been carried out in regard to the mining hazard types and characteristics, mining conditions and measurement techniques, and mitigation and prevention methods, but these hazards in deep coal mines have still not been fundamentally solved. This calls for a systematic and insightful research into the mechanism and combatting methods of the violent rock and coal failure phenomenon.

To be specific, knowledge gaps on the following aspects still exist:

- seismic response of naturally fractured coal to stress and fracturing has not been well investigated;
- little systematic field investigation has been conducted to reveal the respective role of stress concentration, fracture field, and mining intensity in contributing to microseismicity associated with longwall coal mining;
- no effective physical-based short-term forecasting methods are available against rock bursts and gas outbursts in coal mining;
- the synthetic microseismicity in a 3D numerical model has not been well developed and calibrated against continuously processed microseismic monitoring datasets;

- the role of dynamic stress perturbances induced by excavation unloading in contributing to unstable rock failure such as rock bursts has not been quantified; and
- the accelerated propagation of gas-containing fractures subparallel to the unloading face in coal and gas outbursts has not been fully understood.

To this end, the following aspects were investigated in order to gain a better insight into mining induced microseismicity and dynamic unstable failure of rock/coal, as well as forecast underground seismic hazards and reduce the potential for those hazards:

- True triaxial experiments to monitor seismic response of naturally fractured coal to stress and fracturing
- A conceptual model for mining-induced microseismicity considering fracture abundance, fracture slip criterion and the resulting stress drop
- A short-term forecasting method for rock bursts and gas outbursts based on the fracture-slip seismic-generation mechanism
- A discrete fracture network (DFN) based model to numerically replicate longwall coal mining-induced microseismicity
- Theoretical verification of excavation induced dynamic stress perturbations on underground structures and openings
- A coal and gas outburst model considering the rapid propagation of gas desorption driven fractures

The detailed investigation into rock burst and coal and gas outburst hazards is conducive not only to fundamental research but also to practical applications. Therefore, this research is expected to contribute to the safe exploitation of underground coal resources and development of mitigation measures.

1.2 Thesis overview

This thesis presents research into the monitoring, forecasting and modelling of mining-induced microseismicity sequentially, followed by an investigation into mechanisms of rock bursts and coal and gas outbursts. The main structure of the thesis is depicted in Figure 1.1.

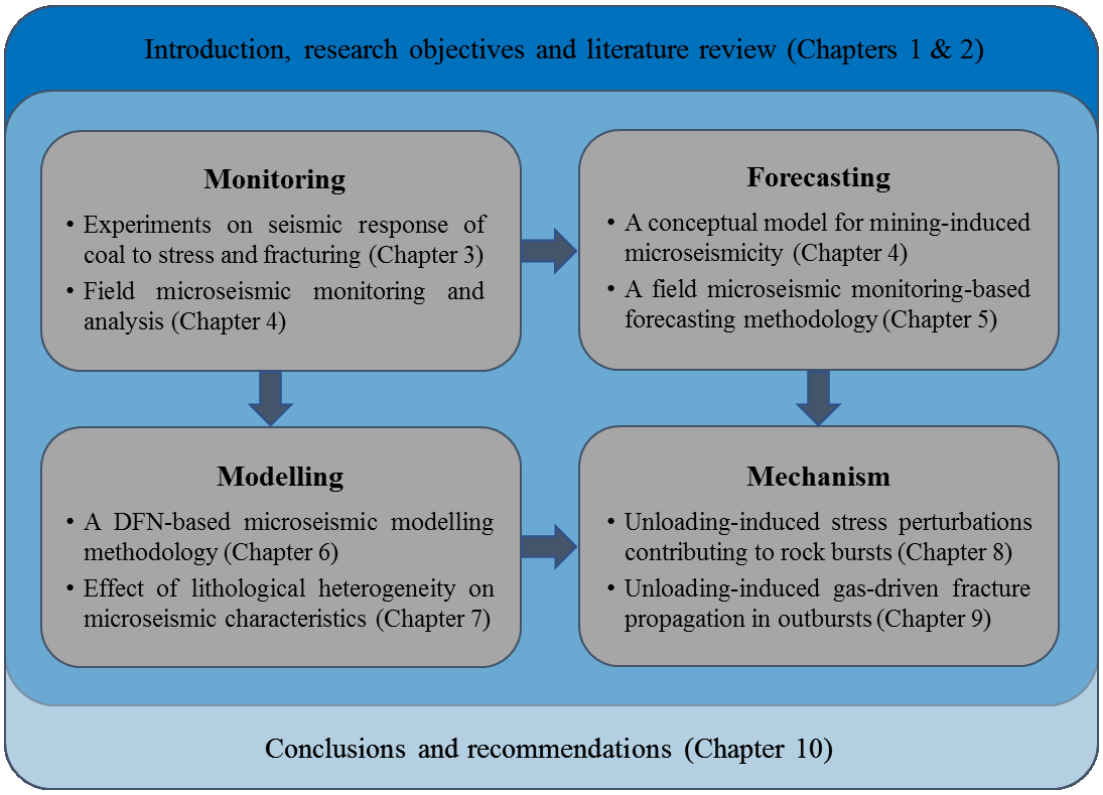


Figure 1.1. Thesis structure and inter-relationships between individual chapters.

Chapter 2 presents the fundamentals of coal structure, gas adsorption mechanism and permeability behaviour in coal, followed by an extensive literature review on the monitoring, mechanism and forecasting of rock burst and coal and gas outburst hazards. Knowledge gaps, which are to be addressed in the main body of the thesis, are identified.

Chapter 3 presents experimental investigations into seismic response and fracturing behaviour of naturally fractured coal blocks under true triaxial stress states. The fracturing behaviour, including the initiation of hydraulically induced fracture and its subsequent interaction with natural fractures, is analysed and interpreted in combination with the associated seismograms. The understanding of seismic response of coal obtained formed the background for the analysis and interpretation of field recorded microseismicity in coal mines.

Chapter 4 presents the field monitoring and analysis of microseismicity associated with Longwall Top Coal Caving (LTCC) mining at Coal Mine Velenje in 2011 and during 2016-2018 respectively. A conceptual model for mining-induced microseismicity has been developed based on the fracture slip seismicity-generation

mechanism, which highlights the role of attributes of pre-existing natural fractures throughout the active mining region. Based upon the conceptual model and the premise that natural fractures are characterised by spatial continuity, a data-driven yet physics-based statistical forecasting methodology has been established using microseismic monitoring records with concurrent face advance records in Chapter 5.

Chapter 6 presents the development of a microseismicity modelling approach combining deterministic stress and failure analysis and stochastic fracture slip evaluation. The modelling approach developed is adopted to simulate the evolution of microseismicity induced by the progressive face advance in a longwall panel over an eight-week period in 2011 at Coal Mine Velenje. Following Chapter 6, Chapter 7 presents the application of the modelling approach to further simulate the longwall coal extraction towards a heterogeneous zone detected from active seismic tomography measurements, in an effort to reveal the effects of heterogeneity (coal strength and fracture attributes) on microseismic characteristics.

In Chapter 8 and Chapter 9, rock bursts and coal and gas outbursts are categorised as dynamic unstable failure problems, which are the transformation from a critical equilibrium state to an unstable state as a consequence of mining operations such as dynamic excavation unloading. Chapter 8 examines two types of unloading (pillar recovery and mine opening excavation) induced dynamic stress perturbations contributing to rock bursts by quantifying the dynamic stress concentration around underground openings and structures. Chapter 9 presents the theoretical formulation and numerical implementation of a coal and gas outburst model based on fracture mechanics and gas dynamics, which is then applied to model coal and gas outbursts during roadway developments and to identify key factors affecting outburst initiation and its temporal evolution.

Finally, Chapter 10 summarises the main conclusions from the research presented and makes recommendations for future research.

Chapter 2 Previous research on underground hazards in coal mining

2.1 Introduction

This chapter presents basic principles and previous research on the mechanisms, monitoring and forecasting of rock burst and coal and gas outburst hazards in coal mining. The chapter starts from the fundamentals of coal structure, gas adsorption mechanism and permeability behaviour in coal. Characteristics of rock burst and coal and gas outburst hazards are then summarised, followed by the generalisation of both hazards as dynamic unstable failure problems. Next, mining-induced microseismicity intimately associated with rock bursts and coal outbursts are reviewed, and previous research on forecasting and assessment of rock bursts and coal outbursts using microseismic monitoring data are introduced. Knowledge gaps in the literature are also identified and addressed.

2.2 Coal as a porous gas reservoir

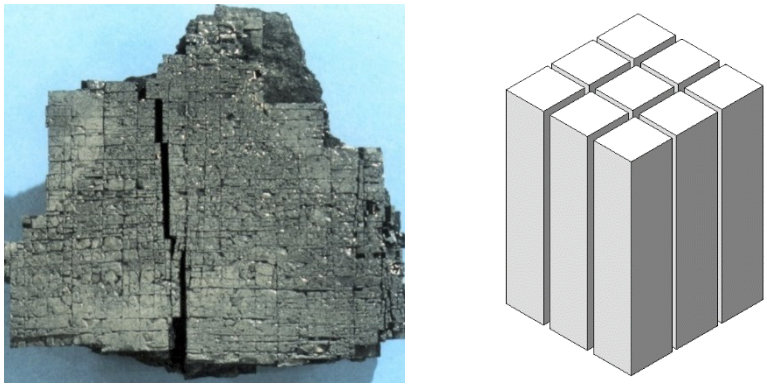
2.2.1 Coal structure

As a porous medium, coal can be characterised by two porosity systems: an interconnected, uniformly distributed fracture network with pore sizes in the range between 10 nm and 100 nm, and matrix blocks containing heterogeneous micro-pores with diameters from 0.5 nm to 1.0 nm (Paterson, 1986).

The fracture network is made up of two sets of orthogonal cleats with a spacing between 2 and 25 mm (Figure 2.1a), which act as major conduits for fluid flow (Seidle, 2011). The primary fracture system, defined as face cleats, are continuous, well-developed, nearly parallel fissures throughout coal seams. The secondary fracture system, referred to as butt cleats, are discontinuous, less well-developed fissures

perpendicular to and often terminating at the face cleats. Both sets of cleats are subvertically oriented with respect to the bedding planes. Cleats are generated as a result of lateral compressive tectonic stress, and often terminate at stratigraphic boundaries with mechanical heterogeneity (Close, 1993).

The fracture network of reservoirs can be represented by idealised models such as sheets, match-sticks, cubes and cubes with impermeable horizontal edges (Reiss, 1980). The dual porosity nature of coal has been best characterised by the bundled matchstick geometry, as shown in Figure 2.1b. While face and butt cleats are well defined in this model, the bedding planes are not considered due to their limited role in contributing to gas migration. This model is widely accepted in theoretical investigations on the stress dependence of coal permeability (Seidle *et al*., 1992; Shi and Durucan, 2004).



(a) (b)

Figure 2.1. The cleat system in coal: (a) an image showing face and butt cleats in coal, and (b) the idealised bundled matchstick geometry as proposed by Seidle *et al*., 1992).

2.2.2 Gas sorption and desorption behaviour

Gas exists in 3 states in coal seams, i.e., adsorbed gas on pore surface, free gas, and dissolved gas in water (Paterson, 1986). But coal deposits show considerable differences from natural gas reservoirs in that most of the gas is adsorbed on the surface of micro-pores, rather than compressed and contained in pore structures (Jeu *et al*., 1988). Typically about 95% of gas contained in the coal is in the adsorbed state, while the rest exists in the gaseous state in void spaces (Odintsev, 1997). The adsorbed and

free gas are in thermodynamic equilibrium, which is dependent on the gas pressure and temperature.

Single-component gas adsorption within the coal seam is assumed to follow the Langmuir isotherm equation (Langmuir, 1918), which is given by:

$$V = \frac{V_L P}{P_L + P} \tag{2.1}$$

where V is the adsorbed gas volume per unit mass of coal at pressure P, V_L is the Langmuir volume, which is the monolayer volumetric adsorption capacity per unit mass of coal, and P_L is the Langmuir pressure, referred to as the pressure at which half of the Langmuir volume is adsorbed. As examples, high-pressure methane adsorption isotherms measured on dry samples from Zofiowka Colliery seams 411, 412, 413 and the Monsacro Colliery #8 seam at 45°C are shown in Figure 2.2.

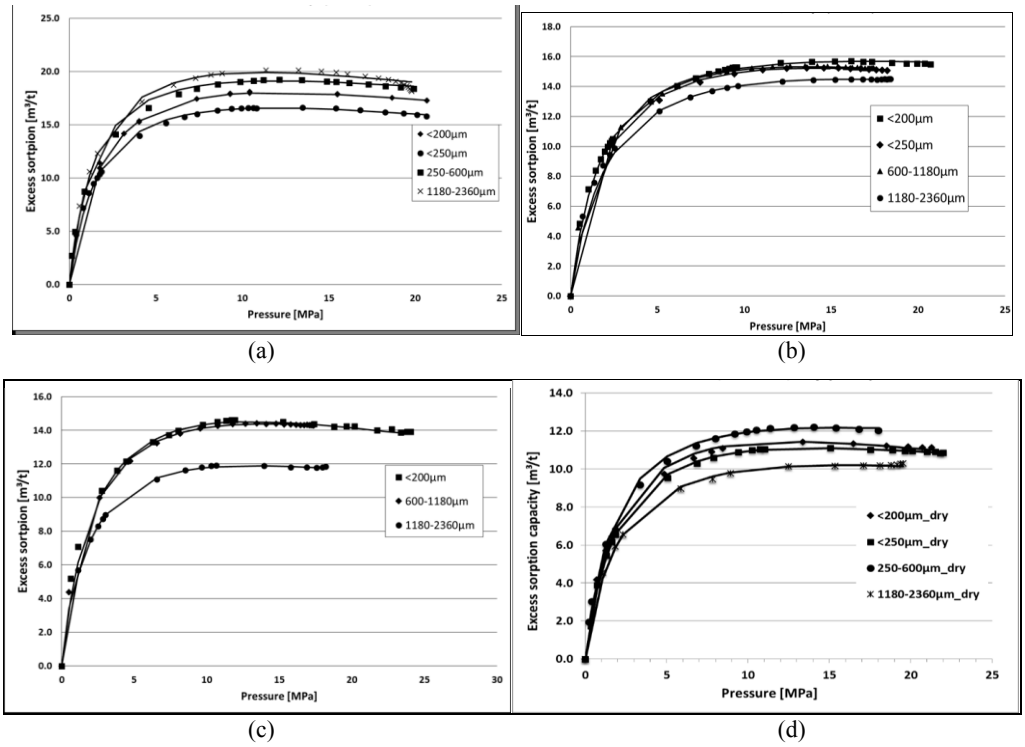


Figure 2.2. Langmuir 3 parameter fitted high pressure isotherms of (a) seam 411 samples, (b) seam 412, (c) seam 413 from the Zofiowka Colliery Poland, and (d) from the #8 seam from the Monsacro Colleiry, Spain. Samples from each coal seam were tested for different particle sizes. All isotherms were measured in dry conditions and at a temperature of 45°C (after RWTH Aachen, 2016).

The Langmuir equation can be extended to describe cases with multi-component gas adsorbed in the coal, which has an analogous expression:

$$V_i = \frac{V_{Li} P}{P_{Li} + P} \tag{2.2}$$

where subscript i denotes the i^{th} gas component.

Adsorption and desorption kinetics are useful to describe the coal adsorption-desorption behaviour. Inversely proportional to the diffusion coefficient, sorption time varies over a large range and can be up to 70 days for certain coal types (McElhiney, 1993). Langmuir (1918) considered adsorption rate as the rate at which gas molecules strike the surface. Based on theoretical and experimetal investigations, Airey (1968) proposed an empirical equation for the release rate of gas at different gas pressures:

$$V(t) = A\left(1 - e^{-(t/t_0)^n}\right) \tag{2.3}$$

where $V(t)$ is the desorbed gas volume after time t, A is the content of gas contained in the coal, t_0 is a time constant associated with coal particle size, and n is a constant related to coal type.

In addition, gas storage in the coal matrix has a large influence on the coal properties. Li *et al*. (2012) found a considerable reduction in the strength of coal due to high gas content. The coal matrix also swells with gas adsorption and shrinks with desorption, which in turn has an impact on stress state and permeability (Connell and Detournay, 2009; Gray, 1987; Seidle and Huitt, 1995).

2.2.3 Coal permeability

Coal permeability is of vital importance to outburst occurrences in that it controls gas migration within the coal seam. It is dependent on a number of factors such as coal structure, gas pressure, stress condition, water saturation, etc. The permeability varies over a large range as a result of the combined action of effective stress change and matrix shrinkage (Gray, 1987). One of the most remarkable factors is the stress dependence of the coal permeability because underground coal seams are naturally stressed, and mining activities usually induce great stress variation close to the working face.

Gray (1987) correlated coal matrix shrinkage with sorption pressure and then with permeability. By idealising fractured reservoir geometry as a collection of matchsticks, coal permeability can be linked with the effective stress, which can be written as (Durucan and Edwards, 1986; Seidle *et al*., 1992):

$$k = k_0 e^{-3C_f(\sigma-\sigma_0)} \tag{2.4}$$

in which k and k_0 are the final and initial permeabilities respectively, σ and σ_0 are the final and initial effective hydrostatic stresses respectively, and C_f represents the cleat volume compressibility.

However, *in-situ* coal formations are laterally confined, which is much closer to a uniaxial strain condition. Two widely used models were developed under this assumption. One is the Palmer and Mansoori (1996) model, which derived an equation for absolute permeability variation in response to reservoir pressure decrease. This model described the porosity behaviour and evaluated the permeability variation by the porosity-permeability relationship (McKee *et al*., 1988):

$$k = k_0 \left(\frac{\phi}{\phi_0} \right)^3 \tag{2.5}$$

where ϕ and ϕ_0 are the final and initial porosities respectively.

The other is the Shi and Durucan (2004) model, which assumes that the effective horizontal stress normal to the cleats plays a prevailing role in controlling coal permeability. The model correlates permeability to the change in the effective horizontal stress $\Delta\sigma$ by the above exponential relation (Equation (2.4)), where the change in the effective horizontal stress under uniaxial strain conditions is given by:

$$\Delta\sigma = \sigma - \sigma_0 = -\frac{\upsilon}{1-\upsilon}\Delta p + \frac{E\varepsilon_{\text{smax}}}{3(1-\upsilon)}\left(\frac{p}{p+P_\varepsilon} - \frac{p_0}{p_0+P_\varepsilon} \right) \tag{2.6}$$

where E and υ are Young's modulus and Poisson's ratio of coal, $\varepsilon_{\text{smax}}$ is the maximum volumetric swelling strain, p_0 is the initial pore pressure, and P_ε is the pressure at which the swelling strain $\varepsilon_s = 0.5\varepsilon_{\text{smax}}$.

2.2.4 Gas flow in coal seams

Only free gas can flow into mine openings. The flow in coal is considered to consist of two stages: the first stage is diffusion through the matrix and micro-pores of the coal, and the second is migration of free gas along cleats and fissures in the coal seam (Curl, 1978; Xue *et al*., 2011).

As mentioned above, initially adsorbed gas is in a thermodynamic equilibrium with the free gas in the coal seam. Adsorbed gas begins to desorb due to stress and gas pressure change during mining activities, and then diffusion flow takes place. In the process, the desorbed gas migrates from micro-pores to the interconnected fracture network in coal, which is driven by the concentration gradient and obeys Fick's Law. The general equation for *n*-dimensional diffusion can be written as (Crank, 1979):

$$\frac{\partial C}{\partial t} = \frac{1}{r^{V-1}} \frac{\partial}{\partial r}\left(r^{V-1} D \frac{\partial C}{\partial r} \right) \tag{2.7}$$

where C is the gas concentration, t is time, r is the distance from the diffusion source, and D is the diffusion coefficient.

With a comparatively larger permeability, the macro-porosity of the coal dominates the following gas flow through the interconnected fracture network (Connell, 2009). The flow is driven by pressure gradient and follows Darcy's Law. For laminar flow of an incompressible fluid through a homogeneous porous media, Darcy's Law is given by:

$$Q = -\frac{kA}{\mu} \nabla P \tag{2.8}$$

in which Q is gas flow rate, k is the coal permeability, A is the cross-sectional area, μ is the gas viscosity and ∇P is the pressure gradient.

For flow of compressible gases (CH_4 and CO_2) in coal, Darcy's law can be modified as (Hildenbrand *et al*., 2002; M. Li *et al*., 2016):

$$Q = -\frac{kA(P_1^2 - P_2^2)}{2\mu P_2 L} \tag{2.9}$$

where P_1 - P_2 is the gas pressure gradient, and L is the length of coal.

2.3 Characteristics of rock burst hazards

2.3.1 Influencing factors and mechanisms of rock bursts

Underground coal extraction activities lead to continuous stress and pressure redistributions around mine openings. For coal measure rocks and coal, which can store considerable amount of elastic strain energy, failure can induce dynamic stress wave propagations which may damage infrastructures and put human health at risk in mines. For gassy coal seams, even though in the cases that not much elastic strain energy can be stored, the presence of high-pressure gas may provide sufficient energy to break rock/coal and eject a considerable amount of coal-gas mixture into mine openings. The former, known as rock bursts, has been extensively studied in hard rock mines, and less so in coal mines.

A rock burst is an underground mining hazard involving a sudden and violent ejection of rock mass from solid walls into mine openings. This issue is acute in deep hard rock mining, and has been reported in most mining areas all over the world such as Germany, France, China, South Africa and Canada. Many researchers have suggested that a rock burst can only be triggered at certain conditions in which rock mass or geological structure under high stress or equilibrium state is perturbed by excavation to instantly release the stored strain energy, causing part of the surrounding rock to be dramatically extruded or ejected (Ortlepp and Stacey, 1994; Zubelewicz and Mroz, 1983). Based on the field observations and laboratory experiments, Kidybiński (1981) proposed three bursting liability indices for coal to characterise the rock burst potential during coal mining. Essentially, all rock bursts are recognised as seismic events (Salamon, 1983), and its magnitude can be measured in the Richter magnitude scale.

The observations and understandings of rock bursts in different mining areas are not uniform. Based on different mechanisms, Board *et al*. (1992) categorised rock bursts into two types: crush-type and shear-type rock bursts The source and damage positions are said to be identical in the crush-type rock bursts, which are related to stress concentration at the near surface of mine openings. Whereas the second type of rock bursts are believed to be imposed by seismic waves and normally more widespread and destructive (Ryder, 1988). The source of seismic waves can be the initiation of new fractures or slippage of existing fractures/faults. Therefore, source and damage in this case are not necessarily coincident (Ortlepp and Stacey, 1994). On the other hand,

based on the source mechanisms, rock bursts are classified into five types: strainburst, buckling, face crushing, shear rupture, and fault-slip burst (Ortlepp and Stacey, 1994). By grouping buckling into strain burst, and shear rupture into fault-slip burst, a general classification comprising of strainburst, pillar burst and fault-slip burst were proposed by Kaiser and Cai (2012). Strainburst is the most frequently encountered type, and fault-slip releases the most energy during the incidence.

The analyses of the triggering mechanism indicate that factors influencing rock burst potential should include excavation size, abutment size, mining depth, dykes and faults, stoping width and advancing rate (Cook *et al*., 1966; Salamon, 1983). Durrheim *et al* (1998) found that the source mechanism of rock bursts is associated with regional structures and the mine layout, while the location and severity of rock burst damage significantly depend on the rock conditions and mining support systems.

Evaluation criteria for rock bursts evolved from the use of empirical thresholds to theoretical criteria. Empirical criteria usually utilise a single indicator as the threshold for rock bursts, and thus are commonly used in the early stages of a project for preliminary design purposes to assess the rock burst risk of mine openings. Based on literature survey regarding the main results of rock burst risk evaluation, a large number of single indicators for evaluating the occurrence and intensity of rock bursts have been proposed based on the analysis from different perspectives. They can be classified as (1) strength/stress-related thresholds, and (2) brittleness-related thresholds. Most strength/stress-related thresholds consider both the state of *in-situ* stress in rock masses/coal seams as well as mechanical properties of rock/coal, and reflect the influence of excavation process and deviatoric stress characteristics of the stress field.

Over the years, there have been some successful attempts to determine the potential for rock burst occurrences by considering multiple indicators. Based on different perspectives, a large variety of theoretical criteria were put forward. These theoretical criteria can be categorised into (1) stress/strain failure criteria, (2) energy type failure criteria, and (3) fracture/damage mechanics-based criteria. Stress/strain-based criteria for rock burst risk assessment are based on rock fracture theories under certain circumstances, such as shear rupture along planes of weakness, or failure under coupled static and loads. Energy criteria for rock burst risk assessment are based on

the relationship between the damage characteristics and strain energy change of surrounding rocks in response to mining activities. Therefore, these criteria reflect not only the capacity to store strain energy in rocks, but also the environment for strain energy accumulation.

Table 2.1. Empirical thresholds and theoretical criteria for rock bursts.

Categories	Evaluation indices	Remarks/Evaluation criteria
Strength/stress	Stress-strength ratio index	$(\sigma_{\theta max}+\sigma_L)/\sigma_c>0.8$ (Turchaninov *et al*., 1972) $\sigma_c/\sigma_1<2.5$, $\sigma_t/\sigma_1<0.16$ (Barton *et al*., 1974) $\sigma_{\theta max}/\sigma_c>0.55$ (heavy) (Russenes, 1974); $\sigma_\theta/\sigma_c>0.7$ (strong) (Hoek and Brown, 1980) $\sigma_1/\sigma_c>0.40$ (Zhang *et al*., 2011) $\sigma_{rm}/\sigma_{max}<2$ (intensive) (C. S. Ma *et al*., 2018)
	Excess shear stress (ESS)	>15 (Ryder, 1988)
	Brittle shear ratio (BSR)	>0.7 (Castro *et al*., 2012)
	Coupled static and dynamic loads	The coupled static and dynamic loads exceed the critical stress limits of rock/coal (Li *et al*., 2008b; Z. Li *et al*., 2014).
	Tensile effective stress (TES)	The stress of a rock/coal element changes from compression to tension.
Brittleness	Brittleness	$B_1=(\sigma_c-\sigma_t)/(\sigma_c+\sigma_t)$; $B_2=\sin\varphi$ (Hucka and Das, 1974) $B=\sigma_c/\sigma_t>22$ (Zhang *et al*., 2011)
Energy	Strain energy density (SED)	The maximum elastic strain energy per unit volume exceeds a threshold.
	Burst energy coefficient (R)	$W_E/W_P>1$ (Goodman, 1989)
	Strain energy storage coefficient (F)	$W_{st}/W_{sp}>5$ (Kidybiński, 1981)
	Energy release rate (ERR)	>4.7% (Salamon, 1984)
	Strain energy storage index (W_{et})	>5.0 (Neyman *et al*., 1972)
	Potential energy of elastic strain (PES)	>150 (Wang and Park, 2001)
Fracture/damage	Fracture mechanics-based criterion	$K_I>K_{Ic}$ (Dyskin and Germanovich, 1993)

Note: $\sigma_{\theta max}$ is the maximum tangential stress of cross section in disturbed zone; σ_L is the radial stress of cross section in disturbed zone; σ_c is the uniaxial compressive strength; σ_t is the tensile strength; σ_1 is the maximum principal stress of *in situ* stress; σ_{rm} is the triaxial rockmass strength based on the Hoek-Brown strength criterion; σ_{max} is the maximum horizontal stress on the boundary of an opening, $\sigma_{max}<\sigma_{\theta max}$; φ is the frictional angle; W_E is the elastic strain energy accumulated before rock failure; W_P is the dissipated energy in the post-failure stage; W_{sp} is the energy dissipated by plastic deformation during unloading process; W_{st} is the stored energy in rock; K_I is the stress intensity factor; and K_{Ic} is the fracture toughness of rock.

Table 2.1 summarises some common empirical thresholds and theoretical criteria used for evaluation of rock burst risk. A detailed summary of rock burst criteria and evaluation of rock burst classification can be found in the state-of-the-art review by Zhou *et al*. (2018).

2.3.2 Coupled static and dynamic theory

Many researchers have concluded that hazards like rock bursts are only triggered at certain circumstances. On the one hand, if the stress approaches the compressive strength, the fractured soft coal can store internal gas energy (Valliappan and Wohua, 1999) while the intact hard rock can serve as a medium to store large strain energy (Wang and Park, 2001). On the other hand, there must be some kind of external dynamic excitation to trigger the instability (Ortlepp and Stacey, 1998).

Most early studies primarily focused on the theory of statics that is dependent on the rock/coal properties, geological structure, gas desorption and the high initial stress level, etc. (Beamish and Crosdale, 1998; Durrheim *et al*., 1998; Hanes and Shepherd, 1981). In reality, mine exploitation is conducted at multi-stages. They are simultaneous in underground excavations, with the frequent ore drawing, ore caving, and excavations by drilling and blasting or by roadheaders or longwall shearers, which are considered as loading and unloading disturbances.

Recently, it has been accepted that the mechanical characteristics of the deep coal and rock mass are under combined static and dynamic loads. Zubelewicz and Mroz (1983) have specifically suggested that rock burst hazards are deemed to occur when the static stability conditions of the rock mass are perturbed. This can then bring about dynamic failure as a consequence of dynamic instability. Wang and Cai (2015) stated that a small seismic wave disturbance can trigger failure of a rock mass in a near-failure stress state, and that a large one can cause failure of a rock mass in a stress state not near failure. Using superposition of static and dynamic stresses, Wang *et al*. (2016) successfully analysed two rock bursts and concluded that they were primarily induced by dynamic stress and tectonic stress respectively. The effect of coupled static and dynamic stress state was also confirmed by a series of experimental investigations and numerical studies (Li *et al*., 2008a, 2005; Zhu *et al*., 2010; Zuo *et al*., 2005).

This theory also holds for coal and gas outbursts. In the course of coal mining, an outburst can be initiated by the impact of roof breakage and sudden caving, but not

likely only by great geostress which would lead to large plastic zones (Jin *et al*., 2011). It was also found that blasting-induced damage accelerates gas desorption, which in turn increases the gas gradient and outburst possibility (Nie and Li, 2012). Zhang *et al*. (1991) considered coal/rock bursts and outbursts to result from a mini disturbance of the unstable equilibrium state of the coal/rock system.

2.3.3 Strain energy release, migration and dissipation in mining

The analysis of energy change during mining is imperative in understanding the formation of rock bursts. As is well known, the pre-mining tractions on excavation surface are reduced to zero during rock extraction, rendering the stress state in the boundary of excavation to change from triaxial to biaxial or uniaxial. Increased strain energy imposed by the external forces accumulates around the excavation, and the remnant energy is either consumed in rock fracturing or released in the form of an episode of acoustic energy (Brady and Brown, 2013). Rock bursts occur when the kinetic energy is released in a violent manner.

Cook *et al*. (1966) first conducted energy analyses for an excavation in an elastic rock mass, and rock burst is considered to occur if the geometrical rate at which energy must be released exceeds the energy dissipation rate in a non-violent manner during mining excavations. Salamon (1984) further examined the energy transfer during the course of mining, and the energy balance can be written as:

$$(W + U_{\mathrm{m}}) - (U_{\mathrm{C}} + W_{\mathrm{S}}) = W_{\mathrm{r}} > 0 \tag{2.10}$$

where W is the work done by external forces, U_{m} is the stored strain energy in mined-out rock, U_{C} is the increased strain energy, W_{S} is the work done on mining support, and W_{r} is the released energy.

Based on the energy considerations, several indices were proposed to describe the rock burst tendency. One of the most widely accepted indices is energy release rate (ERR), which is the energy released per unit mined area. Another one is strain energy density (SED), defined as the maximum elastic strain energy per unit volume, which can be expressed as follows:

$$\mathrm{SED} = \frac{\sigma^2}{2E} \tag{2.11}$$

in which σ is the axial stress, E is the Young's modulus. This indicates that weak rock is not likely to burst compared to strong one.

Based on the concept of SED, the total strain energy stored in an elastic column under axial compression can be given by:

$$U = \frac{\sigma^2 AL}{2E} \tag{2.12}$$

where A is cross-sectional area, L is the length of the sample. This suggests that more energy can accumulate in large and soft (e.g., with a small E) materials subjected to high stress, which can provide explanations for some features of rock bursts (Manouchehrian and Cai, 2015). This is also why rock is crushed more violently using a soft loading system rather than a stiff one. As illustrated in Figure 2.3, excess energy stored in the soft loading system is instantaneously released in the post-peak stage of the stress-strain curve, which largely aggravates the violence of the rock destruction process.

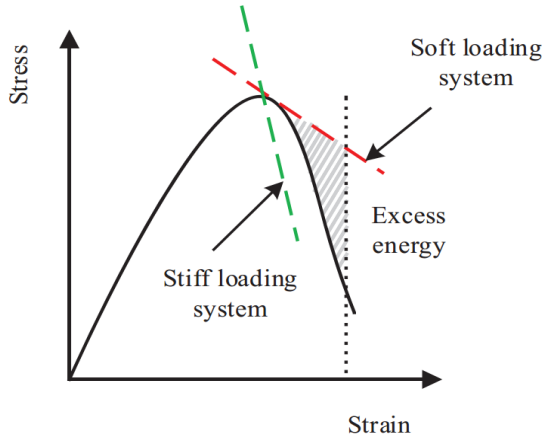


Figure 2.3. Schematic of loading system stiffness for rocks in compression (after Manouchehrian and Cai, 2015).

Recently, the energy approach has been extensively applied in rock burst intensity classification (Chen *et al*., 2015), numerical assessment of rock burst tendency (Jiang *et al*., 2010; Miao *et al*., 2016), and rock burst control (Hua and You, 2001).

2.3.4 The influence of stress release rate on excavation response

During underground excavations, the work done by external forces is either stored as elastic strain energy, consumed in rock fracturing and plastic deformation, or released as kinetic (seismic) energy. In this process, the dynamic responses of rock are closely associated with the energy storage and release, which can be clearly reflected in stress-strain curves. Zubelewicz and Mroz (1983) demonstrated the dynamic effect in the loading scenario by assuming that a step loading ΔP is applied to a rock specimen with pre-pressed stress P_1. As illustrated in Figure 2.4, the area 1-2-3 is the released seismic energy due to the step loading, and the area 3-A-4 is the required energy to pass into the unstable stage. The system becomes unstable as long as the area 1-2-3 is larger than the area 3-A-4, regardless that the sum of P_1 and ΔP is smaller than the peak load P_A.

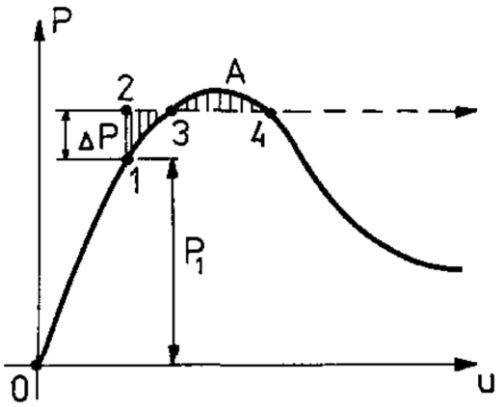


Figure 2.4. Schematic of dynamic instability (after Zubelewicz and Mroz, 1983).

This can also be introduced to illustrate the effect of unloading rate during underground excavations (Mitri *et al*., 1999; Sirait *et al*., 2013). In Figure 2.5, ESR denotes the energy storage rate, and ERR is the energy release rate. The area below the stress-strain curve is referred to as the stored energy per unit volume during excavations, and the red and blue triangle areas correspond to the released energy per unit volume in the first and second excavation steps respectively. Therefore, the green rectangular area represents the reduction of ERR when excavating in two steps instead of one step. From the figure, half of the work done by external forces are released for mining in one step, which is consistent with the calculation for the creation of an unsupported cavity in an elastic rock mass (Salamon, 1984). It can also be deduced

that quasi-static unloading (i.e., mining in very small steps) barely releases kinetic (seismic) energy, which contributes to the reduction of strainburst possibility. This is supported by both field observations (Hodgson and Joughin, 1966) and theoretical derivations (Salamon, 1984, 1983).

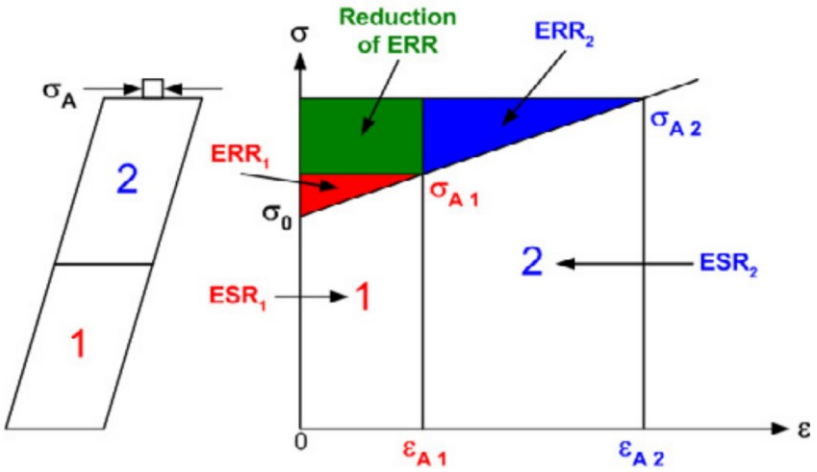


Figure 2.5.Mining-induced energy change during excavations by steps (after Mitri *et al*., 1999; Sirait *et al*., 2013).

From this prospective, the unloading rate seems to be one of the primary factors influencing the unloading process. Except experiments mentioned above (Huang and Li, 2014; Huang *et al*., 2001; X. G. Zhao *et al*., 2014), extensive research has also been carried out to justify the influence of unloading rate using theoretical and numerical methods. Tao *et al*. (2012) conducted one dimensional analysis of axial unloading of both unconfined and confined elastic rock bar under high initial stress state, and introduced the initial stress release rate and strain energy density rate to characterise the unloading process. Results showed that rock failure can be induced by the rapid unloading of the initial strain energy even when axial stress is far less than the compression strength. Through two-dimensional analysis for tunnel excavation unloading, Li *et al*. (2014) and Cao *et al*. (2016) identified observable unloading disturbance under high initial stresses and unloading rates in both near and far field.

This may also be introduced to the interpretation of coal and gas outbursts. In coal mining practice, the manner in which stress releases is also associated with gas pressure relief, which is controlled by the gas desorption and migration behaviour within the coal seam. Despite field observations (Chen, 2011; Hargraves, 1980) and

potential explanations (Chen, 2011; Paterson, 1986) of the effect of mining advance rate, experimental investigations on its resultant dynamic responses should also be emphasised in future research.

2.4 Characteristics of coal and gas outburst hazards

2.4.1 Factors influencing the outburst potential

Four significant factors have been shown to account for outburst occurrences (Beamish and Crosdale, 1998; Farmer and Pooley, 1967; Jackson, 1984): (1) the microstructure and properties of the coal; (2) the content and pressure of gas retained in the coal seam; (3) geological deformation and depositional structures, and (4) the stress conditions around the coal seam.

In addition, some other factors are also considered to combine and exacerbate the hazards, such as thick seams, steeply inclined seams, low permeability seams, characteristically dry seams, mining layouts and advance rates (Aguado and Nicieza, 2007; Jackson, 1984; Li, 2001). The major factors are classified into intrinsic factors and extrinsic factors, as summarised in Table 2.2. Some major factors are elucidated in detail below.

Intrinsic factors

Coal composition and properties: Farmer and Pooley (1967) reported that outburst-prone coal normally found in anthracite seams consists of interspersed thin layers of clay material. Beamish and Crosdale (1998) found coals rich in vitrinite and inertodetrinite have larger outburst proneness. They provided an explanation that these coal lithotypes have high adsorption capacity and low strength, once large particles in the coal face usually with slow desorption rate are reduced to smaller particle sizes, the retained gas is released suddenly and the outburst tendency is increased. In addition, the permeability and adsorption/desorption properties of coal are both dependent on the micro-porosity, which is also considered to be important (Lama and Bodziony, 1998).

Gas content, pore pressure and gradient, and gas desorption rate: Cao *et al*. (2001) found the gas content to be the only property which distinguishes the outburst zone from the other mylonitic coal without any outbursts. Choi and Wold (2001) considered pore pressure and its gradient more determinant in terms of outburst potential than gas

content in a mechanistic sense. This is because the accumulation of gas pressure in the outburst-prone area in the coal seam pushes Mohr's circle of stresses closer to its failure envelope (Singh, 1984).

Table 2.2. Factors affecting coal and gas outburst risk in coal mining.

Categories	Factors	Sub-factors
Intrinsic factors	Coal type	Physical properties: coal rank, grain size, porosity.
		Mechanical properties: strength, Young's modulus, Poison's ratio, facture toughness.
		Reservoir properties: permeability, Langmuir pressure and volume.
	Seam thickness	Mine depth
		Seam hardness
		Seam slope
		Seam thickness
	Geological factors	*In situ* stress
		Tectonic structures and discontinuities (faults, shear bedding zones, etc.)
		Tectonic activities (igneous intrusions)
	Gas-related factors	Gas content
		Gas composition
		Gas pressure
		Gas pressure gradient
		Gas adsorption/desorption rate
Extrinsic factors	Mining methods	Thick seam longwall coal mining
		Multi-seam longwall coal mining
		Sublevel caving coal mining
	Stress regime generated	
	Face advance rate	
	Gas control measures	Pre-drainage
		Cross-measure boreholes
		Protective mining
		Drainage borehole stimulation

However, Hargraves (1980) found no relationship between measured maximum gas pressure and subsequent provoked outbursts, but there is a relationship between the emission rate of coal and outburst potential, and no outbursts have been induced with an emission rate below 1.4 cc/g. Hyman (1987) found that, even if with the same gas content as normal coal, outburst prone coal can be distinguished by its sorption-desorption velocity. Williams and Weissmann (1995) addressed the pronounced influence of gas pressure gradient ahead of the working face, and also believed that the prime factor is gas desorption rate.

Geological structures: Farmer and Pooley (1967) found that gas outbursts only occur in severely tectonically-disturbed areas, and Singh (1984) found over 90% of outburst districts are associated with geological structures. Shepherd *et al*. (1981) reported that all 9 collieries where 192 outbursts occurred were subjected to geological disturbance and had soft coal in the vicinity. They also stated that more than 90% of outburst occurrences are concentrated in the narrow seriously distorted areas in the vicinity of geological structures, which made geological structures the most significant factor in outburst hazards.

Complex structures which may induce gas outbursts include folds, fracturing, faults, rolls, slips, dykes, shear zones, magmatic intrusions as well as rapid changes in seam thickness (Farmer and Pooley, 1967; Li, 2001; Shepherd *et al*., 1981). The two most susceptible geological structures are anticlinal folds and floor rolls through which coal formations thin (Shepherd *et al*., 1981). Cao *et al*. (2001) found that almost all outburst occurrences associated with reverse faults are concentrated in footwalls. This is because in the footwall, coal is more likely to lose banded character and microstructurally transform to fractured forms such as cataclastic coal, granular coal and mylonitic coal. Figure 2.6 illustrates the influence of geological structures in conjunction with gas pressure gradient in triggering of an outburst.

In-situ stress conditions: Farmer and Pooley (1967) and Cao *et al*. (2001) found the severity and areas of outbursts to increase with mining depth and stress levels and Shepherd *et al*. (1981) found the critical depth above which outbursts rarely occur to be about 180 m. Although arguments arose regarding if there is a universally applicable relationship between outbursts and depth (Jackson, 1984), the consensus on the influence of stress magnitude holds. Choi and Wold (2001) believed the influence of *in situ* stress on outburst initiation results from anisotropic stresses, which generate shear stresses and increase outburst occurrence sensitivity to stress magnitude. In Spanish coal mines, the increased risk of outbursts at depths more than 1,000 m is thought to be 30%, while for depths between 500 and 1,000 m the risk increment is 10%. For depths less than 500 m, depth does not influence gas outbursts risk.

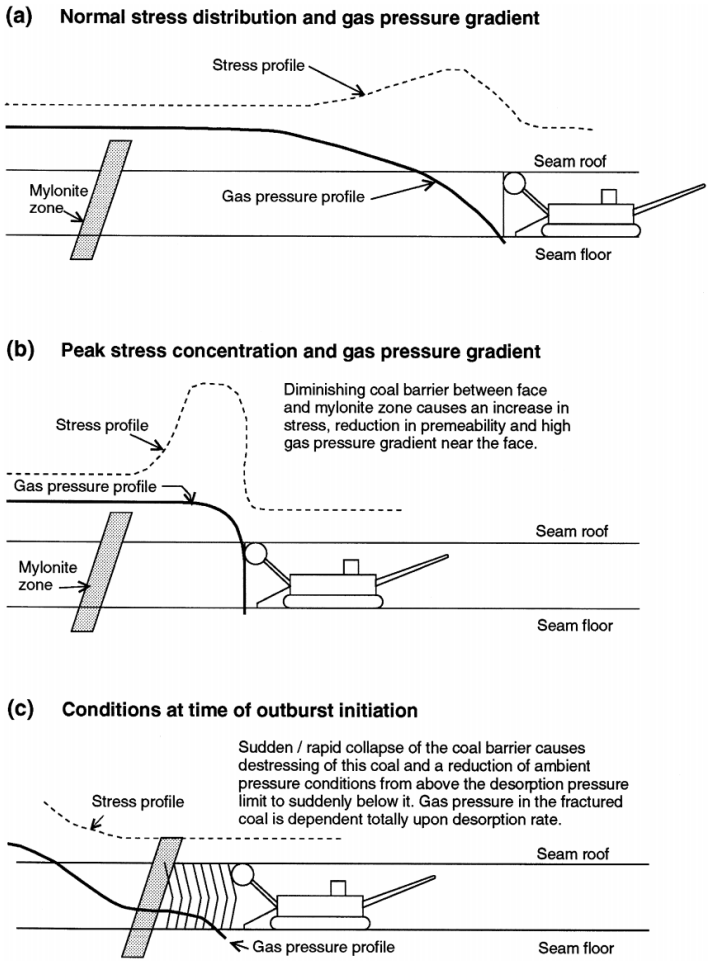


Figure 2.6. Work face conditions in an outburst zone (after Beamish and Crosdale, 1998; Williams and Weissmann, 1995).

Extrinsic factors

Mining methods and stress regimes generated: The mining-induced stress redistribution around the working face acts as a disturbance to the virgin stress field as well as the gas pressure distribution. The mining methods ranked from highest to lowest risk are listed as follows: crosscut seam, in-seam driving, overlapping area between a sublevel and a stope, longwall mining, longwall retreating, room and pillar.

Mining by crosscut seam implies increased risk of coal and gas outbursts because the working face is progressing from a competent material (wall) towards a weaker one (coal). When cutting the coal, the confining stress of the surrounding rock/coal is suddenly affected and, if gas of sufficient quantity is present in the seam, it can be emitted very quickly.

Mining intensity: The coal production creates atmospheric pressure conditions at the coalface, while the gas pressure is much higher in unexploited virgin coal a few meters ahead. The gas pressure gradient ahead of the face achieves the greatest value after a rapid advance (Paterson, 1986). Therefore, there is an increased potential of coal and gas outbursts when any weakness/discontinuity zones in the coal are reached. The increased probability of outburst accidents both in working days (Hargraves, 1980) and near the end of shift rather than the beginning (Chen, 2011) is believed to be contributed by the rate-of-advance effect.

Table 2.3 summarises some common empirical thresholds and theoretical criteria used for the evaluation of coal and gas outburst risks.

Table 2.3. Empirical thresholds and theoretical criteria for coal and gas outbursts.

Categories	Evaluation indices	Remarks/Evaluation criteria
Strength/stress	Protodyakonov strength	0.1–0.3 (Youan and Sijing, 1980)
	Drill-cuttings-to-hole volume ratio	>3:1~7:1 (Hyman, 1987)
	Tensile effective stress (TES)	The stress of a coal element changes from compression to tension.
	Unbalanced pressure driven force (UPDF)	The pressure gradient acting on a coal element overcomes the friction.
Gas	Gas volume	>9 m^3/tonne for CH_4 and 6 m^3/tonne for CO_2 (Sydney Basin, Australia) (Beamish and Crosdale, 1998); 10 m^3/tonne for CH_4 (China) (Zhang, 1992)
	Gas pressure	>= 0.74 MPa (China) (Chen *et al*., 2016)
	Gas desorption rate	3 cm^3/35 s/10 g
	Gas emission index	5-15 (liable); 15-20 (highly liable) (Ettinger, 1952)
	Permeability	<= 5 mD (*in situ*) (Lama and Bodziony, 1998); $<10^{-3}$ mD (core sample) (Gil and Swidzinski, 1988)
Fracture/damage	Fracture mechanics-based criterion	$K_I > K_{Ic}$ (Feldman *et al*., 2017).

2.4.2 Mechanisms of coal and gas outbursts

One early model, referred to as the cavity theory, assumed that there are cavities storing high-pressure gas at depth from which outbursts occur during mining (Briggs, 1921). However, no evidence of the presence of such underground cavities was found. Gradually, the concept of "cavity" evolved, and the pocket theory was developed, which assumes that pressurised free gas is contained in reservoirs formed by soft and

crushed coal in the coal seam (Farmer and Pooley, 1967; Shepherd *et al*., 1981). However, the pocket theory cannot account for the large amounts of adsorbed gas. In addition, it cannot explain some observations that newly exposed coal seams are more susceptible to coal and gas outbursts as not all coal mining processes can be carried out in seams with gas-rich coal pockets (Guan *et al*., 2009). Almost at the same time, the dynamic theory was developed to elucidate the outburst mechanism (Hyman, 1987; Shepherd *et al*., 1981). This hypothesis proposes that an outburst results from a tensile-stress induced failure of the coal. Many of the latter models were a combination of the pocket and dynamic theory (Singh, 1984).

In the 1980s, two principle models for outbursts were developed: coal destruction as result of shock-induced phase transition (Litwiniszyn, 1985) and structural failure of coal induced by high gas pressure gradients (Paterson, 1986). Some field observations are in accordance with the Litwiniszyn model: (1) 'bumps' often occur together with instantaneous outbursts, which are supposed to trigger outbursts; and (2) in non-mechanised mines, successive knocks can often be precursors of instantaneous outbursts (Beamish and Crosdale, 1998). However, the Litwiniszyn model was critically reviewed by Paterson (1986) for four reasons: (1) the model cannot explain how outbursts occur in salt and metalliferous mines; (2) the model does not give the origin of shock waves; (3) the model does not consider the rapid attenuation of wave propagation in coal; and (4) an adsorbed liquid-like gas layer should not be regarded as liquid state.

In summary, it is generally agreed that outbursts are first initiated by dynamic failure of coal during stress changes ahead of the working face, and the rapid fracture extension and ensuing expulsion of coal and gas are driven by a large amount of desorbed gas from coal matrix (Farmer and Pooley, 1967; Valliappan and Wohua, 1999; Xue *et al*., 2011). Specifically, this process comprises of several stages: (1) the quasi-static deformation behaviour suddenly transforms to dynamic failure once the triaxial abutment stress states change to biaxial or uniaxial states during exposure; (2) coal is crushed and gas contained in the coal matrix is desorbed and released; (3) coal is further split by gas pressure and mass movement takes place; and (4) all the materials have been ejected (Jackson, 1984).

It is noted that debates arose forever regarding the initiation of an instantaneous outburst. Gray (1980) considered that outbursts are initiated when either gas pressure exceeds the tensile strength of unconfined coal or the minimum confining stress, leading to tensile failure and the piping of sheared materials respectively. Beamish and Crosdale (1998) also supported the gas-initiated failure mechanism by stating that a gas content gradient ahead of working face is sufficient for the initiation. However, other researchers suggested that outbursts are dynamically triggered (Jin *et al*., 2011; Litwiniszyn, 1985). Support for this argument can be found in field observations where shotfiring was thought to account for several outbursts (Hargraves, 1980; Shepherd *et al*., 1981). A report even attributed 96.5% of over 8,600 outburst occurrences to dynamic disturbances such as shotfiring, drilling, falling coal, etc. (Nie and Li, 2012).

2.4.3 Advances in modelling coal and gas outbursts

Due to the difficulties of obtaining field data, and considering the scale differences between field behaviour of rocks and behaviour under laboratory conditions, numerical simulations can be used as a good alternative to verify the influencing factors and explore the underlying mechanisms of coal and gas outbursts.

The pioneering work in this field can be traced back to Paterson (1986), who developed a model capable of replicating the processes to account for the stress evolution, the gas flow behaviour as well as the failure criteria. He developed both one- and two-dimensional gas flow models which explained some key features of outbursts such as the gas pressure gradient driven tensile failure and the effect of face advance rate. Barron and Kullmann (1990) implemented an interactive numerical model for an outburst, based on the proposed hypothesis that outbursts are comprised of a series of instantaneous static events resulting from tensile failures. In this model, the boundary element program evaluates the stress distribution around underground openings under plane strain conditions, and the gas pressure is superposed onto the obtained results for the evaluation of effective stresses in the second program. By integrating time-dependent Navier-Stokes equations with finite-difference scheme, Otuonye and Sheng (1994) developed a two-dimensional model that can reflect the dynamic process involving the gas flow into roadways, a shock wave that propagates into airways and rarefaction wave propagating into the coal seam during a coal outburst.

However, the above early-stage models were somewhat simplified, which could not reflect the whole outburst process from initiation to termination. In addition, an accurate characterisation of the interplay between gas flow and stress evolution is needed. Consequently, two modelling schemes, i.e., fully coupling and iterative coupling, have been introduced and extensively used in outburst modelling.

Fully coupling scheme incorporates both the physics of stress evolution and gas flow and simulates the whole process in one simulator. Xu *et al*. (2006) integrated gas flow in coalbeds with coal deformation and failure in a rock failure process analysis (RFPA)-gas flow model, which successfully modelled the whole outburst process, including stress evolution, coal failure, gas pressure-driven propagation, and ejection of coals.

Iterative coupling scheme solves the stress evolution problem and gas flow problem in a geomechanical simulator and a reservoir simulator respectively and sequentially. At specific time steps, the stress change from the geomechanical simulator is used to evaluate the permeability variation, which is subsequently fed to the reservoir simulator to solve the gas flow equation. The calculated pore pressure change is then transferred back for the calculation of the stress distribution in the next time step. In this way, the interplay between the stress evolution and gas flow behaviour is accounted for.

Choi and Wold (2004, 2001) developed a model by coupling SIMED and FLOMEC, which also considers the dual porosity characteristics of the coal and multi-component gas flow properties. The model successfully reflected the stress-dependent permeability, gas desorption and migration behaviour and large strain deformation, and achieved good agreement with field data of outburst initiation. Based on this model, Wold *et al*. (2008) addressed the influence of spatial variability of coal permeability and strength on outburst behaviour. The results suggested the same property values with different spatial distribution could result in both outburst and non-outburst occurrences.

Xue *et al*. (2011) developed a coupled model using FLAC^{3D} and COMER3, which can explain the progression from gas desorption from coal, gas diffusion and flow in coal, coal deformation to the initiation of outbursts. The main disadvantage was that the

model is only valid until the initiation of outbursts due to the inability to describe the rapid change of the effective stress during the violent progress of an outburst.

Si (2015) performed outburst modelling using a two-way sequential coupled model based on FLAC^{3D} and Eclipse, and outbursts induced by a bedding shear zone and an underlying gassy seam were simulated respectively. This model could simulate the post-initiation process by implementing a stress-permeability relationship for the fractured coal. Results from both modelling cases suggested that unusual gas emission is a precursor for an outburst hazard.

However, the above geomechanical simulators are finite element or finite difference programs based on continuum mechanics, which indicates failed coal is not deemed to be separated from the coal seam. Therefore, current simulations are heavily handicapped by the limitation to reproduce the explicit fracture process and fragmentation of coal. Recently Xue *et al*. (2015) developed a simple two dimensional model coupling a solid and fluid code, in which the lattice Boltzmann method was applied to model the gas flow behaviour, while the discrete element method was used to reflect the coal deformation and fracturing. Nonetheless, a great deal of work still needs to be conducted for more accurate representation of the coal fragmentation and expulsion process.

2.5 Rock bursts and gas outbursts as dynamic unstable failure problems

2.5.1 Similarities and differences between rock bursts and gas outbursts

As serious underground hazards frequently encountered in coal mines, rock bursts and gas outbursts share a number of similarities as follows:

1. In view of the violent nature, both hazards manifest as a dynamic type of violent failure phenomena.

2. More energy is released than absorbed during both hazards (Cook *et al*., 1966; Gray, 1980; Mitri *et al*., 1999; Petukhov and Linkov, 1979). The violent nature results from the total released energy which is much larger than the energy needed to fracture the rock mass. Therefore, these hazards should be distinguished from sudden rock failure phenomena which will not take place without external energy

input, such as roof falls, conventional blasting and blast-induced spalling in adjacent roadways.

3. Both hazards can induce microseismic events and are usually preceded by cracking noises from within the rock mass or coal seam (Cook *et al*., 1966; Jackson, 1984; Lockner, 1993). The microseismic signals of outburst activities differ from those of normal activities in velocity, frequency, duration, waveform and attenuation characteristics (Styles, 1993).

4. Both hazards can be either dynamically-induced or self-initiated. The source and damage locations of rock bursts can be coincident or separate in distance and time, depending on whether it is as a result of strain relaxation under high stress or dynamic wave disturbance (He *et al*., 2012b; Ortlepp and Stacey, 1994). Among 236 outbursts in the Gwendraeth Valley, 113 resulted from shot firing, 105 were spontaneous and 18 were unclassified (Styles, 1993). Another statistical data suggested that dynamic disturbances such as shotfiring, drilling and falling coal accounted for 96.5% of 8,362 outbursts, while only 4.5% were caused by indefinite operation (Nie and Li, 2012).

However, it should be noted that the differences between these hazards also exist in some aspects, which are summarised as follows：

1. *Phenomenon*. Rock bursts result in rock ejection without gas involved, while a large amount of gas, as much as over 100,000 m^3 can be released in an outburst (Styles, 1993). In addition, rock bursts are likely to exhibit little violence and lead to few structural damages after an initial extremely violent shock, but the after-effect of outbursts can cause a small opening to be enlarged to a cavity with thousands of tonnes of pulverised materials ejected (Farmer and Pooley, 1967).

2. *Rock/coal mechanical properties*. Weak and friable, and even powdery and porous coal contributes to the outburst proneness (Singh, 1984). However, strong and hard rock/coal tends to have larger rock burst tendency due to the maximum elastic strain energy storage capacity (Sirait *et al*., 2013). In hard rock mines, weak rock masses are more liable to a large plastic or elastoplastic deformation termed “squeezing ground” rather than sudden ejection of rock particles (Mazaira and Konicek, 2015).

3. *Rock/coal integrity*. Massive rock types are more liable to rock burst occurrences than highly fractured and jointed rock masses (Ortlepp and Stacey, 1994). In contrast, outburst prone coals are usually extensively fractured as a result either of geological structures (such as joints, cleats and faults) or of mining-induced stress (Hyman, 1987; Shepherd *et al*., 1981). This is because fracturing of coal reduces particle sizes and facilities rapid gas release (Shepherd *et al*., 1981), while the hard and intact rock nature guarantees the high strain energy storage capacity.

4. *Energy source*. The main difference is that rock bursts result only from stored elastic strain energy of stressed rock masses, while a large amount of internal gas energy principally contributes to outbursts (Choi and Wold, 2001; Ortlepp and Stacey, 1994; Salamon, 1983). Gray (1980) estimated released gas energy in an outburst in Leichhardt Colliery to be eight times the elastic strain energy. Valliappan and Wohua (1999) compared the elastic work to initiate an outburst from both stored strain energy and internal gas energy, and concluded the stored gas energy in coal seams play a major role. They further pointed out that most of released gas energy is released from gas desorption under low gas pressures, but primarily contributed by gas expansion in the high-pressure case.

2.5.2 Unstable failure problems

The early attention to unstable failure problems in mining can be traced back to the 1960s, when Cook (1965) suggested that rock bursts are deemed to occur once the static stability conditions of the rock mass are perturbed. Salamon (1983) also attributed seismic events to the unstable failure problems and identified several necessary conditions, i.e., unstable equilibrium state, sudden and large enough stress change and a large amount of stored energy. Therefore, it is essential to investigate the problem of stability which can shed light on the mechanisms underlying these violent phenomena.

Several stability criteria were proposed in pioneering works in this field. Salamon (1970) applied the complete stress-strain curve of uniaxial rock tests to explain the pillar collapse phenomena, and suggested pillars will be stable if the sum of the stiffness matrix of mining workings and the slope matrix of the force-displacement curve of pillars is positive definite. Petukhov and Linkov (1979) formulated a stability criterion based on the understanding of post-failure characteristics, which considers

instability occurs when the increment of external energy input exceeds the intrinsic energy increment. Zubelewicz and Mroz (1983) generalised the instability condition as the monotonic increase of the kinetic energy of the system under external excitations. This criterion was further examined by modelling two dynamic rock rupture phenomena induced by the instantaneous excavation of pillars and a plane wave incidence to the excavation face respectively.

The mathematical formulation of a mechanical problem comprises of equilibrium equation, compatibility equation, constitutive equation, and boundary conditions. The nonlinear representation of the latter two conditions makes it possible to describe the physical instability (Linkov, 1996), which indicates numerical modelling as a suitable tool to study the problem. From compression tests of brittle rock, Wawersik and Fairhurst (1970) found that the unstable failure mode results from the low stiffness of loading machine. Manouchehrian and Cai (2015) used an explicit FEM model to simulate the unstable failure close to the unloading face of a polyaxial compressed rock specimen, and suggested to distinguish stable and unstable failure in terms of indicators such as transferred energy ratio (TER) and loading system reaction intensity (LSRI).

Some researchers also investigated unstable failure problems experimentally. Tarokh *et al*. (2015) used a surface instability apparatus to monitor the spalling phenomenon near the free surface of orthogonal prismatic rock specimens under compression. Fakhimi *et al*. (2016) used a steel beam connected to the loading machine as a soft loading system in uniaxial compression tests, and successfully reproduced violent rock destruction which mimics strain bursts of pillars. Recently, the unstable rock failure has also been investigated subjected to unloading conditions, which will be detailed in the next section.

However, most researchers have investigated unstable failure problems in the course of hard rock mining, which usually manifest as rock bursts. In view of the similarities in the violent nature and triggering conditions, outbursts are also believed to be categorised as unstable failure problems, and the crucial role of gas should be incorporated to the reformulation and further investigation of the problems.

2.5.3 Dynamic unloading problems

With increasing mining depths in recent years, underground rock structures or coal seams are subjected to higher *in situ* stress, and more threatening dynamic phenomena such as rock and coal outbursts as a consequence of sudden removal of stress. The traditional rock experiments cannot seem to explain the violent nature of rock and coal outbursts because (1) the loading scheme cannot mimic well the unloading path experienced by the surrounding coal or rock in real mining or excavation scenarios; and (2) the quasi-static loading/unloading scheme does not reflect the rapid abutment stress change during mining practices. Therefore, numerous unloading experiments have been designed to characterise the dynamic behaviour of rock samples during the unloading process.

With hard rock mining in mind, Huang *et al*. (2001) first designed conventional triaxial unloading experiments to simulate rock burst process by progressively unloading the minimum principal stress. The rock strength was found to decrease with increasing unloading rate, which suggested to reduce the excavation rate in rock burst-hazardous areas. From conventional triaxial unloading tests, Huang and Li (2014) found that, with the increase of unloading rate, the pre-peak energy conversion rate increases, and the failure mode of rock samples changes from shear to tensile.

However, the conventional triaxial rock testing machine used was limited in representing the realistic 3D underground stress changes, so a true triaxial testing machine was then employed to gain a better insight into this dynamic process. He *et al*. (2012a, 2012b, 2015, 2010) developed a true triaxial rock burst test apparatus and carried out a series of experiments to simulate strainbursts employing unloading path which mimics the real stress path of the surrounding rock mass during underground excavations. The dynamic process was investigated in terms of crack propagation, acoustic emission energy characteristics, *b* value analysis (He *et al*., 2015), etc. Zhao *et al*. (2014) used the same apparatus to investigate the influence of unloading rate on the strainburst characteristics, and found that the failure mode changes from spalling to strainburst as unloading rate increases. Li *et al*. (2015) carried out a true triaxial unloading test on large-size cubic rock specimens, and observed the failure mode of strong and hard rock samples changes from shear to slabbing when the intermediate principal stress increases to a critical value before unloading the minor principal stress. The fracture evolution and failure mode of cubic specimens containing single or

double pre-existing fractures subjected to two unloading paths were also investigated experimentally (Huang and Huang, 2014).

In coal mining operations, as well as the confining stress, the gas pressure is also released in the event of a rock burst or coal and gas outburst. Alekseev *et al*. (1980) simulated the outburst process by suddenly opening the front plate on cubic gas-saturated coal specimens subjected to triaxial compression. Outbursts were observed if the stress was considerably relieved on the front plate before unloading, but it did not occur if the side plates was largely de-stressed in advance. The explanation was that stress relief induces a set of cracks parallel to the unloading face, which is prone to propagate only in the direction orthogonal to crack orientation under the active participation of gas. Gawor *et al*. (2000) observed that after rapid gas pressure relief, the destruction of gas-bearing cylinder briquettes made of outburst-prone coal dust proceeds layer by layer, which indicates the generation of a rarefaction shock wave inside the briquette. Alexeev *et al*. (2004) developed a triaxial loading system with a high-pressure chamber capable of unloading one face of a pre-compressed gas-saturated specimen partially or completely. Guan *et al*. (2009) performed an unloading-induced outburst experiment, which suggested that sudden decompression brings about drastic fragmentation or even pulverisation of coal saturated in a high-pressured CO_2 environment for long duration. But this experiment used CO_2 instead of CH_4 as the seam gas and ignored the effect of stress change prior to the initiation of the outburst. Choi (2012) conducted an outburst test by releasing gas pressure of a cavity index cell containing a coal sample, which resulted in the formation of a cavity as well as discing type failures. Yin *et al*. (2015) conducted a conventional triaxial unloading experiment under the field-monitored abutment stress path, i.e., unloading confining stress down to 0.2-0.6 times the in-situ stress and loading axial stress up to 1.5-2.0 times the in-situ stress simultaneously, and results showed that the physical mechanical properties of coal were lower than that from conventional triaxial compression tests, and that the high gas pressures further weaken the coal.

2.5.4 Rapid fracture propagation in dynamic problems

Fracturing of rock, especially the failure close to the surface of an underground opening, is of paramount importance to safe underground exploitation. As early as the 1980s, researchers began to recognise that the propagation and coalescence of cracks to form macroscopic splitting fractures is a dynamic process in a wide range of

phenomena such as rock bursts and coal and gas outbursts (Hanes and Shepherd, 1981). In rock bursts, a two-stage process characterised by a slow and creep deformation, followed by rapid fracturing associated with seismic energy release, have been reported (Dyskin and Germanovich, 1993; Linkov, 1996; Rudajev *et al*., 1986). As well as inducing far-field stress disturbances and an excavation damage zone around an underground opening (Cao *et al*., 2016; X. Li *et al*., 2016, 2014; Martino and Chandler, 2004; Tao *et al*., 2012), the release of confining stress also gives rise to some penny-shaped micro-fractures near the opening surface (Khristianovich and Salganik, 1983). These mining-induced fractures usually run subparallel to the excavation face (Cai *et al*., 1998; Dyskin and Germanovich, 1993). This is because fracture initiation in rock can be attributed to cleavage in the direction of maximum compression (Fairhurst and Cook, 1966). Some research also supported that rock bursts take place at stress-concentrated districts as a result of the tensile extension of existing cracks subparallel to the working face (Ewy and Cook, 1990; Nemat-Nasser and Horii, 1982).

In coal formations, pre-existing fractures form hosting sites for high pressure gas, and are thus subjected to the combined action of stress and gas pressure. Gas desorption, which is capable of providing high energy for transporting coal particles over a certain distance, has been reported to be a key factor leading to coal and gas outbursts (Farmer and Pooley, 1967; Feldman *et al*., 2017; Jin *et al*., 2018; Khristianovich and Salganik, 1983; Odintsev, 1997; Wang *et al*., 2013; Zhao *et al*., 2016).

Theoretical models combining rock mechanics, fracture mechanics and gas dynamics have been developed to better understand coal and gas outbursts (Chen, 2011; Feldman *et al*., 2017; Odintsev, 1997). Chen (2011) considered the formation of a group of parallel fractures ahead of a mining face, whose length variation depends on the difference between face advance rate and fracture propagation speed. He reported that the presence of gas weakens the effective rigidity of the coal matrix and has a detrimental effect on the fracture growth, but the choked flow in the fracture zone results in a large gas pressure gradient and effective tensile stress ahead of the coalface to initiate an outburst. Using a theoretical model with a main fracture oriented parallel to the working face, Feldman *et al*. (2017) adopted Griffith's criterion to examine the fracture evolution under the combined action of instantaneous unloading and gas filtration to the fracture in coal mines. However, previous work on coal and gas outburst in coal mines has been mainly concerned with the conditions for its initiation,

and the following dynamic fracture propagation still needs theoretical and numerical investigations.

2.6 Microseismicity associated with rock bursts and gas outbursts

2.6.1 Definition and background

Underground rocks and coal strata are stressed by large overburden pressure and tectonic stresses. The sequence of mining excavation perturbs the initial stress field, which may trigger the formation or re-opening and movement of microfractures around excavation openings and beyond, manifesting as microseismic activities. Gibowicz and Kijko (2013) categorised microseismicity into two types: those related to geological structures, and those associated with mining activities. In the course of mining activities, microseismicity is defined as small and rapid shear movements of rock as a result of abrupt stress changes.

Cracks, delamination and displacement of rock masses cause inelastic deformation in a certain volume of rocks, which causes a sudden release of energy in the form of seismic emissions. The radiated energy comes from the stored strain energy in the immediate vicinity of the event focal region (Cook, 1963). In rock burst situations, the rock mass is believed to behave as an elastic medium based on seismic investigations (Salamon, 1983), and the mechanical behaviour is essentially of elastic nature (Ortlepp, 1983). It turns out that these waves contain in their structure a wealth of useful information regarding the dynamic elastic failure processes induced by mining operations (Lockner, 1993), and thus allows for the determination of important parameters of seismic hazard assessment.

Similar to earthquakes, the Richter magnitude can be applied to evaluate the magnitude of mining-induced seismicity (Richter, 1935), which typically ranges from -3.0 to 4.0 in a mine. A typical mining-induced seismic event can be distinguished from earthquakes by its higher frequency (Cai *et al*., 2007).

It is noteworthy that there are various seismic sources associated with mining activities. During coal extraction process, two distinct types of microseismic events, normal activity and outburst activity, were recognised (Styles, 1993). Normal activities are generated by instantaneous brittle failure as a direct consequence of coal extraction, so it is localised around the working face and closely associated with the extraction rate. They are typically impulsive, and appear to show downwards first motion. The normal

activities are usually with a velocity of around 3.5 km/s and distinguishable P and S waves. The propagation range is around 2 km. In contrast, outburst activities are rare during normal mining excavations, but tend to begin at least 10 days before an outburst and increase rapidly in rate of occurrence until forming a chain of coalescing acoustic events. The signals usually have emergent onsets and short durations, with a principal frequency component of about 32 Hz. The velocity is within the range of 0.3-1 km/s. They are not readily attenuated and can propagate as far as 6 km. Another remarkable feature is that the magnitude varies little, as opposed to varying over a couple of orders of magnitude for normal activities. Talebi *et al*. (1995) obtained the displacement spectra of recorded signals of outburst activities, noises induced by the cutting machine and a microseismic event using a Fast Fourier Transform (FFT) algorithm. The primary differences are that distinct peaks of energy can be found in the signals from artificially-induced noises, and that seismic events have a broad frequency component range from 100 to 600 Hz.

2.6.2 Field monitoring of mining-induced microseismicity

Mine-induced seismicity is an ever-present problem in most mining areas, especially at great depths. Methods used for recording of the dynamic effects of rock mass fracturing related to the seismic emission have been widely used to assess seismic and rock burst hazards. The application of microseismic monitoring technique as a tool to identify the regions prone to underground hazards can be dated back to the late 1930s and early 1940s (Jackson, 1984). In the late 1950s, Cook (1964, 1963) and Cook *et al*. (1966) conducted a systematic investigation on mining-induced seismic events in hard rock mines. All rock bursts were found to be seismic events, but not all seismic events turn out to be rock bursts. The failure foci, radiated energy of seismic events recorded by underground seismometers were also correlated with damage induced by rock bursts. McKavanagh and Enever (1980) appeared to be the first to apply microseismic monitoring system for outburst warning at West Cliff Colliery in Australia. Since then, intensive investigations have been embarked upon in mining countries all over the world.

Central Mining Institute (GIG) in Katowice, Poland has been engaged in monitoring seismic activities induced by mining operations in Upper Silesian Coal Basin (USCB) since the 1950s. In the early years, the monitoring was based only on a few single seismic stations. The archive data shows that about 350 seismic events were recorded

between 1950 and 1973. Since 1974 it has been expanded to form the Upper Silesian Regional Seismological Network (GRSS) consisting of 20 seismic stations, which was able to observe seismic events exceeding magnitude of 4 on the Richter scale. Modernisation of the GRSS network, which took place between 1974 and 1977, enabled tremors recording of energy $E \geq 10^5$ J. Nowadays the database contains seismic parameters of about 61,800 strong seismic events of energy $E \geq 10^5$ J. In the 70s and 80s the seismicity in USCB was very active, with around 2,000-4,000 seismic events per year. Since the 90s there has been a significant reduction in the number of tremors, which was associated with the restructuring of the mining industry and rock burst prevention, including selection of proper exploitation systems, and relaxation of the rock mass by using active prevention methods.

Since the mid-80s, a new project for Ostrava-Karviná Coal Basin (OKCB) mines has focused on developing online, real-time local and regional monitoring systems, which could enable automatic detection and analysis of seismic events. While the local network instruments consisting of monitoring systems distributed in coalfields were developed at the Mining Research Institute in Ostrava, the regional network instrument of the OKCB, Lennartz Electronic, was imported from Germany. Considering that all coal mines, seams and workings in the OKCB are classified into three categories of rock burst hazard according to the so-called regional prognosis, both passive and active preventive measures were proposed, and in special cases, they are even obligatory in order to achieve safe and effective mining.

In Colorado (USA), seismic monitoring of mining activity was conducted by an array of ten tri-axial strong-motion stations (Swanson *et al*., 2009). These stations were installed on the surface above two underground longwall coal mines in western Colorado. The district-scale network monitors mining-related and natural seismicity throughout an area of approximately 250 square kilometres of rugged canyon-mesa terrain. The real-time automated seismic event monitoring and notification tool includes Internet access to raw and processed data, web-client software that provides real-time graphical display of event locations, and email and paging notification of high acceleration levels and large magnitude events. From May 2007 to January 2009, approximately 20,000 events were detected, processed, and located. The level of activity is a strong indication of mining operations, particularly deep longwall mining.

There has been a systematic development of equipment and observation networks for monitoring mining-induced seismicity, including the development of software for interpretation of the recorded seismic events. As a result, a routine procedure for processing the recorded seismic events has been developed that allows for the on-going creation of seismic catalogue, including data such as date, time and location of tremor, seismic moment and seismic energy, stress drop in the seismic source, the source radius, etc. (Mendecki, 1996).

2.6.3 Fracture-slip seismicity-generation mechanism

Mining-induced microseismicity is conventionally considered to be caused by rock fracturing as a result of the sudden release of accumulated strain energy around underground openings. The occurrence and distribution of seismicity are affected by a combination of exploitation-induced, tectonic and coseismic stresses (Fritschen, 2010; Kozłowska *et al*., 2016; Sato and Fujii, 1988). Coal extraction usually has the most pronounced effect on the stress environment. As such, induced microseismic characteristics are closely correlated with mining activity in temporal and spatial sequences.

However, the stress-dominant rock fracturing mechanism for the generation of microseismicity cannot satisfactorily explain the following field observations: (1) source-scaling property of microseismicity; and (2) microseismicity locates mainly in the far field of excavation. Discrete natural fractures have been recognised to play an important role in the geomechanical and hydrological behaviour of underground rocks (Lei *et al*., 2017; Zimmerman and Main, 2003). Extensive research reported that fluid injection-induced seismicity in geological CO_2 storage (Rutqvist *et al*., 2016), hydraulic fracturing of unconventional reservoirs (Zhai and Shirzaei, 2018), enhanced geothermal systems (Staszek *et al*., 2017) and disposal of wastewater (Shah and Keller, 2017) is attributed to the reactivation of natural fractures widely distributed in the upper crust by overpressures. Likewise, mine-induced microseismicity is in essence the slippage of pre-existing subsurface fractures or flaws under the combined effects of tectonic and mining-induced stresses (Rorke and Roering, 1984; Spottiswoode, 1984; Stiller *et al*., 1983). Seismicity as a result of slip along weak planes gives normal seismic signatures as observed in earthquakes, whereas those resulting from crushing of rock material under high stress state generates ‘anomalous’ seismic signatures (Ryder, 1988; Wong and McGarr, 1990). Recent publications confirmed that

hypocentres of mining-induced microseismicity are bound to pre-existing subsurface structures such as faults or fracture-rich regions (Hassani *et al*., 2018; T. Ma *et al*., 2018). Therefore, the role of natural fractures throughout the active mining region needs to be highlighted in the explanation of microseismic response to coal extraction.

2.6.4 Correlation between microseismicity and rock bursts and gas outbursts

In the case of seismic events located in a coal seam, or in hard rock directly above or below the extracted coal panel, seismic activity is an important indicator of high stress zones. This is particularly important if various stress concentration factors (pillars, edges, remnants) are present (Dubiński and Mutke, 1996).

Field monitoring of the normal activities can provide implications for mining exploitation. Jackson (1984) found that the majority of seismic sources were detected at a distance of 10-80 m in front of a longwall face, while few activities were located in the immediate vicinity of the face. The seismic events tend to cluster in one place. Lasocki (1993a) found seismicity closely connected to mining activity, usually located at a distance up to around 100-200 m ahead of the exploitation face. The microseismic events move accordingly with the face advance. Field observations of rock bursts phenomena in Polish coal mines suggested that the destruction in operating workings usually occurred when the hypocentre of seismic events were located near the damaged workings and seismic energy was higher than 1×10^5 J (local magnitude, M_L>1.7) (Mutke, 2008).

Except for the spatial dependence on the working face, microseismic events also display temporal correlation with mining activities. Young *et al*. (2005) observed apparent time dependency of monitored acoustic emission signals at different excavation rounds. The majority of the seismic events take place within the first 24 hours after an excavation, although a few events happen up to 10 days later (Young *et al*., 2005). It is common that event count rates intensify steadily during several days before an outburst, and begin to decrease immediately prior to rock failure (McKavanagh and Enever, 1980; Shen *et al*., 2008).

In the case of coal mining, gas emission was also found to be associated with seismic events, with methane concentrations positively correlating with the acoustic emission rate (Nakajima *et al*., 1984). The remarkable agreement between microseismic activities and gas emission from the face indicated that methane is emitted in response

to the dilatant micro-fracturing which creates acoustic emission activities (Styles, 1993). Si *et al*. (2015) also confirmed that there is a direct correlation between microseismicity and gas emission rate, and that the gas emission rate tends to reach a peak when seismic energy increases dramatically, as shown in Figure 2.7.

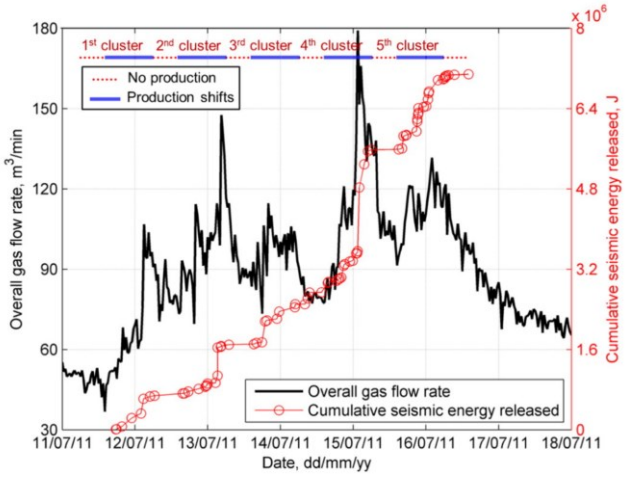


Figure 2.7. Microseismic activities and gas flow rate during the week of increased gas emissions from 11 to 17 July 2011 (after Si *et al*., 2015a).

2.6.5 Evaluation and forecasting of underground hazards using microseismic monitoring

The microseismic monitoring technique has been used as an effective passive seismological monitoring tool to identify regions prone to seismic-induced hazards in the field. Microseismic monitoring prevails over conventional monitoring methods such as stress and displacement measurements in that it can reflect the geomechanical response of individual natural fractures in the rock mass, even distance away from the working face. A wide range of methods have been developed to interpret microseismicity datasets, including spatial plotting of microseismicity magnitude, daily histogram of event frequency, magnitude-time history analysis (Hudyma and Potvin, 2010), frequency-magnitude analysis (Hudyma and Potvin, 2010), cluster tracking monitoring (Leśniak and Isakow, 2009), seismic energy analysis (Van Aswegen and Butler, 1993), seismic hazard mapping (Vasak and Dasys, 2009), etc. Intensive work was also undertaken in regard to the use of passive tomography (Maxwell and Young, 1993), seismic source parameter performance criteria (Alcott *et*

al., 1998) and probabilistic analysis of microseismic source size distribution (Lasocki and Orlecka-Sikora, 2008) in seismic hazard assessment in mines.

The microseismic event datasets have the potential to be used as precursors to the occurrence of outburst and rock burst hazards, as well as early warning of high gas concentration. Initially, the anomalous increase in seismic activity prior to mining hazards, sometimes followed by returning to low levels, was utilised as a predictor of rock bursts (Brady, 1977), outbursts (Styles *et al*., 1988), and roof failure (Shen *et al*., 2008). Local predictions were also made when frequency of noises within the coal reached a high frequency (Hargraves, 1980). Styles (1993) noticed harmonic, mono-phasic tremors with emergent onsets to be precursors to abnormal gas emission and coal and gas outbursts. Later on, extensive seismic risk assessment was performed through recognition of regularity patterns indicative of rock bursts, which are usually characterised by anomalous variations in microseismic precursors. Those microseismic precursors could be categorised as temporally-related (e.g., the number of large events, the ratio of the number of events of different energy, the variance of event counts at two successive time moments), energy-related (e.g., sudden change of apparent volume, seismic stress drop, the deviation of seismicity from the long-term trend, *b* value), and spatially-related (e.g., fractal dimension, median distance between microseismic pairs) (T. Ma *et al*., 2018; Marcak, 1993; Stewart and Spottiswoode, 1993). However, individual seismic index tends to identify different subsets of potentially-damaging events when applied in isolation, and the most effective seismic index may vary from site to site. In this sense, comprehensive evaluation models comprising of multiple weighted microseismic indices were further developed for rock burst risk evaluation (Cai *et al*., 2018, 2014b).

Since 1990s, some comprehensive quantitative methods have been introduced to the forecasting of rock bursts and gas outbursts. Lasocki (1993a) developed a statistical prediction method based on the mining induced seismicity data for a period of time. Kijko *et al*. (1993) identified clusters of microseismicity which may lead to a strong event based on a space and time metric, and further used a probabilistic method to analyse the time occurrence of microseismicity. Based on data from regional seismological monitoring, Melnikov *et al*. (1996) used mathematical and physical modelling to determine stress and strain precursors to rock bursts. Srinivasan *et al*. (1997) found it sufficient to predict mining-induced seismicity and rock bursts by

linear extrapolation based on a deterministic model. The developed model correlates mining with seismological parameters, using parametric pairs such as excavated tonnage and released seismic energy, number of rock bursts and released seismic energy, and number of rock bursts and number of seismic events. Fuji *et al*. (1997) verified the possibility to apply elastic numerical stress analysis in predicting rock bursts in deep longwall coal mining. They suggested that, by examining the maximum shear seismic moment release rate, fracturing at the work face could be successfully predicted even without the help of microseismic monitoring. Feng *et al*. (2015) developed the probability distribution functional relationships between rock bursts and a group of microseismicity parameters, based on which a rock burst warning formula could be used to analyse the real-time microseismic data for early warning of strain bursts and fault-slip bursts. The combination of rock burst databases and statistical seismicity parameters facilitates early risk assessment of mining hazards.

One common drawback of the current rock burst and gas outburst assessment and prevention methods referred to above is that their applications are mostly based on site-specific field experience, as opposed to sound physical foundation. The success of the forecasting at a specific mine cannot necessarily guarantee the success in application to other rock burst-prone mining sites. In addition, mining activities are causes of microseismicity, but most forecasting methods focus only on the microseismic monitoring data itself, without incorporating the concurrent mining intensity. This can sometime lead to unreliable forecasting results, where the risk potential around a longwall face should obviously vary with scheduled mining intensity (ranging from complete cessation to full capacity operation), while the same risk potential would be estimated based solely on previous microseismic datasets.

It is of urgent need in mining practices to make full use of comprehensive monitoring records to realise short-term (in a time range of one day) forecasting of the potential of rock bursts and coal and gas outbursts. In addition, the forecasted results are expected to be used as a feedback to update the excavation schedule, so as to satisfy the requirements of timely scheduling, regulation and production in modern mines.

2.6.6 Advances in modelling of seismic activities in rock formations

Stress and rock failure modelling has been conventionally used in representing mining-induced local overstressed zones (Abdul-Wahed *et al*., 2006; Senfaute *et al*., 2001)

and damaged and failed zones (Read, 2004; Vatcher, 2014) in mining, which were shown to have a strong spatial correlation with the intensive microseismic zones monitored in the mines. However, the shortcoming of the conventional modelling approach is that microseismic events generated at a distance away from the excavation openings could not be represented.

A brief review of the advances made in modelling methods developed to simulate both mining induced microseismic events and acoustic emission (AE) generated in laboratory rock failure experiments is presented in this section. Resulting from the generation of slippage or the propagation of fractures, both microseismicity and AE are low-energy seismic events (Cai *et al*., 2007), even though acoustic emissions in rocks have a much higher frequency (10^4 - 10^5 Hz) than that of the seismic motion wave frequencies (10^2 - 10^3 Hz, audible by human ears). Many AE simulation methods have been developed to reproduce and interpret laboratory experimental results, including continuum damage models, particle-based discrete element method (DEM) models, lattice models, and the combined finite-discrete element method (FEM/DEM) models (Lisjak *et al*., 2013).

Broadly speaking, four approaches may be identified with respect to the source mechanisms for the generation of microseismicity (microseismicity potential or fracture slip) and its model representation (elemental or explicit fracture) in rock formations. The first approach can be traced back to the 1990s, where an evaluation index was introduced to estimate the microseismicity potential at all the grid blocks in the model domain representing an isotropic medium. Fujii *et al*. (1997) used the total maximum shear seismic moment of fractured elements during one mining step as the indicator in three coal mining case studies, and successfully predicted burst-susceptible areas, and even rock burst occurrences. Nazimko and Babenko (2011) proposed an empirical criterion comprising of equivalent stress and stress relaxation rate, in order to account for dynamic failure of rock mass effectively. The spatial distribution of experimental and simulated events demonstrated good agreement. Shnorhokian *et al*. (2014) constructed four spatial clusters in a FLAC^{3D} model based on 24 events within three geological formations, and used the maximum shear stress, brittle shear ratio (BSR), and the continuous change in differential stress (CC-DS) as potential criterion of mining-induced seismicity. They found that CC-DS achieved the best result by conducting a quantitative evaluation for all the locations in the model. A

major limitation of this approach, which assumes isotropic rock properties, is that the predicted microseismic events are usually located in close proximity of mine openings, and thus the spatial dispersion nature of seismic events cannot be realised.

The second approach aimed at taking into account the presence of pervasive heterogeneity in rock and its effect on the occurrence of microseismicity during mining, or laboratory rock failure tests. Tang (1997) used a Weibull distribution to describe the heterogeneity of rock strength in a finite element code RFPA, and simulated seismicity generated during the progressive failure of rock in the laboratory. Fang and Harrison (2002) developed a local degradation model in FLAC to simulate brittle fracture of heterogeneous rock in the laboratory, whereby material strength of zone elements are represented by the Weibull distribution, and the bulk and shear moduli of zone elements degrade once the Mohr-Coulomb failure criterion is reached. Boltz (2014) adopted a strain-hardening/softening ubiquitous-joint model in the same simulator, while the heterogeneity in the rocks is represented by scaling-down rock properties of the elements representing the joints in the model. One limitation of this approach is that the size of the fractures generated is constrained by the size of the elements, which results in the simulated energy release falling into a much narrower range compared with that typically recorded in laboratory experiments.

The third approach, which simulates large displacements and represents rock fracture phenomena explicitly using discrete element method (DEM) or its coupling with finite element method (FEM), allows micro-fracture nucleation and propagation during rock failure processes to be modelled in a more realistic manner compared with the continuum mechanics-based methods described above. Hazzard and Young (2004, 2000) used a DEM code, Particle Flow Code, to simulate rock failure, which is represented by the breakage of bonds between neighbouring particles. The clustering of the microcracks created, both in space and time, is deemed to form an AE event. Lisjak *et al*. (2013) developed a quasi-dynamic technique, whereby the fracture is represented by means of cohesive discrete joint elements in a FEM/DEM code to model AE activities resulting from brittle failure of rock. Although capable of capturing the intrinsic nature of AE activities, this approach is computationally intensive, which limits its application to field-scale models.

The fourth approach was developed to address the knowledge gaps in the simulation of microseismicity generation in field-scale models in a more efficient and realistic manner. In the pioneering work of Salamon (1993), a reasonable approximation of microfractures, along which slip can occur to form a microseismic event according to the Mohr-Coulomb failure criterion, was implemented in the model prior to mining. Board (1994) applied the excess-shear-stress (ESS) criterion for fracture slip, and found that the produced seismic responses, such as slip radii and stress drop, were correlated well with the observed data. Linkov (1997) developed an elasticity-softening-creep (ESC) model to simulate both seismic (unstable) and aseismic (stable) events. Wiles *et al*. (2000) used monitored field seismic events data, believed to be caused by the slip of an existing fault, to estimate its location and orientation. This inferred fault was then implemented in the numerical model. Malovichko and Basson (2014) introduced a set of sub-flaws to account for the partial slip of a mother flaw, so that rather complex flaw shapes can be modelled.

This last approach has so far been applied mostly to hard rocks, whose response to excavation remains predominantly elastic, and where the induced microseismicity usually concentrates around underground openings such as tunnels and caverns. In contrast, microseismic events induced from longwall coal mining can occur up to 100 m ahead of a working face. Jackson (1984) reported that the majority of microseismic activities are located at a distance 10-80 m ahead of longwall faces, and yet little activity was detected in close proximity of the faces in Polish collieries. Sato and Fujii (1988) found that up to two thirds of the microseismic events were located in a zone 60 m in front of and 20 m behind the longwall face, and that the hypocentre distribution along the direction of advance was about symmetrical with regard to a position 10-30 m ahead of the longwall face. Simulation studies of microseismicity resulting from longwall coal mining have so far not been reported in the literature.

2.6.7 Effect of heterogeneity on microseismic characteristics

Occurrences of microseismic anomaly have been reported to be associated with geometric and structural complexities, such as bedding shear zones in coal seams and stiff structures in hard rock mines. The presence of these geological structures influences the rock mass response to loading conditions, and thus microseismic characteristics. For example, Sato and Fujii (1988) reported that the seismic energy release rate was significantly suppressed before passing through a fault in the hanging

wall. It has been observed that the largest seismic events tended to fall into the largest vein in an American deep hard rock mine (Swanson, 1992). It was also reported that two stiff reef structures led to decreases in both seismic event rate and seismogenic movement rate in an Australian gold mine (Abolfazlzadeh and Hudyma, 2016).

The impact of local heterogeneity in rock properties such as permeability and strength on the response of rock masses to excavation has been studied numerically. An and Cheng (2014) adopted a one-dimensional flow model with a low-permeability zone to study the gas distribution patterns, and showed that both the magnitude of permeability and the extent of the low-permeability zone affect the abundance of gas in the coal seam. Using a coupled fluid flow-geomechanical model, Si (2015) simulated the advance of a development heading approaching two different types of local heterogeneities, i.e., a low permeability zone representing a tectonic intrusion, and an elevated-strength zone, to study the impact of local heterogeneity on gas emission and outburst tendency. The simulation results have shown that the presence of a low permeability area results in an increased gas pressure gradient with the approaching of the heading, and an increase in the outburst tendency shortly after the passage of the heading; meanwhile, the presence of an enhanced-strength region leads to a significant suppression in gas emission when the heading approaches, and a rapid increase in gas emission with the passing of the development heading.

The impact of material heterogeneity arisen from geological structures such as faults or shear zones has been investigated by a number of researchers. Lei *et al*. (2004) conducted triaxial loading experiments on rock samples containing pre-existing joints with various healing strength and asperities, and found that while the failure of homogeneous faults gives no clear early warning signals and is unpredictable, heterogeneous faults fracture after a crack nucleation phase with distinct statistical variation of AE activity parameters. Sainoki and Mitri (2014) used a transversely isotropic, linear elastic model to verify the increase in fault-slip potential as a result of heterogeneity of shear stiffness in the weak zone. Zhao *et al*. (2014) modelled the response of the rock mass containing a brittle fault zone in TBM excavations, in which the Mohr-Coulomb yield criterion was adopted to evaluate the failure of the fault zone, and interface elements were used to represent the interaction between the fault and the rock mass. Xu *et al*. (2015) used an equivalent continuum approach to model a cavern

excavation near an interlayer shear weakness zone, where the thickness, strength and orientation of the zone were characterised.

However, there are no systematic numerical investigations regarding the influence of material heterogeneity or geological discontinuities on microseismic occurrences and evolution as most current numerical modelling research are based on continuum mechanics which is limited to deterministic stress and fracture analyses. The heterogeneity effect can be modelled using the last approach reviewed in Section 2.6.6, which is capable of taking the stochastic nature of microseismicity into account.

2.7 Summary

Coal is a weak and friable porous medium characterised by dual porosity systems: an interconnected fracture network and matrix blocks containing heterogeneous micro-pores. Gases such as CH_4 and CO_2 contained in coal is primarily adsorbed on the surface of micro-pores under gas pressure. Coal follows basic geomechanical principles like other rocks, and the migration of gas in coal deposits is controlled by the stress-dependent permeability of coal. The unique physical, mechanical, adsorption and hydraulic properties of coal (i.e., low integrity, low strength, rapid gas desorption and low permeability) provide favourable intrinsic conditions for underground hazards such as rock bursts and coal and gas outbursts in coal mining.

Rock bursts and coal and gas outbursts are attributed to combined impacts of intrinsic and extrinsic influencing factors. The primary difference between the two hazards is the energy source, which is elastic strain energy of stressed rock masses for rock bursts, and internal gas energy for outbursts. A number of theories have been proposed to explain the triggering mechanisms for both hazards, and a variety of empirical thresholds and theoretical criteria have been developed for the evaluation of burst risks. Since both hazards are triggered under combined static and dynamic loads, they can be generalised as problems of dynamic instability under excavation unloading conditions. Therefore, the stress and fracture behaviour of rock/coal needs to be analysed from the perspective of dynamics, where unloading-induced stress perturbations serve as a source of dynamic disturbances. Furthermore, the crucial role of gas should be incorporated to the reformulation and further investigation of the problems.

Microseismicity intimately associated with mining activities in temporal and spatial sequences has been recognised as the slippage of pre-existing fractures or flaws under the combined effects of tectonic and mining-induced stresses. Mining-induced microseismicity is an important indicator of high stress zones, excessive gas emission, and unstable rock fracture. As such, the microseismic monitoring technique has long been used to provide precursors and even early warnings to rock burst and coal and gas outburst hazards. However, while most of previous research interpreted microseismic response to coal extraction from the perspective of stress concentration, the role of attributes of natural fractures throughout the active mining region needs to be highlighted in contributing to microseismicity.

Chapter 3 Seismic response and fracturing behaviour of coal under true triaxial stress conditions

3.1 Introduction

This chapter aims at exploring the seismic response of naturally fractured coal to stress and fracturing, with an emphasis on identifying temporal and spatial behaviour of fractures using the active acoustic monitoring technique. The author carried out laboratory hydraulic stimulation experiments to create fractures in two naturally fractured cubic coal blocks under pre-stressed conditions, using a true triaxial rock testing machine equipped with an acoustic system. Recorded seismograms are correlated with the initiation of hydraulically-induced fractures, followed by interaction with interior natural fractures. A suite of processing techniques, such as Fourier frequency analysis and seismic velocity tomography, are performed to supplement the analyses of seismograms. X-ray computed tomography (CT) is further conducted before and after the experiments in order to identify the location and geometry of hydraulic and natural fractures.

3.2 Effective detection of fracturing behaviour

Intensive efforts have been put into accurately tracking and characterising fracture propagation and interaction in laboratory fracturing experiments, either on cylindrical coal samples using conventional triaxial setup (Hou *et al*., 2016; Liang *et al*., 2017) or on cubic coal blocks using true triaxial setup (Huang *et al*., 2017; Li *et al*., 2018; Jun Liu *et al*., 2018). One straightforward method to observe hydraulic fractures is to open up a sample after fracturing and inspect fracture features in great details, or to use an optical scanning system or X-ray computed tomography (CT) system to measure the geometry of fracture surface after experiments (P. Liu *et al*., 2018). Slickwater or gel

coloured with dye (Fan and Zhang, 2014; Olson *et al*., 2012; Zhao *et al*., 2018) and thermos-setting resin mixed with a fluorescent compound (Naoi *et al*., 2018) were reported to be used as fracturing fluid to indicate the propagation path and even leakage into fractured rocks. Various techniques have been developed in order to reveal the fracture propagation or detect the locations of fractures in real time. Acoustic emission (AE) monitoring, following the same principle as passive microseismicity monitoring in the field, is widely used in laboratory fracturing experiments (Hou *et al*., 2016; Liang *et al*., 2017; Naoi *et al*., 2018; Zhao *et al*., 2018). Another promising method is to use transparent rock-analogue samples containing a pre-existing fracture network for optical visualisation of hydraulic fracture propagation in experiments (Nakagawa *et al*., 2015). The images can be enhanced by using ultraviolet (UV) light and fluorescent dyes.

From the 1990s, an acoustic imaging system with acoustic source-receiver pairs as active sources was first developed and applied in laboratory hydraulic experiments under true triaxial stress conditions at Delft University of Technology, Netherlands (Savic, 1995). The system could scan the accommodated block at a certain time interval, and locate positions of the fracture tip, fracture interface, fracture width and intersection between fractures and the borehole. The diffraction seismic waves scattered from fracture tips could be used to reveal complete fracture growth path in time and space, whilst the compressional transmission seismic waves could be applied to estimate the fracture width profile during its growth (Groenenboom, 1998). A large number of hydraulic experiments were conducted using this experimental setup, and the influence of borehole orientation, perforation parameters, flow rate and viscosity, horizontal differential stress on characteristics of near-wellbore fracture geometries such as orientation, smoothness, reorientation and number were systematically investigated (Van de Ketterij, 2001; Weijers, 1995). In order to investigate the fracture interaction with pre-existing fractures, Meng (2010) created a single pre-existing fracture representing a natural fracture by cleaving the block into dual-layer or tri-layer that would intersect with the borehole. It was found that the recorded acoustic data well located the geometry of the growing fracture, and that the hydraulic fracture initiation could trigger pre-existing fractures to open. However, the artificially created fracture does not realistically represent a natural fracture in terms of aperture and

roughness, and much more complex interaction behaviours of fractures need to be considered when a natural fracture network is involved.

Unlike most rock types, coal is typically characterised by face and butt cleats distributed orthogonally to bedding planes. In addition, as a week and friable geomaterial, coal usually hosts a system of natural fractures, which constitute a unique discrete fracture network (DFN). Therefore, the spatial and temporal fracturing behaviour in naturally fractured coal needs to be further investigated.

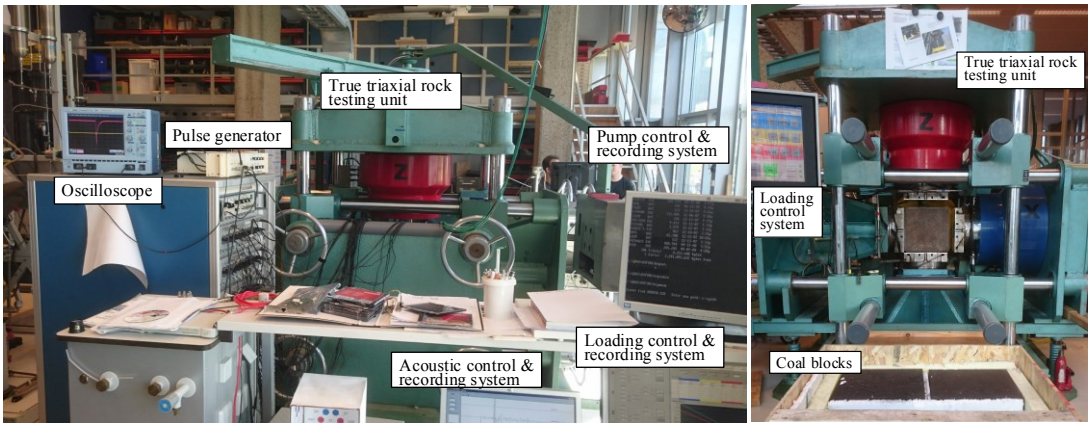
3.3 Equipment and experimental procedure

3.3.1 Experimental set-up

The experiments were conducted using the true triaxial rock testing machine in the Geoscience and Engineering Laboratory at Delft University of Technology. Experimental apparatuses used include a true triaxial rock testing machine to apply mechanical loads, an injection system for hydraulic fracturing, and an ultrasonic monitoring system with active sources to record seismic response during experiments.

The true triaxial rock testing machine

The true triaxial rock testing machine has large loading plates which are used to apply stress as well as measuring the generated acoustic signals through the transducers inserted in the plates (Figure 3.1). It is comprised of three orthogonal uniaxial compression systems. Each uniaxial system has a loading platen (cylinder) with a piston on one side and a removable pressure platen (door) on the other side. The two platens are connected by four tension bars to impose pressure to the accommodated sample. The cylinder pressures can be either controlled manually or by servo valves via a control computer. Each of the three axes of the machine can independently exert a maximum force of 3,500 kN, corresponding to a 38.9 MPa maximum normal stress on the sample surface.



(a) (b)

Figure 3.1. (a) True triaxial rock testing set-up equipped with loading, injection and acoustic systems, and (b) external view of the true triaxial rock testing unit.

The size of the loading platens is 294 mm, 6 mm smaller than the dimensions of the accommodated test block to prevent the platens from touching when the displacements are large. The loading platens are covered by 0.1 mm thick Teflon sheets greased with vaseline to minimise the friction between the loading platens and the sample, thus avoiding inhomogeneous stress distribution inside the sample.

The movements of the frame are measured by linear voltage displacement transducers (LVDTs) to represent the deformation of the sample. 3 pairs of LVDTs, 2 in each direction, are mounted in the facing sides of the block for displacement measurements along the three loading directions. The displacement in each direction is calculated as the average of displacements from both transducers. The range of the displacement measurement is 5 mm.

Injection system

The injection system is designed for accurate control of fluid injection into the sample. Fluid is injected to a pre-drilled borehole in the sample through an injection tube, which is connected to an injection pump via a valve. The pressure is produced by the pump controlled by a computer, and both injection and borehole pressures can be measured by pressure gauges.

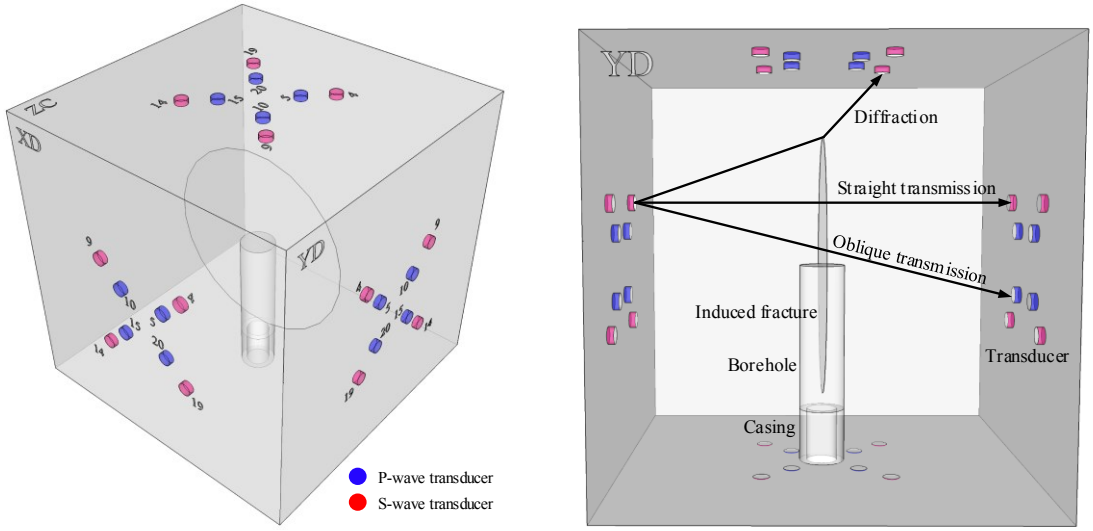
Either silicon oil or slick water can be used as a fracturing fluid. Fracturing fluid can be injected at a rate within a range of 0.1-100 mL/min, and achieve an injection pressure of up to 50 MPa. The volume of the pump is 300 mL.

Ultrasonic monitoring system

The ultrasonic monitoring system is designed for recording elastodynamic waves associated with stress variation and fracturing behaviour. Unlike passive monitoring techniques which record acoustic emission (AE) whose source is the fracturing itself, this system uses piezoelectric transducers inserted in the loading platens as active sources. The system is controlled by a switch box, which interconnects a pulse generator, emitting and receiving piezoelectric transducers, an oscilloscope and a control computer. The generation and acquisition of acoustic signals are controlled by the computer, and the emitted signal can be visualised on the oscilloscope.

The system has a maximum capacity of 48 transducers channels, 8 on each steel loading platen, as shown in Figure 3.2. They are 12.7 mm in diameter and 16 mm in height. The Teflon sheets between loading platens and the sample have holes at the transducer locations so as to keep direct contact between transducers and the sample. A spring behind each transducer pushes the transducer face against the sample surface, and the contact coupling is enhanced by ultrasonic couplant.

Each transducer can function in source and receiver modes in a sequence. The piezoelectric transducers can generate either compression or shear waves (P or S waves) by converting electric pulses into mechanical waveforms. Half of the transducers are P-wave transducers mounted on the outer ring (Nos. 5, 10, 15 and 20, coloured in blue), whilst the rest are S-wave transducers on the inner ring (Nos. 4, 9, 14 and 19, coloured in red). All the transducers can receive both P and S waves in the receiver mode. A transducer is named according to its orientation and position, with a character representing the normal direction of the host platen (X, Y or Z), another character denoting the host platen (C for Cylinder, or D for Door), and a number indicating the position on the platen. For example, XC14 refers to the No. 14 transducer located on the cylinder facing the x direction.



(*a*) (*b*)

Figure 3.2. (a) Transducer configuration used during ultrasonic monitoring of the true triaxial experiment, and (b) trace types including straight transmission, oblique transmission and diffraction (XD: platen normal to the x direction, YD: platen normal to the y direction, ZC: platen normal to the z direction).

The source-receiver combination sequence is given by the host computer. When a transducer emits an acoustic signal, all 40 transducers from other five platens act as receivers. The transducers are organised into 960 source-receiver pairs in total, which can be categorised into six raypath types: P wave straight transmission (stP, 6 pairs), P wave oblique transmission (otP, 63 pairs), P wave diffraction (dP, 88 pairs), S wave straight transmission (stS, 36 pairs), S wave oblique transmission (otS, 279 pairs), S wave diffraction (dS, 488 pairs), as illustrated in Figure 3.2b. A source-receiver pair is named by linking the names of emitting and receiving transducers, e.g., XC14-YD15. All of these combinations can be measured within a couple of seconds, which is referred to as an acoustic scan. The time interval between two acoustic scans is 30 s.

The response of a receiving transducer to a source signal is a wide band compression or shear wave with a central frequency of 0.5 MHz. The ultrasonic acoustic signals are sampled with a frequency of 5 MHz and a resolution of 12 bits (2 bytes in storage). Each record contains 2,048 sampling points, which corresponds to a recording period of around 0.4 ms. The signals are visualised using the WimScan software in real time during the experiments.

3.3.2 Sample preparation

Large coal blocks from an underground coal mine in Poland have been collected and cut to shape (300 × 300 × 300 mm cubes), ready for testing. These required several batches of very large intact coal blocks being brought out from the mines and be carefully cut.

The coal blocks had a few sets of natural fractures which outcrop at surfaces, as shown in Figure 3.3. Cleat patterns (face and butt cleats) orthogonal to bedding planes on both coal blocks can be observed clearly, with an average spacing of 8-10 mm between face cleats. The orientation of face cleats on coal block 1 and 2 are around 25° with respect to the x and z directions, respectively. Considering that the same stress magnitudes and directions would be applied on the two coal blocks with the minimum stress being along the x direction, the coal blocks were placed into the testing machine in the direction marked in the figure, where the induced fracture in coal block 1 was expected to be sub-perpendicular to bedding planes and face cleats, while that in coal block 2 being sub-perpendicular to bedding planes and butt cleats. Before putting the coal blocks into the test rig, it was made sure that opposite faces of the blocks were parallel to each other. Rough surfaces and loose corners were repaired with gypsum and polished by sandpaper, so as to achieve full contact with loading platens and avoid inhomogeneous loading inside the coal blocks.

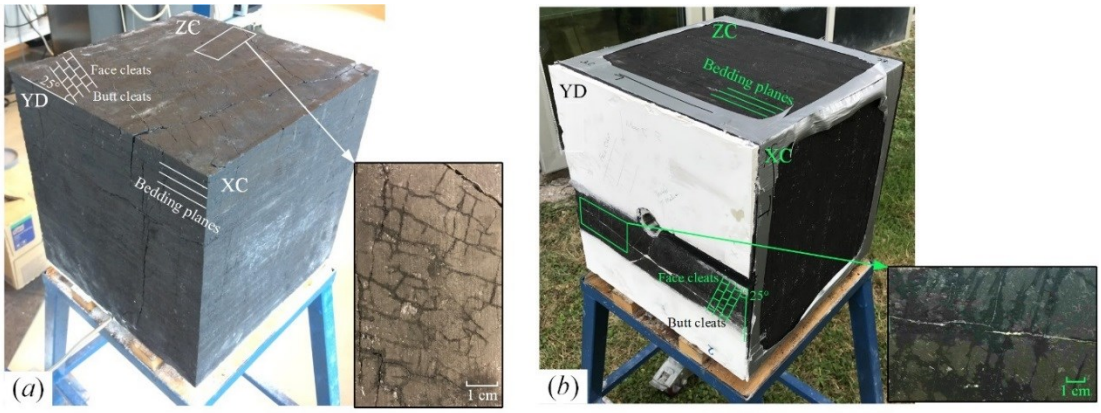


Figure 3.3. Cubic coal blocks used in the experiments: (a) coal block 1, and (b) coal block 2.

In preparing for the fluid injection experiment to create further fractures and monitor acoustic response, an injection borehole (15 cm in length and 34 mm in diameter) was

drilled into the middle of the coal blocks (from the faces ZD and YD for coal blocks 1 and 2 respectively), and a short steel casing (4 cm in length and 23 mm in inner diameter) was glued inside the first 4 cm section of the borehole. An injection tube was connected to the steel casing via a connector, and two rubber rings were put between the casing and the connector for sealing purposes. The injection tube was embedded along a pre-drilled groove on the block face to avoid interference with loading platens. Before the experiments, solid core samples from the same coals were characterised, as presented in the next section.

3.3.3 Laboratory characterisation of mechanical and hydraulic properties of coal

Permeability characterisation

Three 38 mm diameter solid core samples (1 cored parallel and 2 cored perpendicular to the bedding planes) were characterised in terms of their mechanical and hydraulic properties. The permeability characterisation of coal samples was carried out in two stages.

In the first stage, the permeability was measured at 2.4 MPa confining stress and at pore pressures of up to 0.6 MPa in a Hassler cell, using nitrogen as the gas flowing through the coal sample. Figure 3.4 presents two examples of Hassler cell permeability test results for two coal samples.

In the second stage, multi-stage triaxial testing of 38 mm core samples was used for stress-strain-permeability characterisation, which also yielded the elastic properties (Young's modulus and Poisson's ratio) for the coals tested. The multistage triaxial tests were carried out using a four column 2,000 kN capacity rock testing system (ESH Testing Limited, Brierley, UK) at Imperial College (Figure 3.5). The hydrostatic and deviatoric loads are controlled independently using servo-controlled systems while the upstream and downstream pore pressures are applied using manually controlled pressure regulators. The flow rate is measured using a flow meter. Coal permeability is measured by applying a differential pressure of gas between the upper and lower platens. The components of the testing system and the triaxial cell used for 38 mm diameter stress-permeability testing is illustrated in Figure 3.5a and b.

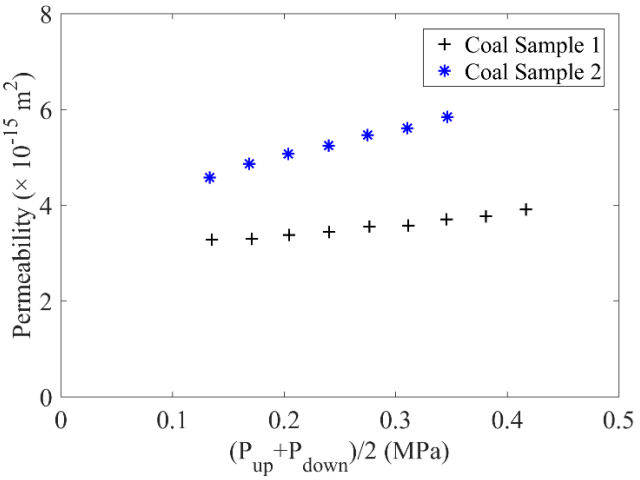
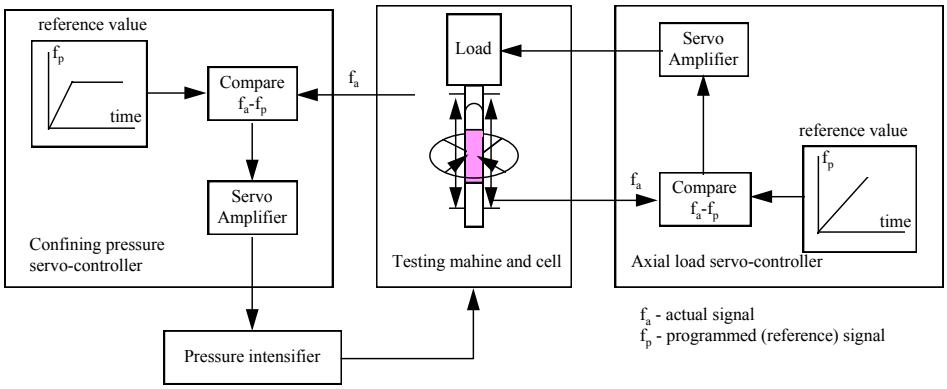


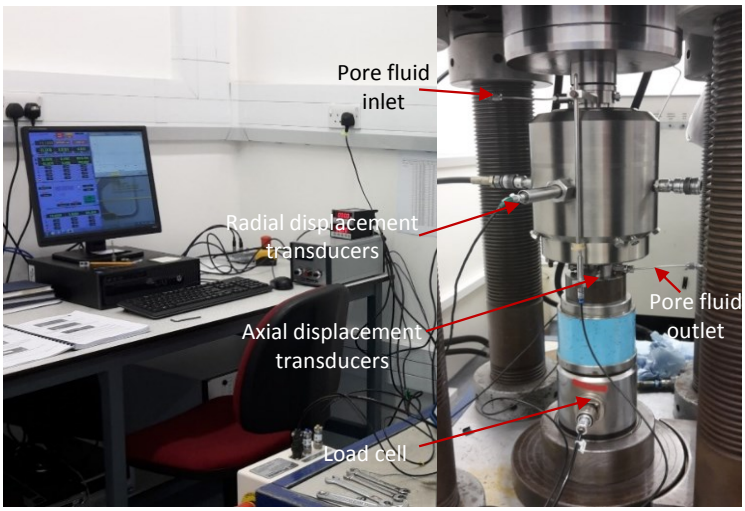
Figure 3.4. Permeability values for two coal samples measured using a Hassler cell (Each reading represents a different differential pressure across the sample also showing the Klinkenberg Effect).

During the multistage triaxial experiments, Helium was used as the gas flowing through the coal sample. At each stage, a confining stress was first applied and at least five readings for permeability were made under different upstream pore pressures. Axial loading was then increased at a loading rate of 1.5 mm/h until the coal sample was about to yield. Meanwhile, permeability was continuously measured throughout the experiment to indicate its variation in relation to the increased axial and radial stress. The coal samples were brought to failure at a confining stress of 18 MPa at the sixth stage.

Figure 3.6 presents three examples of multistage triaxial test results for coal samples characterised. It can be seen that the permeability values at the same confining stress and pore pressures for the coal sample cored parallel to the bedding planes are around one order of magnitude larger than those for the coal sample cored perpendicular to the bedding planes. This is because the connectivity of coal is primarily controlled by face and butt cleat systems orthogonal to the orientation of bedding planes.



(a)



(b)

Figure 3.5. (a) A schematic of the triaxial testing system, (b) 38 mm diameter core triaxial cell and stress-permeability testing components.

Based on the compressive strength with increasing confining stresses, the cohesion and friction angle of a given coal specimen can be determined by adjusting a straight line tangential to the Mohr's circle diagram showing a Coulomb failure envelope. The cohesion and friction angle for the coal samples are 8.7 MPa and 36°, respectively. Physical, mechanical and hydraulic properties for the three coal samples tested are summarised in Table 3.1.

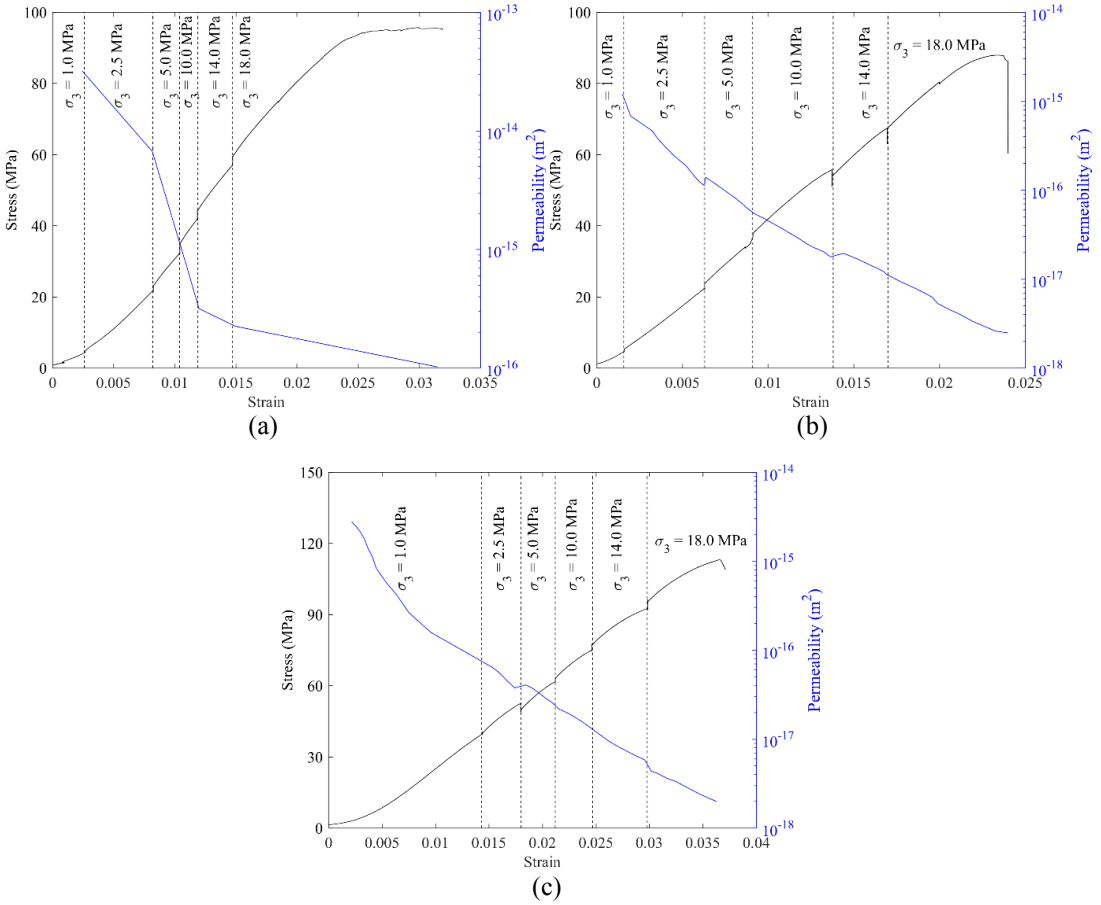


Figure 3.6. Axial stress-strain-permeability behaviour of coal determined through multi-stage triaxial testing: stress-strain curve and permeability values for (a) a coal sample cored parallel to bedding planes, and (b) and (c) two coal samples cored perpendicular to bedding planes.

Table 3.1. Physical, mechanical and hydraulic properties for coal samples tested.

Sample No.	Grain density (kg/m^3)	Porosity (%)	E (GPa)	υ	Average permeability* ($\times 10^{-15}$ m^2)
M-Coal_1	--	--	2.57	0.22	--
M-Coal_A	1.24	3	3.08	0.21	3.6
M-Coal_B	1.28	2	2.72	0.33	5.2

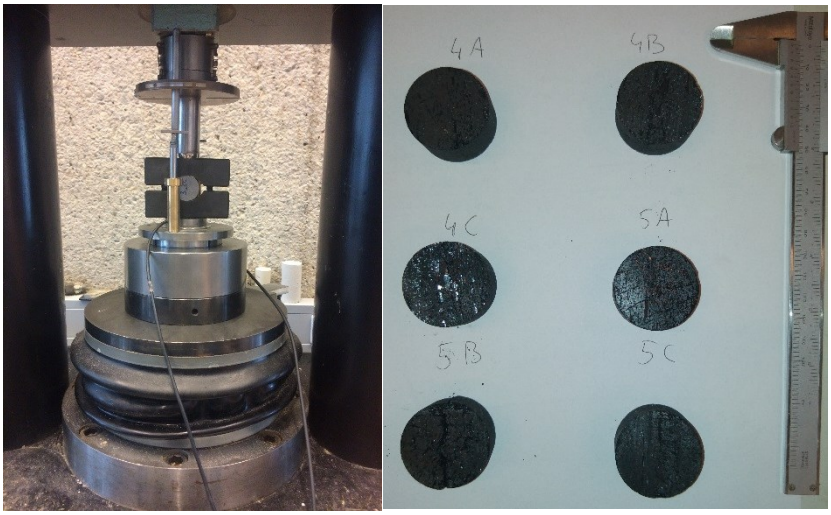
* The average permeability is calculated based on measurements using the Hassler cell.

Brazilian tests

To characterise the tensile strength and fracture toughness of coal, Brazilian tests were further carried out on six 20 mm length and 38 mm diameter core samples (Figure 3.7). The suggested formula for calculating the tensile strength σ_t (MPa), based on the Brazilian test is written as (Guo *et al*., 1993):

$$\sigma_t = \frac{2P}{\pi Dt} = 0.636\frac{P}{Dt} \tag{3.1}$$

where P is the load at failure (N), D is the diameter of the test specimen (mm), and t is the thickness of the test specimen measured at the centre (mm).



(a) (b)

Figure 3.7. (a) A schematic of the Brazilian testing system, (b) six 38 mm diameter coal disks prepared for Brazilian tests.

The fracture toughness determined from the Brazilian tests is given by (Li and Wong, 2013):

$$K_I = \frac{2P\Phi(c/R)}{\pi^{3/2}R^{1/2}t\alpha} \tag{3.2}$$

where 2α is the arc distance in which P is assumed to be distributed radially, R is the disc radius, $2c$ is the fracture length, and $\Phi(c/R)$ is a dimensionless stress intensity factor coefficient.

The results of six tests were comparable in that all samples were loaded along the orientation of observed bedding planes, assuming that this is the weakest plane in terms of tensile strength. Cracking at the first stress drop could be observed or heard in all cases, although the load did increase afterwards. The post-failure load increase is because the two halves of the coal disk are clamped in the mould and bear the increased axial load. Therefore, the first stress drop was picked for calculation of tensile strength and fracture toughness. Figure 3.8 presents the stress-strain curves from the Brazilian

tests for six coal samples. Only the post-failure part immediately after the first drop are plotted for better visualisation. The calculated tensile strength and fracture toughness values for the six samples are summarised in Table 3.2.

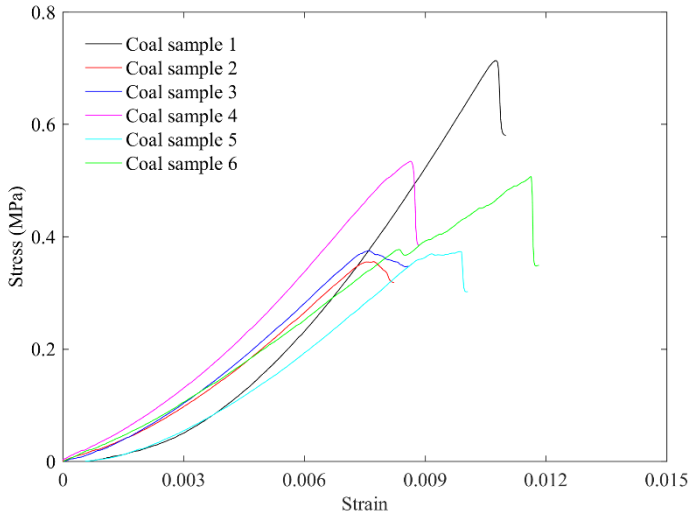


Figure 3.8. Stress-strain curves of the Brazilian tests for the six coal samples.

Table 3.2. Tensile strength and fracture toughness for the coal samples tested.

Sample No.	4A	4B	4C	5A	5B	5C	Mean
Tensile strength (MPa)	0.71	0.35	0.37	0.53	0.37	0.51	0.47
Fracture toughness (MPa·m$^{1/2}$)	0.14	0.07	0.07	0.11	0.07	0.10	0.09

3.3.4 Experimental procedure for the true triaxial tests

Considering the relatively smaller dimensions of loading platens used to apply triaxial loads in the experiments, a preliminary numerical modelling was conducted to ensure that the edge effect caused does not have a notable impact on the interior stress distribution. In order to set up the computer system and to calibrate the experimental rig, preliminary tests on two concrete blocks of the same size with cased-perforated boreholes were performed and good acoustic signals and stress were obtained. The experiments on two coal blocks were then carried out according to the following procedure:

(1) Experiment preparation and instrument setup: After all the acoustic transducers are embedded in the loading platens for acoustic measurements, the coal block is placed in the true triaxial apparatus, with the borehole at the bottom for coal

block 1, or at the front for coal block 2 (see Figure 3.3). The injection tube is then connected to the injection system, and LVDTs are set up for displacement measurements.

(2) Initial acoustic measurements: The 300 mm cubic coal block is loaded stepwise to 50, 100, 150, 200, and 270 kN in x, y and z directions at a loading rate of 2 kN/s. Higher confining stresses are not applied due to the large deformation undergone by coal which may cause collision of loading platens with each other. Elastic properties of the coal block are determined during the loading process to check the quality of the block. If the values for these parameters differ from the previously determined values, the block is rejected for the experiment. At each confining stress condition, a single acoustic measurement is taken for each source-receiver pair to obtain the seismic response as an initial baseline for the coal block before further fracturing.

(3) Hydraulic fracturing with repetitive acoustic measurements: The confining stress in the x direction is unloaded to 225 kN at a constant rate of 2 kN/s, in order to create deviatoric stress conditions in favour of a fracture running perpendicular to the x direction. Considering large amounts of fractures inside the coal block, silicon oil with high viscosity is used as fracturing fluid to generate hydraulic fractures with as less leakage to natural fractures as possible. The borehole assembly is connected to the injection system, and then filled with silicon oil from the injection side by using a pump. Air bubbles inside the borehole are gently discharged to guarantee a steady borehole pressure. Silicon oil is then injected at a constant flow rate (1 mL/min), which gives rise to an increase of the pressure in the borehole. A fracture is initiated and takes fluid under increasing borehole pressure. When the fracture propagates and connects with natural fractures, leak-off occurs and the borehole pressure begins to decrease. When the borehole pressure drops below the minimum confining stress, the fluid injection is shut in and the borehole is closed for over 200 s to check leak-off under the residual borehole pressure. The fluid injection rate and the effective volume that has been injected in to the fracture are continuously monitored during the injection process, and acoustic measurements are repetitively conducted at an interval of 30 s until the injection is shut in. Meanwhile, leakage in the rest of the system is consecutively checked for safety purposes.

(4) Final acoustic measurements: The confining stress in the x direction is reloaded to 270 kN at a constant rate of 2 kN/s to resume the hydrostatic stress conditions. Then silicon oil is released from the system until the borehole pressure drops to 0. The confining stresses are unloaded stepwise from 270 to 200, 150, 100, 50 and 0 kN in x, y and z directions at a rate of 2 kN/s. At each stress condition, a single acoustic measurement is conducted again for each source-receiver pair to obtain a series of final seismic response for the post-fractured cubic block, which could be compared to the pre-fractured acoustic data. The mechanical measurements (stress and displacement), injection measurements (borehole pressure and injected volume), and acoustic measurements are processed and correlated.

The whole process is divided into various stages depending on experimental operations, as shown in Table 3.3. To observe the variation in geometry of interior fracture networks, computed tomography (CT) scan was performed for both coal blocks using a medical CT scanner with a maximum resolution of 0.3 mm before and after the hydraulic fracturing experiment. Multiple scanned images were then used to synthesise the coal blocks in 3D, and both natural and induced fracture traces marked in slice views were used to extract 3D fracture networks. In addition, the coal blocks were further split for observation of the location and size of natural and induced fractures as well as the fluid-intruded regions. The fractured regions were avoided in splitting to conserve the geometry and size of induced fractures.

3.4 Results and analysis

3.4.1 Stress and hydraulic fracturing response

Figure 3.9 presents the mechanical behaviour of the coal blocks shown in Figure 3.3 in response to true triaxial loading and the injection measurements during the hydraulic fracturing process. The displacement of the coal blocks in each direction is positively correlated with the corresponding stress, showing that the deformation of the coal blocks was mostly within the elastic range. The residual displacement after complete unloading (Figure 3.9ii) indicates that irreversible plastic deformation also occurred in the coal blocks. In addition, it is obvious that there was anisotropy in displacement in both coal blocks, which favours deformation perpendicular to bedding planes (z and y directions for coal blocks 1 and 2, respectively).

Table 3.3. Experimental operations in sequential stages of the true triaxial experiment.

Stages	Experimental operations
a-e	Stepwise hydrostatic loading to 50, 100, 150, 200, and 270 kN
f	Unload stress in the x direction to 225 kN
g	Begin silicon oil injection
h	Close injection borehole
i	Reload stress in the x direction to 270 kN
j	Unload borehole pressure to 0
k-o	Stepwise hydrostatic unloading to 200, 150, 100, 50, and 0 kN

Hydraulic injection at a constant injection rate began at 1,213 s and 747 s after the start of the experiments for coal blocks 1 and 2, respectively. The borehole pressure increased quickly, and an induced fracture was initiated. Since fractures tend to grow orthogonal to the orientation of the minimum principal stress, the induced fracture was expected to be a vertical fracture running perpendicular to the x direction. Leak-off was believed to have happened when the borehole pressure reached the peak, which was 4.7 MPa at 1,443 s (230 s after the injection) for coal block 1, and 4.4 MPa at 1,115 s (368 s after the injection) for coal block 2. Afterwards the borehole pressure experienced a gradual decline, which indicates that the induced fracture coalesced with the natural fracture system which provided conduits for the silicon oil. It is noted that while it took only 1.5 minutes for the borehole pressure inside coal block 1 to drop below the applied maximum confining stress, the post-peak borehole pressure inside coal block 2 stayed at a plateau of around 3.5 MPa for around 1 hour. This indicates the existence of a much more complex yet insulated interior natural fracture system inside coal block 2, which is capable of holding the steady borehole pressure, as well as accommodating much more oil. In addition, while no leakage was observed from surfaces of coal block 1, oil leaked from the face XC of coal block 2 at around 53 minutes after injection, followed by leakage from faces ZC, XD and YD. After closing the injection borehole, the borehole pressure continued decreasing as silicon oil entered natural fractures at the *h* stage. Compared to an injected volume of around 11 mL for coal block 1, an injected volume of around 61 mL was not retrieved from coal block 2, after the borehole pressure was completely released (the *j* stage). The *g* stage (1,158-1,993 s for coal block 1, and 747-5,129 s for coal block 2) is the most concerned stage covering the process from fluid injection to pressure breakdown, when a total of 28 and 146 acoustic scans were recorded for coal blocks 1 and 2 respectively to reveal the evolution of induced fractures.

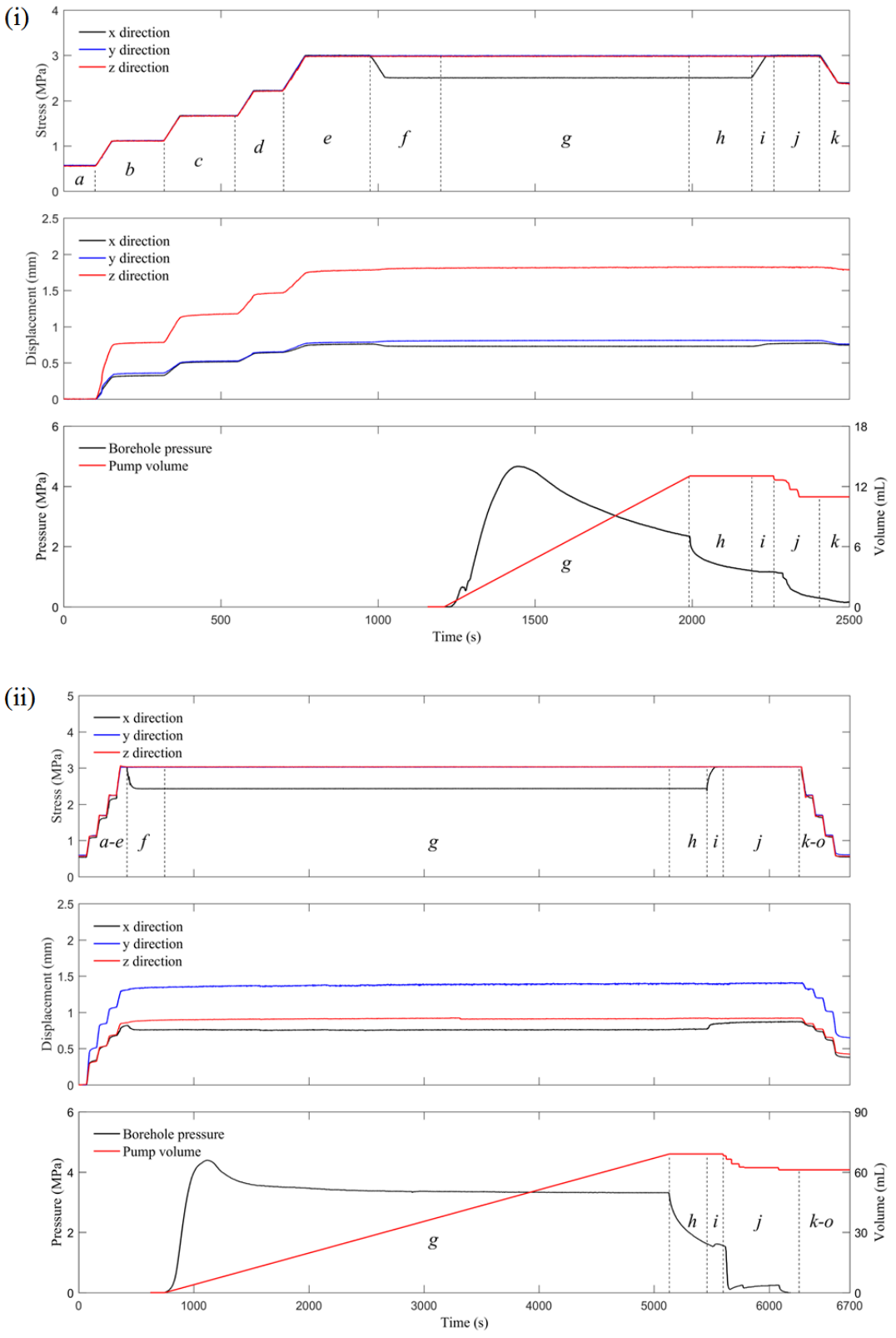


Figure 3.9. Stress, displacement and injection histories during the true triaxial experiments: (i) coal block 1, and (ii) coal block 2.

3.4.2 Geometry of hydraulic and natural fractures

Figure 3.10 presents the split coal block 1 showing the geometry of the hydraulic and natural fractures as well as oil intrusion. The hydraulic fracture propagates from around the middle of the coal block to the block border near the injection borehole, running sub-parallel to the expected orientation. The induced hydraulic fracture is observable at both the bottom and side wall of the injection borehole via a monocular zoom television microscope. The hydraulic fracture intersects with two main natural fractures aligning with the bedding plane orientation, and the injected oil has intruded into these two fractures under the borehole pressure, with the fluid front penetrating to branches of natural fractures (mainly face and butt cleats). In contrast, other natural fractures remain non-intruded.

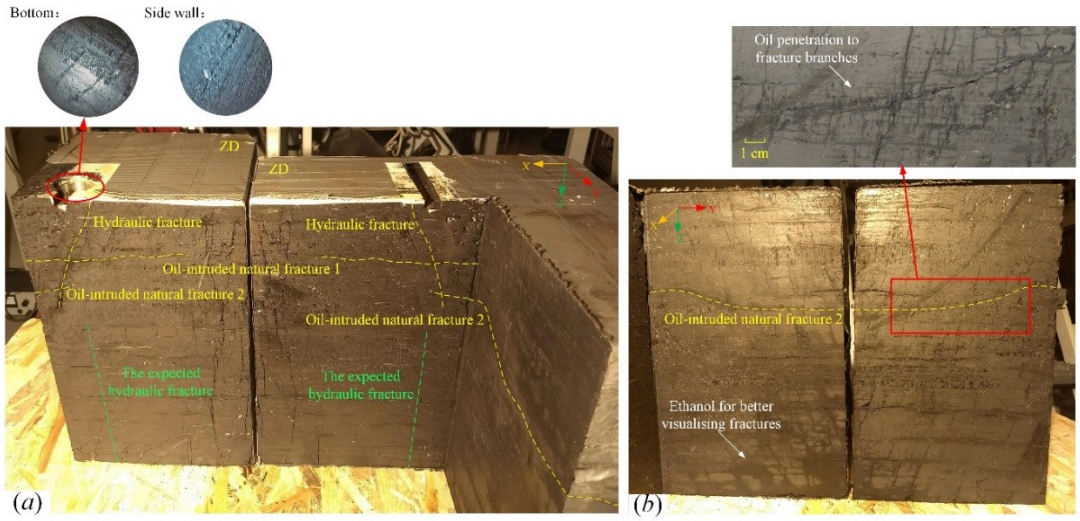


Figure 3.10. Interior fracture distribution in the split coal block 1 after hydraulic fracturing (only the hydraulic fracture and main natural fractures intruded by injected fluid are marked).

Figure 3.11 shows the comparison between CT-scanned images before and after the hydraulic fracturing experiment for coal block 2. The post-fracturing CT scan was performed immediately after the experiment, so the injection borehole was filled with injection oil. Reconstruction of grey scale CT images is based on the fundamental principal that density of the material being scanned can be measured by calculating the attenuation coefficient of X-ray beams. By convention, dark shades of grey display low-attenuation or low-density regions, whereas high-attenuation or high-density

regions are represented by light shades. Since air-filled fractures do not attenuate X-rays as solids or fluids do, fractures appear dark or even black, while coal and oil are grey, and steel and high-density mineral contents are white in the CT-scanned images. But due to similar density and in turn similar attenuation coefficients of coal and oil, some obvious natural fractures before the experiment, such as oil-intruded natural fractures (ONF) 1, 2, 3, 4 and 5 on block faces (Figure 3.11a) and ONF 1, 2 and 3 in slice views (Figure 3.11b), become blurred by oil trapped inside fractures. Because of the same reason, the hydraulically induced fracture in coal block 2 is indistinguishable from coal in CT images.

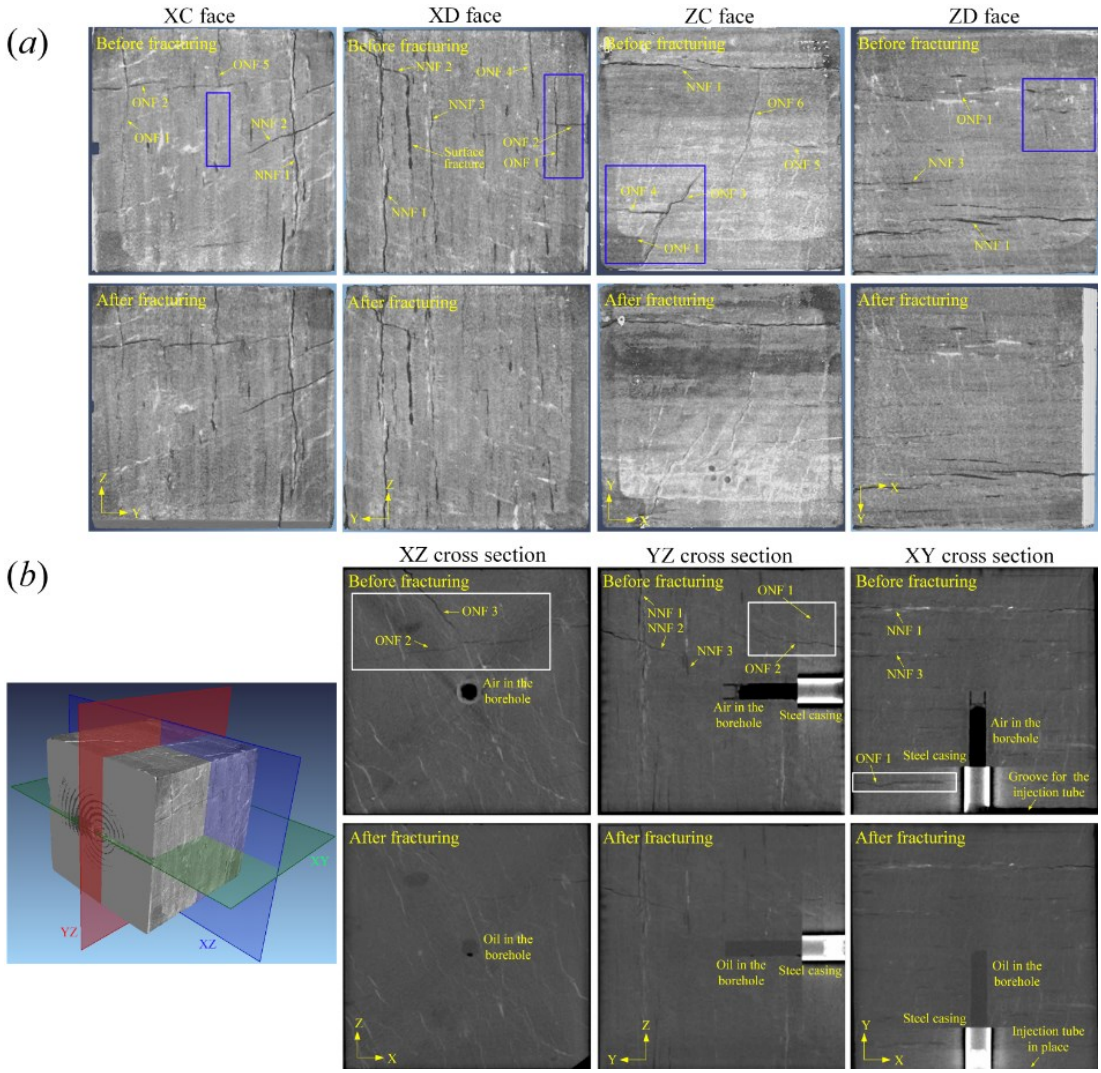


Figure 3.11. CT-scanned images before and after hydraulic fracturing for coal block 2: (a) surfaces, and (b) slice views (ONF: oil-intruded natural fractures; NNF: non-intruded natural fractures).

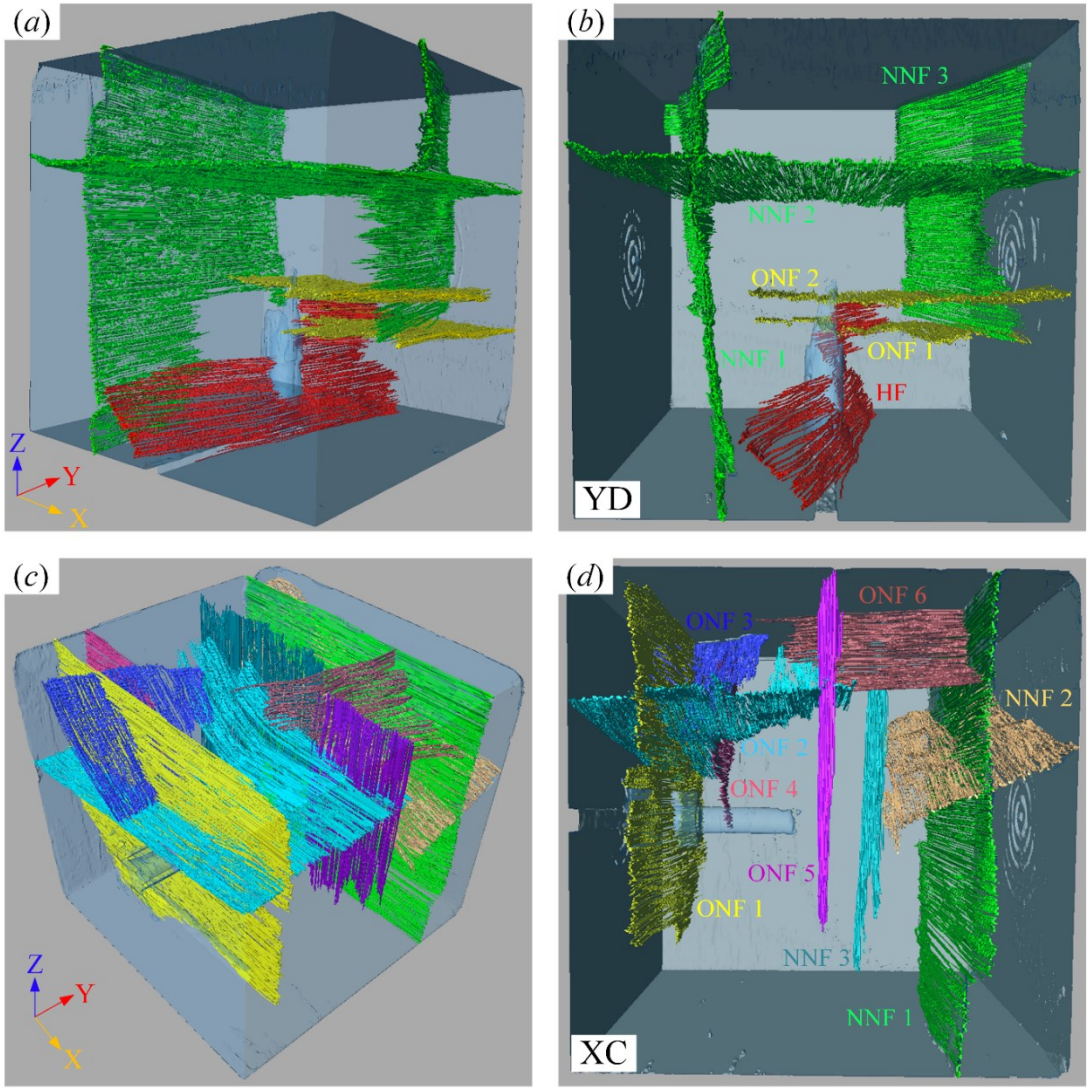


Figure 3.12. Reconstructed natural and hydraulic fracture networks from CT scan images: (a) 3D view for coal block 1, (b) front view for coal block 1, (c) 3D view for coal block 2, and (d) side view for coal block 2 (HF: hydraulic fractures; ONF: oil-intruded natural fractures; NNF: non-intruded natural fractures).

Figure 3.12 illustrates the interior natural and hydraulic fracture networks extracted from CT scan images for both coal blocks after hydraulic fracturing. A system of microscopic fractures nonuniformly distributed throughout the coal blocks was filtered out, and only main fractures at the block scale are presented. Natural fractures in both coal blocks are well-connected. Oil injected in coal block 1 intruded into two natural fractures parallel to bedding planes via the hydraulic fracture, which is consistent with Figure 3.10. In contrast, most oil injected in coal block 2 entered natural fractures including three parallel and three perpendicular to bedding planes, rather than to drive the continuous propagation of a hydraulic fracture. After oil leaked into multiple

natural fractures and reached the block border, the borehole pressure decreased below what could drive oil to enter natural fractures at the far end, such as NNF 3 in coal block 1 and NNF 1 in coal block 2, although they intersected with oil-intruded ones. This shows that the interior natural fracture networks of fractured coal blocks, instead of orientations and patterns of face and butt cleats, dominate hydraulic fracturing behaviour and the associated intrusion of injected oil.

3.4.3 Seismograms under different confining stresses

Figure 3.14 and Figure 3.14 present examples of pre- and post-fracturing seismograms and Fourier spectrum analyses for different S wave raypath types at five hydrostatic confining stress conditions for the coal cubes shown in Figure 3.3. Recorded data from P wave raypaths had very poor signal to noise ratios, therefore, mostly the analyses for S wave raypaths are presented here. To facilitate comparison of seismic response under different stress conditions, magnitudes of both seismograms and Fourier spectrums are normalised by dividing each value by the maximum value recorded under the five confining stress conditions. A seismogram recorded from dS raypaths is the result of superposition of different diffracted acoustic signals via multiple diffractors, such as borehole, casing, and pre-existing and induced fractures, so seismic waves from dS raypaths are more scattered and last longer time compared to those from stS and otS raypaths. It can be seen that the seismic magnitudes and velocities for all the three raypaths increase with increasing confining stress. This is because the natural fractures as well as micro fissures and pores inside the coal block are gradually closed with increasing stress, thus reducing the attenuation of the seismic waves.

Frequencies of the seismic waves primarily fall into the range of 0-0.2 MHz, which are largely below that of the initial pulse (0.5 MHz). This indicates that the high frequency components of seismic waves are filtered out in the propagation. Likewise, as confining stress increases, the enhanced wave propagation enlarges both frequency magnitudes and ranges, and shifts the peak frequency towards the right end.

There are noticeable changes in seismic magnitudes and frequencies after injection, which is indicative of the generation of induced fractures or oil intrusion into pre-existing fractures. The post-fracturing arrival times of signals from some transducer pairs decline compared to their pre-fracturing counterparts. It is probably because the induced fracture did not block wave propagation, but the injection led to local stress

concentration inside coal blocks which contributed to an increase in seismic wave velocities.

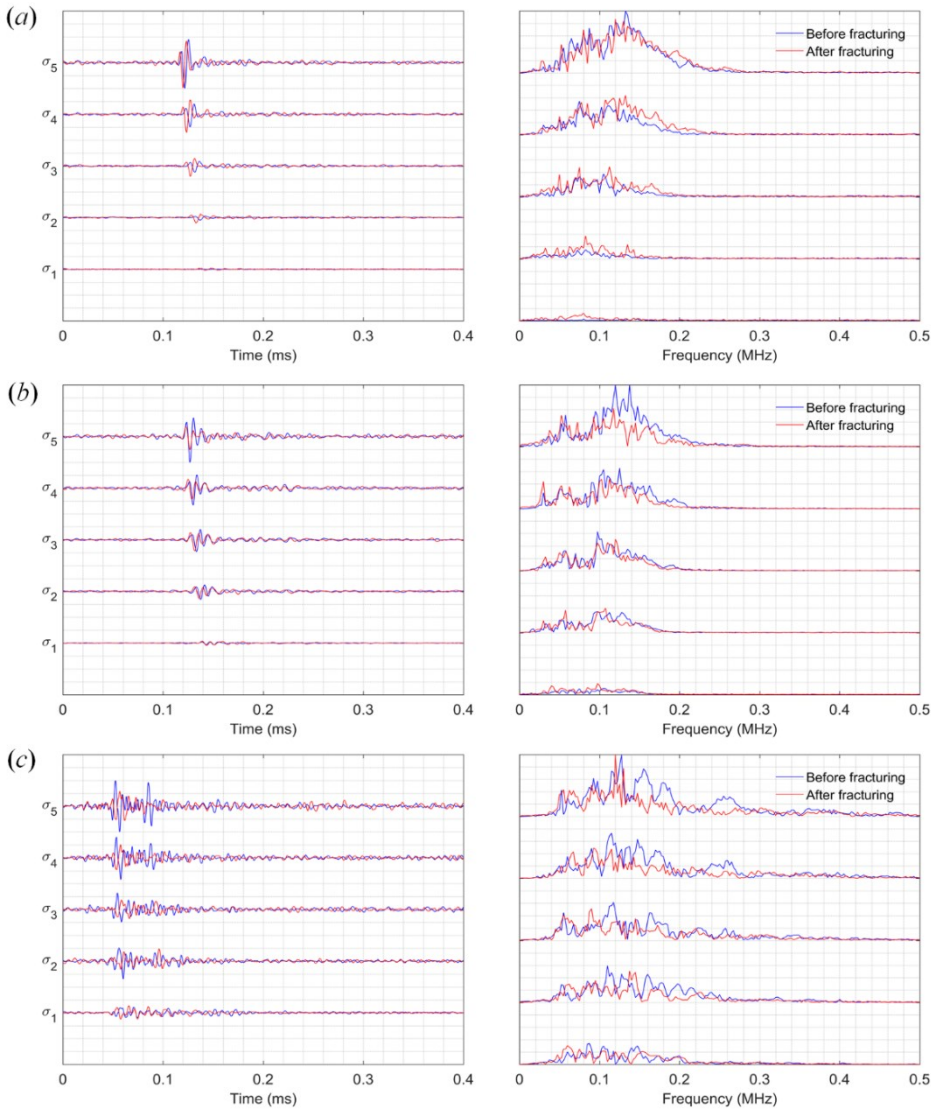


Figure 3.13. Examples of seismograms and Fourier spectrums under five hydrostatic confining stress conditions for coal black 1. The raypaths are classified to (a) S wave straight transmission (stS, pair ZC4-ZD4), (b) S wave oblique transmission (otS, pair YC14-YD9), and (c) S wave diffraction (dS, pair XC14-YC14).

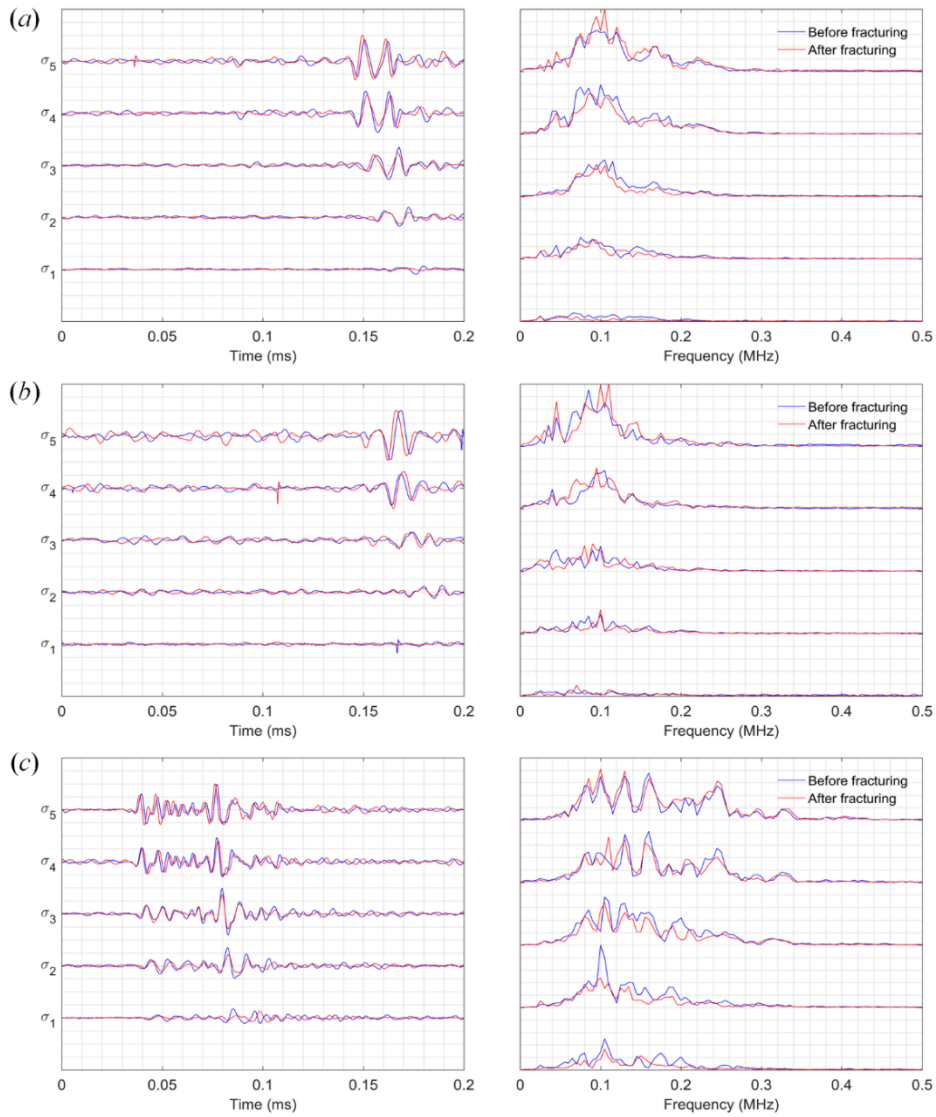


Figure 3.14. Examples of seismograms and Fourier spectrums under five hydrostatic confining stress conditions for coal block 2. The raypaths are classified to (a) S wave straight transmission (stS, pair ZC14-ZD14), (b) S wave oblique transmission (otS, pair ZC19-ZD14), and (c) S wave diffraction (dS, pair ZC14-XD10).

Figure 3.15 illustrates the velocities of seismic waves relative to hydrostatic confining stresses. Seismic wave velocities were calculated from transmission raypaths (stS and otS) with clear arrival times and plotted in groups so as to observe anisotropy. It can be seen that the average seismic wave velocity increases with increasing confining stress. Under each confining stress, the scatter plot shows apparent anisotropy in seismic wave velocities: $v_y > v_z >= v_x$ for coal block 1, and $v_x > v_y \approx v_z$ for coal block 2. For both coal blocks, seismic waves travelling along bedding planes but sub-perpendicular to face cleats achieved the maximum velocity. On top of the effects of cleat patterns,

the low velocity values in the other two directions can be attributed to the blockage of macroscopic fracture planes perpendicular to these two directions, as can be observed in fracture outcrops (Figure 3.3) and post-fractured CT images (Figure 3.12). In addition, seismic wave velocities largely disperse even in one direction, such as the y direction in coal block 1, which indicates the highly heterogeneous distribution of natural fractures in the coal blocks.

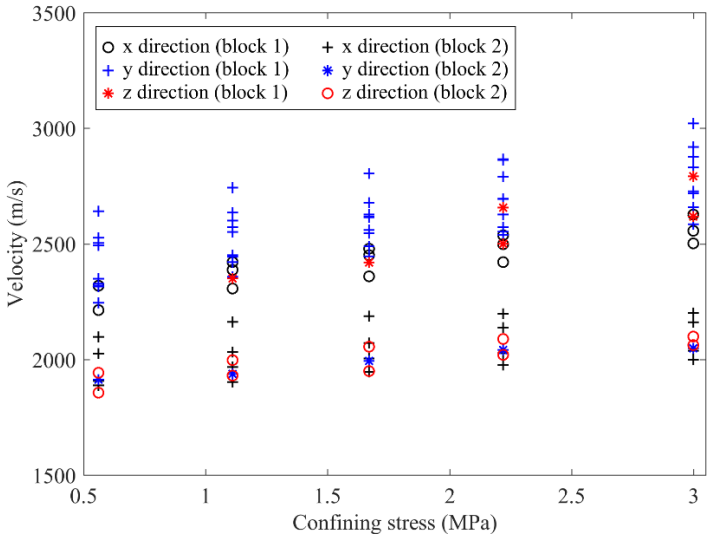


Figure 3.15. S wave velocity as a function of hydrostatic confining stress.

3.4.4 Seismic and frequency spectrograms

Only a few out of these 960 transducer pairs had a full record of clear seismograms over the hydraulic injection process due to the obstruction of the borehole, casing and multiple pre-existing fractures inside the coal sample. Raypaths that interfered with the borehole and casing were filtered out in the subsequent analysis. The remaining recorded seismograms can be grouped into four raypaths, namely stS, otS, dS and dP.

Apart from only a few original seismograms that manifested evident changes, most seismograms needed processing to visualise changes caused by the hydraulic injection. This was performed by subtracting the first scan from each subsequent scan and normalising the subtracted scans by the maximum value over the injection process. Seismic and frequency spectrograms were further performed to obtain time-varying variations in time and frequency domains, respectively. Representative seismograms and associated analyses are presented for each raypath.

Figure 3.16 presents two examples of seismic and frequency spectrograms for the S wave straight transmission raypath (stS). Both the original and the processed seismograms are pulse-shaped, indicating that the waveform of the seismic signal is not largely changed after propagation. Figure 3.16ia shows that the seismic magnitude reduces gradually over the hydraulic injection process. Evident changes can be clearly identified in Figure 3.16ib and ic to start from the scan number 7, corresponding to around 210 s after the injection begins. This is believed to match the initiation of injection-induced fracture, which is before the leak-off at 230 s after injection, as presented in Figure 3.9. As shown in Figure 3.16id, the frequencies of original seismograms primarily fall below 0.07 MHz. Higher frequency components ranging from 0.07 to 0.12 MHz emerge after the initiation of the injection-induced fracture and persist over the injection process. Similar variations can be observed from Figure 3.16ii for coal block 2, where the 10^{th} acoustic scan captures the initiation of hydraulic fracture before the pressure breakdown at 368 s after injection. This verifies that the induced fracture and fracturing fluid interfere with the propagation of stS seismic waves and influence seismic characteristics.

Figure 3.17 presents two examples of seismic and frequency spectrograms for the S wave oblique transmission raypath (otS). Both seismograms and spectrograms of otS seismic waves are quite similar to those of stS seismic waves. Recorded acoustic signals are pulse-shaped and without much dispersion. Seismic magnitude of original seismograms in Figure 3.17ia experiences a gentle reduction, while that in Figure 3.17iia manifests unobservable variations over the hydraulic injection process. But the processed seismograms and seismic spectrogram of otS seismic waves for both coal blocks can successfully capture the fracture initiation, as presented in Figure 3.17ib, ic, iib and iic. In addition, the hydraulic injection enlarges the upper range of frequency components from below 0.07 to above 0.12 MHz, and the post-injection peak frequencies concentrate between 0.05 and 0.07 MHz (Figure 3.17id and iid).

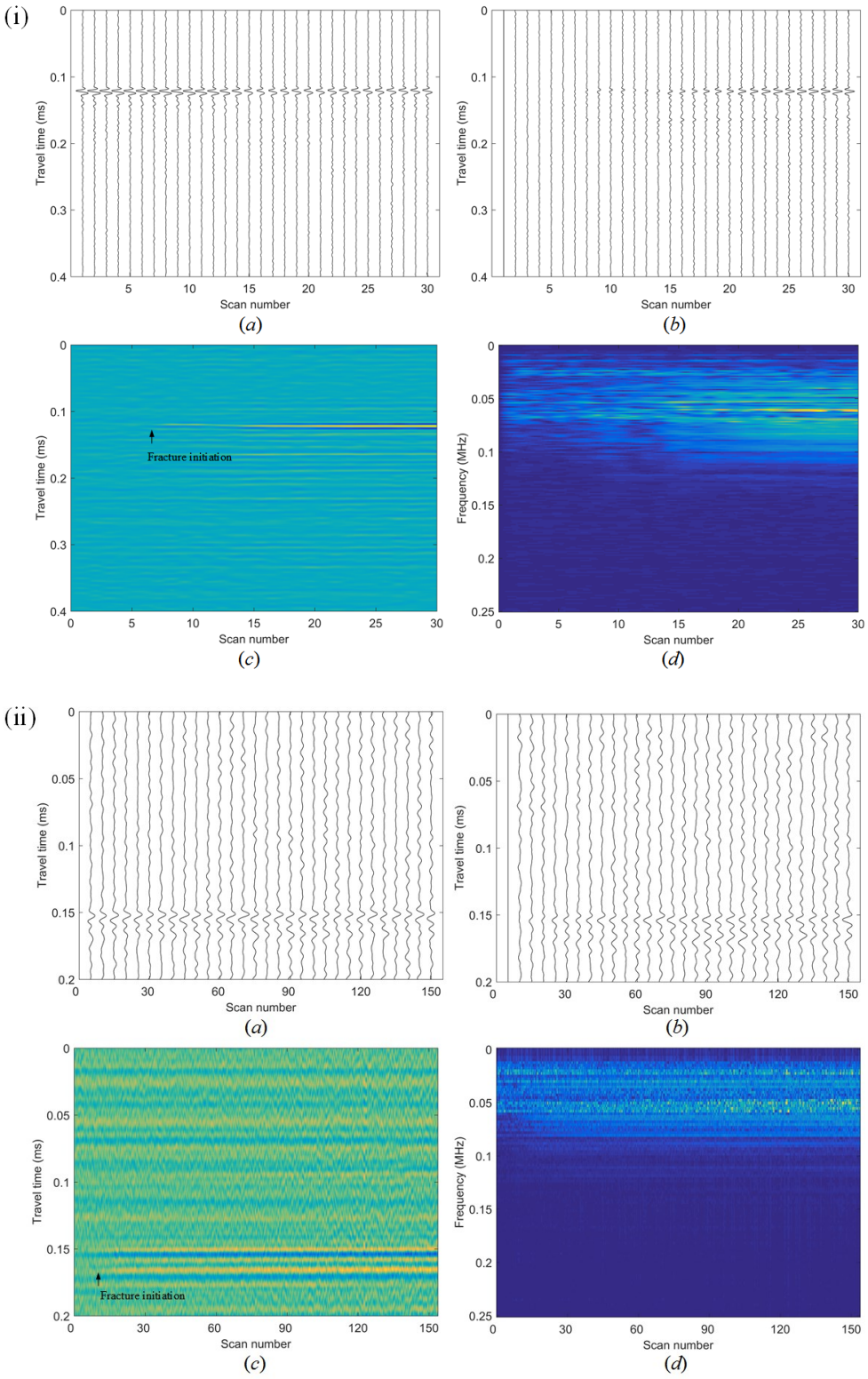


Figure 3.16. Examples of seismic and frequency spectrograms for S wave straight transmission (stS, i: pair ZC4-ZD4 for coal block 1; ii: pair YC4-YD4 for coal block 2): (a) original seismograms, (b) processed seismograms (by subtracting the first scan from each subsequent scan), (c) seismic spectrogram, and (d) frequency spectrogram.

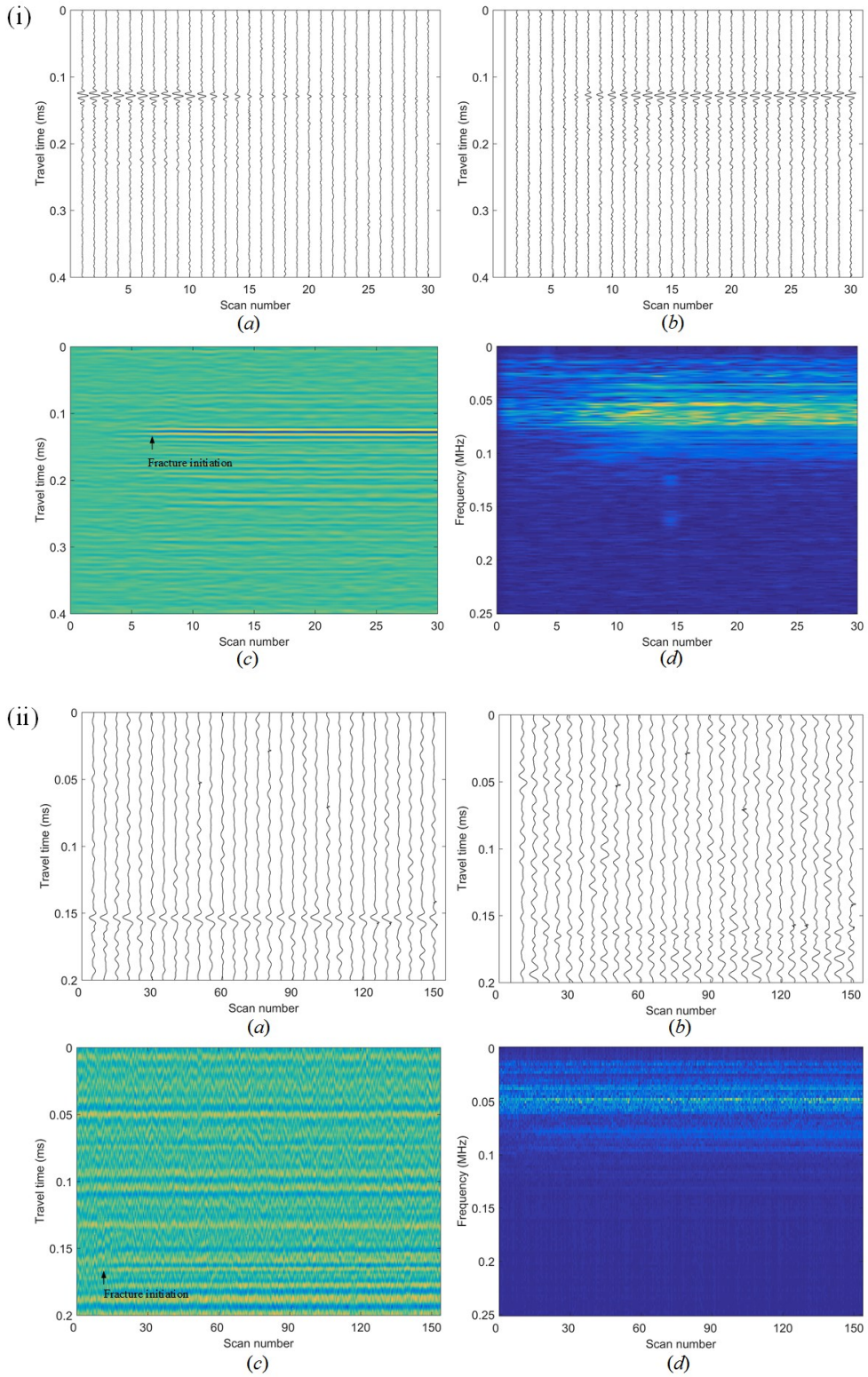


Figure 3.17. Examples of seismic and frequency spectrograms for S wave oblique transmission (otS, i: pair ZC19-ZD20 for coal block 1; ii: pair XC9-XD4 for coal block 2): (a) original seismograms, (b) processed seismograms (by subtracting the first scan from each subsequent scan), (c) seismic spectrogram, and (d) frequency spectrogram.

Figure 3.18 presents two examples of seismic and frequency spectrograms for the S wave diffraction raypath (dS). Both the original and processed seismograms are much scattered than those of stS and otS seismic waves. In addition to reflecting fracture initiation, processed seismograms and seismic spectrograms in both Figure 3.18i and ii show apparent changes after fracture initiation, which indicates that the induced fracture interacts with pre-existing natural fractures, and that the subsequent inflow of silicon oil leads to diffraction of the seismic waves. It is noted that for each coal block, the interactions between the induced and natural fractures could be captured in different scan numbers. This suggests that the induced fracture continues growth under borehole pressure over the injection process, leading to connection with multiple natural fractures and associated intrusion of fracturing fluid. Each interaction between the induced and natural fractures introduces a new diffractor for the seismic wave, and can be captured by different transducers. To obtain more detailed information regarding interaction between fractures, it is suggested to analyse as many dS seismograms as possible. Furthermore, the frequencies of the original dS seismograms fall below 0.07 MHz, but frequency components caused by the injection-induced diffraction primarily range from 0.05-0.15 MHz. This indicates that the injection-induced diffraction can be readily differentiated from straight/oblique transmitted seismic waves by the higher frequency components.

Figure 3.19 presents two examples of seismic and frequency spectrograms for the P wave diffraction raypath (dP). Recorded acoustic signals are more dispersed than straight/oblique transmitted seismic waves. Both seismograms and spectrograms of dP seismic waves are quite similar to those of dS seismic waves. There is a marginal variation in seismic magnitude in Figure 3.19ia, but an obvious change in that in Figure 3.19iia over the injection process. The processed seismograms and seismic spectrogram of dP seismic waves can successfully capture both the fracture initiation and its following interaction with natural fractures. In addition, the upper range of P wave frequencies is increased from 0.07 to 0.15 MHz due to the injection-induced diffraction after the fracture initiation.

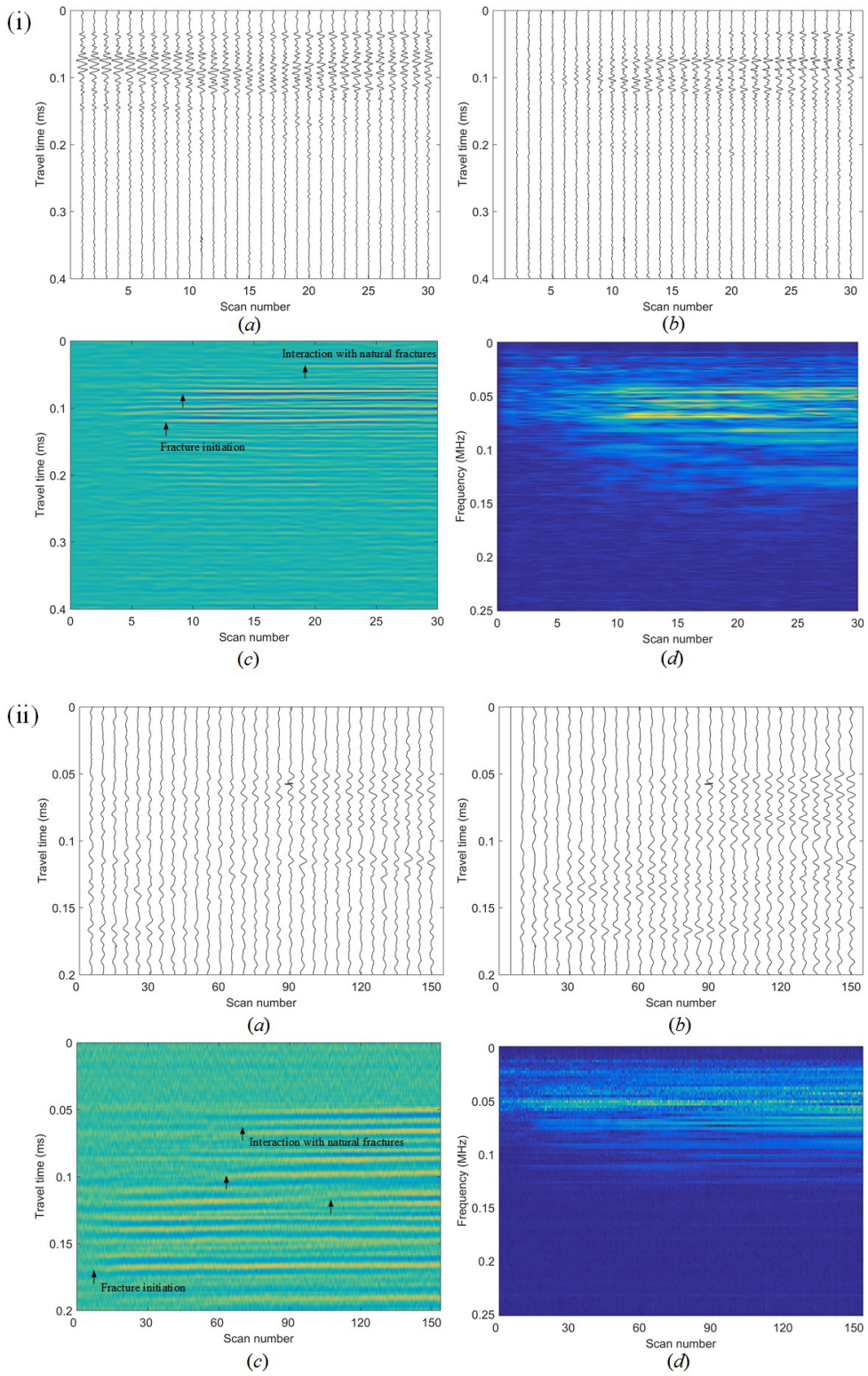


Figure 3.18. Examples of seismic and frequency spectrograms for S wave diffraction (dS, i: pair XC14-ZD5 for coal block 1, ii: pair YD14-ZD10 for coal block 2): (a) original seismograms, (b) processed seismograms (by subtracting the first scan from each subsequent scan), (c) seismic spectrogram, and (d) frequency spectrogram.

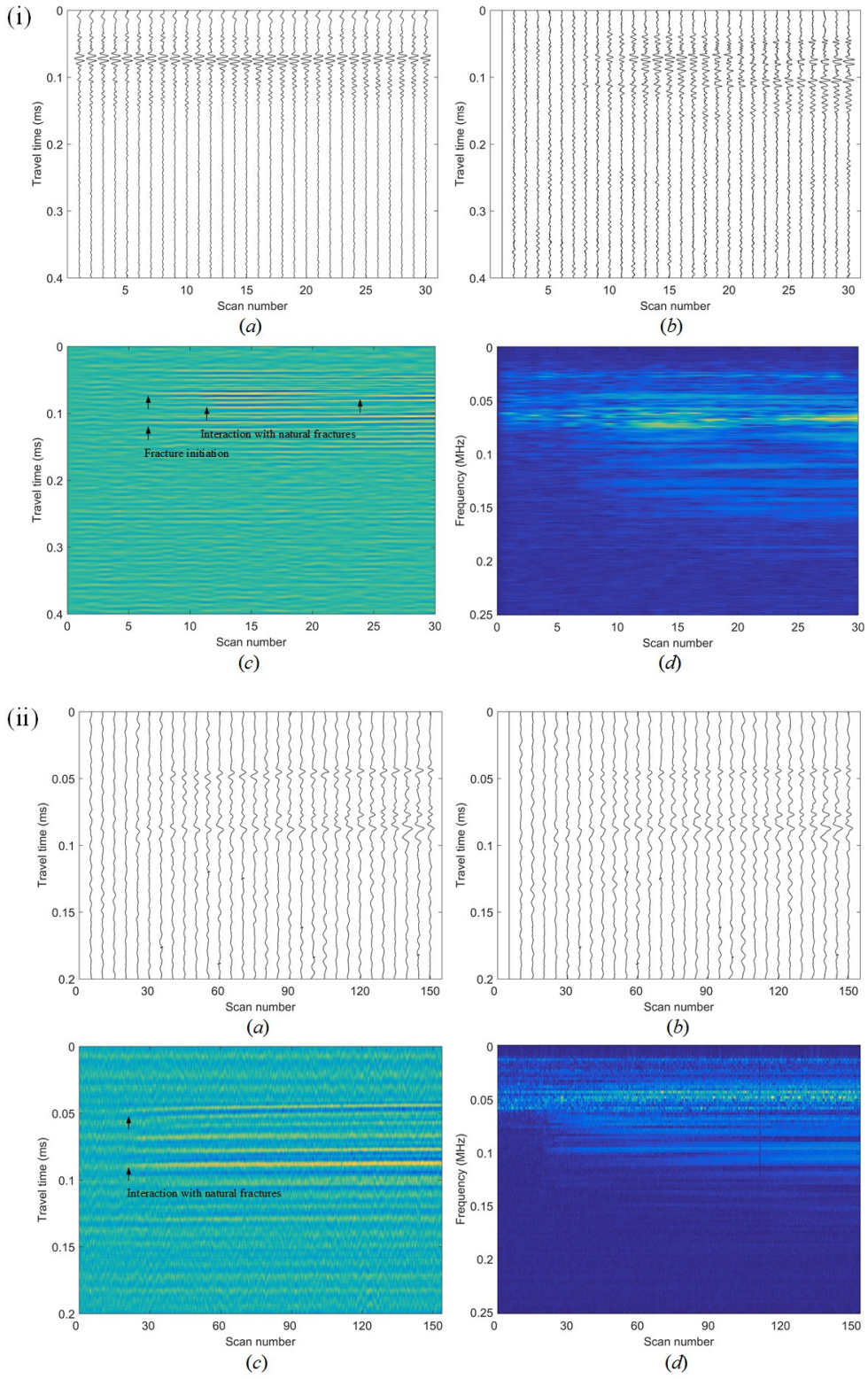


Figure 3.19. Examples of seismic and frequency spectrograms for P wave diffraction (dP, i: pair YD15-ZD10 for coal block 1; ii: pair XD20-YD20 for coal block 2): (a) original seismograms, (b) processed seismograms (by subtracting the first scan from each subsequent scan), (c) seismic spectrogram, and (d) frequency spectrogram.

3.4.5 Seismic velocity tomography

Seismic velocity tomography is a geophysical technique widely applied to image the interior of rock structures. It is hypothesised that wave propagation velocity in the same rock type varies, depending on the intactness and stress states of the rock. High-velocity regions represent relatively intact and/or pressurised rock mass, while low-velocity regions are indicative of highly fractured rock mass. Seismic velocity tomography makes use of travelling times of massive seismic waves to inverse the velocity distribution with respect to the spatial location. This requires first dividing a rock structure into grid cells called pixels in 2D, or cubes called voxels in 3D, each representing a unit element with a uniform velocity. The fundamental principle is that the distance of a travelling path can be calculated by integrating element-scale velocity values over the proportional distances passing through the corresponding elements. When a collection of travelling paths are considered, the error of seismic velocity in each element with regard to all the travelling paths can be minimised through iterative calculation, and the velocity in each pixel or voxel can be obtained. It is noted that there are multiple raypaths between a source and a receiver, and that the raypath with the shortest travelling time is not necessarily the straight raypath in some cases. A widely used algorithm referred to as the Simultaneous Iterative Reconstructive Technique (SIRT) (Cai *et al*., 2014a; Gilbert, 1972) was adopted for seismic velocity tomography in this work.

Seismic velocity tomography calculations were performed before and after hydraulic injection using first arrival times in seismograms recorded from 70 and 93 transducer pairs for coal blocks 1 and 2 respectively, which are categorised in stS, otS, and dS raypaths. The coal blocks were divided into 16×16×16 voxels in the calculation. It should be noted that seismic velocity tomograms produced could not cover regions close to block borders and corners, due to very few seismic raypaths passing through these regions. These regions were assigned with the average S-wave seismic velocity.

Figure 3.20 illustrates the influence of hydraulic fracturing on the S-wave velocity tomograms. The average S-wave velocities calculated from the tomography for coal blocks 1 and 2 are around 2.7 and 2.1 km/s respectively, which are consistent with those in Figure 3.15. It can be seen that seismic velocity tomograms for both coal blocks 1 and 2 do not change much after hydraulic fracturing, and they represent the intrinsic properties and natural fracture distribution of the coal blocks. In comparison

with CT-scanned images from Figure 3.12, low-velocity regions from tomography before injection for coal block 2 correlate fairly well with locations of natural fractures, but the correspondence is not so good for coal block 1. This can probably be explained that the heterogeneity in lithotype components or physical properties contributes to the heterogeneity of seismic velocity, in addition to the unfavourable impact of fractures on seismic velocity. Since coal block 1 hosts a small number of macroscopic natural fractures, the impact of coal properties on seismic velocity is dominant in coal block 1.

After the hydraulic injection into coal block 1, velocity-reduced regions emerge around the injection borehole, extending roughly along the y direction (Figure 3.20ic). The location and orientation of velocity-reduced regions are consistent with those of the hydraulic induced fracture. In coal block 2, the bulk of velocity-reduced regions (Figure 3.20iic) overlap with distribution regions of oil-intruded fractures (Figure 3.12iib), which indicates that oil intrusion into fractures could increase the damping to seismic wave propagation and thus reduce seismic velocity.

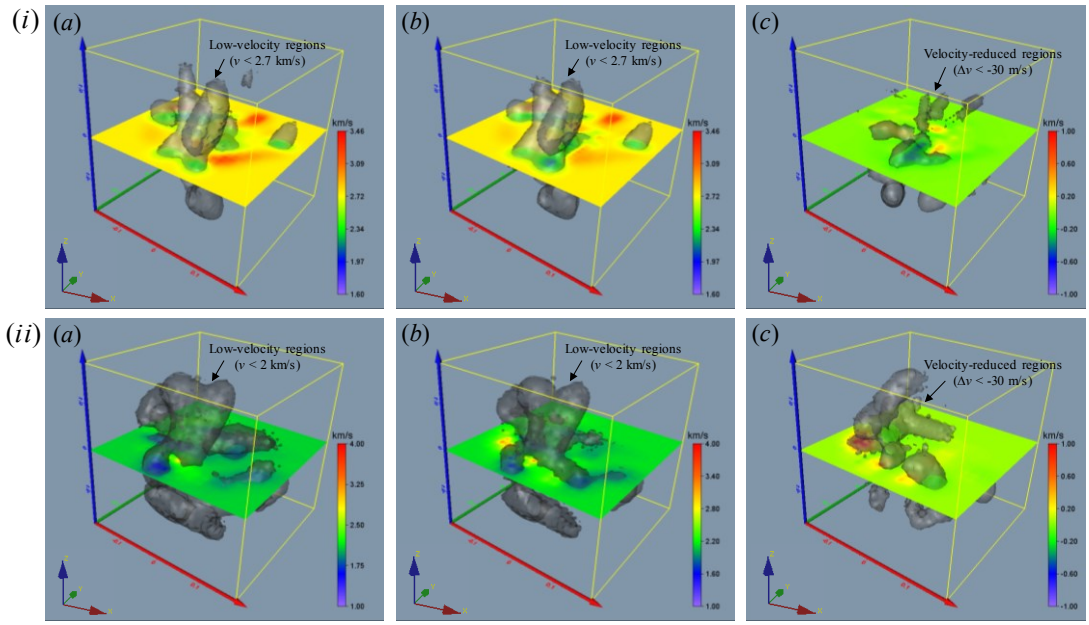


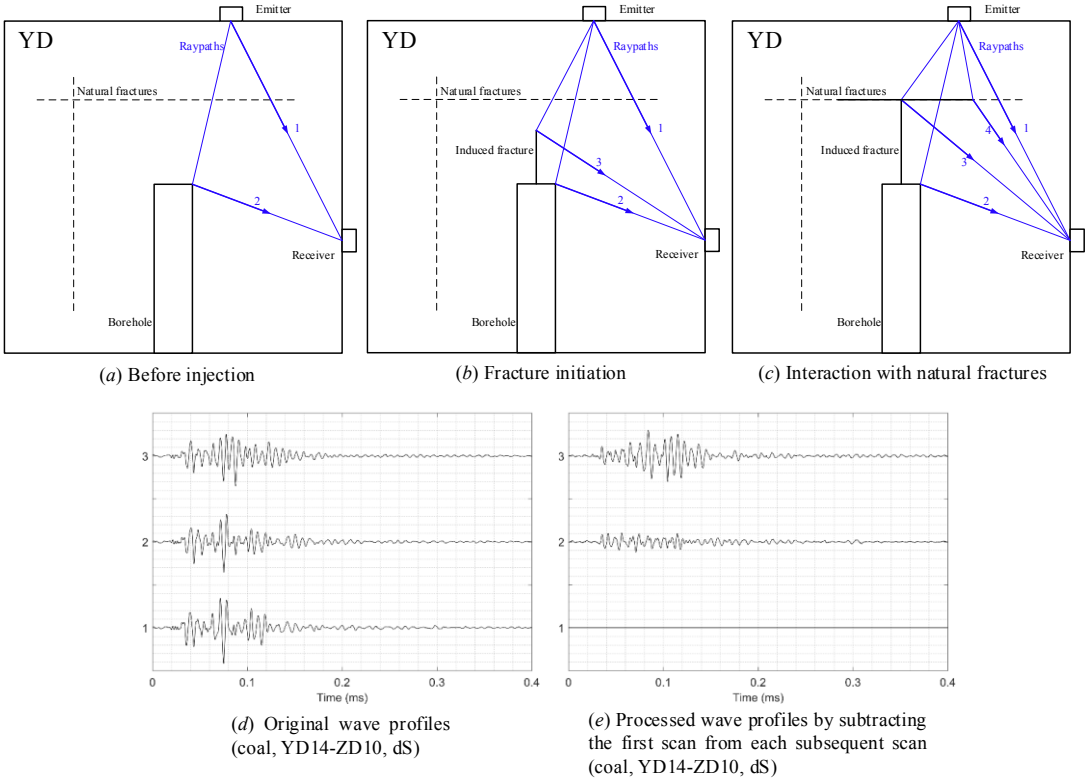
Figure 3.20. S-wave velocity tomograms for coal blocks 1 (i) and 2 (ii): (a) before hydraulic fracturing, (b) after hydraulic fracturing, and (c) the difference induced by hydraulic fracturing.

Restricted by the total number of seismic raypaths, the seismic velocity tomography in this work could only reflect approximate locations of pre-existing fractures and injection-disturbed regions. Nevertheless, the application of seismic velocity tomography on fractured regions is promising in field practices, where the assessment of performances requires the knowledge of the location of hydraulically fractured regions rather than that of every individual hydraulic fracture.

3.5 Discussion

Figure 3.21 presents schematic diagrams showing how seismograms are correlated with induced/propagating fractures and their interaction with natural fractures. An emitted acoustic signal propagates radially from the emitting transducer and can be reflected or diffracted when encountering obstacles. As a result, the received acoustic signal is the superposition of seismic waves from different raypaths. Before the initiation of the induced fracture in an intact block, two obvious raypaths from the emitting to receiving transducers involve a straight transmitted raypath 1, and a diffracted raypath 2 via the borehole end, as shown in Figure 3.21a. Other raypaths where steel casing and other pre-existing natural fractures act as diffractors are ignored for the simplification of analysis.

For coal, which has a number of embedded natural fractures, the seismic raypaths are expected to be similar to those for an intact rock before the induced fracture interacts with a natural fracture (Figure 3.21a). The generation of the hydraulically induced fracture forms a new raypath 3, where the seismic wave diffracts via the tip of the induced fracture (Figure 3.21b), leading to the superposition of a new wave component to the received seismic wave. After coalescence between induced and natural fractures, the fracturing fluid intrudes into the natural fracture and the fluid front acts as a diffractor, introducing more raypaths, as illustrated in Figure 3.21c. Even more raypaths may emerge when the fracturing fluid is connected to a natural fracture system. Figure 3.21d and e present the original and processed seismograms of the same transducer pair on the fractured coal block 1 over the injection process. It can be seen that the injection-induced diffraction can be treated as a scattered wave packet arriving almost simultaneously as the original acoustic signal.



(*a*) Before injection (*b*) Fracture initiation (*c*) Interaction with natural fractures

(*d*) Original wave profiles (coal, YD14-ZD10, dS)

(*e*) Processed wave profiles by subtracting the first scan from each subsequent scan (coal, YD14-ZD10, dS)

Figure 3.21. Interpretation of seismograms in response to injection to naturally fractured blocks.

It is difficult to correlate fluid intrusion into each natural fracture branch with induced diffraction waves due to the geometrical complexity of natural fracture networks and the associated multiple reflection and diffraction before reaching receiving transducers. Nevertheless, analysis of recorded seismograms of elastodynamic waves, in combination with extracted fracture networks from CT scan and observed fluid-intruded regions from the split post-fractured block, provides a new alternative to detect and analyse the initiation of a hydraulic fracture and its subsequent interaction with the complex natural fracture system inside rock masses. This method might be promising to be applied in analysing field-scale injection-induced fracture behaviour.

3.6 Conclusions

Laboratory experiments were carried out on two cubic coal blocks containing a host of natural fractures using a true triaxial rock testing machine, with the associated seismic response monitored using an ultrasonic monitoring system with active sources. The seismic characteristics of the coal block under various hydrostatic stress conditions were first compared to investigate their dependency on hydrostatic stress

levels. Then the seismic response was recorded repetitively over silicon oil injection into the middle of the block under deviatoric stress conditions, in order to reveal the initiation of induced fracture and its subsequent interaction with the natural fracture system. A suite of processing techniques, such as Fourier frequency analysis and seismic velocity tomography, were performed to supplement the analyses of seismograms. X-ray computed tomography (CT) was further conducted before and after the experiments in order to identify the location and geometry of hydraulic and natural fractures.

Results found that seismic waves propagating through naturally fractured coal blocks experience multiple reflection and diffraction and become more scattered than those in intact rock blocks. It was observed that the magnitude of seismic response as well as seismic wave velocity through the coal blocks are positively correlated with confining stresses. This is because the natural fractures as well as micro fissures and pores inside coal blocks are gradually closed with increasing stress, thus reducing the attenuation of the seismic waves. There were also noticeable changes in seismic magnitudes and frequencies after high pressure fluid injection in the blocks, which is indicative of the initiation or growth of an induced fracture.

The recorded seismograms of S wave, categorised into straight transmission (stS), oblique transmission (otS) and diffraction (dS) raypaths, are found to be helpful to reflect the fracture behaviour. During the fluid injection process, seismograms of stS and otS raypaths could only capture the initiation of induced fracture, whilst those of dS raypaths could reflect both the fracture initiation and subsequent interactions with the natural fracture system in coal blocks. In addition, the seismic velocity tomography based on first arrival time of S waves before and after hydraulic fracturing could approximately locate pre-existing fractures and injection-disturbed regions. The active acoustic monitoring technique, in combination with seismogram processing, active seismic tomography and X-ray CT techniques, provides a new alternative to detect and analyse the initiation of hydraulic fracture and its subsequent interaction with the complex natural fracture system within coal.

Chapter 4 Field monitoring and analysis of microseismicity associated with longwall top coal caving mining

4.1 Introduction

This chapter presents the implementation and analysis of recorded data from continuous microseismic monitoring carried out in a previous project CoGasOUT at Coal Mine Velenje in 2011, and during a much longer period in 2016-2018 in the MapROC project respectively, in an effort to assess the dynamic behaviour of the coal seam in response to longwall mining and to provide a methodology for early warning of rock bursts and coal and gas outbursts. Microseismic data recorded around a longwall top coal caving panel over a 12-week period in 2011 was analysed in combination with active time-lapse seismic tomography measurements carried out by K-UTEC of Germany, which provided the author with the background for his analysis of 2016-2018 microseismic monitoring data from Coal Mine Velenje. Microseismic data recorded around a highly stressed central coal pillar and nine surrounding longwall top coal caving (LTCC) mining panels over a 27-month period during 2016-2018 was analysed by the author in conjunction with concurrent records of longwall face advance. The respective role of stress concentration, fracture field, and mining intensity is investigated for their contribution to spatial, temporal and magnitude characteristics of microseismicity. Based on the monitoring results and the fracture-slip seismic-generation mechanism, a conceptual model is further developed to shed light on the causes of anomalous microseismicity and statistical estimation of microseismicity to be triggered. The data and experience gained through these analyses will be utilised in forecasting large microseismicity in Chapter 5 and modelling microseismicity in Chapter 6 and Chapter 7.

4.2 The field monitoring site

4.2.1 Geological conditions

Coal Mine Velenje is located in North East Slovenia. The coal basin lies in a synclinal valley, which extends between the Šoštanj and Smrekovec faults. The Pliocene coal seam is overlain by a layer of clay and sand, which are followed by several younger rock layers. The sequence was caused by the subsidence of the area between faults and the simultaneous backfilling of continuous alluvial deposits (sand, silt, and marl).

Coal Mine Velenje currently mines a lens-shaped deposit, which extends to a length of 8.3 km in the WNW-ESE direction and has a width between 1.5 and 2.5 km (Figure 4.1). The coal seam is 165 m thick in the central part and pinches out towards the margins. The bedding planes are nearly horizontal or slightly inclined. The Velenje Coal is a humic type lignite, the matrix of which is detrite-dominated, dark brownish to dusky brown in colour. Other lithotypes are composed by varying amounts of xylite, fusinite and mineral matter such as alumosilicates and carbonate minerals.

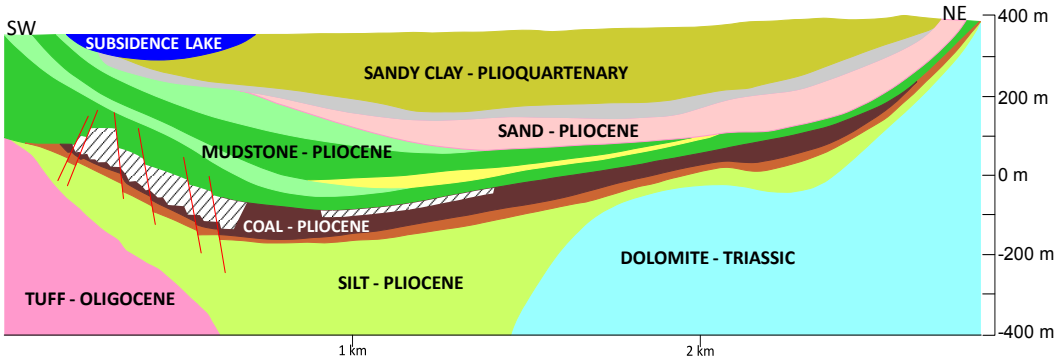
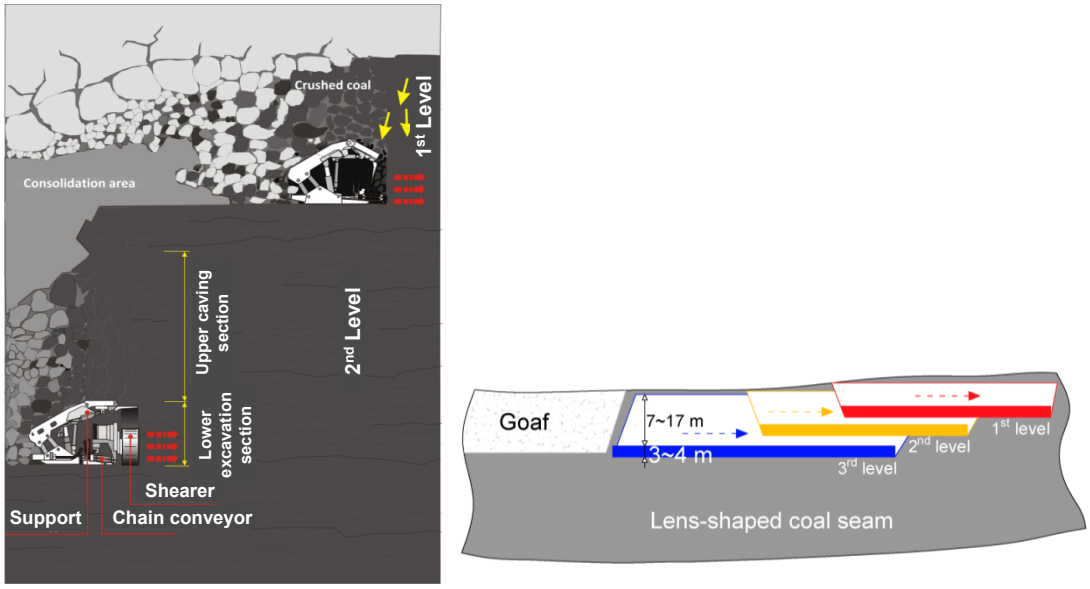


Figure 4.1. Schematic SW–NE trending geological cross-section of the Velenje coalfield (after Markič and Sachsenhofer, 2010).

4.2.2 Mining method and mine production schedule

For efficient coal extraction from the ultra-thick coal seam, multi-level longwall top coal caving (LTCC) is practiced at the mine. Specifically, the entire coal deposit is divided into a number of levels ranging from 10 to 20 m in thickness, and extracted sequentially from the top to the bottom. At each level, the lower section of the seam (3-4 m in thickness) is cut by a shearer under the hydraulic supports, and the top coal (7-17 m in thickness) is allowed to cave by gravity and be recovered in front of the

supports (Si *et al*., 2015b). During coal extraction, the extending canopy is collapsed, and the top coal is caved after several cuts at the face, allowing for a steady face advance. The extracted zone is filled with caved roof material and recompacted to restore the stress states.



(a) (b)

Figure 4.2. (a) Schematic of the multi-level longwall top coal caving mining method implemented at the ultra-thick coal deposit of Coal Mine Velenje; (b) schematic of the multi-level longwall layout (after Jeromel *et al*., 2010; Si *et al*., 2015).

The LTCC panel K. -50/C was selected as the field site for monitoring mining-induced seismic activities in 2011. This longwall panel lies at a depth of -350 m, underlain by thick floor coal, and overlain half by an intact clay layer and half by a layer of caved roof goaf, formed as a result of previous coal extraction (Si *et al*., 2015b). Coal at LTCC panel K. -50/C was mined from November 2010 to October 2011. The mine normally works five days per week, and three 8-hour shifts per day. The average face advance rate in 2011 was approximately 11-12 m per week, yielding a daily coal production of 7,930 tonnes.

Nine LTCC panels were selected as the field site for monitoring mining-induced seismic activities in 2016-2018 (Figure 4.3). Five panels, i.e. K.-80/B, K.-80/C, K.-80/D, K.-80/E, and CD2, are at -80 m level, with the other three (K.-95/A, K.-95/E, K.-95/D and CD3G) at -95 m level. These panels surrounded a highly stressed central coal pillar protecting the main infrastructure in the production districts, which was left

by over one hundred years of coal production. This high stress concentration has considerably increased the risk of rock burst and coal and gas outburst.

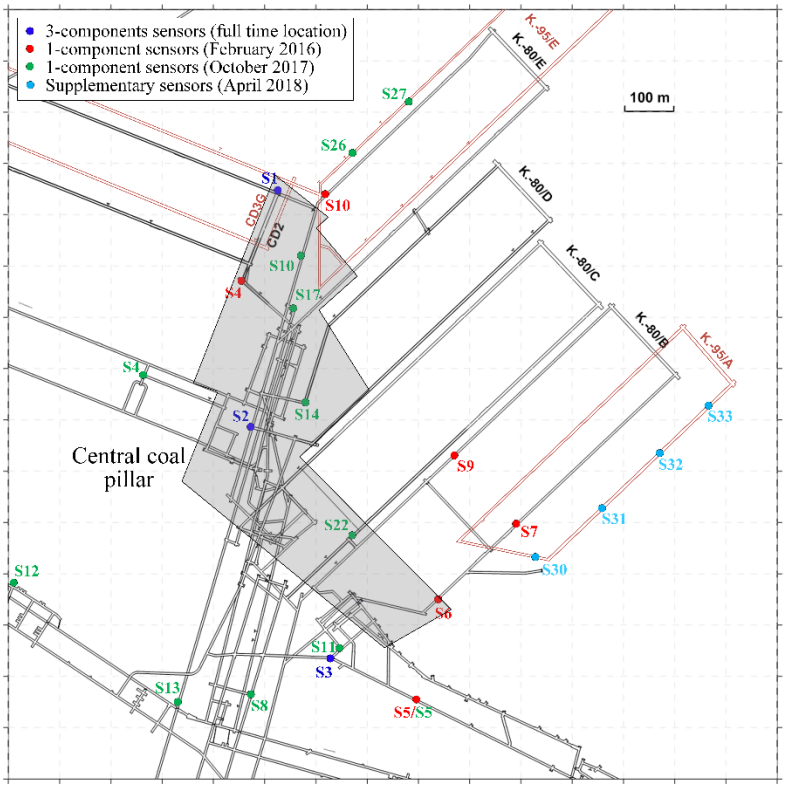


Figure 4.3. Mine production layout at -80 and -95 m production levels during 2016-2018 at Coal Mine Velenje, and the distribution of installed seismic stations of the microseismic monitoring system. The grey zone indicates the approximate shape of the central coal pillar protecting the main infrastructure in the production district.

Longwall coal production started at -80 m depth in 2015, and gradually transferred below to -95 m depth from 2017. Until today, panels K.-80/B, K.-80/C, K.-80/D, K.-80/E, K.-95/A, and K.-95/E advanced in the southwest direction towards the central coal pillar, while CD2 and CD3G advanced at an angle of about 120° to the other panels away from the coal pillar. Coal production at longwall panel K.-95/D was delayed, and started in February 2019, after the completion of this thesis. K.-95/E and CD3G had production heights limited to 5 m and 9 m, respectively, which was believed to be beneficial in terms of reduced stress on the mine main infrastructure in the central coal pillar.

To achieve full operational capacity with the mine staff and facilities, there were two longwall panels working concurrently over most of the production period. The two

working panels were usually chosen separated spatially to spread out stress concentration around the mined-out areas. However, due to ventilation and coal transportation limitations, mine production plans included a relatively unfavourable sequence of two neighbouring panels (K.-80/D and K.-80/C) in production between January and March 2017. There were also periods with only one longwall panel in operation (June-August 2016), and up to three longwall panels working at the same time (August-October 2016 and January-March 2017). The operational sequence for eight longwall panels followed during this research are summarised in Table 4.1. The average face advance rate during 2016-2018 was approximately 10-20 m per week, yielding a daily coal production of 4,000-9,000 tonnes.

Table 4.1. Longwall panel operational sequence and the associated recorded microseismicity during the monitoring period (29/02/2016-20/05/2018) at Coal Mine Velenje.

Panel name	Start date	Completion date	Accumulated face advancement (m)	Event counts
K.-80/B	11/10/2015	19/10/2016	539.9	5084*
K.-80/E	15/10/2015	06/06/2016	647.5	261*
CD2	12/08/2016	12/07/2017	441.0	1157
K.-80/D	16/08/2016	28/02/2017	632.8	2736
K.-80/C	19/01/2017	05/02/2018	654.4	6803
K.-95/E	11/07/2017	15/03/2018	635.2	502
K.-95/A	12/02/2018	-	166.1	49
CD3G	26/03/2018	-	114.2	510

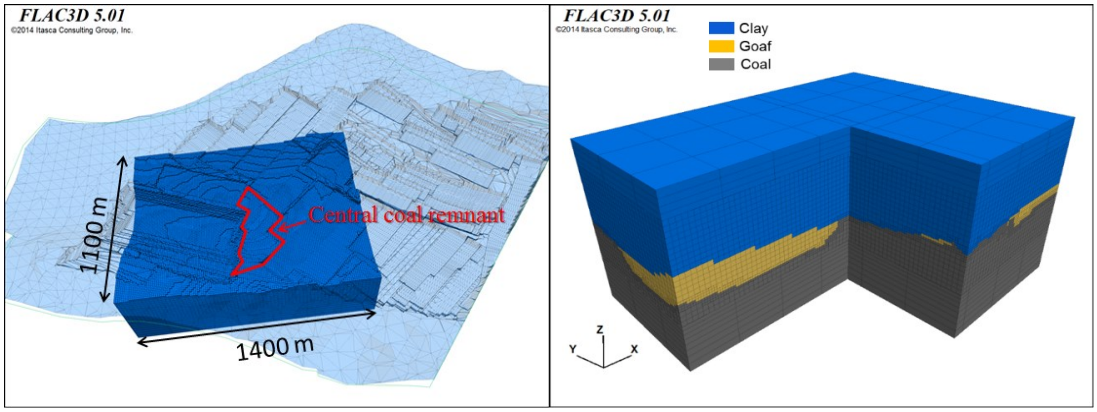
* Numbers of microseismic events for K.-80/B and K.-80/E panels were counted since 29/02/2016.

4.2.3 Stress states assessed by numerical modelling

Numerical geomechanical modelling was carried out to determine the initial stress state around the central unexploited coal pillar and surrounding longwall panels prior to the longwall coal mining at -80 m depth and the post-mining stress concentration at the coal pillar.

Based on the coal deposit and extraction history data, a 1400 × 1100 × 700 m (length × width × height) rectangular block containing the central coal pillar and surrounding longwall panels was extracted from a mine-scale geological model to construct the geomechanical model in FLAC^{3D} (Figure 4.4a). The model domain includes three different structures, i.e. coal, clay, and failed clay representing the goaf (Figure 4.4b). Finer grids were used close to the interfaces between geological structures to better fit

the shape of interfaces, as well as around the coal to be extracted to accommodate elevated stress gradients.

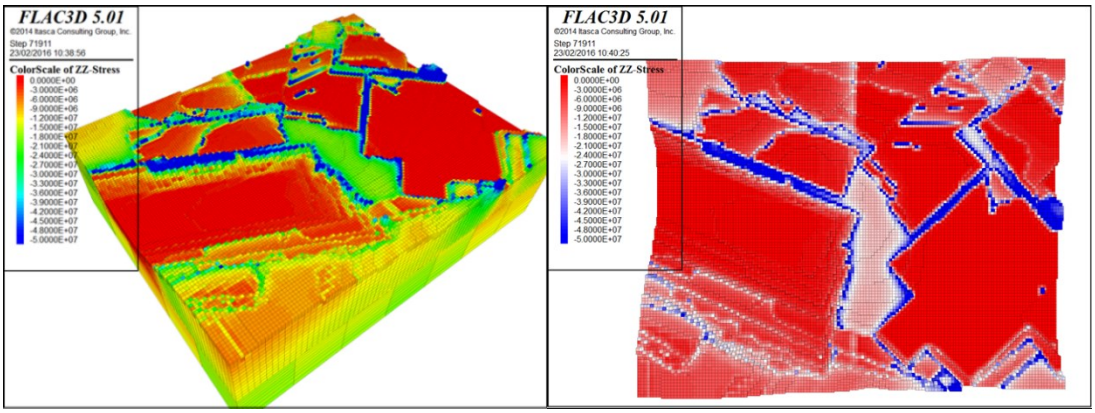


(a) (b)

Figure 4.4. Geometry of the geomechanical model containing the central coal pillar and surrounding longwall panels: (a) overview, and (b) cross-sections showing three geological structures.

The vertical stress was determined by computing the overburden weight using an average rock density of 2,360 kg/m^3. The horizontal stresses were assumed to be equal and are a result of the rock Poisson's ratio response to gravity loading. The boundary conditions of the model were such that it is laterally confined and the model base is fixed. The consitutive model used is the elastic model and the elastic parameters for coal, clay and failed clay used in the model were obtained from laboratory experiments on samples from Coal Mine Velenje (Si *et al*., 2015b).

Stress equilibrium was first established to obtain the simulated *in-situ* field stress state prior to any mining activities. Then grids representing the extracted coal were removed in steps and replaced with the mechanical properties of goaf material in the model to yield the stress state prior to the longwall mining of the nine panels of interest here. Figure 4.5 presents the resulting vertical stress distribution showing a high stress concentration zone, with the average stress at 19.8 MPa, which is more than two times higher than the *in-situ* vertical stress (8.6 MPa).



(a) (b)

Figure 4.5. Vertical stress field around the central coal pillar before the start of coal extraction at -80 m depth at Coal Mine Velenje (in October 2015): (a) 3D view, and (b) plan view.

To evaluate the impact of subsequent mining activities on the central coal pillar, coal production at the longwall panels K.-80/B and K.-80/E (Table 4.1) was simulated following the actual monthly mine schedule (Figure 4.6). To track stress variations over the coal production period, two monitoring points and one monitoring profile-line (as marked in Figure 4.6) were set within the central coal pillar close to the active panels.

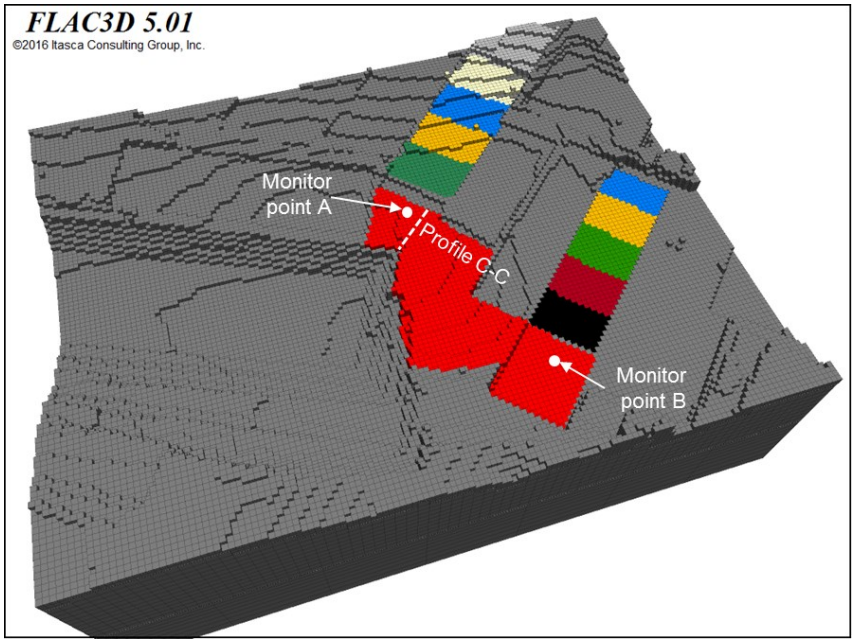


Figure 4.6. Coal extraction simulated following the production schedule at K.-80/E and K.-80/B LTCC panels at Coal Mine Velenje.

Figure 4.7 presents the contour of stress changes caused by the LTCC face advance at different mining production periods. As can be seen, compared with the extraction of K.-80/B panel, the mining of K.-80/E panel has a greater impact on the stress state at the central coal pillar, with the incremental stress reaching as high as 0.7 MPa after the extraction. Monitored dynamic stress responses to coal extraction at the K.-80/E and K.-80/B panels are shown in Figure 4.8 and Figure 4.9 respectively. The modelling results show that the extraction of K.-80/E panel produces a moderate stress increment at the 'upper corner' of the central coal pillar. This disturbance may induce seismic events if coal or rock mass is already under critical stress conditions.

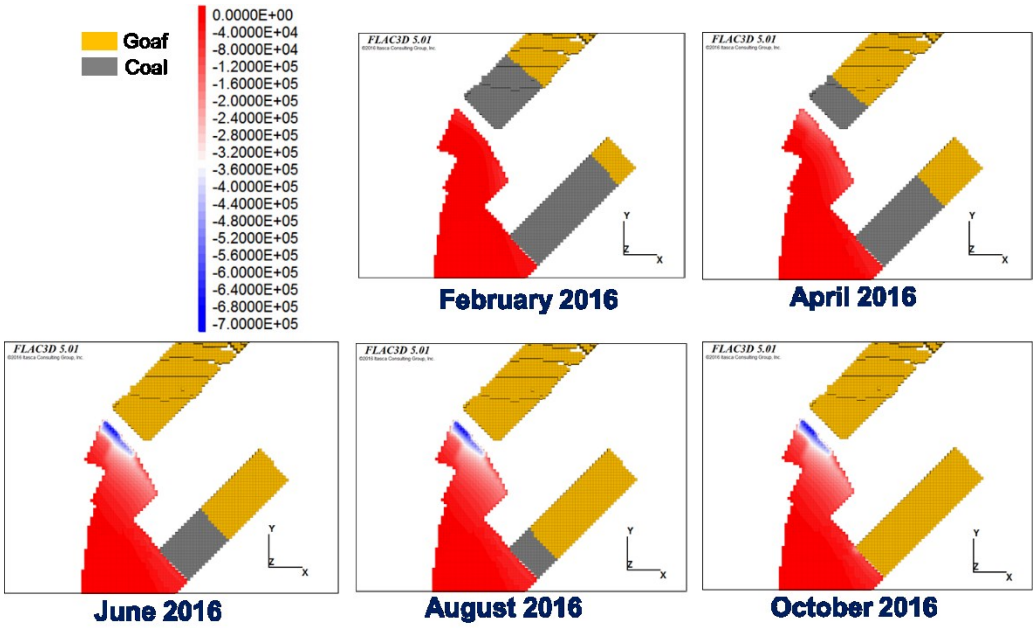


Figure 4.7. Stress variation in the central coal pillar affected by coal mining at K.-80/E and K.-80/B LTCC panels at Coal Mine Velenje.

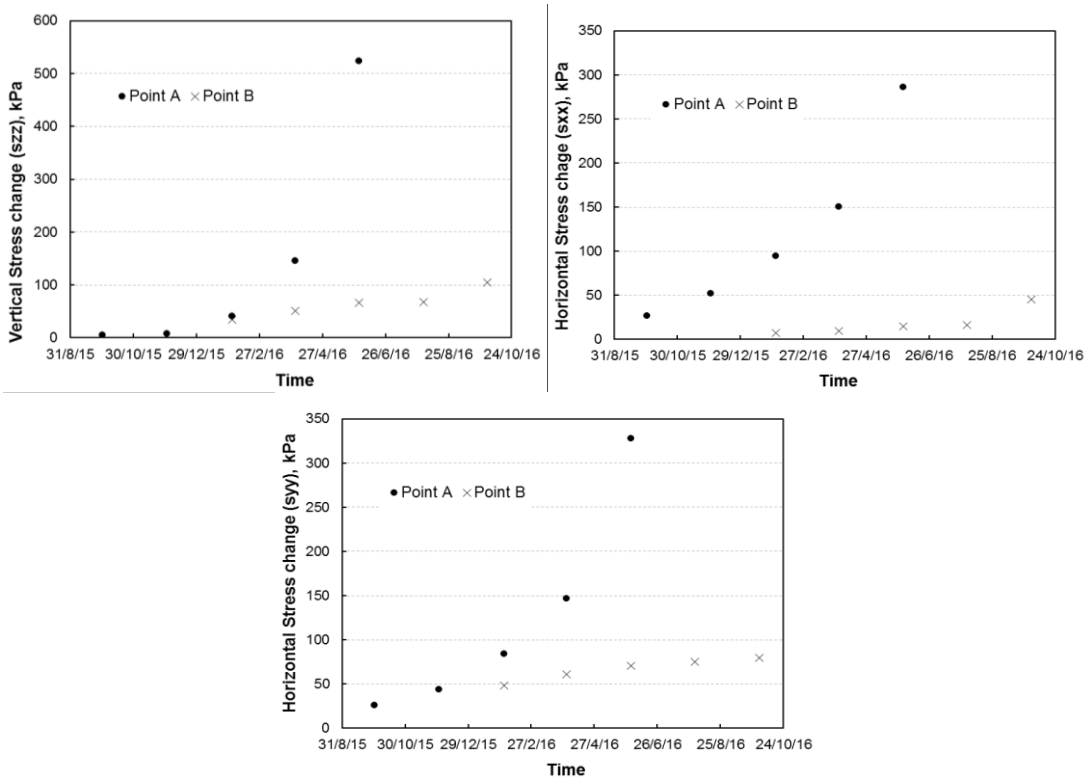


Figure 4.8. Horizontal stress changes (monitor points) induced by the approaching LTCC face.

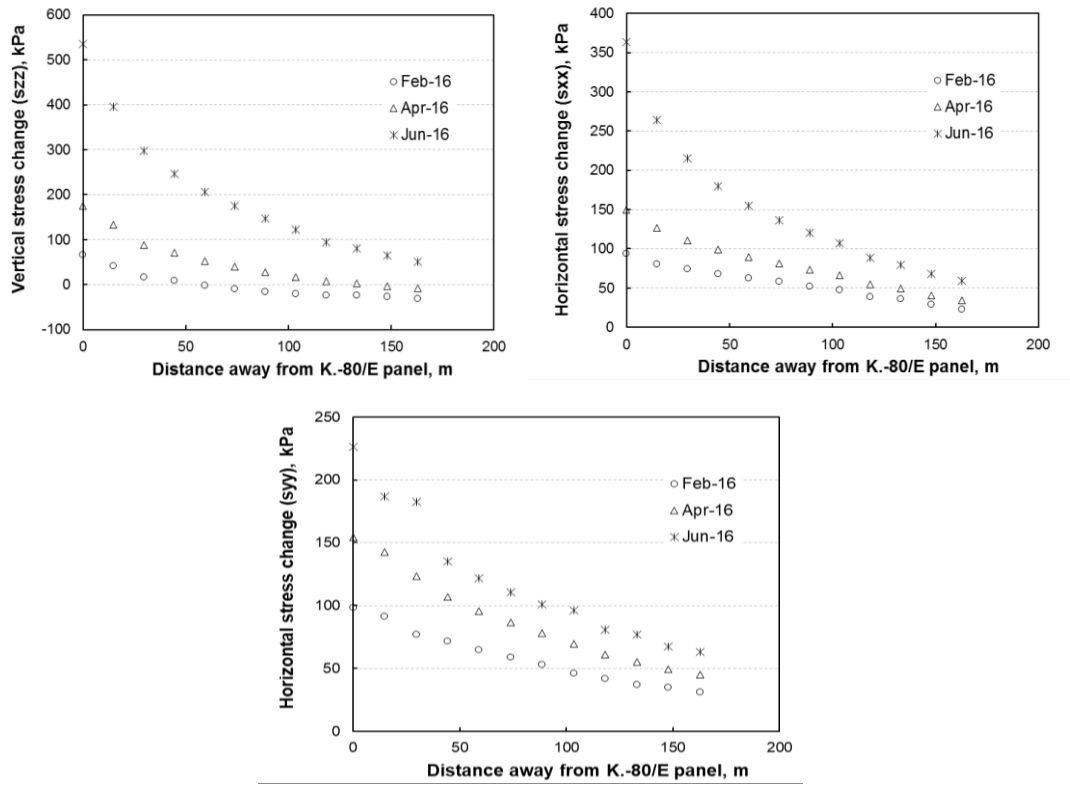


Figure 4.9. Vertical stress changes (monitor lines) induced by the approaching LTCC face.

4.3 Field implementation of the seismic monitoring technique

In order to assess the dynamic behaviour of the coal seam in response to longwall mining, the underground microseismic monitoring at Coal Mine Velenje was conducted during two periods, first around a longwall panel in 2011, followed by monitoring around multiple longwall panels in 2016-2018. The monitoring was jointly conducted by Laboratory of Mining Geophysics of Central Mining Institute (GIG) in Poland and the mine staff. A 32-channel flameproof automated seismic observation system (SOS) developed in GIG was used for the underground microseismic monitoring. The system consists of both underground and surface components, as illustrated in Figure 4.10. The underground component comprises of DLM 2001A or DLM3Dam seismic monitoring sensors and the transmission system using current modulation over twisted pair of wires. The surface part comprises of a demodulation DLM-SO receiver unit which is connected to a seismic recording system. Once the sensors are triggered, the raw signals in the DLM type are amplified and filtered. After the amplitude and frequency characteristics of signals are stabilised, the signals pass through the transmission circuit to be current-modulated. Afterwards they are sent to the demodulation DLM-SO receiver unit, and are converted into the voltage signals in the flameproof, optoelectronic circuit. Next, the signals are transmitted through the analogue filter which determines the frequency characteristics of the receiver unit. A gain is applied to the signals through an amplifier circuit, and an additional 50 Hz band-pass filter is switched on to eliminate the 50 Hz noise from power supply. Finally, the seismic signal outputs from the DLM-SO receiver unit are sent to the A/D input of the seismic recording system and saved in digital form.

4.3.1 Field seismic monitoring at longwall panel K.-50/C in 2011

Continuous microseismic monitoring measurements were carried out at longwall panel K.-50/C during a four-month period from 27 April to 30 August 2011 (Si *et al*., 2015a). A total of eight seismic sensors (four uniaxial and four triaxial) were installed at the panel, placed parallel to the coal face in pairs, with a spacing of around 100 m.

The seismic sensors should ideally be placed in a non-planar array. However, due to limited access to the longwall panels from the gateroads, the geophones were installed at the same level of the LTCC panels, which means that only microseismic activities that occurred close to this horizontal plane were accurately identified. The seismic

sensors were installed on steel anchors in the floor coal. These anchors measured 1 m in length and were placed in the boreholes drilled and stabilised with cement to ensure the coupling between the probes and coal (Figure 4.11).

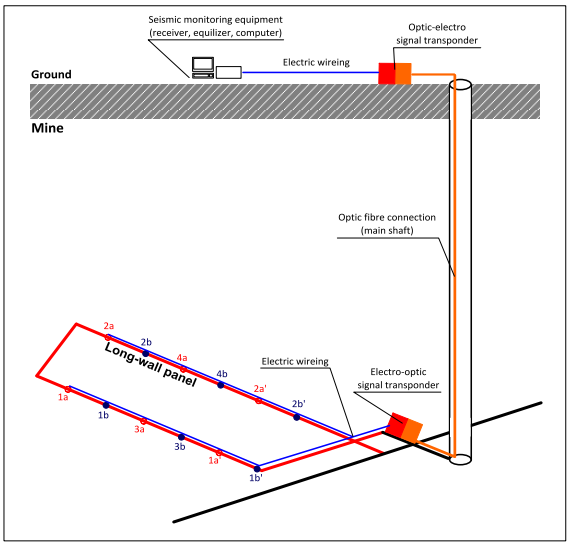


Figure 4.10. The seismic monitoring data transmission system at Coal Mine Velenje (after Si *et al*., 2015).

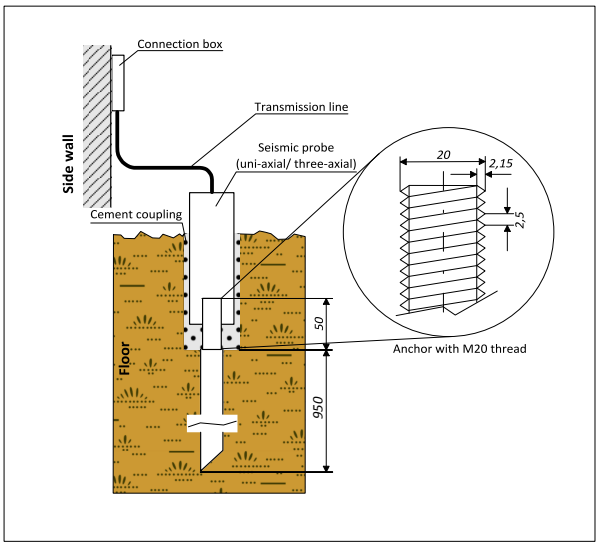


Figure 4.11. Schematic of seismic sensor probe installation (after Si *et al*., 2015).

The seismic sensors measure particle velocities caused by vibrations propagating from microseismic sources. The recording system detects seismic events automatically, and could record for up to 16 s. The data sampling rate is 500 Hz, which covers the recordable frequency bandwidth of microseismicity from 0.8 to 250 Hz.

The recorded raw data were transferred via Internet connection to the server in GIG Katowice, and then post-processed using the SEISGRAM and MULTILOK software to identify microseismic events and obtain source parameters and event locations. First arrival and end times of seismic P and S waves needed to be determined for each seismic station (channel) and for each recorded seismic event to obtain location and seismic energy for each seismic event. As these parameters directly affect accuracy of seismic event location and seismic energy calculation, those times were picked manually in order to obtain maximum possible accuracy.

As most microseismic hypocentres are relatively close to the seismic sensors, the attenuation of energy released from microseismic events at Coal Mine Velenje was assumed to be less than 10%. The energy radiated from each microseismic event was calculated in the MULTILOK software, on the basis of time-integrated values of particle vibration velocities of P and S waves, $u_P(t)$ and $u_S(t)$ respectively (Shearer, 1975):

$$E_r = 4\pi\rho v_P r^2 \frac{<U_{Pm}^2>}{U_P^2}\int_{t_1}^{t_2} |u_P(t)|^2 dt + 4\pi\rho v_S r^2 \frac{<U_{Sm}^2>}{U_S^2}\int_{t_1}^{t_2} |u_S(t)|^2 dt \qquad (4.1)$$

where r is the distance between the source and receiver, ρ is the density of medium, v_P and v_S are P and S wave velocities travelling through the medium, U_P^2 and U_S^2 are the radiation pattern terms, $<U_{Pm}^2>$ and $<U_{Sm}^2>$ are the mean values over the local sphere of U_P^2 and U_S^2 for P and S waves, and t_1 and t_2 are times bounding a group of P and S waves. The minimum accurate detectable energy level of the SOS microseismic monitoring system is around 10^2 J.

During LTCC extraction at longwall panel K.-50/C, and in parallel with the passive microseismic monitoring work carried out, active time-lapse seismic tomography measurements were performed over a 100 m × 141 m area ahead of the advancing longwall face (Si *et al*., 2015a). Specifically, a total of 40 receiver and 40 source boreholes were placed along the intake and return gateroads with a regular spacing of around 2.5 m (Figure 4.12). Each receiver was equipped with 3 receiver components, i.e., X-, Y- and Z-components, monitoring the P-wave velocities parallel to the gateroad, perpendicular to the gateroad and in the vertical direction, respectively. During the survey, explosives in boreholes were used to generate P-waves, and P-wave velocities were computed and interpolated to produce velocity tomograms for every

receiver component. Two seismic tomography measurement campaigns were carried out on the weekend of 21st/22nd May 2011 and 18th/19th June 2011, where the LTCC face was 95 m and 47 m away from the tomography zone respectively.

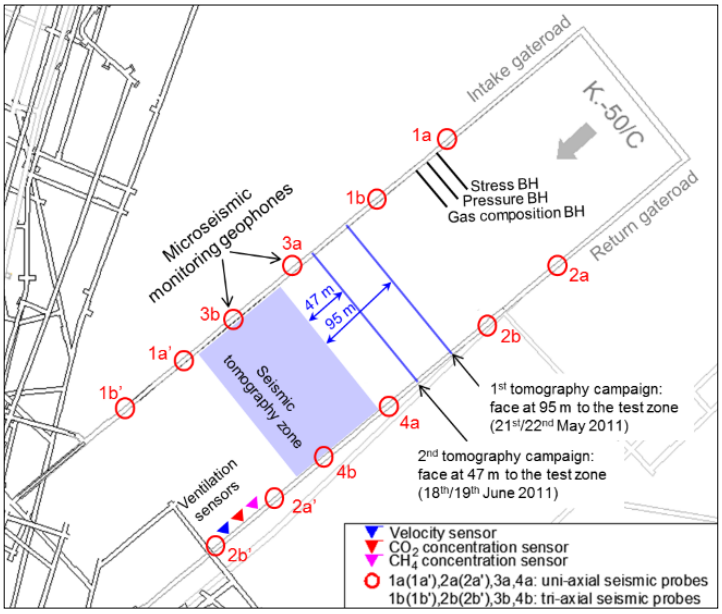


Figure 4.12. The time-lapse seismic tomography zone and the configuration of sensors used for microseismic monitoring and ventilation measurements at LTCC panel K.-50/C.

4.3.2 Field seismic monitoring around multiple longwall panels in 2016-2018

The installed microseismic monitoring system at Coal Mine Velenje in 2016-2018 encompassed the nine LTCC panels in production around the central coal pillar. The number and locations of seismic sensors were determined on the basis that the investigated area should be surrounded by seismic sensors. Although attempts have been made to achieve full coverage of the investigated area, panels CD2, CD3g, and K.-95/E were not fully covered due to technical limits such as access to longwall panels and gateroads, available cable lines and seismic sensors, and noise levels. The SOS system consisting of 3 triaxial seismic sensors and 7 uniaxial seismic sensors was initially installed in the area of active longwall panels K.-80/B and K.-80/E at the beginning of seismic monitoring in February 2016. With the coal face movement, as well as to accommodate larger longwall coal mining-disturbed areas, later on the number of uniaxial seismic sensors in the SOS system was increased to 9 (from August 2016) and then 12 (from October 2017) (Figure 4.3).

The triaxial seismic sensors installed at the permanent roadways were kept permanent throughout the whole period of the project, whereas other sensors were relocated to the new longwall panel gateroads according to technical and mining conditions. As longwall mining was completed at the -80 m level, seismic sensors were gradually moved to active panels K.-95/E and K.-95/A at the lower level. Due to the limited vertical coverage of the seismic sensor network, only microseismic activities that occurred close to the two production levels were accurately identified.

Using the same system and procedure as described in Section 4.3.1, recorded seismic data were collected automatically in these seismic sensors, transferred to surface data loggers via fibreoptic cables, and then processed to obtain source parameters and event locations. Figure 4.13 illustrates an example of picked up arrival times for recorded P and S waves in different geophones.

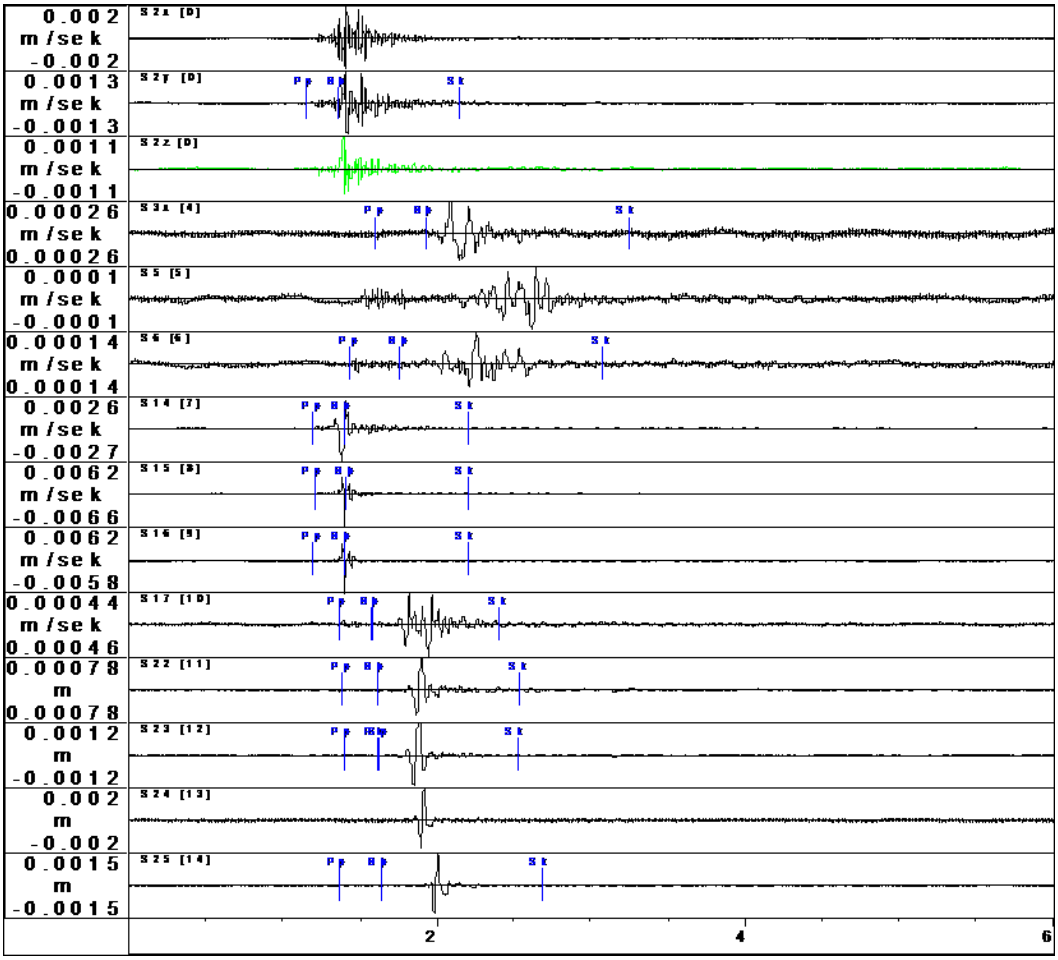
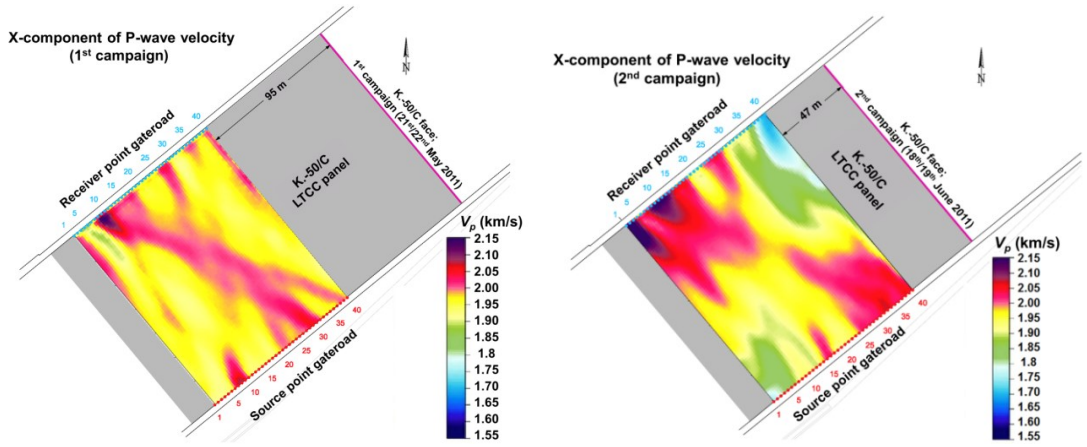


Figure 4.13. An example of recorded raw microseismic signals and the pickup of arrival time for P and S waves (the seismic event occurred at 19:35:23 on 26/09/2016, with a seismic energy of 10^4 J).

4.4 Analysis of mining-induced microseismicity in 2011

4.4.1 Active time-lapse seismic tomography measurements

Figure 4.14 (Si *et al*., 2015a) presents the P-wave velocity tomograms of the 1st and 2nd campaigns for the X component when the longwall face was 95 m and 47 m away from the tomography area respectively. During the first campaign, a relatively high velocity zone was detected diagonally across the centre of the tomography zone. This heterogeneous zone is considered to be xylite-dominated coal with a relatively high strength, as compared to less strong detritic coal that also occurs in the coal deposit. The unconfined compressive strength of xylite in the mine is known to be around twice of that for detrite. The second tomogram, taken when the LTCC face advanced further closer to the tomography zone, indicates even higher velocities over the heterogeneous zone, and much lower seismic velocities over the weaker coal, which is now closer to the advancing face, indicating intensified but preferential fracturing of the weaker coal due to abutment stresses.



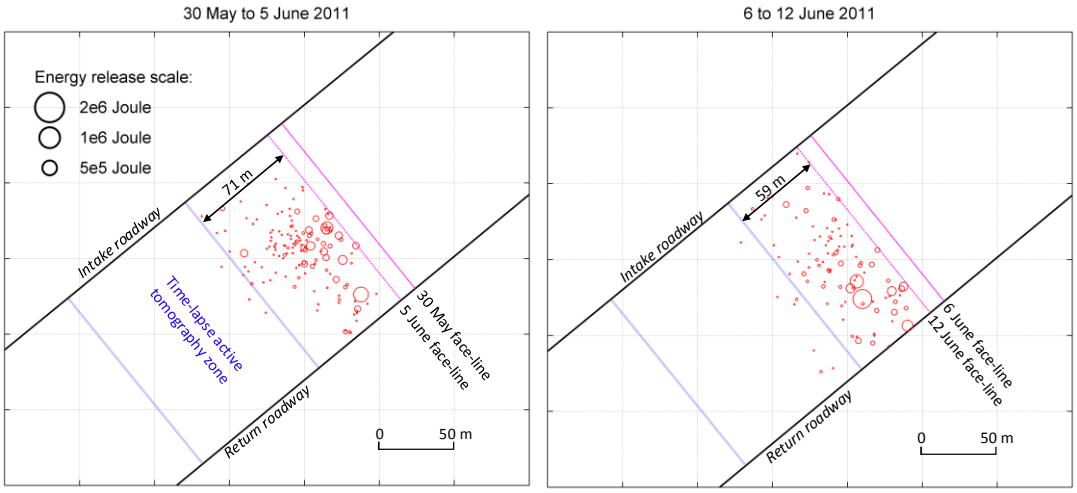
(a) (b)

Figure 4.14. LTCC face K. -50/C P-wave velocity tomograms in X-component for the (a) 1st tomography campaign and (b) 2nd tomography campaign (after Si *et al*., 2015a).

4.4.2 Continuous microseismic monitoring measurements

Over 2,000 microseismic events were recorded around the panel K.-50/C during the four-month monitoring period in 2011. It was observed that the range of seismic energy released spanned by up to four orders of magnitude (from 10^2 to ~10^6 J). Furthermore, the spatial distribution of weekly microseismic events generally scattered over an area approximately 70-80 m ahead of the advancing face-line (Figure

4.15). When the longwall face reached the xylite-rich zone, a seismic anomaly characterised by a decrease in event counts and an increase in the average seismic energy released was observed (Figure 4.16), which coincided with a recorded episode of excessive gas emission at the same longwall district. The spatial and energy distribution of the recorded microseismicity and their strong correlation with gas emission have been reported by Si *et al*. (2015a).



(a) 30 May to 5 June 2011 (b) 6 to 12 June 2011

Figure 4.15. Recorded microseismic events within 100 m ahead of the face-line at the K. -50/C LTCC panel level (after Si *et al*., 2015a).

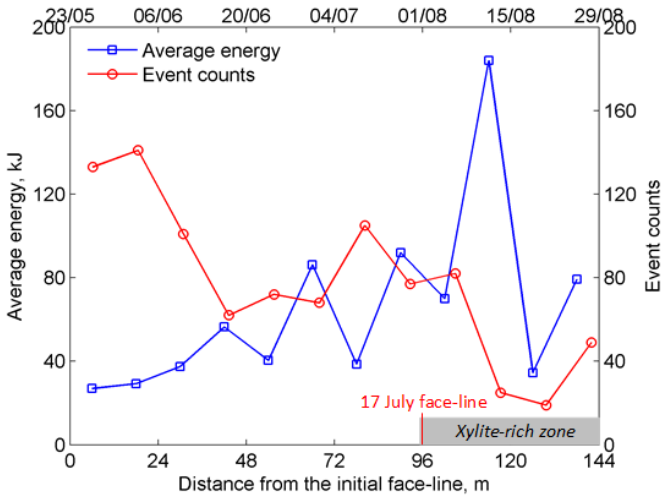


Figure 4.16. Recorded weekly average released energy from microseismic events and event counts against face advance.

In the current work, the microseismic events were further analysed in terms of frequency-magnitude distribution and seismic energy distribution, focusing on the events recorded during twelve coal production weeks from 23 May to 30 August 2011 (excluding a two-week summer holiday period from 18 to 31 July).

In earthquake seismology, the seismicity frequency-magnitude distribution, i.e., the proportional relationship between the event magnitude M_L and the cumulative number N of seismic events with a magnitude greater than M_L, has been found to obey the Gutenberg-Richter relationship (Richter, 1958):

$$\log_{10} N = a - bM_L \tag{4.2}$$

where a and b are constants, and M_L is a function of the seismic energy released:

$$\log_{10} E = 1.5M_L + 4.8 \tag{4.3}$$

The parameter b gives a measure of the scaling of seismicity magnitude distribution, with a higher value of b indicating a higher proportion of small seismic events in the population. b may be estimated by fitting a straight line in a log$N$ - M_L plot.

Monitoring changes in the value of b has been proposed as a potential precursor to tectonic earthquakes (Segger, 1980). A reduction in b associated with macroscopic rupture of rock samples in laboratory experiments has been reported (Lisjak *et al*., 2013; Lockner *et al*., 1991). It has also been reported that the magnitude of b for mining-induced microseismicity typically falls in the range between around 0.6 and over 1.0 (Board, 1994).

A frequency-magnitude analysis was carried out on the recorded microseismicity around LTCC panel K. -50/C at Coal Mine Velenje. It was decided to group the microseismic data in two-week intervals to ensure that there is sufficient number of events in the population. Figure 4.17 presents curves fitted on the frequency-magnitude distribution. In order to minimise the influence of incomplete detection of small seismic events and statistical variations due to small samples of large seismic events, the magnitude range on which a linear regression fitting can be applied was taken as the range of regression fitting, which mostly lies between the magnitude -0.6 and 0. The fitted bi-weekly b values were found to be fairly consistent with each other (~1.0) throughout the first eight weeks, until the xylite rich heterogeneous zone is

approached during the week 11 to 17 July 2011 (Figure 4.18). A drop in *b* value to ~0.8 was noted as and after the xylite rich heterogeneous zone is reached.

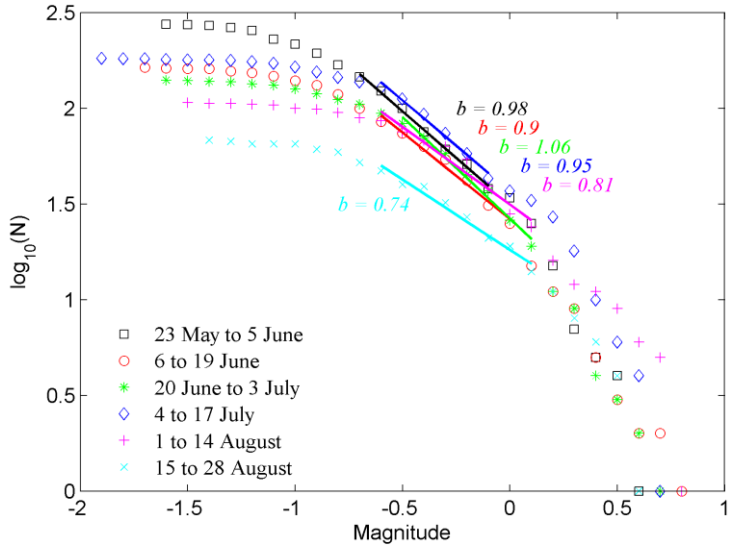


Figure 4.17. Frequency-magnitude plots of the recorded seismic events around LTCC panel K. -50/C during the study period.

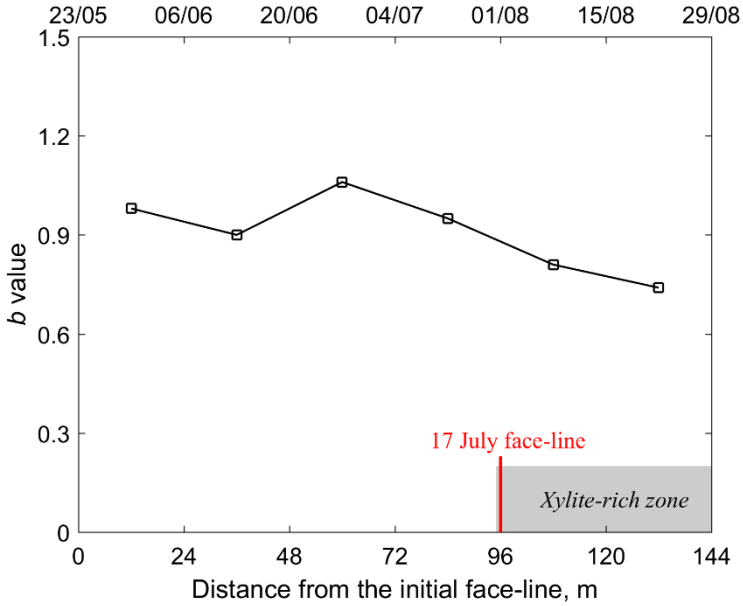
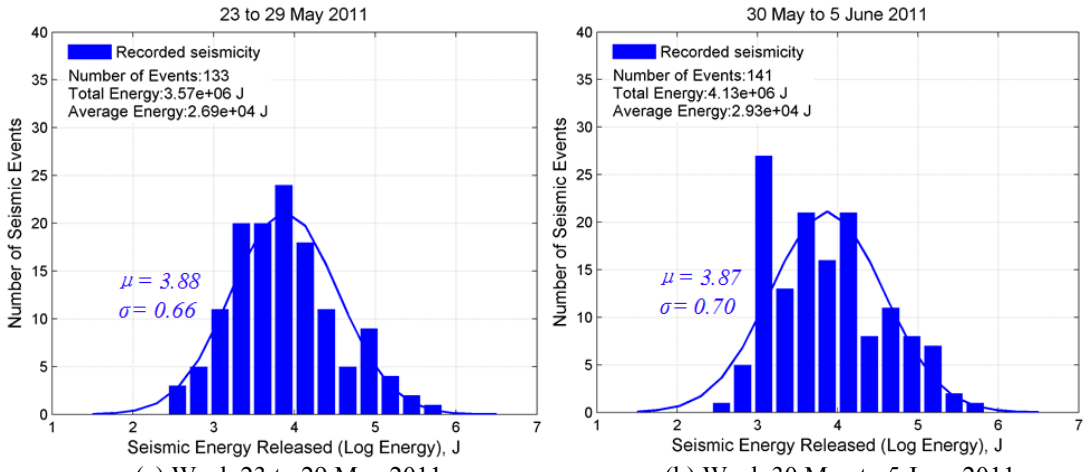


Figure 4.18. Fitted *b* values at a two-week interval over a 12-week period showing a notable reduction in *b* as the longwall panel K. -50/C face-line reached the xylite-rich heterogeneous zone.

A range of factors influencing the fracturing process of rock masses contribute to the complexity of the seismic energy distribution (Lasocki and Orlecka-Sikora, 2008).

Zhang *et al*. (2013) conducted a statistical energy analysis on different seismic datasets and found that no common distribution patterns (normal, Weibull, exponential and lognormal distributions) could be universally applied to describe seismic energy distribution. Nonetheless, a number of statistical distribution models, such as truncated Pareto distribution (Lasocki, 1992) and Weibull distribution (Lasocki, 1993b), have been used to fit the logarithm of energy released from microseismic events taking place in specific geological and mining conditions.

Si *et al*. (2015a) reported that the weekly microseismic energy released at longwall panel K. -50/C recorded at Coal Mine Velenje followed a Gaussian distribution. A Gaussian distribution is characterised by a mean value μ and standard deviation σ as illustrated in Figure 4.19. In the current work, Gaussian distribution curves were fitted to the weekly histograms over the monitoring period between 27 April and 30 August 2011. With the exception of two weeks' data, for which there were too few events (8 to 21 August 2011), a good fit was achieved for 10 weekly histograms. The goodness of fitting using the Chi-square test has shown that a *p*-value greater than 0.05 (95% confidence) was achieved for 8 out of the 10 weeks evaluated (except for weeks May 30 to 5 June, and 6 to 19 June 2011). The fitted parameter values and their variation with face advance are plotted in Figure 4.20. It was observed that the mean value μ and the standard deviation σ remained fairly constant during the first eight weeks, and deviated after reaching the xylite-rich zone.



(a) Week 23 to 29 May 2011 (b) Week 30 May to 5 June 2011

Figure 4.19. Recorded seismic energy released in two consecutive production weeks around LTCC panel K. -50/C at Coal Mine Velenje.

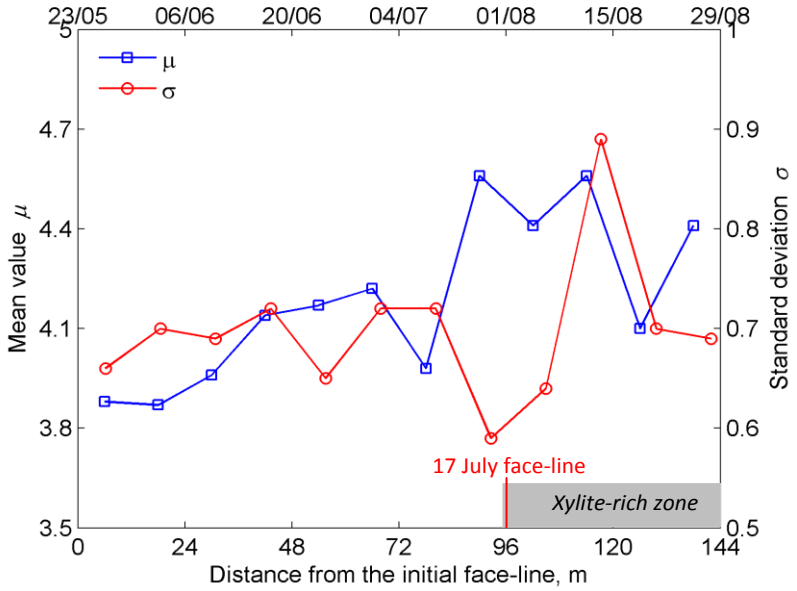


Figure 4.20. Fitted Gaussian distribution parameters for the microseismic event energy recorded during each production week of the study period at LTCC panel K. -50/C, Coal Mine Velenje.

Since the recorded microseismic event energy is to a large extent reflecting the size of slipped fractures (Salamon, 1993), the fitted Gaussian distribution mean value μ may be related to the mean sizes of slipped fractures, and both the standard deviation σ of the logarithmic event energy and the b value for the Gutenberg-Richter relationship reflect the fracture size distribution within the coal seam. Consequently, the consistency in both the σ and b values before the week 11 to 17 July 2011 implies that fracture size distribution within the extracted coal panel was fairly constant before the longwall face-line reached the inferred xylite rich heterogeneous zone.

4.5 Analysis of mining-induced microseismicity during 2016-2018

During the monitoring period between 29 February 2016 and 20 May 2018, a total of over 17,000 microseismic events were identified around the nine LTCC panels at different levels. The complete record of the daily face advance at each LTCC panel is also available, which allows the recorded microseismicity to be correlated with the prevailing face-line positions.

To facilitate analysis in this work, each microseismic event was to be associated with one of the nine panels, which is active and whose working face-line position is located closest to the event. Here, a longwall panel is considered to remain active within 7 days after the coal production is completed. It has been recognised that it usually takes

a period of time for the stress fields disturbed by longwall mining to reach a new state of equilibrium (Styles *et al*., 1988). Indeed, a few microseismic events were recorded at weekends when there was no active mining.

Overall, this grouping of the microseismic events has proved to be largely effective since 1) mining-induced stress redistribution usually affects a limited area around LTCC panels; and 2) most simultaneously active LTCC panels were not immediately adjacent to each other over the monitoring period. In some occasions, mining induced stress disturbance may trigger microseismicity in coals or rock masses at a distance from the working LTCC panel, but are under critical stress state. In this case, the induced microseismicity is also considered to be associated with the working LTCC panel. It is recognised that microseismicity might also be triggered by roof collapse in the goaf area or roadway development in the coal mine, rather than by coal excavation at a particular longwall panel. The resulting mis-association is believed to constitute only a small fraction of the whole datasets, considering the limited disturbed areas compared to the LTCC panels. Microseismic event counts associated with each panel are presented in Table 4.1.

Microseismic events at six completed LTCC panels (K.-80/B, K.-80/E, CD2, K.-80/D, K.-80/C and K.-95/E) were analysed as presented below. Longwall mining at panels K.-95/A and CD3G was still underway after 20/05/2018, therefore, microseismicity associated with these panels is not discussed here.

4.5.1 Spatial distribution

To illustrate the correlation of mining production and the induced microseismicity, the spatial distribution of recorded microseismic events at the starting and ending weeks for each panel are presented in Figure 4.21, whilst the others are presented in Appendix 1. The face-line positions of longwall panels (on the first day of each week) at the same production level are also presented according to daily face advance records. The active longwall panels serve as the sources of dynamic mining disturbances, while the inactive longwall panels indicate areas of possible large stress concentration.

For most of the time, microseismicity was located around the active longwall panels but was relatively scattered with respect to the working face-line positions. There was an apparent trend at certain times for induced microseismicity to cluster in the vicinity of the advancing longwall faces, such as K.-80/B in Figure 4.21c, d, K.-80/D in Figure

4.21f, g, and K.-80/C in Figure 4.21g, h. When a longwall panel was in operation, the induced microseismicity located either ahead of or behind the face-line, due to the frequent mining-induced stress movement and adjustment with the face advance. After mining was completed at a longwall panel, microseismicity still occurred close to the abandoned inactive longwall face subjected to stress disturbances from other longwall panels. In this case, microseismicity tended to occur primarily in front of the inactive face-line (K.-80/E in Figure 4.21c, d, K.-80/D and K.-80/C in Figure 4.21j). This is because the stress behind the face-line stabilised as the caved roof gradually hardened, while the relatively intact coal (the barrier pillar) in front of the face-line took most of the vertical stress, as well as was subjected to continuous mining disturbances from other longwall panels. According to the geometry of the central coal pillar (Figure 4.3), the stresses in front of the final face-line position of K.-80/B are expected to be less concentrated compared to those ahead of panels K.-80/E, K.-80/D and K.-80/C. Consequently, the microseismic event counts were relatively small in K.-80/B compared to those in the other three panels. Overall, the spatial distribution of microseismicity, specifically its location with respect to longwall faces, is panel-specific.

There is a large variation in the magnitude of seismic energy released from different LTCC panels, albeit under similar mining conditions. For example, microseismic energy around panel K.-80/C (Figure 4.21g, h) were about one order of magnitude larger than those around panel K.-80/B (Figure 4.21c, d), even though the two panels lie adjacent to each other, and had the same mining layouts and similar face advance rates. This difference in the microseismic energy indicates general heterogeneity in the coal seams, in particular attributes of pre-existing natural fractures.

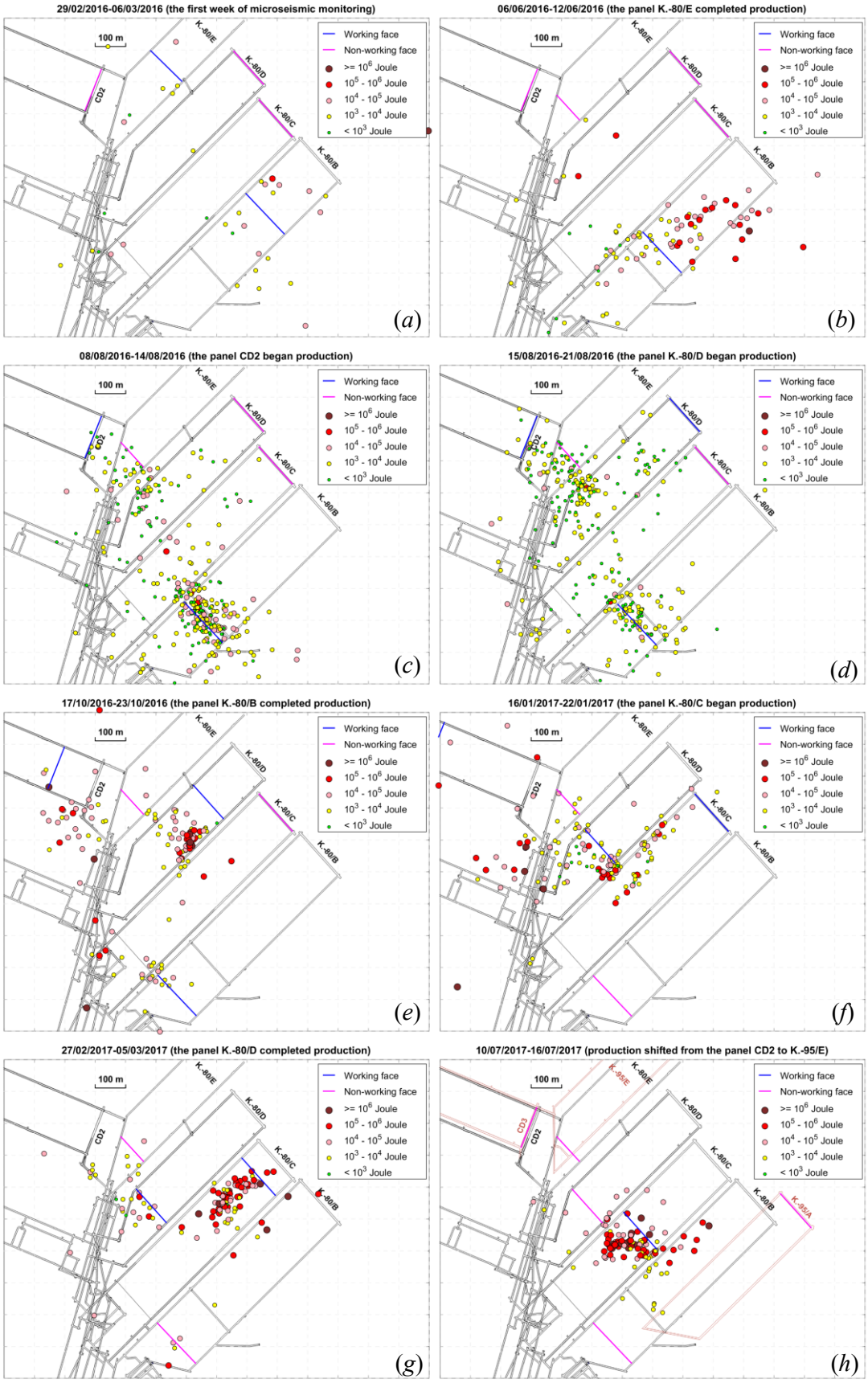


Figure 4.21. Spatial distribution of weekly recorded microseismic events around six longwall panels at Coal Mine Velenje.

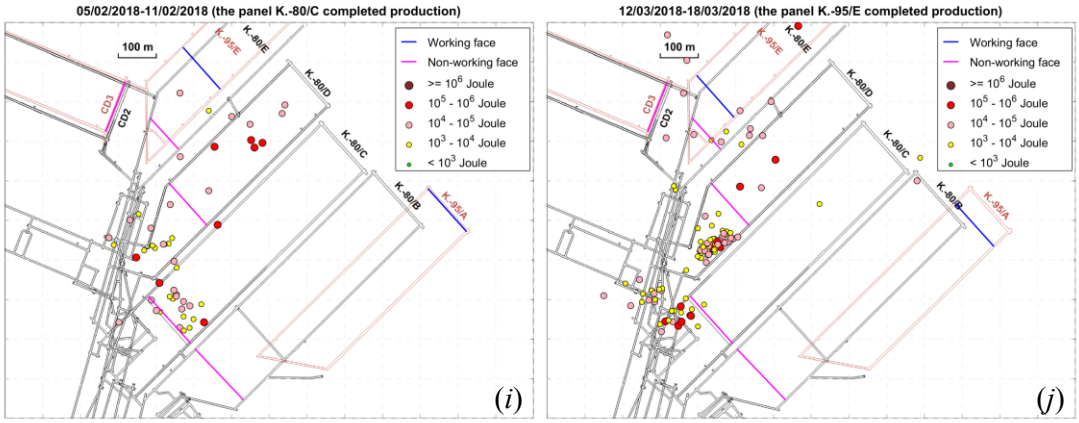


Figure 4.21. (Continued). Spatial distribution of weekly recorded microseismic events around six longwall panels at Coal Mine Velenje.

Figure 4.22 presents the mined-out area and distribution of the associated microseismic events for each panel. The majority of microseismicity located within and close to the mined area, as illustrated in Figure 4.21. It is further noted that there was a kidney-shaped area where the density of the seismic events was relatively higher, indicating elevated stress concentration. A large part of this area is seen to overlap with the central coal pillar after the longwall panels were mined out. The spatial location and extent of this area has been undergoing continuous changes with the advance of the longwall faces, and is subject to further variation. Furthermore, microseismic events occurred more frequently around gateroads in the vicinity of the central coal pillar, where hydraulic supports were removed during the abandonment of longwall panels.

Microseismic events close in space tended to have similar energy levels, regardless of the time of occurrence, an indication of spatial continuity of the fracture attributes. For example, for microseismicity induced by LTCC mining at K.-80/E, the majority that fell within the mined-out area had an energy release lower than 10^4 J, while most of those located at the northeast have an energy release greater than 10^4 J (Figure 4.22b). Likewise, the induced microseismicity in the kidney-shaped stress concentration area has a relatively lower energy release than those outside (Figure 4.22e). The difference in seismic energy released reflects the heterogeneity of the coal seam. In this sense, it indicates the feasibility of applying the elevated energy levels from microseismic monitoring as precursors to subsequent large microseismic events.

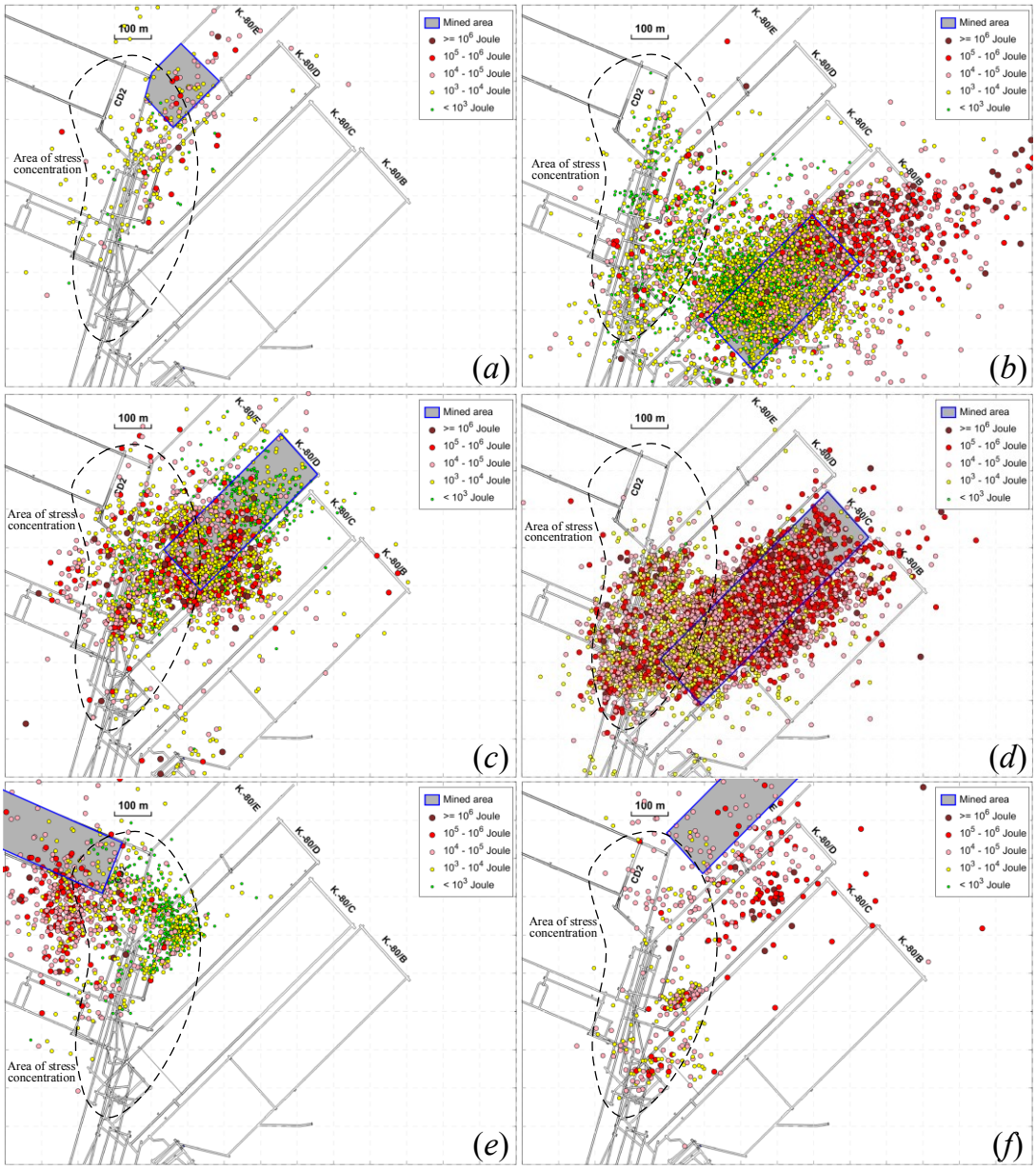
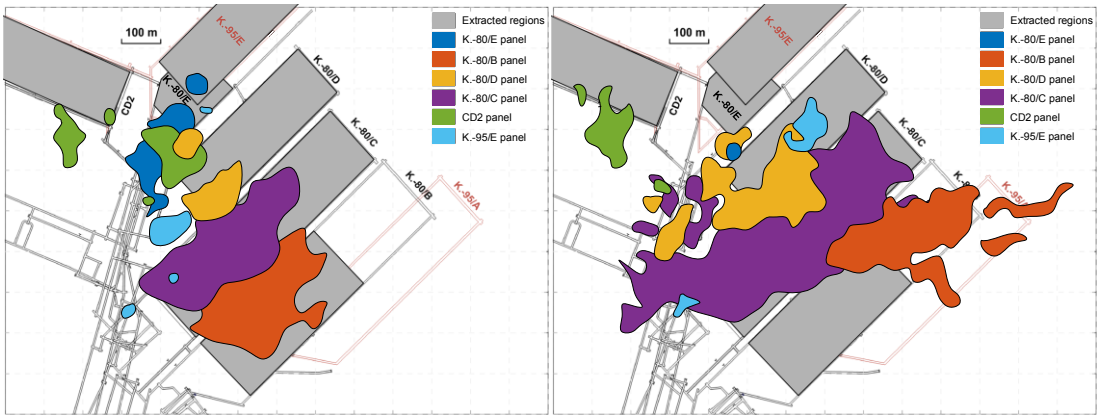


Figure 4.22. Spatial distribution of microseismicity associated with: (a) panel K.-80/E, (b) panel K.-80/B, (c) panel K.-80/D, (d) panel K.-80/C, (e) panel CD2, and (f) panel K.-95/E.

Figure 4.23 presents both seismic event counts and energy intensive regions associated with longwall coal mining around each LTCC panel. It can be seen from Figure 4.23a that although the distribution of seismic intensive regions follow a different pattern in each panel, extensive events tended to occur where the stress environment was significantly disturbed, either within the mined-out areas (for microseismicity around K.-80/B, K.-80/D and K.-80/C panels) or at the central coal pillar (for microseismicity around K.-80/E, CD2 and K.-95/E panels). In contrast to the seismic intensive regions,

the energy release intensive regions in Figure 4.23b are distributed around the corresponding longwall panels, but are not overlapped with regions where seismicity is the mostly concentrated. The seismic energy intensive regions associated with panel K.-80/C have the largest coverage area, covering the majority of the longwall panel in addition to the central part of the central coal pillar. However, it is noteworthy that both microseismicity intensive regions and seismic energy intensive regions associated with coal mining in different panels are spatially connected, and that are not fully overlapped with the mined-out or stress concentrated areas. This strongly suggests that spatial and magnitude characteristics of the microseismicity induced by the LTCC mining at the panels around the central pillar region are to a large extent dominated by the attributes of local fractures. In addition, this verifies that the attributes of fractures throughout the coal seam are characterised by spatial continuity.



(a) (b)

Figure 4.23. Microseismicity intensive regions associated with different longwall panels: (a) event count intensive regions (>30% of the maximum seismicity density), and (b) seismic energy intensive regions (>10^3 J/m^2).

4.5.2 Energy magnitude and scaling

Figure 4.24a presents the frequency-magnitude relationship for all the microseismicity recorded. The resulting bell-shaped histogram has been reported previously for mining-induced microseismicity at -350 m depth at the same coal mine (Si *et al.*, 2015a). The shape of the frequency-magnitude distribution for each panel resembles that for the whole datasets. Examples are given in Figure 4.24b and c for the microseismicity around panels E.-80/B and E.-80/C. More examples are presented in Appendix 1.

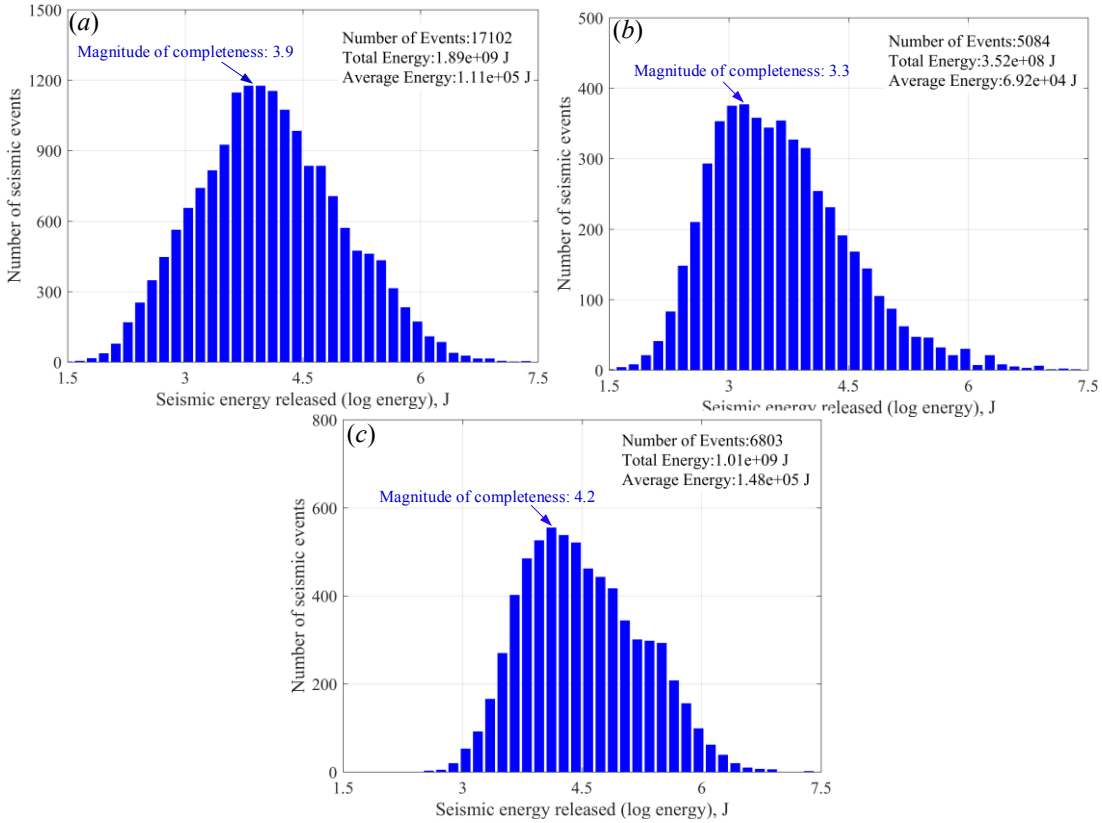


Figure 4.24. Histograms of released energy of microseismic events recorded around: (a) all panels, (b) panel K.-80/B, and (c) panel K.-80/C.

In view of the limited energy detection range of geophones and relatively long distance between microseismic sources and geophones, a portion of microseismicity with low energy levels could not have been picked up by the monitoring system. The minimum complete detection magnitude (or the magnitude of completeness), defined as the minimum magnitude at which all the microseismic events are detected in spatial and temporal scales, can be an indicator of the energy levels released around each panel (X. Ma *et al*., 2018; Woessner and Wiemer, 2005). The minimum complete detection magnitude for the whole datasets was estimated to be 3.9 by visualising the frequency-magnitude relationship of microseismicity, while those for microseismicity around each panel vary from 3.3 to 4.2. The magnitude is positively correlated with the average seismic energy released, except for microseismicity around CD2 panel which forms a plateau at the peak in the histogram. The microseismicity around panel K.-80/C, whose seismic energy released constitutes more than half of the total energy released, has a relatively high minimum complete detection magnitude of 4.2.

Figure 4.25 shows the cumulative frequency-magnitude relationship of the recorded microseismicity. The *b* value in the Gutenberg-Richter law for microseismicity around each LTCC panel was obtained by a linear regression fitting starting from the minimum complete detection magnitude. The *b* value fitted for seismic energy released for the whole dataset is 1, and those around the six LTCC panels fall into the range of 0.87-1.13. Although the magnitude of completeness varies from panel to panel, the scaling of seismic energy released was relatively consistent between different panels.

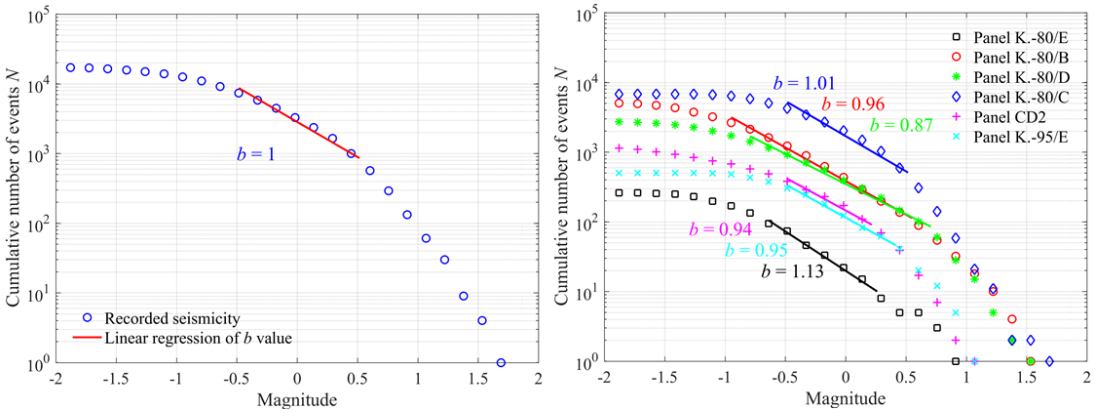


Figure 4.25. Frequency-magnitude relationship of the recorded microseismicity around: (a) all panels, and (b) each panel.

4.5.3 Evolutional characteristics

Figure 4.26 plots the daily event number, seismic energy released and the distance to the closest face-line, together with the daily face advance rate at two representative panels K.-80/B and K.-80/C, (the remaining results are presented in Appendix 1). The distance to the closest face-line position is taken as the distance of microseismicity to the nearest point of the closest active longwall face.

The results show that the daily microseismic intensity (top panel) closely follows the mine production schedule (bottom panel), with reduced values at weekends and holidays. In contrast, the average seismic energy and distance to the nearest face-line remained relatively consistent throughout, with the exception of a few outliers due to the scarcity of event numbers at weekends. The latter suggests that the face advance rate had much less impact on the magnitude and spatial distribution of microseismicity.

While the majority of microseismic events occurred within 400 m distance from the closest face-line, a small fraction was triggered as far as 800 m away from the active longwall face. Similar distance has also been reported by Marcak and Mutke (2013), where the hypocentres of strongest seismic events are 300-800 m deeper than the level of coal mining. The observation of microseismicity induced at a long distance from the active longwall face has been attributed to the reactivation of the fractures already under critical stress state by minute stress perturbations (Grasso and Sornette, 1998). Elastic mechanics analysis indicates that stress environments at a distance of five times of the excavation size may be perturbed. The extracted longwall panels had a width of 150-180 m, which gives rise to an influence zone of between 750 and 900 m. For LTCC panels, an even larger area could be affected since coal around longwall faces fails and stress concentrations are shifted further ahead.

The results in Figure 4.26 represent spatial distribution of the majority of microseismicity with respect to face-line positions. However, the start and completion of operational longwall panels could result in a period of overlapping in coal production at multiple longwall panels, and the resulting combined stress disturbance would in turn have an impact on the induced microseismicity accordingly. For example, the completion of panel K.-80/B in October 2016, panel K.-80/D (see Appendix 1) in February 2017, and panel K.-80/C in February 2018 led to sharp rises in numbers of far-field microseismicity around panels K.-80/D, K.-80/C and K.-95/E (see Appendix 1), respectively.

As the longwall face moved towards/away from the microseismic monitoring zone, a steady increase, as in the case of panel K.-95/E, or decline, as in the case of panel CD2, in the microseismic event counts was recorded, the latter being due to the increased attenuation in long travelling distances and reduced accuracy in locating event sources. Nevertheless, the average seismic energy and spatial distribution with respect to face-line positions were not influenced by the incomplete sampling of microseismic events.

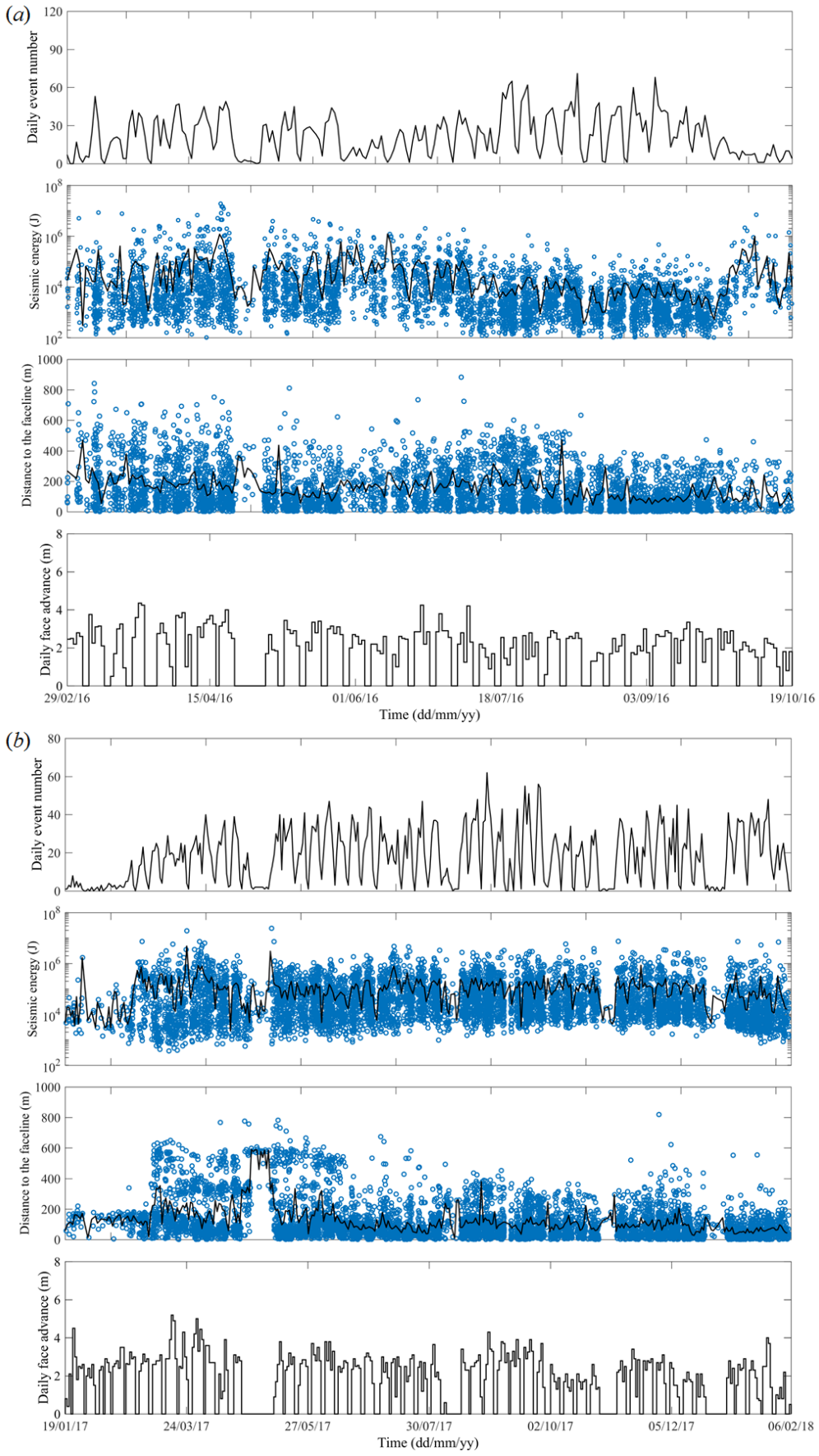


Figure 4.26. Evolutional characteristics of LTCC mining-induced microseismicity on a daily basis around: (a) panel K.-80/B, and (b) panel K.-80/C.

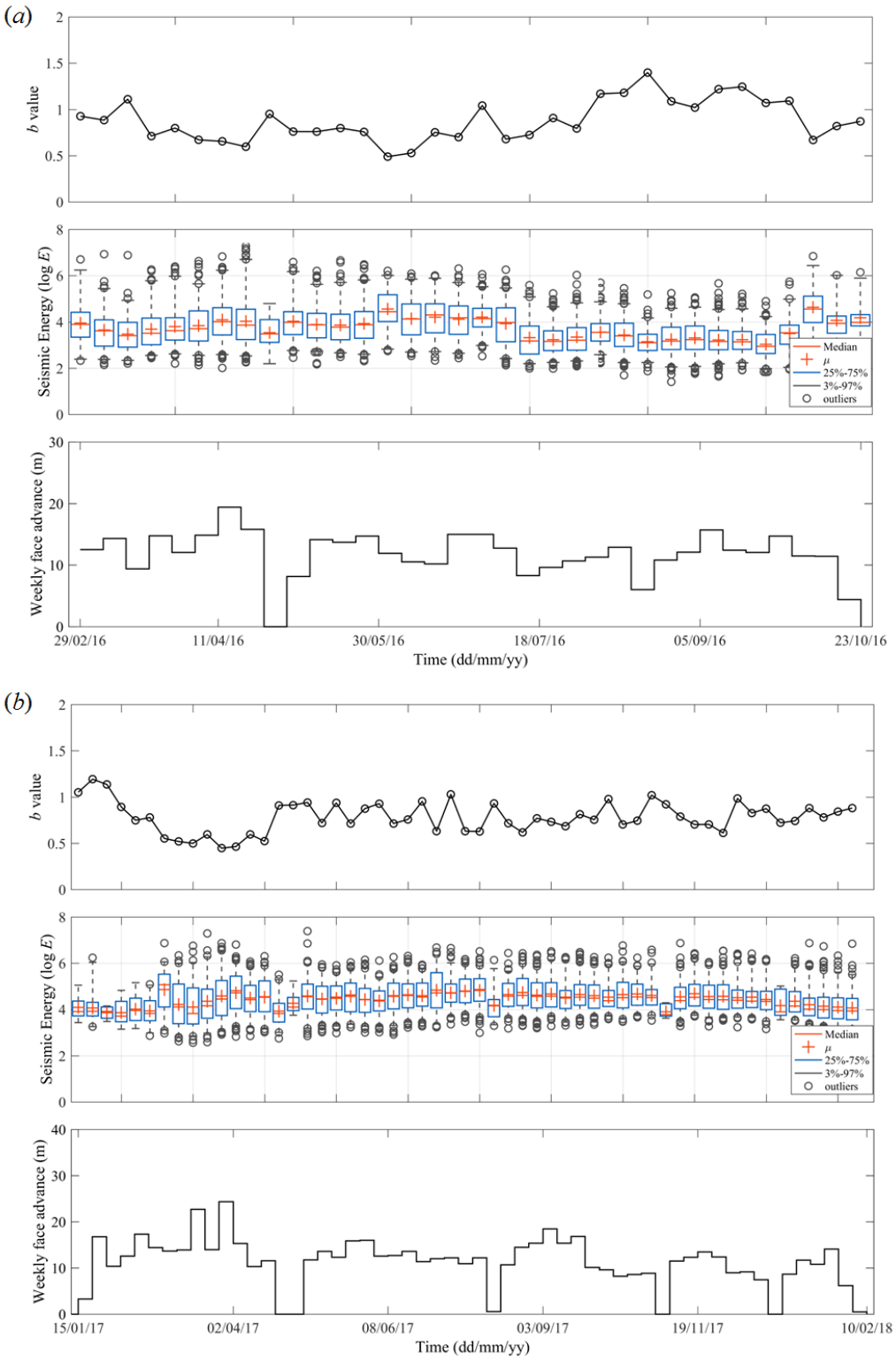


Figure 4.27. Evolutional characteristics of LTCC mining-induced microseismicity on a weekly basis around: (a) panel K.-80/B, and (b) panel K.-80/C.

In an effort to minimise deviations caused by the insufficient number of events, analyses of seismic energy, in terms of the estimation of *b* value in the Gutenberg-

Richter law and the box-and-whisker diagrams, were performed based on weekly events. To yield a reliable *b* value, which represents the scaling of seismic energy, the regression fitting was made over a linear part of the weekly frequency-magnitude plots, while discarding those weeks with few microseismic events. The plot of box-and-whisker diagrams for each sub-group seismicity allows a visually better display of the seismic energy distribution through upper and lower quartiles and extremes. Box-and-whisker diagrams have the added advantage of taking up less space in exhibiting multi-group datasets in comparison to histograms without losing key information, such as the range of magnitudes, statistical dispersion, and skewness. Two representative examples of the results are presented in Figure 4.27, with the remaining ones given in Appendix 1.

The *b* values for the weekly microseismicity around each panel generally fluctuated around 1 (top panel, Figure 4.27). As the *b* value has an inverse correlation with the average seismic energy, the elevated level at panel K.-80/B during the period 17/07/16-02/10/16 indicates supressed seismic energy release, and vice versa when it subsequently dropped to the normal level (Figure 4.27a). Microseismicity around panel K.-80/C experienced a sharp decrease in the *b* value as the average seismic energy increased from 13/02/17, followed by a low-*b* value period until 23/04/17 (Figure 4.27b).

It is noted that the face advance rate had little impacts on either the *b* value or the average seismic energy. In those weeks when coal extraction was halted in particular, both the *b* value and the average seismic energy remained fairly stable, albeit the number of newly generated microseismic events dropped significantly. This indicates that mine production as a trigger of microseismicity does not dominate the magnitude and scaling of the resulting energy release.

In the box-and-whisker diagrams (middle panel, Figure 4.27), the interquartile range, which is between the upper and lower quartiles, are more concentrated around the median value. A nearly symmetrical distribution of seismic energy with respect to the median value within the interquartile range during the majority of weeks is observed. However, the upper and lower extremes, represented by the 97^{th} and 3^{th} percentiles respectively in this work, are not symmetrical with respect to the median value. For most weeks, the top whisker (distance from the upper extreme to the median value) is

longer than the bottom one, and the mean seismic energy is larger than the median value, both of which suggest that the distribution of released energy is positively skewed, corresponding to the elongated tails in the histograms of released microseismic energy (Figure 4.24b and c).

4.6 Discussions

Field recorded microseismicity corresponding to the mining of six longwall top coal caving panels over a 27-month coal production period during 2016-2018 were analysed with reference to concurrent face advance records and the stress disturbances from previous mining activities. The following conclusions were made:

(1) microseismicity occurred up to 800 m away from the extracted panel, which may be explained by the reactivation of fractures at critical stress states subjected to minute stress perturbations;

(2) the source-scaling property of microseismicity is dominated by that of natural fractures; and

(3) both spatial and energy distribution of mining-induced microseismicity are panel specific, which is believed to be attributed to attributes of underlying natural fractures.

These findings have provided further evidence for the fracture-slip seismicity-generation mechanism.

4.6.1 Microseismic characteristics influenced by LTCC mining

The characteristics of longwall coal mining-induced microseismicity depend on the interplay of intrinsic and extrinsic factors. Intrinsic factors include primarily attributes of fractures, such as the spatial distribution (density and local heterogeneity), the length size and scaling, and mechanical properties (frictional coefficient). Extrinsic factors are the prevailing stress environments typically experienced by longwall coal mining, including gravitational and tectonic stresses, and stress perturbations from mining activities. The fracture attributes in the field are largely unknown.

Analysis of the monitoring data in this work revealed how mine production influenced individual characteristic of induced microseismicity, which in turn shed light on to which extent each microseismic characteristic could reflect the fracture attributes.

Figure 4.28 presents the daily event number, average seismic energy released, and average distance to the nearest working face against face advance rate for microseismicity around two LTCC panels. It can be seen from Figure 4.28a that the daily event number is moderately correlated with the face advance rate, which is consistent with previous reports (Bishop *et al*., 1993; Shen *et al*., 2008; Si *et al*., 2015a; Tang *et al*., 2018). This is because the number of slipped fractures triggered by mining activities is approximately proportional to the extracted volume of coal per unit time, or the mining intensity. This also provides an explanation for observations that the amount of seismic energy released depends on the volume of extracted coal for South African mines (McGarr, 1976), Czech and Polish mines (Głowacka, 1992) and some German mines (Fritschen, 2010). The not strong correlation between seismic intensity and mining progression is believed to be caused by the heterogeneous distribution of natural fractures throughout the coal seam.

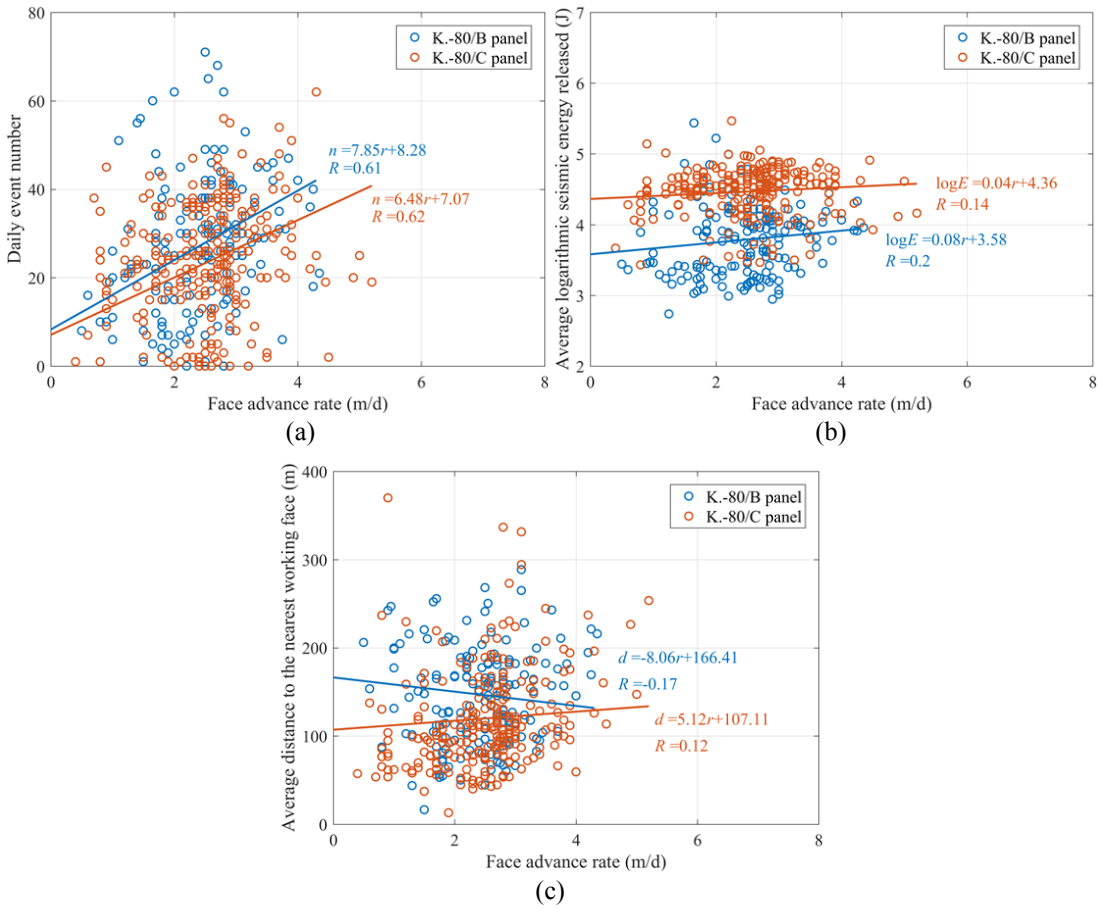


Figure 4.28. The relationship between the daily event counts, average seismic energy released, average distance to the nearest operating longwall face and mining intensity.

From Figure 4.28b and c, it can be seen that both the average seismic energy and the average distance to the nearest working face are poorly related to the face advance rate. This is consistent with the observations from China that the seismic energy release has no clear relationship with mining intensity in a coal mine (Y. Li *et al*., 2016). It is believed that, although microseismicity is induced by the longwall coal mining production, its energy and spatial distribution are controlled by the attributes of natural fractures around the coal seam. Specifically, seismic energy released is dominated by the length size and scaling of fractures, while spatial distribution of microseismicity is governed by that of local underlying fractures. This has significant implications in accurate evaluation of hazards and risk, and associated adjustment of face advance in that spatial and magnitude information of microseismicity is isolated from mining production and can be taken as independent variables.

4.6.2 A conceptual model for mining-induced microseismicity

Based on the analyses of stress concentration within the central coal pillar, recorded microseismicity, and continuous records of face advance above, a conceptual model has been developed to describe the longwall top coal caving mining-induced microseismicity at Coal Mine Velenje. Since progressive longwall mining can be considered as a plane strain problem, a cross section of the multi-level LTCC mining layout is depicted in Figure 4.29. Pre-existing fractures within coal as potential sources of microseismicity are projected to the cross section as 2D fracture traces. The distribution of fracture sizes can be characterised by the power law:

$$n(l) = \alpha \cdot l^{-a} \tag{4.4}$$

where $n(l)$ is the number of fractures with size l per unit volume, α is the density term which gives the number of fractures with unit fracture size, and a (>1) is the power law scaling exponent which defines the relative abundance of fractures with different sizes within the population.

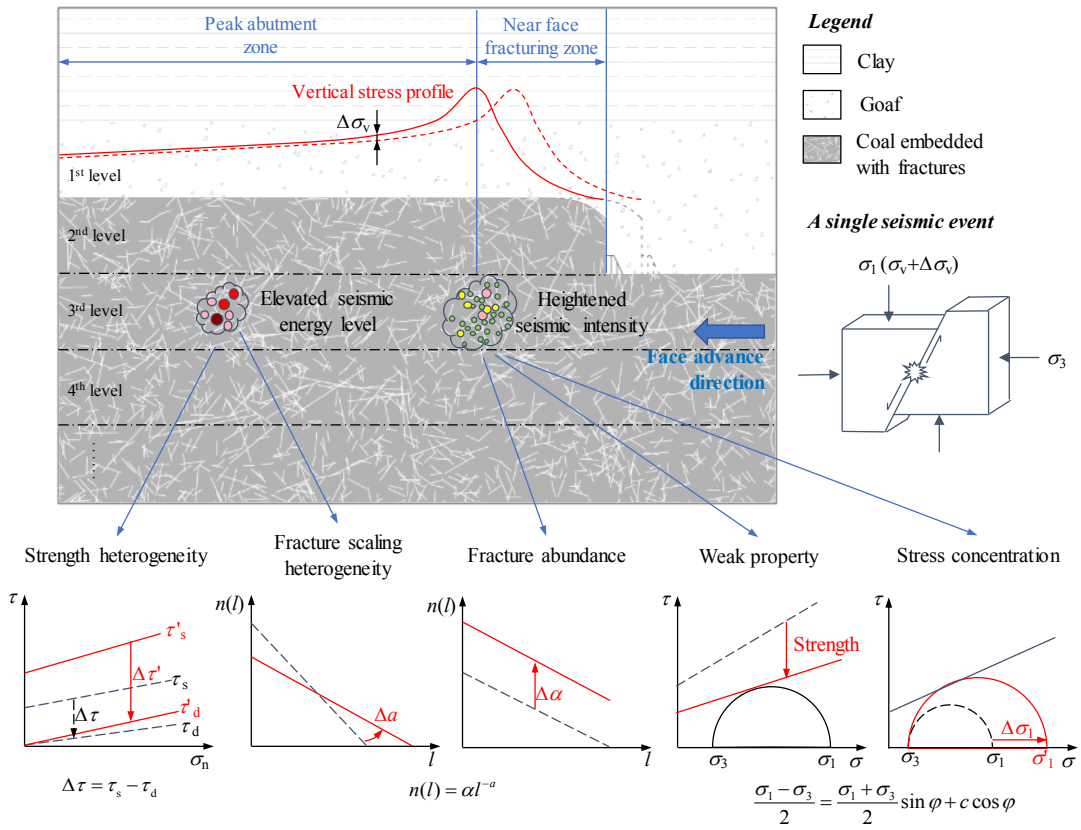


Figure 4.29. Schematic illustrating longwall coal mining-induced microseismicity as a result of fracture slippage subjected to stress perturbations.

Longwall mining creates a fractured area ahead of the longwall face, and stress concentrates over a large region around the fractured area. The vertical stress abutment extends from the near face fracturing zone to the far field. As the longwall face advances progressively, the abutment stress concentration moves forward, and creates an incremental vertical stress $\Delta\sigma_v$, contributing to slippage of fractures at critical stress states. Fractures are considered to be activated in the form of microseismicity when the prevailing stresses satisfy the Mohr-Coulomb criterion:

$$\frac{\sigma_1-\sigma_3}{2} = \frac{\sigma_1+\sigma_3}{2}\sin\varphi + c\cos\varphi \tag{4.5}$$

where σ_1 and σ_3 are the maximum and minimum principal stresses, and c and φ are the cohesion and frictional angle of the fracture plane.

The change in shear stress $\Delta\tau$ along the fracture plane, i.e., the stress drop, can be approximated as the difference between the resistance τ_{sf} prior to slip and the dynamic strength τ_{df} of the fracture surface:

$$\Delta\tau = \tau_{sf} - \tau_{df} \tag{4.6}$$

The static stress changes associated with progressive longwall mining can be quantified by changes of the Coulomb Failure Function, ΔCFF (Scholz, 2002):

$$\Delta CFF = \Delta\tau - \mu\Delta\sigma_n \tag{4.7}$$

where $\Delta\sigma_n$ is the stress change normal to the fracture plane, and μ is the coefficient of friction. Under favourable conditions, far field fractures under critical stress states can be perturbed to slip subjected to minute stress perturbations. It was reported that an incremental differential stress of < 1 MPa is sufficient to trigger seismic instabilities, and that once triggered, stress variations of at least 1 order of magnitude less (around 0.1 MPa) could sustain seismic activities (Grasso and Sornette, 1998). A statistical test indicated that a ΔCFF as low as 0.005 MPa has a significant impact in triggering mining-induced seismicity (Orlecka-Sikora, 2010).

Longwall coal mining-induced microseismicity can be considered as a sampling of fractures within the coal seam, conditional on the prevailing stress environment, coal properties and fracture attributes. The triggered microseismicity and associated energy release can be analysed in terms of the aforementioned three mechanisms: fracture abundance, fracture slip criterion, and resulting stress drop. Therefore, variations in these influencing factors lead to microseismic anomaly. Figure 4.29 demonstrates possible causes for two types of anomalous microseismicity: elevated seismic energy level and heightened microseismic intensity. The elevated seismic energy level can be significantly attributed to:

(1) large stress drop along the fracture surface during slip, which is related to strong shear strength of the fracture surface; and

(2) source-scaling heterogeneity of fractures, where the relative abundance of large fractures increases the possibility of large microseismicity.

Three possible reasons responsible for heightened microseismic intensity are:

(1) the presence of highly fracture-populated regions,

(2) weak fracture properties which lower the Mohr-Coulomb failure envelope; and

(3) high stress concentration which brings the Mohr stress circle towards the failure envelope.

This conceptual model provides new insights into the role of fracture attributes in contributing to anomalous microseismicity.

From this model, it can be seen that spatial and magnitude characteristics of microseismicity are dominated by attributes of underlying natural fractures, except that the event counts frequency is further influenced by the volume of extracted coal (or the mining intensity). Since attributes of fractures embedded in geomaterials are spatially continuous, fractures that are triggered close in time and space tend to have similar characteristics. These provide a sound physical foundation for estimating characteristics of microseismicity to be triggered during progressive coal mining, given attributes of local fractures reflected from previous microseismic records. In the context of this conceptual model, the spatial and magnitude distribution of microseismicity can be estimated solely from the most recent microseismic records. However, the impacts of fracture abundance and mining intensity on the event counts frequency need to be decoupled, and the recorded microseismicity should be interpreted in such a way that the processed data only contains information regarding attributes of local fractures. The details of a probabilistic methodology developed for forecasting of hazardous microseismicity on the basis of this improved understanding will be presented in Chapter 5.

4.7 Conclusions

Continuous microseismic monitoring was first carried out around a LTCC panel at Coal Mine Velenje over a 4-month coal production period in 2011. The analysis of 12-week long microseismic data has shown that the bi-weekly frequency-magnitude distribution of recorded microseismic events follows the Gutenberg-Richter relationship, with the b value reflecting the scaling of microseismic event magnitude. In addition, the weekly histogram of the released seismic energy follows a Gaussian distribution, which is characterised by the mean of the distribution μ, and the standard deviation σ, which are associated with the fracture sizes and size distribution, respectively. These microseismic characteristics were fairly constant during the first eight weeks monitoring period, but deviated after the advancing face approached a heterogeneous zone. Microseismic characteristics during the first eight weeks will be

simulated in a homogeneous coal seam model in Chapter 6, and those afterwards will further be modelled using heterogeneous rock strength and fracture attributes for the xylite-rich zone in Chapter 7.

Microseismic monitoring was then carried out around a central unexploited coal pillar and nine surrounding LTCC panels at Coal Mine Velenje over a 27-month coal production period during 2016-2018. The temporal, spatial and magnitude distribution of microseismicity and their evolutional characteristics around six completed longwall panels were analysed in integration with preceding stress assessment and concurrent face advance records. The following observations were made:

- Long-time mining history at the mine leads to stress accumulation around the central coal pillar, and progressive longwall mining around the central coal pillar even exacerbates the stress concentration.
- Microseismicity is mostly concentrated around extracted regions and the kidney-shaped stress concentration region within the central coal pillar, although some events can occur as far as 800 m away from the closest longwall face.
- The microseismic intensity and energy range vary from panel to panel even at the same mine, but both seismic count and energy intensive regions associated with coal mining in different panels are spatially connected.
- Microseismic event counts frequency is moderately correlated with mining intensity, while seismic energy magnitude and spatial distribution are poorly related with mining intensity.

A conceptual model has been developed to explain the aforementioned observations by interpreting mining-induced microseismicity as slippages of natural fractures in response to progressive longwall coal mining. It is believed that, although microseismicity is induced by the longwall coal mining production, its energy and spatial distribution are controlled by the attributes of natural fractures throughout the coal seam. Built upon this sound physical foundation, the conceptual model highlights the role of pre-existing natural fractures throughout the coal seam in controlling microseismic characteristics, and sheds light on possible causes of anomalous microseismicity.

The conceptual model developed will be used as the basis to develop a statistical model to characterise temporal, magnitude and spatial characteristics of microseismicity in

Chapter 5, which could then be applied to risk evaluation of hazardous events and regulation of face advance in real time.

Chapter 5 Development of a short-term statistical method to forecast microseismicity associated with longwall coal mining

5.1 Introduction

Based on the conceptual model presented in Chapter 4, this chapter presents data-driven yet physics-based methodology developed to forecast mining seismicity hazards. The physical nature of the modelling approach originates from characteristics of pre-existing natural fractures throughout the coal seam, which dominate the resulting microseismic patterns. A similar physics-based hypothesis has recently been employed to forecast the maximum magnitude of fluid injection-induced microseismicity by Afshari Moein *et al*. (2018). In addition, mining intensity which plays a significant role in affecting event counts frequency is considered by coupling real time processing of the microseismic sequence data with mining exploitation schedule in this work. The physical base of the model allows to examine respective contributions of different influencing factors to the hazard potential, and to determine the dominant factor. To take a step further, the forecasting model can be used to regulate the face advance rate of longwall coal mining in real time.

5.2 A statistical model to forecast hazardous microseismicity

The statistical forecasting model developed in the present work is built based upon the understanding that mining-induced microseismicity is considered as slippage of fractures throughout the coal seam and surrounding rock strata triggered by mining excavation. Although discrete natural fractures are heterogeneously distributed and independent of each other, they are characterised by spatial continuity in terms of attributes, i.e., two regions close to each other are likely to have similar attributes (e.g., the density, size, scaling of nature fractures, etc.) than those that are far apart (Journel

and Huijbregts, 1978). As such, the spatial continuity in geology would result in the segmental stationarity of microseismic characteristics, where statistical features of microseismicity happening close in time are relatively steady. On the other hand, anomalous variations in mining-induced microseismicity reflect variations in corresponding attributes of the fracture field, which are indicative of stress or geological heterogeneity and give pre-warnings for the increased hazard potential.

Microseismic events that are either of a large magnitude or with a short distance to working faces, are indicative of large potential of rock burst and gas outburst hazards in coal mines. This work focuses on hazardous microseismicity having large energy release and occurring close to working faces or roadways, which are the most threatening to mine workers and mining equipment. The real time forecasting of hazardous microseismicity, in this context, becomes the problem of estimating the time-varying possibility that at least one large fracture slips in the vicinity of coal extraction over a certain period, given the local fracture field and production schedule (Figure 5.1). The statistical forecasting methodology presented in this work aims at resolving this problem by continuous evaluation of microseismic features representing characteristics of the local fracture field and mining intensity.

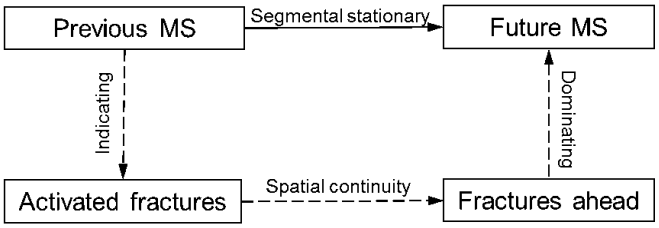


Figure 5.1 Schematic diagram illustrating the physical basis of the statistical forecasting method for hazardous microseismicity.

As the first step for the risk assessment of rock bursts and gas outbursts, a sequence of longwall face advance and the associated microseismicity are recorded as inputs of the methodology developed. Considering that geological conditions (fracture attributes in particular) and production schedule (represented by the face advance rate) are panel specific, the methodology is applied to microseismicity associated with mining at each individual LTCC panel. This requires each recorded microseismic event to be pre-classified to its closest panel in operation, which is presented in detail in Section 4.5.

The assessment of recorded sequence of microseismicity around a certain longwall panel involves filtering the most recent events using a moving time window of ΔT, assessing microseismic characteristics in a statistical manner, and using the fitted microseismic parameters as a basis for forecasting microseismicity that would occur over the next time interval Δt. This process is updated at the time interval Δt until the completion of the LTCC panel. The procedure to forecast rock burst potential at time t for the next time interval $[t, t+\Delta t]$ using microseismicity recorded in the time window $[t-\Delta T, t]$ involves the following steps.

The *fitting of distribution and parameter estimation* are first conducted for a suite of relevant characteristics such as event counts frequency, energy magnitude distribution and spatial distribution of mining-induced microseismicity within the time window. The statistical description of microseismic characteristics are described in Section 5.2.1, and parameter estimation for each statistical distribution is presented in Section 5.2.2.

Next, *estimation of probability of hazardous events* is performed based on the fitted statistical models of temporal, spatial and magnitude characteristics of microseismicity over the time window. The probability of hazardous events is regarded as the joint probability considering the aforementioned characteristics. In particular, the statistical forecasting model of event counts frequency incorporates the impact of the current face advance rate. The risk assessment of hazardous events is presented in Section 5.2.3.

In the final step, *computation of recommended upper limit of face advance* is carried out if the estimated probability exceeds a certain threshold. This is achieved by inversely calculating the face advance rate based on the statistical model of joint probability developed. A flow chart of the forecasting methodology developed is presented in Figure 5.2.

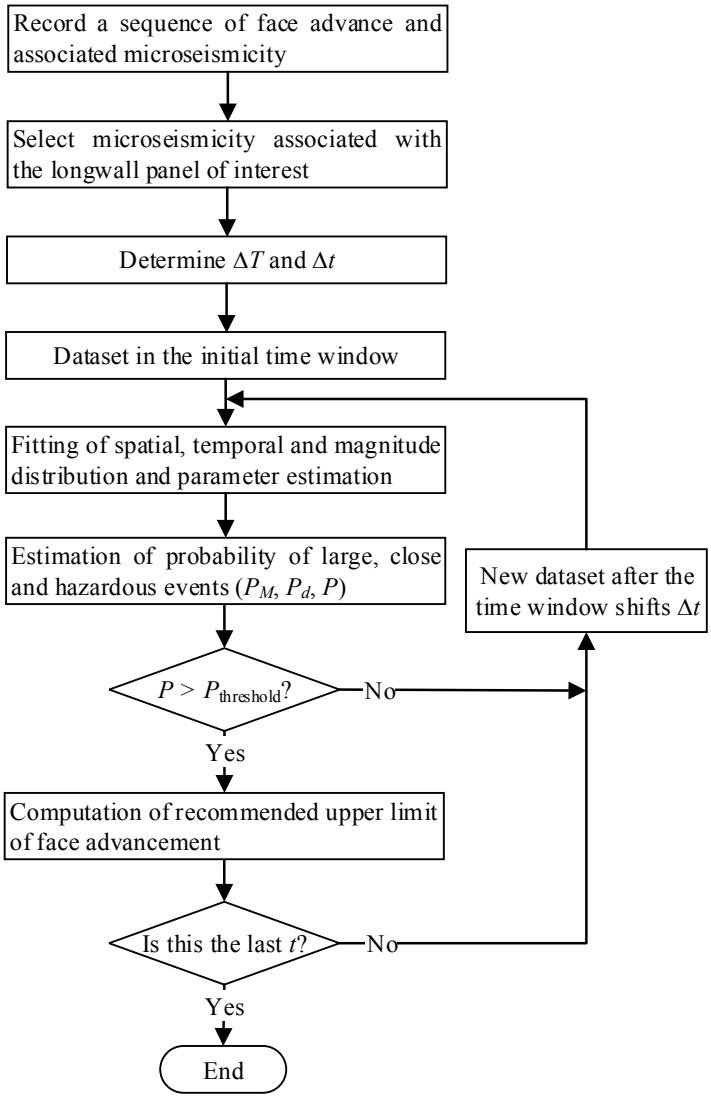


Figure 5.2. Flow chart of the forecasting procedure using longwall mining-induced microseismic sequence datasets with concurrent face advance records around a LTCC panel.

5.2.1 Spatial, temporal and magnitude distribution

Event counts frequency

Event counts is defined as the number of microseismic events occurring over a time interval of Δt. Given a constant face advance rate, the generation of microseismicity can be approximately considered as a Poisson point process, which is described by the Poisson distribution. The probability distribution function (PDF) for n microseismic events taking place over a time interval of Δt from time t is a discrete probability distribution given by:

$$p(n) = \frac{[\lambda(t)\Delta t]^n e^{-\lambda(t)\Delta t}}{n!} \tag{5.1}$$

where $\lambda(t)$ is the average event counts per unit time at time t. The evolution of $\lambda(t)$ reflects the varying abundance, or the local heterogeneity of fractures around the mining-disturbed region. Figure 5.3 presents examples of the monitored and fitted event counts frequency of microseismicity around three LTCC panels at Coal Mine Velenje. Due to the wide dispersion of the daily event counts, they are presented in groups with a bin interval of 10. It can be seen that the Poisson distribution gives a good fit to the frequency of daily microseismic event counts around each panel.

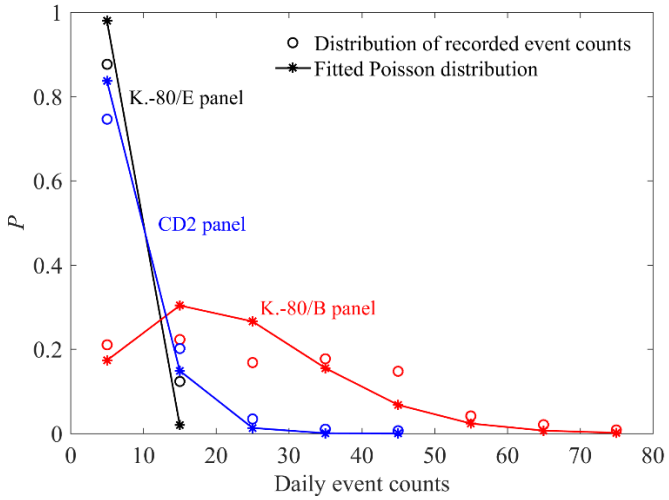


Figure 5.3. Frequency of daily microseismic event counts associated with longwall coal mining at three LTCC panels at the -80 m level at Coal Mine Velenje (the connecting lines are only guides for the eye).

Equation (5.1) can be used to forecast the frequency of daily event counts to be induced under the same mining conditions (represented by the face advance rate). Since mining operation is a dynamic process, the ever-varying face advance rate should be accounted for in forecasting event counts. Based upon the analysis from Section 4.5, the face advance rate has a positive correlation with the number of recorded microseismicity, owing to the physical nature that the area of mining-disturbed region is linearly correlated with the number of slipped fractures for a relatively homogeneous fracture field. Therefore, a ratio η, defined as the face advance rate r during the next time interval over the average rate $\bar{r}$ during the previous monitoring period, should be used as a tuning coefficient in estimating the event counts frequency:

$$\eta = r / \bar{r} \tag{5.2}$$

The modified PDF can be used to estimate the frequency of microseismic event counts over the next time interval Δt by fitting microseismic data within the time window of ΔT:

$$p(n) = \frac{[\eta\lambda(t)\Delta t]^n e^{-\eta\lambda(t)\Delta t}}{n!} \tag{5.3}$$

The most probable seismic event count over the next time interval Δt is forecasted as $\eta\lambda(t)$.

Energy magnitude distribution

The magnitude distribution of microseismic energy released is dominated by the size and scaling of slipped fractures. According to the Gutenberg-Richter law, the cumulative number N of microseismicity with an energy release greater than E is:

$$\log_{10} N = a - bM \tag{5.4}$$

where $M = \log_{10} E$.

Considering that there is a minimum energy magnitude $M_{\min}$ for field microseismic monitoring data due to the limited energy detection range of the geophones, the aforementioned relationship can be re-arranged to the following form:

$$\log_{10} N = a - b(M - M_{\min}) \tag{5.5}$$

The cumulative distribution function (CDF) of the frequency-magnitude relationship takes the form of exponential distribution:

$$F(M) = 1 - (E_{\min} / E)^{b(t)} \quad (M \geq M_{\min}) \tag{5.6}$$

where $b(t)$ is a constant at time t.

It was found that the Weibull distribution achieves a better fit than exponential distribution to empirical distribution of logarithmical seismic energy (Kijko et al., 1993; Lasocki, 1993a). The PDF and CDF of the Weibull distribution are given by:

$$f(M) = \frac{k_e(t)}{l_e(t)} \left[\frac{M - M_{\min}}{l_e(t)} \right]^{k_e(t)-1} \exp\left[-\left(\frac{M - M_{\min}}{l_e(t)} \right)^{k_e(t)} \right] \quad (M \geq M_{\min}) \tag{5.7}$$

$$F(M)=1-\exp\left[-\left(\frac{M-M_{\min}}{l_e(t)}\right)^{k_e(t)}\right] \quad (M \geq M_{\min}) \tag{5.8}$$

where $k_e(t)$ and $l_e(t)$ are shape and scale parameters at time t, respectively.

The CDF of the energy magnitude distribution can be fitted using microseismic data within the time window of ΔT to estimate the probability of a microseismic event with energy greater than a threshold over the next time interval Δt. Figure 5.4 presents examples of the frequency-magnitude distribution and fitted Weibull distribution for field microseismic monitoring data at Coal Mine Velenje (the minimum detectable energy is around 10^2 J so $M_{\min} = 2$).

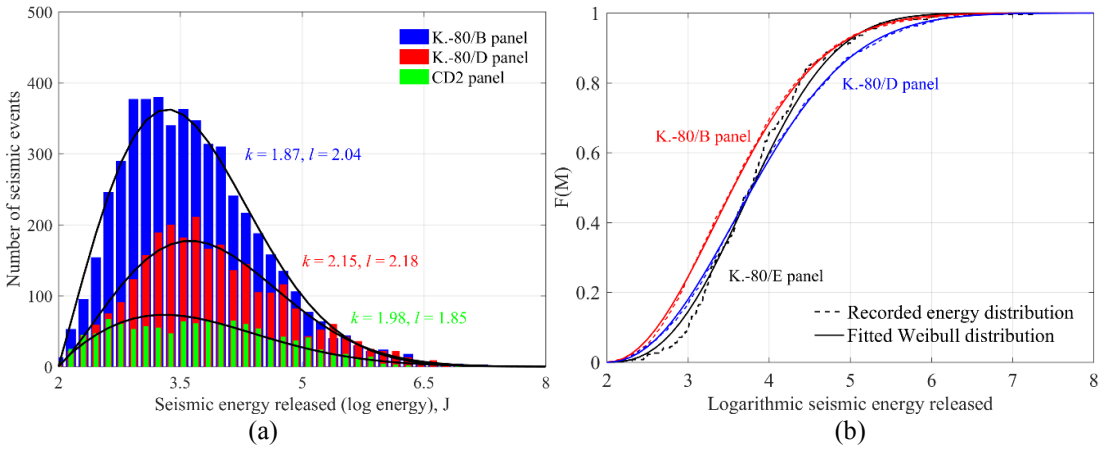


Figure 5.4. Examples of recorded and fitted energy magnitude distribution for mining-induced microseismic events around different LTCC panels at Coal Mine Velenje: (a) histograms, and (b) cumulative distribution.

Distance to the face-line position

The location of microseismicity reflects the spatial distribution of pre-existing natural fractures to a large extent. Given the same mining and stress conditions, the spatial clustering of microseismicity is attributed to the heterogeneous distribution of fractures. In this work, the distance of microseismicity to the face-line is introduced to represent the spatial distribution of underlying natural fractures. Spatial clustering of a group of microseismic events can be characterised by a tall and thin histogram of distances to the face-line, while relatively homogeneous distribution of microseismicity yields a squat and fat histogram. Since microseismicity tends to cluster at fracture-intense regions, the average distance of microseismicity to the face-

line dynamically changes with the advancing longwall face. A decrease in the average distance of microseismicity to the face-line suggests a higher chance of microseismicity occurring close to the longwall face as the mine production progresses, while an increase indicates the opposite.

Similar to the microseismic energy magnitude distribution, the spatial distribution of microseismicity with respect to the face-line is a continuous probability distribution and can be described by the Weibull distribution. The CDF is written as:

$$F(d) = 1 - \exp\left[-[d / l_{\mathrm{d}}(t)]^{k_{\mathrm{d}}(t)}\right] \tag{5.9}$$

where $k_{\mathrm{d}}(t)$ and $l_{\mathrm{d}}(t)$ are shape and scale parameters at time t, respectively.

The CDF of the spatial distribution of microseismicity with respect to the face-line can be fitted using microseismic data within the time window of ΔT to estimate the probability of a microseismic event falling within a certain distance to the face-line over the next time interval Δt. Figure 5.5 presents examples of the spatial distribution with respect to the face-line and fitted Weibull distribution for field recorded microseismicity at Coal Mine Velenje. The distribution in the histograms for the three panels in Figure 5.5a is skewed, with the peak located from 40 to 200 m from the longwall face. The histograms suggest that microseismic events associated with coal mining at K.-80/B and K.-80/D panels are more spatially concentrated, while those at CD2 panel are much more scattered, which is consistent with the observations presented in Section 4.5.1. The Weibull distribution is well-adapted to different histograms and fits the general trend well.

5.2.2 Parameter estimation

Considering that the statistical models describing microseismic characteristics are known, the maximum likelihood method is applied to estimate relevant parameters. The method consists of calculating the maximum likelihood function, which is considered as the joint probability for sampling the set of observations. The parameters are estimated by maximising the likelihood function of the known distribution, given a sample of observations. This method can be applied for fitting either observations such as seismic event counts to discrete probability distributions, or observations such as energy magnitude distribution and spatial distribution to continuous probability distributions.

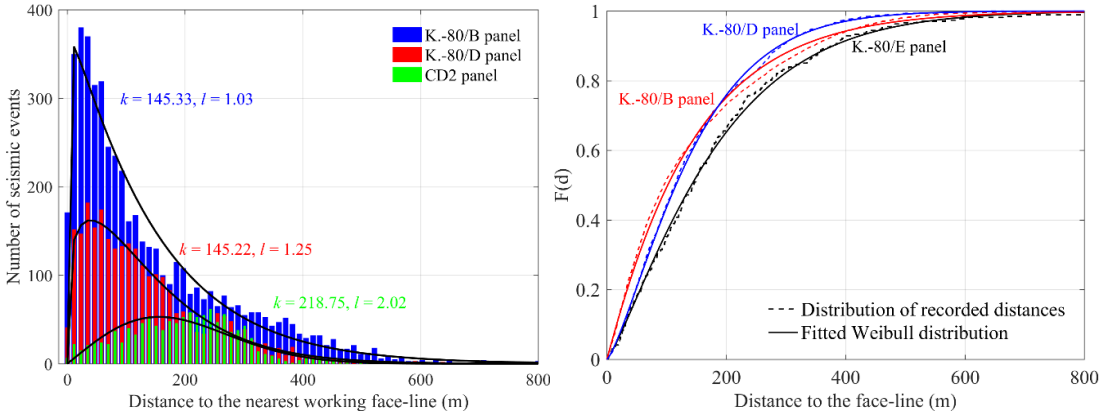


Figure 5.5. Examples of recorded and fitted spatial distribution with respect to the face-line for microseismic events around different LTCC panels at Coal Mine Velenje: (a) histograms, and (b) cumulative distribution.

The logarithmic maximum likelihood function for seismic event counts is the sum of the logarithmic probability for each individual observation:

$$L\left(\lambda|n_1,n_2,\ldots,n_m\right)=\sum_{i=1}^{m}\ln[p(n_i\mid\lambda)] \tag{5.10}$$

where m is the number of time intervals within the time window, n_1, n_2, …, n_m are seismic event counts over each time interval Δt in the time window, and $p(n_i \mid \lambda)$ is the probability that n_i seismic events take place within a time interval Δt.

The average seismic event count λ could be estimated by solving the equation:

$$\frac{\partial L\left(\lambda|n_1,n_2,\ldots,n_m\right)}{\partial\lambda}=0 \tag{5.11}$$

The logarithmic maximum likelihood function for the energy magnitude distribution is given by:

$$L\left(k_e,l_e|M_1,M_2,\ldots,M_n\right)=\sum_{i=1}^{n}\ln[f(M_i\mid k_e,l_e)] \tag{5.12}$$

where n is the seismic event counts, and $f(M_i \mid k_e,l_e)$ is the probability that a seismic event has a magnitude of M_i.

Both shape and scale parameters k_e and l_e need to be estimated from the set of recorded seismic magnitudes, so the partial derivatives of the likelihood function with respect to each parameter are taken to form a system of equations:

$$\begin{cases} \dfrac{\partial L\left(k_e, l_e | M_1, M_2, \ldots, M_n\right)}{\partial k_e} = 0 \\ \dfrac{\partial L\left(k_e, l_e | M_1, M_2, \ldots, M_n\right)}{\partial l_e} = 0 \end{cases} \tag{5.13}$$

Likewise, the parameters for the spatial distribution of microseismicity with respect to the face-line can be estimated. The estimated parameters for the fitted distributions are considered to represent attributes of slipped fractures during [t-ΔT, t], and used to approximately represent attributes of fractures to be reactivated under the same mining conditions over the next time interval, due to the spatial continuity of geological conditions.

5.2.3 Risk assessment of hazardous events

As suggested by previous researchers (Lasocki, 1993a) and observations reported in Section 4.5, the spatial distribution of fractures, attributes of fractures, and mining activities can be considered as mutually independent. In particular, mining progression influences the area of extracted regions and in turn the number of slipped fractures per unit time, but not the size and scaling of fractures. Therefore, it is justified to estimate the probability of hazardous microseismicity as the joint probability of event occurrence, the probability of an event being a large event, and the probability of an event being close to the longwall face.

The probability that at least one event with a magnitude greater than M occurs in n microseismic events is written as:

$$p_M = 1 - F(M)^n \tag{5.14}$$

Considering the estimated event counts frequency from the Poisson distribution for field microseismic monitoring data over the most recent period ΔT, the probability that at least one event with a magnitude greater than M occurs over the next time interval Δt is:

$$P_M = \sum_n p(n)\left[1 - F(M)^n\right] \tag{5.15}$$

Likewise, the probability that at least one event with a distance less than d to the face-line occurs over the next time interval Δt is written as:

$$P_d = \sum_n p(n)\left[1-(1-F(d))^n\right] \tag{5.16}$$

In this work, a hazardous event is defined as a microseismic event with released energy greater than M and falling within a distance of d to the face-line. The probability of an individual seismic event being a hazardous event is the joint probability considering both the spatial and magnitude distributions:

$$p = [1-F(M)]F(d) \tag{5.17}$$

The probability that at least one hazardous event occurs over the next time interval Δt is:

$$P = \sum_n p(n)\left[1-(1-p)^n\right] \tag{5.18}$$

Given a threshold for the probability of hazardous microseismicity, the inverse calculation of face advance can be achieved by combining equations (5.3) and (5.18).

5.3 Application of the forecasting methodology at Coal Mine Velenje

The forecasting methodology developed was applied to longwall coal mining-induced microseismicity recorded during 2016-2018 at each of three completed LTCC panels (panels K.-80/B, K.-80/D and K.-80/C), which were considered to have a complete record of mining-induced microseismicity and consist of a relatively large number of events (>2,500 events each).

The length of time window ΔT needs to be determined based on the event rate and mining schedule. Segmental stationarity needs to be achieved for microseismicity within this interval to give a reliable estimation of parameters. In this sense, the interval should be sufficiently long to allow for mining-induced stress adjustment and re-equilibrium. As a reference, the time needed for microseismicity to fade out after mining completion or to achieve normal levels of seismicity after re-operation was around 1 week, according to the observations reported in Section 4.5 and literature (Styles *et al.*, 1988). On the other hand, the time window should be constrained in length in order not to compromise the capability to reflect local variability of mining

conditions and indicate anomalous variations in seismic activities in time. Based on reported field observations (McKavanagh and Enever, 1980; Styles *et al*., 1988), the time between the first notice of anomalous changes in microseismicity patterns and visible macroscopic failure or even rock bursts and outbursts span over a wide range from 10 minutes, several hours, several days, to up to 17 days. As such, a ΔT of 14 days was used in this work, which covers microseismicity recorded over the last 10 working days. During holidays, when coal extraction was halted for a longer time, ΔT was extended to cover the last 10 working days to avoid the unfavourable impact of scarcity in recorded microseismicity. The forecasted probability of hazardous microseismic events was updated on a daily basis (Δt = 1 day) as a reference in order for a timely evaluation of the hazard potential.

Due to the local clustering of fracture distribution, it could be postulated that among microseismic events in the time window, those occurring more recently are more important. Lasocki (1993a) used a temporal exponential weighting metric which assigns larger weights to those taking place close to the next day in time. To account for the spatial clustering, a space and time weighting metric was used which is a spatial distance weighted by the product of a time constant and the time difference between the occurrence of events (Kijko *et al*., 1993; Jian-po Liu *et al*., 2018). Since it is rather difficult to accurately determine the weighting metric, all the microseismic events in the time window were assigned the same weights in this work.

Following the procedure described in Section 5.2, the probability of hazardous microseismicity and recommended upper limit of face advance were updated for each day from 14 days after the start of coal production until abandonment for each panel.

5.4 Results and analysis

Figure 5.6 presents the correlation between event counts frequency, seismic energy and spatial distribution of microseismicity for the three LTCC panels. It can be seen that very low correlation coefficient is obtained for each variable pair, indicating that each variable is barely influenced by, or at least very weakly correlated with the other two variables. As such, the density, size and scaling, and spatial distribution of fractures around the three longwall panels are verified to be mutually independent, and it is practically feasible to employ the joint probability for hazardous microseismicity forecasting.

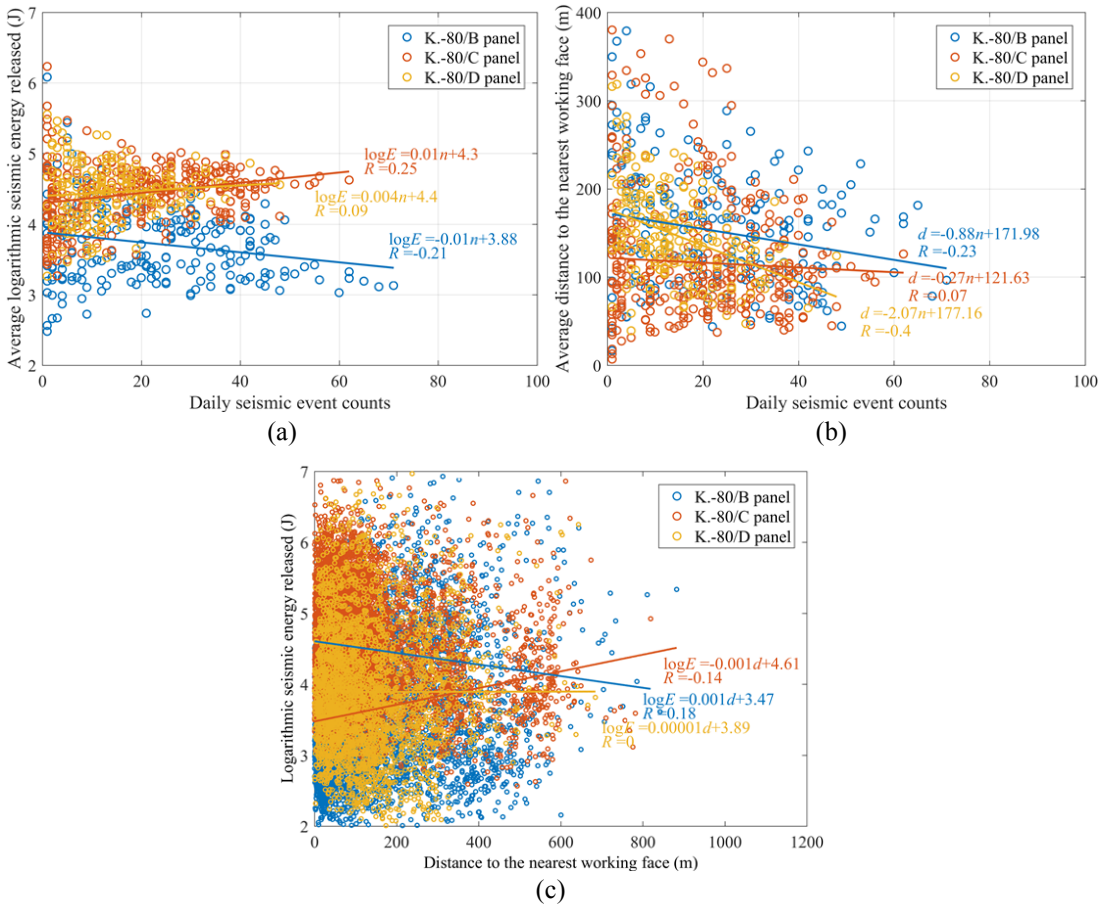


Figure 5.6. Independence between the daily seismic event rate, average seismic energy released, and spatial distribution of recorded microseismicity around three longwall panels at Coal Mine Velenje.

Figure 5.7 presents three examples of temporal, magnitude and spatial distributions of recorded microseismicity within the time window associated with longwall mining around K.-80/D panel. These microseismic characteristics within each time window manifest segmental stationary. The distributions proposed could still describe characteristics of microseismicity within the moving time window, with good fitting performances achieved for microseismicity around each panel. As can be seen from the figure, microseismic characteristics within time windows 23/03-06/04/2016 and 05/07-18/07/2016 are similar, but the average daily event count increases, and both energy magnitude distribution and spatial distribution with respect to the face-line shift to the lower end during the time window 02/09-15/09/2016, indicating the variation of local fracture attributes around K.-80/D panel.

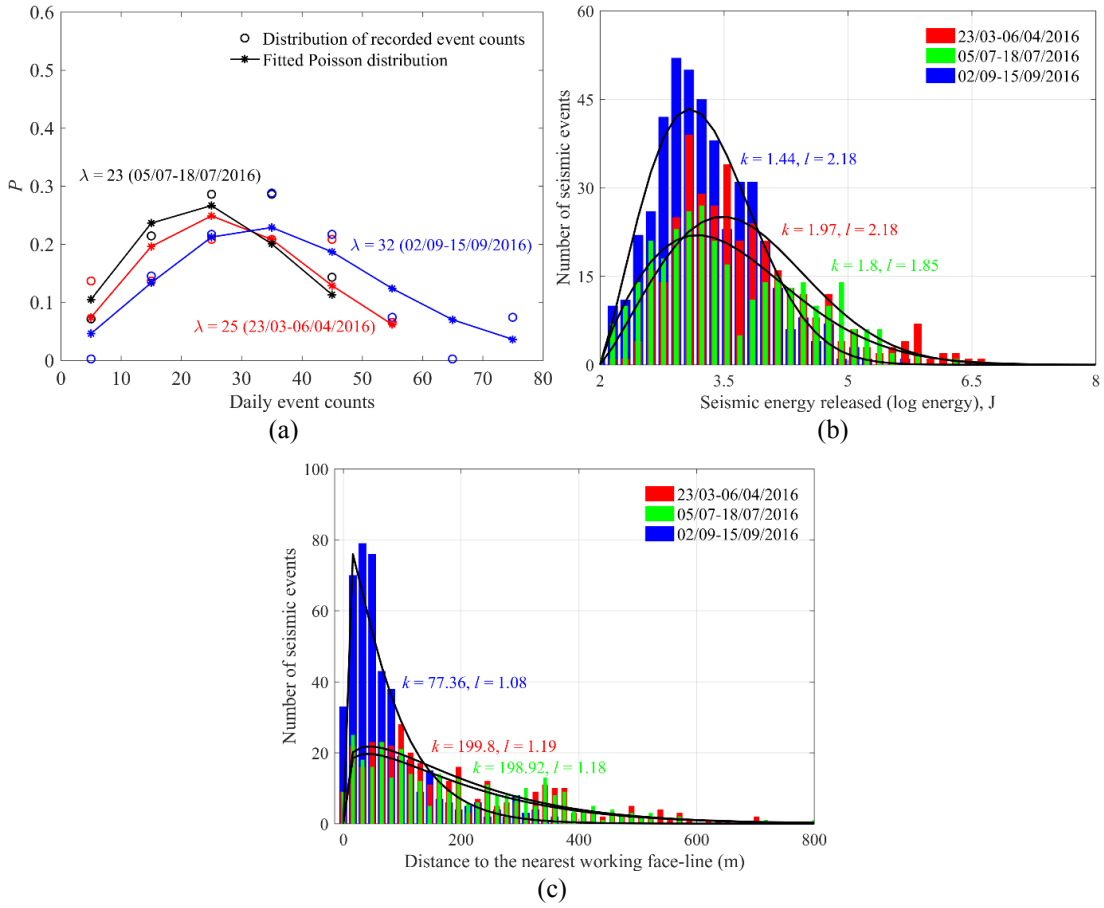


Figure 5.7. Temporal, magnitude and spatial distributions of field monitored microseismicity within the time window around K.-80/D panel: (a) daily event counts frequency (the connecting lines are only guides for the eye), (b) energy magnitude distribution, and (c) spatial distribution with respect to the nearest longwall face in operation.

It is noted that, although fitted magnitude and spatial distribution of recorded microseismicity represent those of fractures, the daily microseismic event count needs to be disentangled from the impact of mining intensity to reveal the abundance of fractures around the longwall panel. To do so, the average daily event count within the time window was scaled by assuming that the longwall panel is mined at a constant face advance rate. The face advance rate ratio used is the average face advance rate within the time window over the average face advance rate during the whole monitoring period for the corresponding LTCC panel.

Figure 5.8 - Figure 5.10 present the time-varying scaled daily event count, the probability of a single microseismic event being a large event, and the probability of a single microseismic event being close to the face-line, based on fitted distributions for microseismicity within the moving time window around the three longwall panels.

This figure represents the dynamic evolution of abundance, magnitude and spatial distribution of fractures around the panels as longwall faces advance. The curves are fairly continuous, which verifies that attributes of fractures around longwall panels reflected from the recorded microseismicity are spatially continuous.

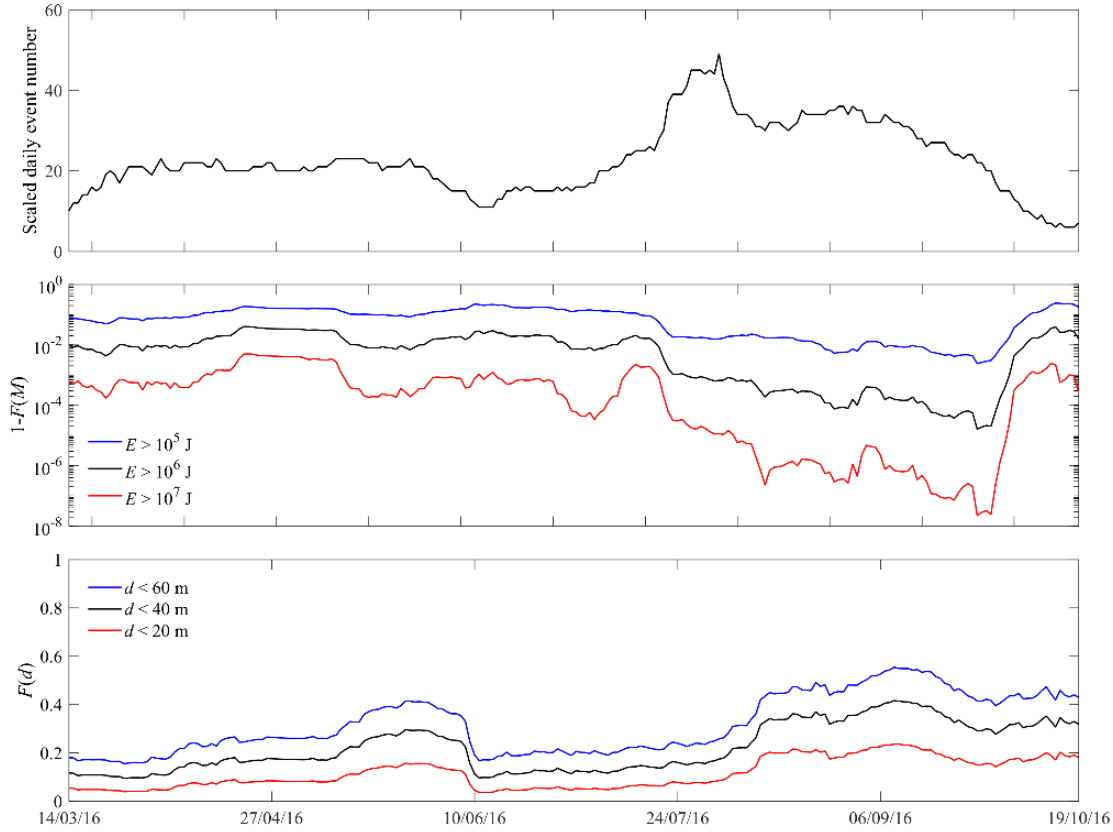


Figure 5.8. Time-varying temporal, magnitude and spatial seismic indicators decoupled from mining activities for microseismicity around panel K.-80/B. (Scaled daily event number under the average face advance rate represents the density of underlying fractures; the probability of a single microseismic event being a large event reflects the size distribution of underlying fractures; the probability of a single microseismic event being close to the longwall face reveals the spatial distribution of underlying fractures.)

Although the three longwall panels are adjacent to each other, their fracture attributes manifest different features. The abundance of local fractures around K.-80/B panel remains fairly steady in the first four months of coal production, stays at a heightened level between 18/07-15/10/2016, and decreases below the normal level afterwards. The abundance of fractures around K.-80/D panel is also steady in the first three months of coal production, but then gradually increases around fivefold by the completion of the panel. By contrast, the local fracture density around K.-80/C panel

is continuously steady after achieving normal levels of seismicity. The fracture size distribution is mostly stable for all three longwall panels, with reduced risks of large events in some periods, such as 18/07-15/10/2016 for K.-80/B panel and 30/08-15/10/2016 for K.-80/D panel.

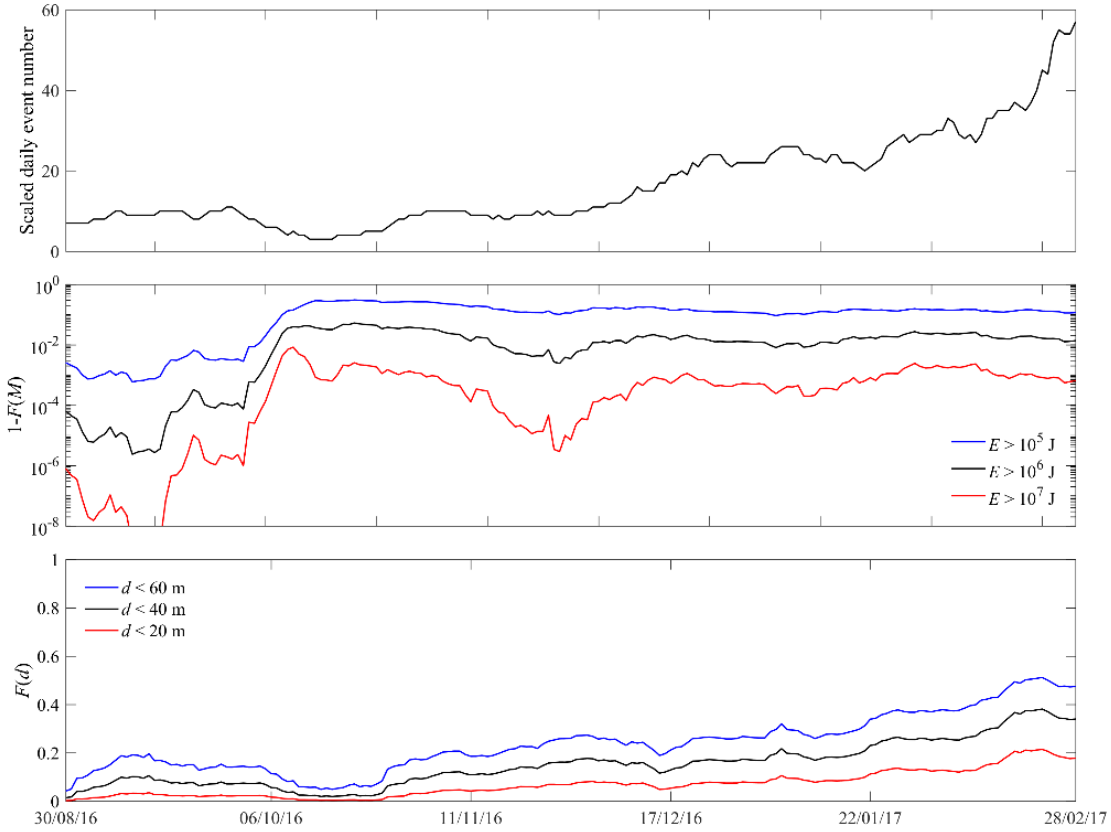


Figure 5.9. Time-varying temporal, magnitude and spatial seismic indicators decoupled from mining activities for microseismicity around panel K.-80/D. (Scaled daily event number under the average face advance rate represents the density of underlying fractures; the probability of a single microseismic event being a large event reflects the size distribution of underlying fractures; the probability of a single microseismic event being close to the longwall face reveals the spatial distribution of underlying fractures.)

It is interesting to note that the probability of a single microseismic event being close to the face-line shows a general increasing trend for each of the three panels during coal production, which results from the shift of a squat and fat to a tall and thin distribution of the distance to the face-line (Figure 5.7c). This change indicates elevated levels of spatial clustering of fractures, since all the three longwall faces were advancing towards the central coal pillar with high stress concentration.

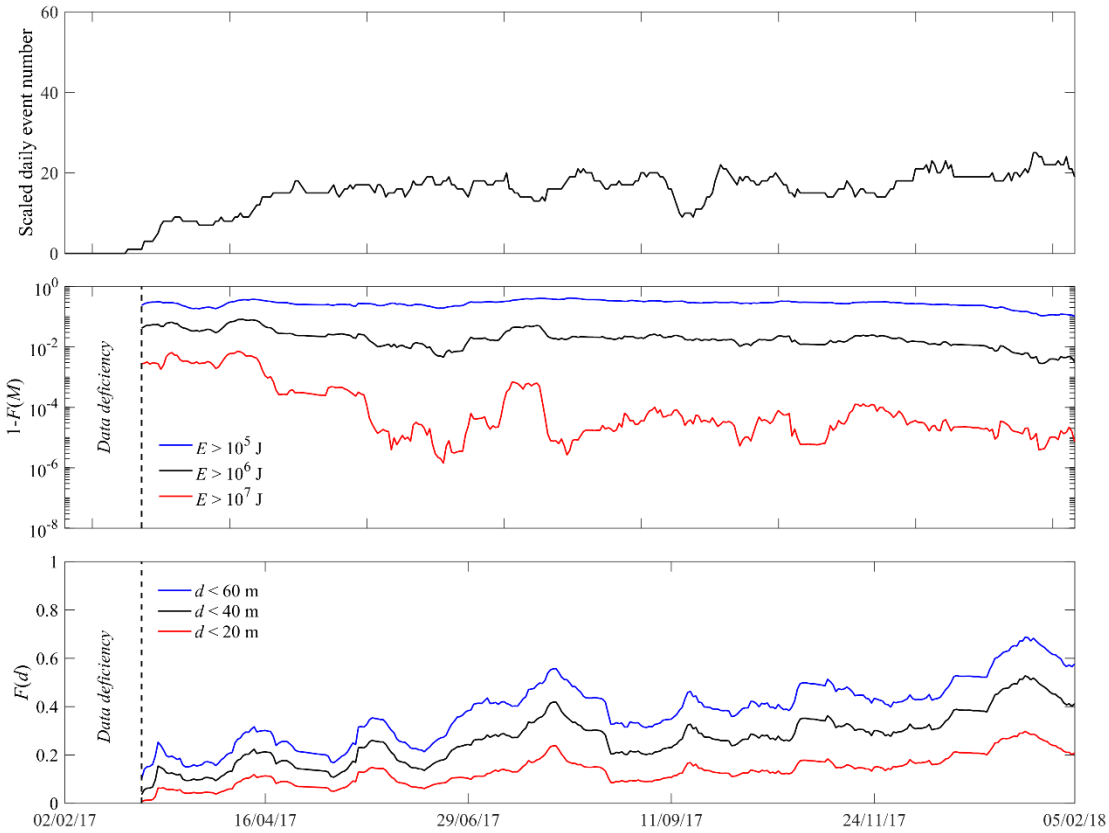


Figure 5.10. Time-varying temporal, magnitude and spatial seismic indicators decoupled from mining activities for microseismicity around panel K.-80/C. (Scaled daily event number under the average face advance rate represents the density of underlying fractures; the probability of a single microseismic event being a large event reflects the size distribution of underlying fractures; the probability of a single microseismic event being close to the longwall face reveals the spatial distribution of underlying fractures.)

Figure 5.11 - Figure 5.13 present the time-varying forecasted daily event number, and probability that large microseismicity, microseismicity close to the working face, and hazardous microseismicity occur on the day of forecasting for the three LTCC panels. Recorded daily numbers of total microseismic events, large events, events close to the working face, and hazardous events are plotted respectively for validation.

The forecasted daily event counts from the statistical model show excellent agreement with recorded numbers of microseismicity, with large event counts being forecasted at high face advance rates, and no events being forecasted when the coal production ceases.

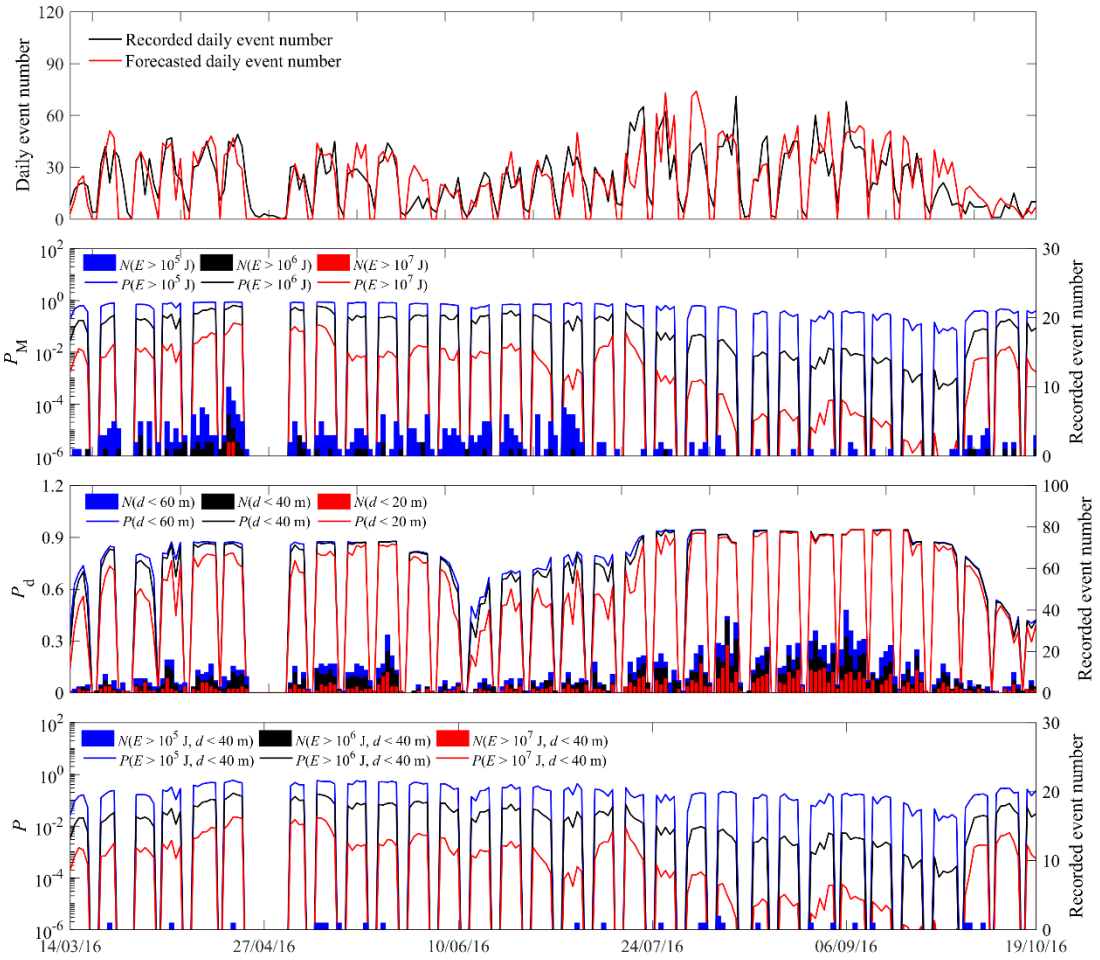


Figure 5.11. Time-varying forecasted daily event number, and forecasted probability that at least one large microseismic event, a microseismic event close to the face-line, and a hazardous microseismic event occurs on the day of forecasting around panel K.-80/B.

The forecasted probability of large microseismicity P_M, which was estimated according to Equations (5.3) and (5.15), approximately follows the general trend of 1-$F(M)$ in Figure 5.8 - Figure 5.10. The face advance rate on the day of forecasting affects the forecasted probability by tuning the forecasted event counts. When the coal production ceases at weekends or during holidays, the probability of large microseismicity is forecasted as 0 since the forecasted event count is 0. By comparison to b values analysis for weekly microseismicity around the corresponding panel in Section 4.5.3, the evolution of P_M and b values display distinctly opposite trends, which verifies that the decrease in the b value indicates an increase in the large event risk. The forecasted probability for microseismicity with an energy released greater than 10^5 J mostly stays at a high level above 70% on working days for all three longwall panels, and it can be seen that these events are quite common. By contrast,

the forecasted probabilities for microseismicity at energy levels of 10^6 and 10^7 J show a tremendous decrease of several orders of magnitude, and such events are much less frequent. As can be seen from Figure 5.11, when the forecasted probability of microseismicity with $E > 10^7$ J around the K.-80/B panel reaches a peak of 6.5% and 12.9% on 19 and 20 April 2016, four such large microseismic events occurred around the same panel, two on each of those two days, respectively.

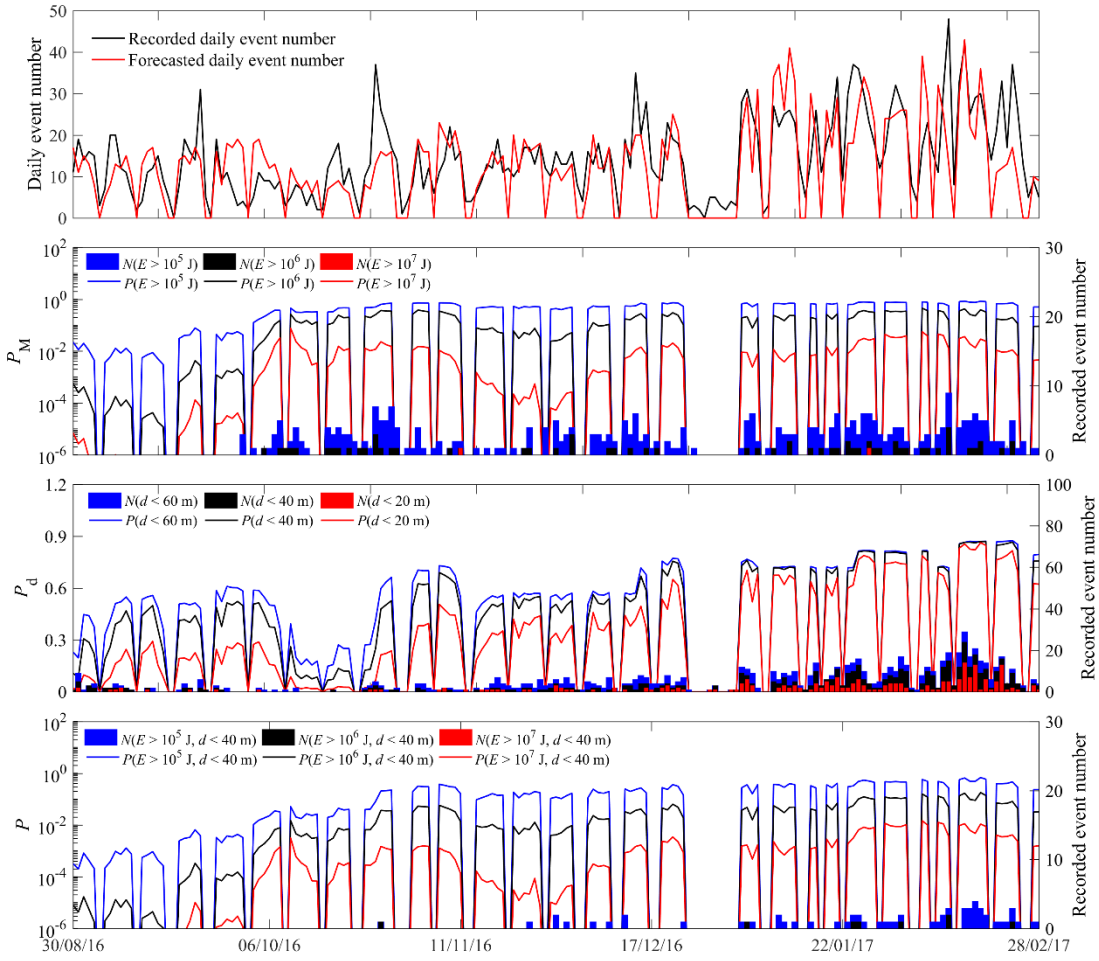


Figure 5.12. Time-varying forecasted daily event number, and forecasted probability that at least one large microseismic event, a microseismic event close to the face-line, and a hazardous microseismic event occurs on the day of forecasting around panel K.-80/D.

The forecasted probability of microseismicity close to the working face, which was estimated according to Equations (5.3) and (5.16), approximately follows the general trend of $F(d)$ in Figure 5.8 - Figure 5.10. This forecasted probability was also tuned by the face advance rate ratio. Considering the spatial distribution of microseismicity

(Figure 5.5), microseismicity close to the working face are not as rare as large microseismicity. For all three longwall panels, more microseismicity were recorded close to the working face when the statistical model estimates a higher probability of such events. As an example, the statistical model estimates the probability that at least one microseismic event occurs close to the working face to be above 90% on working days between 25/07-23/09/2016 around K.-80/B panel, and the forecasted probabilities of microseismicity with $d < 60$ m, $d < 40$ m and $d < 20$ m have little differences. This is verified by recording a large number of microseismicity within 20 m distance to the K.-80/B face during these dates.

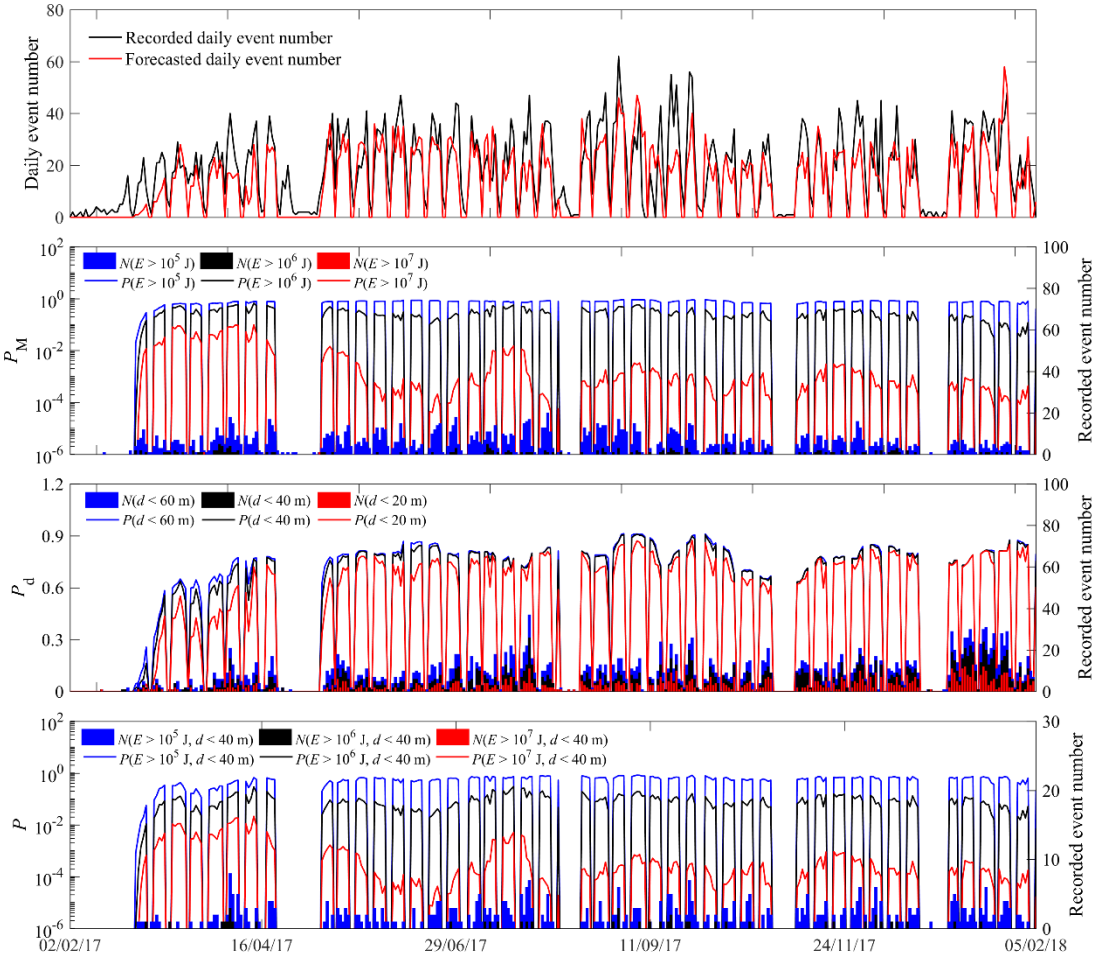


Figure 5.13. Time-varying forecasted daily event number, and forecasted probability that at least one large microseismic event, a microseismic event close to the face-line, and a hazardous microseismic event occurs on the day of forecasting around panel K.-80/C.

The forecasted probability of hazardous microseismicity, which was estimated according to Equations (5.3) and (5.18), depends on all three aforementioned forecasted results. In this forecasting, events within 40 m distance to the working face and having energy greater than 10^5, 10^6 and 10^7 J are considered as hazardous microseismicity. The forecasted time-varying probability of hazardous microseismicity closely follows the variation of that of large microseismicity (P_M) for all three longwall panels, which means that the forecasting result is dominated by the impact of magnitude distribution of recorded microseismicity. By contrast, the forecasted probabilities of hazardous microseismicity for all three longwall panels are around one order of magnitude lower than those of large microseismicity with the same energy. As a result, only a few microseismicity with $E > 10^6$ J and $d < 40$ m and no microseismicity with $E > 10^7$ J and $d < 40$ m were recorded around the three longwall panels over the coal production period.

To optimise real-time control of longwall coal mining based on the probability forecasting, the recommended face advances for the three longwall panels were calculated over the coal production period, using three probability limits (1%, 0.1% and 0.01%) for hazardous microseismicity ($E > 10^7$ J and $d < 40$ m), as shown in Figure 5.14. Due to the large span of fracture sizes obeying the power law distribution, the back-calculated upper limits of daily face advance fluctuate greatly at a linear scale from day to day. While a probability limit of 0.01% prohibits longwall mining over a considerable portion of the production period, probability limits of 0.1% and 1% allow higher face advance rates over the period of high hazard risk for the three longwall panels. It is believed that, the face advance rates back-calculated using site specific definition of hazardous microseismicity and probability thresholds can be used as a reference in adjusting the mine production schedule.

5.5 Discussion

In the present work, a probabilistic approach combining temporal, magnitude and spatial microseismic characteristics is used in forecasting hazardous microseismicity in longwall coal mining. The methodology was demonstrated using long term monitored data for three LTCC panels at Coal Mine Velenje. This methodology is advantageous in that the estimated probability is given in the form of a joint probability, which allows for quantifying the respective contribution of each influencing factor. The results have important implications for seismic hazard assessment in field sites

which keep track of face advance with concurrent monitoring of mining-induced microseismicity. The feasibility and efficiency of this statistical forecasting methodology are highly dependent on the volume and quality of source microseismicity data. For example, the gap of estimated probabilities at the start of LTCC mining around K.-80/C panel in Figure 5.10 results from the scarcity of recorded microseismic events. To obtain reliable forecasting results based on microseismic monitoring data, possible sources of error need to be controlled in the whole process from field monitoring, pre-processing to data analysis. In field monitoring, geophones with large energy detection ranges are favourable to avoid incomplete sampling of microseismicity, and thus an incomplete representation of local fractures. To obtain microseismic events associated with the longwall panel of interest, great effort needs to be devoted to the proper pre-processing of recorded raw data, including pickup of events, filtering out irrelevant events, and classification of events. In data analysis, an appropriate length of time window needs to be determined to ensure that the segmental stationary of microseismicity can be achieved within that time window.

The statistical model developed could well represent time-varying temporal, magnitude and spatial microseismic characteristics, based on which a fairly satisfactory forecasting results can be achieved. However, it should be borne in mind that the forecasted results of large microseismicity from this statistical model is very sensitive to statistical variations due to small samples of large microseismicity. It can be seen from Figure 5.10 that, while the estimated 1-$F(M)$ for events with $E > 10^5$ J is fairly stable over the coal production period, that for events with $E > 10^7$ J has a larger fluctuation spanning over three orders of magnitude. Consequently, the recommended upper limit of daily face advance has a large degree of fluctuation. This is because given the large population of not so large seismic events (at 10^5 J energy level) and small population of very large ones (at 10^7 J energy level), the relative abundance of the former tends to be steady over the coal production period, while that of the latter is susceptible to fluctuations in the recorded number of such events. Therefore, albeit the results obtained are statistically correct, they are susceptible to biases caused by inaccurate source data, in particular the recorded number of large microseismicity. However, the occurrence of large mining-induced microseismicity is not frequent, and it can be hard to obtain very complete records of large microseismicity due to limits

of technical and mining conditions in some mining fields. It is thus suggested that geological surveys and a geophysical exploration are conducted before longwall mining to reveal strong fracture heterogeneity regions, which can significantly contribute to the knowledge of the local fracture field and supplement the hazard assessment using recorded microseismicity.

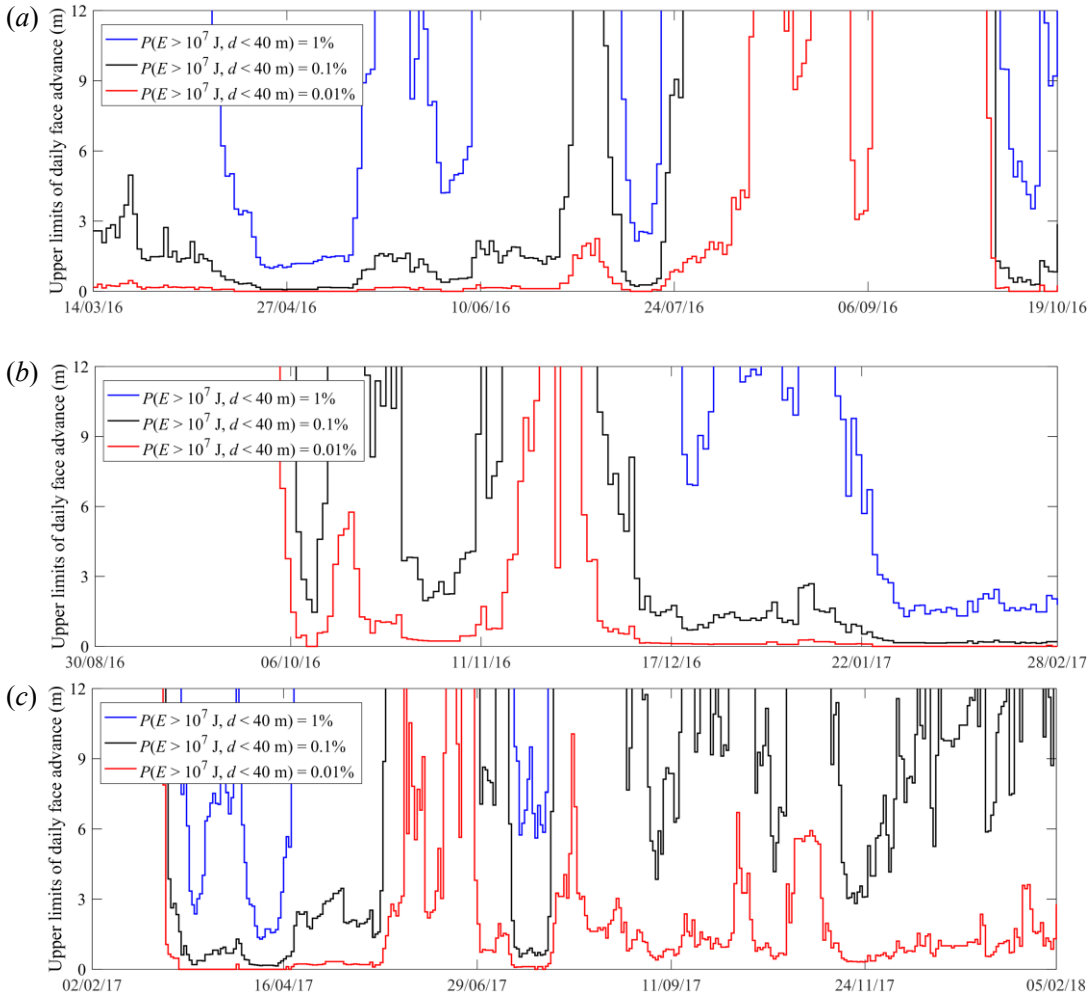


Figure 5.14. Recommended upper limits of daily face advance given probability thresholds of hazardous events for (a) panel K.-80/B, (b) panel K.-80/D, and (c) panel K.-80/C.

The statistical method provides a probabilistic perspective to the evaluation of hazard risks. However, the method does not explicitly consider the impact of stress environment and coal properties, and it lacks a stress change perspective to forecast the generation of an individual microseismic event. Thus, the inherent weakness of this method is that it could not identify the most probable location of potential hazards. To address this problem, hazardous regions should be analysed and identified using a

mechanical approach by reference to the physical mechanism, which is that fracture slippage is susceptible to be triggered under critical stress states (Grasso and Sornette, 1998; Harris, 1998; Marcak and Mutke, 2013; Orlecka-Sikora *et al*., 2012).

5.6 Conclusions

Based on the relationship between fracture attributes, longwall coal mining and mining-induced microseismicity elaborated in Chapter 4, the probability that at least one hazardous microseismic event occurs over the next time interval is considered as the joint probability considering the event counts frequency, energy magnitude distribution and spatial distribution with respect to the longwall face. In this chapter, a statistical model to characterise microseismicity, which considers the event counts frequency to obey a Poisson distribution, and both energy magnitude distribution and spatial distribution with respect to the longwall face to follow a Weibull distribution, was developed. Based on the segmental stationarity of microseismicity (the spatial continuity of fracture attributes in essence), the probability of hazardous microseismicity could be estimated from fitted distributions of microseismic characteristics using recent microseismic sequence datasets and face advance records. On this basis, time-varying hazard risks could be evaluated by daily update of the fitted statistical model of microseismicity within a moving time window. The statistical model developed was applied to forecast the potential for hazardous microseismicity for three longwall panels at Coal Mine Velenje. Upper limits of daily face advance for these LTCC panels were obtained based on forecasted microseismicity risk.

Results have shown that the forecasted daily event counts are in excellent agreement with recorded ones. The increase of forecasted probability of large microseismicity is consistent with the decrease of *b* values for weekly microseismicity. The high forecasted probabilities for large microseismicity and microseismicity within a short distance to the face-line were verified by high recorded numbers of such events. Results suggest that the energy magnitude distribution of microseismicity plays a dominant role in the potential for hazardous microseismicity. This statistical model using microseismic monitoring data has important implications in the evaluation of mining-induced hazards and optimal control of longwall face advance in burst-prone deep-level mining sites.

Chapter 6 A DFN-based model to simulate microseismicity associated with longwall mining

6.1 Introduction

In this chapter, a microseismicity modelling approach, developed based on the shear slip mechanism of mining-induced microseismicity, which is applicable to longwall coal mining, is presented. This approach makes use of the built-in discrete fracture network (DFN) capability in the commercial software FLAC^{3D} to form stochastically distributed hypocentres for generating synthetic seismic events in a 3D continuum model. After each longwall face advance, deterministic global elastoplastic stress analysis is first performed, followed by evaluation for fracture slip at all discrete fractures. The released energy from a microseismic event is estimated by considering both the fracture size and stress drop along the fracture surface. A distinctive feature of the developed methodology is the use of a strain-softening constitutive model to better represent the effect of plastic zones around underground openings on microseismicity distributions. This model provides a tool for numerical interpretation of longwall coal mining-induced microseismicity, and its implications for the assessment of seismic response in different geological realisations.

The microseismic modelling approach developed is applied to simulate microseismic events induced by the progressive advance of the coal face over the twelve-week period in 2011 at Coal Mine Velenje. The results obtained are compared to the field monitored data in terms of spatial distribution, released energy magnitude and frequency-magnitude distribution in Section 6.4. In Section 6.5, the spatial distribution of microseismic events, and the fracture size range and distribution are further discussed.

6.2 Methodology development for microseismicity modelling in longwall coal mines

The microseismicity modelling procedure developed involves three main steps.

The *model set-up and initialisation* starts with the building of a 3D model representing the working longwall panel and the surrounding strata in FLAC^{3D}. A group of discrete fractures (DFN) statistically characterised as described in Section 6.2.1 are implemented into the 3D model using the built-in logic in FLAC^{3D}. Mechanical and strength properties for stress and failure analysis are assigned to the grid blocks representing different rock materials. The boundary and initial conditions are then applied to the model so as to reach an initial equilibrium state.

Next, the s*imulation of mining induced stress redistribution and associated failure analysis* step is performed. Progressive longwall mining is simulated by a series of coal excavation steps, each of which typically reflects face advance in one or a few working days. In each excavation step, coal extraction is mimicked by "removing" grid elements (or cells) representing the coal to be extracted by a shearer. This is achieved by assigning null mechanical and strength properties to these cells. In this way, the loads previously withstood by the "removed" cells are redistributed to the surrounding cells and a new stress equilibrium is established. Failure analysis is then performed throughout the model domain to determine whether local shear or tensile failure has occurred, which is described in more detail in Section 6.2.2 below. At the next excavation step, concurrent to the simulation of coal extraction, these cells are "reinstated" to simulate the recompaction of the goaf created by the previous excavation step, and this is achieved by assigning the same cells with the mechanical and strength properties of roof goaf materials.

In the final modelling step, *microseismic event generation and associated energy release estimation* are achieved. At the end of each coal extraction step, a specially-written subroutine is invoked to check whether slip, and thus a microseismic event, has occurred for each individual fracture based upon the prevailing stress states. This process is described in Section 6.2.3. The evaluation of energy release that accompanies a microseismic event is presented in Section 6.2.4.

Steps 2 and 3 described above are repeated in each coal excavation step until the completion of longwall mining simulation in one study area. A flow chart of the

modelling procedure is presented in Figure 6.1. Note that the model progress from Step 2 to Step 3 is a one-way process, i.e. the initiation of microseismic events are determined by stress states, while it is assumed that the stress states of the continuum rock mass are not affected by fracture slippage. In this respect, the implemented DFN is self-contained, which means that the fracture slip can be evaluated at the end of each excavation step, rather than interacting with model elements during the cycling process. Nevertheless, in view of the mesh size used in the current model and computational efficiency achieved, it was found that the one-way coupling scheme implemented was adequate to represent the key characteristics of microseismicity associated with longwall mining without a significant loss of accuracy.

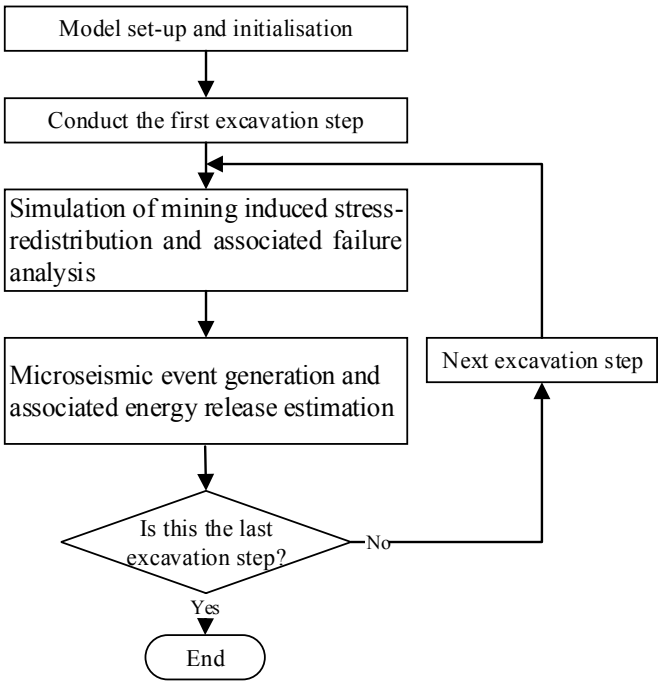


Figure 6.1. Flow chart for the modelling procedure.

6.2.1 DFN in FLAC^{3D}

Using a set of pre-defined attributes, a randomly-distributed network of disc-shaped discrete planar fractures can be created in a 3D continuum model in FLAC^{3D} by using various random seeds. The set of attributes includes fracture intensity, fracture size range, fracture size distribution (power law, Gaussian, uniform and bootstrapped distributions), and fracture orientation (random or pre-specified).

Fracture intensity

The facture intensity (total number of fractures per unit volume) is related to the average fracture spacing d:

$$N = V / d^3 \tag{6.1}$$

where N is the total number of fractures, and V is the volume of the 3D model domain. Thus, the total number of fractures may be determined if the average fracture spacing data are available from field measurements, such as the use of borehole/scanline surveys, face/bench/outcrop mapping, or 3D seismic data. In the absence of these data, N is first assigned a value, which is then varied through trial and error until a satisfactory match to the recorded field data is achieved in numerical simulations of microseismicity.

Fracture size range

As discussed in Section 6.2.4, the energy released by fracture slip forming a microseismic event is proportional to the cube of the fracture size. The range of the fracture sizes may thus be constrained by the range of recorded energy release magnitude. Figure 6.2a presents an example of the spatial distribution and the energy level, represented by the size of individual circles, of the microseismic events recorded at Coal Mine Velenje over one production week (Si *et al*., 2015a). The corresponding histogram of the magnitude of the recorded energy is presented in Figure 6.2b, where the recorded energy values range from 10^2 to 10^6 J. In addition, a small number of recorded events fell into low energy ranges, which is due to the limited energy detection range of the geophones. This suggest that only microseismic events above the magnitude level with the maximum event counts ($>\sim10^{3.8}$ J) can be completely recorded, from which the corresponding fracture size range may be estimated.

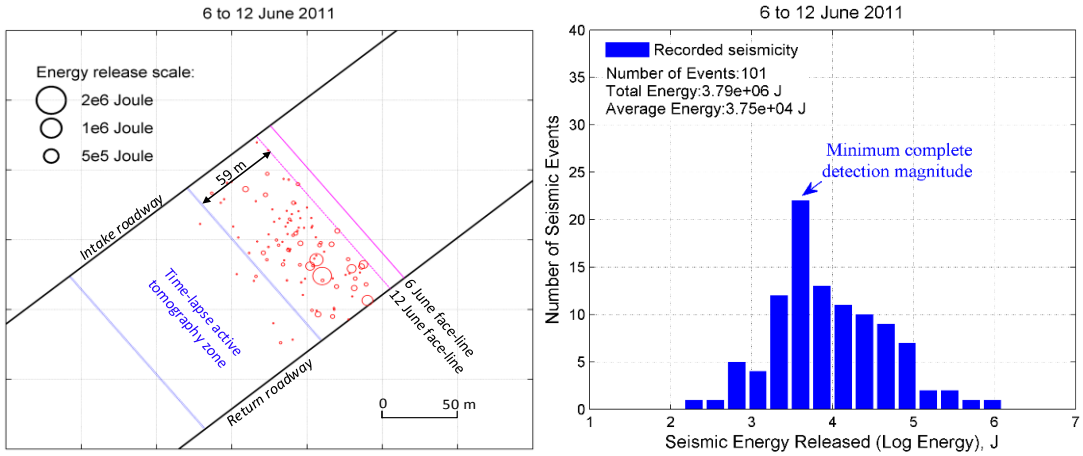


Figure 6.2. (a) Spatial distribution and (b) histogram of released energy of microseismic events recorded around LTCC panel K. -50/C at Coal Mine Velenje during 6 to 12 June 2011.

Fracture size distribution

In previous studies, fracture sizes were randomly sampled from a Weibull probability density distribution (Salamon, 1993) or a negative-exponential distribution (Board, 1994). In recent years, the power law relationship, which more closely represents the natural distribution of fractures, has been widely accepted to describe the frequency distribution of fracture sizes (Bonnet *et al*., 2001), which was also applied in this work (Equation (4.4)). The scaling exponent a usually ranges between 2 and 4. The total number of fractures within the range [$l_{\min}$, $l_{\max}$] may be obtained by integrating Equation (4.4):

$$N[l_{\min}, l_{\max}] = \frac{\alpha}{1-a} \cdot (l_{\max}^{1-a} - l_{\min}^{1-a}) \tag{6.2}$$

The cumulative distribution function is then given by:

$$F = \frac{N[l_{\min}, l]}{N[l_{\min}, l_{\max}]} = \frac{l^{1-a} - l_{\min}^{1-a}}{l_{\max}^{1-a} - l_{\min}^{1-a}} \tag{6.3}$$

As illustrated in Figure 6.3, as a increases, the distribution progressively skews to small fracture sizes. In this particular case, the fracture length varies from 1.8 m to 13 m.

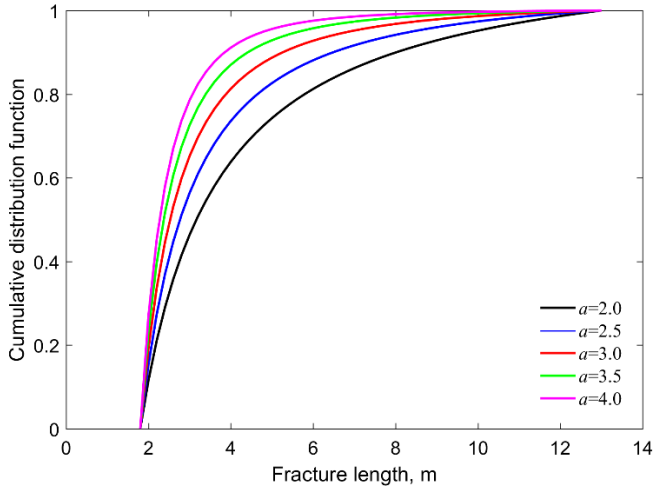


Figure 6.3. Cumulative distribution function of the power law distribution.

Spatial distribution and orientation of fractures

The fracture distribution is generated from a Poisson process, leading to a uniform spatial distribution throughout the volume. The fracture orientation is determined by the dip and dip direction. Either preferential joint orientation or random fracture distribution can be assigned to the rock material, depending on the availability of geological measurements. The latter was used in this work.

6.2.2 Strain-softening post-failure constitutive model for coal

Laboratory triaxial experiments have shown that coal samples generally exhibit strain-softening behaviour after failure under confinement, whereby the strength of coal reduces steadily with further straining until a plateau, i.e. the residual strength, is reached (Figure 6.4a). As shown in Figure 6.4, the residual strength is reached when the plastic strain approaches to 0.001. The Mohr-Coulomb failure criterion is widely used for evaluating shear failure of rocks. It states that shear failure would occur if the prevailing shear stress on a plane exceeds its shear strength:

$$\tau > \tau_s = \mu_s \sigma + c_p \tag{6.4}$$

where μ_s is the static friction coefficient, σ is the normal stress on the plane, and c_p is the peak cohesion (for intact coal). The corresponding post failure residual strength may be expressed as:

$$\tau > \mu_d \sigma + c_r \tag{6.5}$$

where μ_d is the dynamic friction coefficient, and c_r is the residual cohesion (for failed coal). The dynamic friction coefficient is typically assumed to be 0.9 times the static friction coefficient. The Mohr-Coulomb failure criteria for intact and failed coal are illustrated in Figure 6.4b.

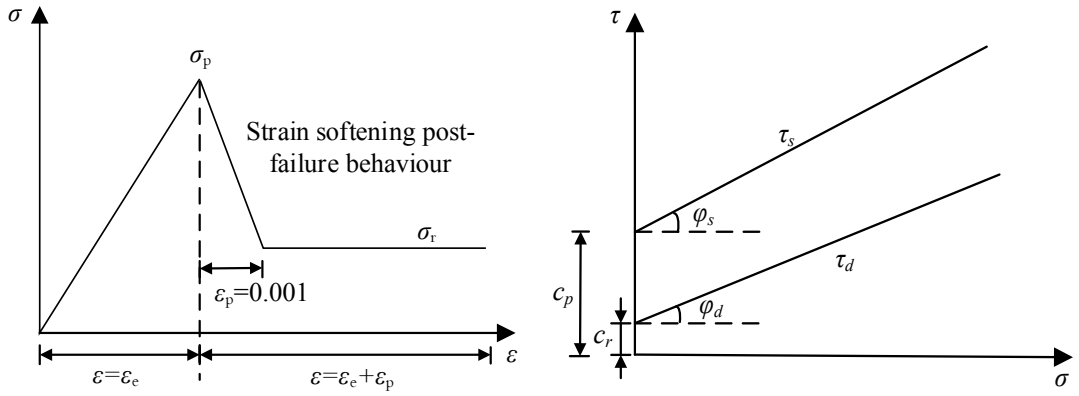


Figure 6.4. (a) Strain-softening post-failure behaviour; and (b) Mohr-Coulomb failure criterion for intact and failed coal under confinement.

Coal has a relatively low strength and strain-softening post-failure behaviour, therefore, a sizeable shear failure zone is usually formed ahead of an advancing longwall face as a result of the stress redistribution around working coal faces. Si *et al*. (2015b, 2015c) reported a failure zone extending up to 40 m ahead of the LTCC faces in Coal Mine Velenje, where the ultra thick coal seam is mined. In addition, a front abutment pressure zone is formed ahead of the failure (de-stressed) zone, and the stress disturbance can be discerned as far as 100 m above and 50 m below the working panel (Durucan, 1981).

6.2.3 Fracture slip evaluation

Previous modelling work on mining or rock excavation induced microseismicity has been mainly concerned with hard rocks where rock mass around underground openings behaved predominantly as an elastic medium (Board, 1994; Salamon, 1993). In longwall coal mining, it has been reported (Jackson, 1984; Yu *et al*., 2017) that microseismic events tended to occur at a distance ahead of the longwall face, where the coal is likely to remain elastic (intact). In this work, it is assumed that

microseismicity is predominantly generated in regions where coal remains intact, and behaves elastically.

The Mohr-Coulomb slip condition is used to evaluate if a fracture has slipped or not. The fracture is considered to have slipped if the shear stress along the fracture plane exceeds its resistance τ_{sf}, which can be described as:

$$\tau > \tau_{sf} \tag{6.6}$$

The resistance to slip, which is provided by the bonding and frictional properties of the fracture surfaces, is given by:

$$\tau_{sf} = \mu_{sf}\sigma + c_f \tag{6.7}$$

where σ is the normal stress on the fracture surface, and μ_{sf} and c_f are the static friction coefficient and the cohesion along the fracture, respectively. Alternatively, the fracture shear strength in Equation (6.7) can be estimated by applying a strength reduction factor β to the intact rock strength given by Equation (6.8):

$$\tau_{sf} = \beta\tau_s \tag{6.8}$$

The shear and normal stress used in Equations (6.6) and (6.7) may be calculated using the prevailing stresses on the element closest to the centroid of a fracture, hereafter referred to as the zone element. Salamon (1993) used this method for fracture slip evaluation. This approach is valid if the fracture size is small compared to that of the zone element. Otherwise, more test points for slip within a fracture are warranted. Board (1994) employed square-shaped fractures, each containing 9 test points for slip, with 8 of them located on the periphery of the square (4 corner points plus 4 in the middle), and one in the centre. In this work, circular discrete fractures provided in FLAC^{3D} were used and, following Broad (1994), a total of nine test points, eight of them uniformly distributed around the periphery of the circle and one at the centre were adopted (Figure 6.5).

The test points within a fracture are examined for slip sequentially, using the prevailing stresses of its zone element (closest to the test point). Slip is deemed to have occurred over the entire fracture face and a microseismic event is generated if Equation (6.6) is satisfied at any test point, and the fracture is not considered for slip again in subsequent simulations. The workflow implemented in this modelling work for testing for fracture

slip is presented in Figure 6.6. The detailed stress computation at a test point is described below.

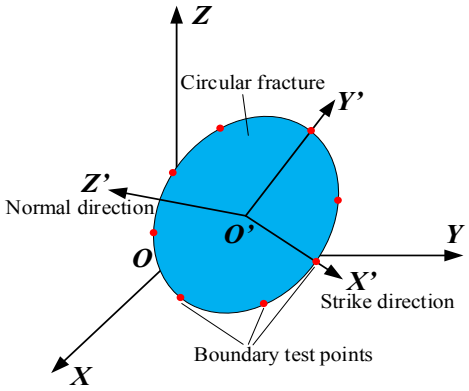


Figure 6.5.Slip test points on the periphery and centre of a circular fracture in local coordinates.

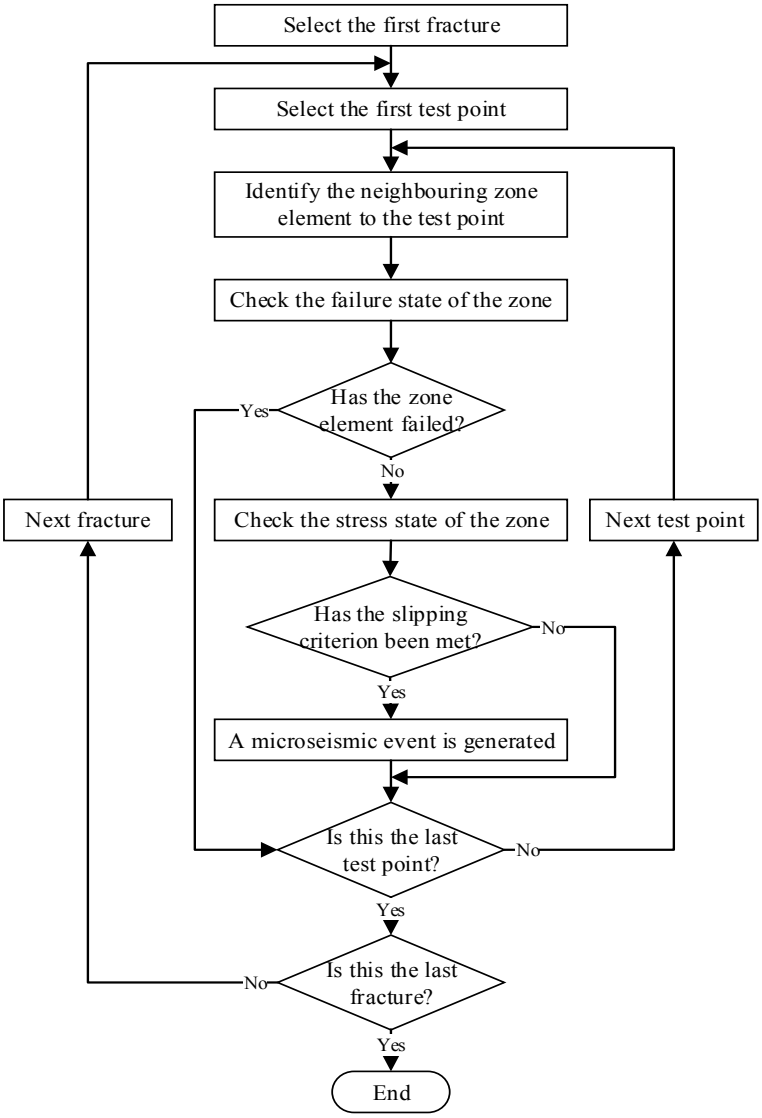


Figure 6.6. Flow diagram for the evaluation of a shear slip leading to microseismicity.

For convenience the test points within a discrete fracture are specified in local coordinates with its origin at (x_0, y_0, z_0) in the global coordinate system (Figure 6.5). The direction cosines of axis *OX'* (or the strike direction vector) are l_1, m_1 and n_1, and those of axis *OY'* and *OZ'* (or the fracture normal vector) are l_2, m_2 and n_2, and l_3, m_3 and n_3 respectively. The transformation for the *i*th test point from its local coordinates to the global ones is given by:

$$x_i = l_1 x_i' + l_2 y_i' + l_3 z_i' + x_0$$

$$y_i = m_1 x_i' + m_2 y_i' + m_3 z_i' + y_0$$

$$z_i = n_1 x_i' + n_2 y_i' + n_3 z_i' + z_0$$

The normal stresses along the local-coordinate axis directions at the test point can be written as:

$$X = l_3 \sigma_x + m_3 \tau_{yx} + n_3 \tau_{zx}$$

$$Y = m_3 \sigma_y + n_3 \tau_{zy} + l_3 \tau_{xy}$$

$$Z = n_3 \sigma_z + l_3 \tau_{xz} + m_3 \tau_{yz}$$

where σ_x, σ_y, σ_z and τ_{xy}, τ_{xz}, τ_{yx}, τ_{yz}, τ_{zx}, τ_{zy} are the normal and shear stresses of its zone element, respectively. The corresponding normal and shear stresses on the fracture plane associated with the test point are then given by:

$$\sigma = l_3 X + m_3 Y + n_3 Z$$

$$\tau = \sqrt{X^2 + Y^2 + Z^2 - \sigma^2}$$

The computed normal and shear stresses are used in Equations (6.6) and (6.7) to evaluate for fracture slippage.

6.2.4 Microseismic energy release

The concept of excess shear stress (ESS) proposed by Ryder (1988), which has been extensively used for numerical evaluation of rupture along weak planes (Salamon, 1993), is used to evaluate the energy released during fracture slip. The excess shear stress, i.e., the stress drop during slip, has been defined in Equation (4.6), and can be re-arranged to:

$$\Delta\tau = (\mu_{sf} - \mu_{df})\sigma + c_f \qquad (6.9)$$

where $\tau_{df} = \mu_{df}\sigma$ is the dynamic strength of the fracture surfaces, and μ_{df} is the dynamic friction coefficient along the fracture.

The stress drop is graphically illustrated in Figure 6.7. Due to the small difference between μ_{sf} and μ_{df}, the stress drop is expected to be strongly influenced by the bonding properties of the fracture surface.

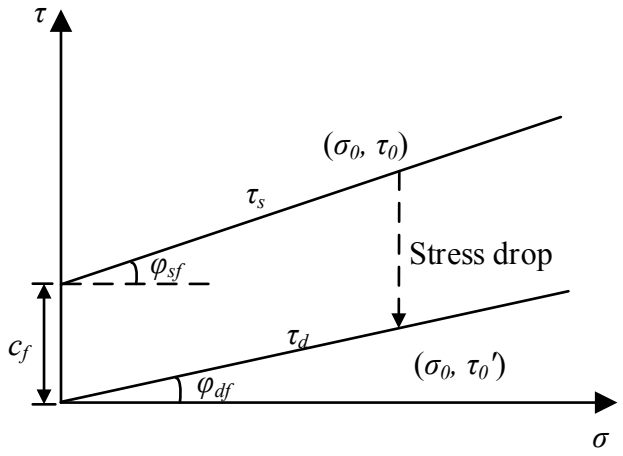


Figure 6.7. Failure criterion for fracture slip and associated stress drop after the fracture slips.

The resultant seismic moment M_0 is given by (Salamon, 1993):

$$M_0 = \frac{8(1-\nu)\Delta\tau R^3}{3(1-\nu/2)} \tag{6.10}$$

where υ is the Poisson's ratio of the host rock, and R is the fracture radius.

The local Richter magnitude M_L is expressed in terms of M_0 (Board, 1994; Salamon, 1993):

$$\log_{10} M_0 = 1.2M_L + 4.7 \tag{6.11}$$

The released kinetic energy E_k from the fracture slip is related to M_0 by (Salamon, 1993):

$$E_k = \frac{\Delta\tau M_0}{2G} \tag{6.12}$$

where G is the shear modulus of the host rock. Substituting Equation (6.10) into (6.12), one has:

$$E_{\mathrm{k}} = \frac{4(1-\nu)\Delta\tau^2 R^3}{3G(1-\nu/2)} \tag{6.13}$$

Equation (6.13) shows that the released kinetic energy is proportional to the cube of fracture size (radius) and square of the stress drop, suggesting that it is strongly affected by the fracture size and to a less extent by the rock strength (through stress drop) and mechanical properties.

6.3 Numerical modelling of microseismic events at panel K. -50/C at Coal Mine Velenje

The microseismic modelling approach developed was applied to model microseismicity at panel K. -50/C before the heterogeneity zone was reached on the week 11 to 17 July 2011. In view of the consistency in σ and b values mentioned in Section 4.4.2, a numerical model built for the LTCC panel K. -50/C can be assumed as homogeneous at the element scale, and a group of discrete fractures characterised by one set of intensity term and size distribution can be applied throughout the model domain. The following sections present the findings of a numerical modelling work carried out at panel K. -50/C. The model results are compared to the recorded data in terms of weekly histograms of released event energy and the microseismic frequency-magnitude distribution.

6.3.1 Model set-up and generation of a discrete fracture network

A three-dimensional model measuring 300 m × 350 m × 200 m in x, y and z directions respectively was constructed in FLAC^{3D} to represent the LTCC panel K. -50/C, the floor coal and the overlying strata (Figure 6.8a). In the model, the coal panel was at a depth of -350 m and had a thickness of 20 m, the top 15 m of which is caved when the bottom 5m of coal is extracted by the shearer. The longwall panel modelled was 150 m wide, including both the intake and return gateroads. The coal panel was underlain by a 100 m thick floor coal, and overlain by a 20 m thick mixed roof layer, half of which was clay on the intake gateroad side, and the other half was caved roof goaf on the return gateroad side. This mixed layer was further overlain by a clay layer of 50 m in thickness. The model comprised of 280,000 elements, each with a dimension of 3 m × 5 m × 5 m.

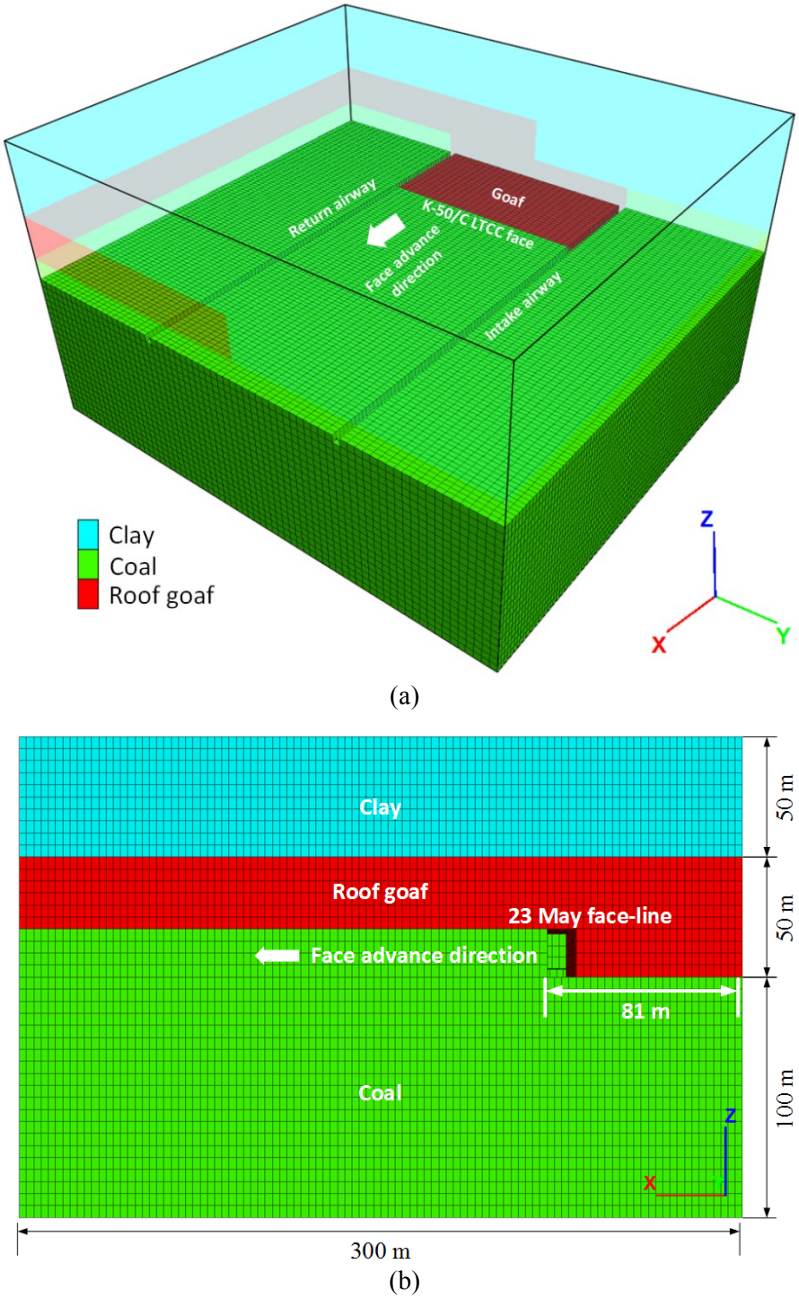


Figure 6.8. Mining geometry and geological implementation: (a) 3D model geometry, and (b) a cross-section of the model along the face advance direction at LTCC panel K.-50/C.

Three geological formations, i.e., primarily detritic coal, clay, and failed clay (for roof goaf) were used in the model. Elastic (bulk modulus, shear modulus) and strength (cohesion) properties for detritic coal matrix, clay and failed clay were obtained from laboratory experiments on samples from Coal Mine Velenje, which are presented in Table 6.1. Strain-softening constitutive model was used to describe post-failure rock behaviour. The residual cohesions of the coal matrix and clay represent a reduction of

83% from their intact values. In the post-failure phase, it was assumed that the residual cohesion of detritic coal matrix and clay is reached when the plastic strain exceeds 0.001. Considering the mesh size dependency of the strain-softening constitutive model, a preliminary sensitivity study was performed to ensure that the mesh size used in the model did not have a notable effect on the model performance.

Table 6.1. Rock mechanical properties used in the K.-50/C LTCC model (after Si *et al*., 2015c; Zavšek, 1993).

Lithology	E (GPa)	υ	K (GPa)	G (GPa)	c (MPa)	φ (°)	σ_t (MPa)	c_r (MPa)	σ_{tc} (MPa)
Coal matrix	0.53	0.40	0.90	0.19	2.10	23	0.92	0.35	0.52
Clay	0.67	0.40	1.10	0.24	1.90	30	0.92	0.63	0.52
Failed clay	0.48	0.40	0.77	0.17	0.63	30	0.52	0.63	0.52

The *in situ* vertical stress in the model was induced by the overburden weight (using a density of 2,360 kg/m^3), and the horizontal stresses were estimated by the Poisson's effect under gravity loading of the overburden. The vertical and horizontal stress gradients were computed based on the Poisson's ratio of the rock types used in the model. The boundary conditions were set in such a way that normal stresses calculated from the horizontal stress gradient were applied to the lateral boundaries, and the bottom boundary was fixed.

The methodology followed in generating the DFN for modelling microseismicity in FLAC^{3D} has been described in Section 6.2.1. The attributes of fractures required for model implementation include total number of fractures, their size range, the scaling exponent in power law distribution, and spatial distribution and orientation. Out of these, random fracture positions and orientations were assigned to the rock types used in the work. The total number of fractures and the scaling exponent needed to be determined during the simulation to match the field monitored data. A strength reduction factor of 0.4 was used in Equation (6.8) to determine the shear strength of each fracture.

It has been shown that the recorded event energy range may be used to estimate the range of fracture size in the model implementation using Equation (6.13). Based on the complete detection range of released energy (~$10^{3.8}$ to ~10^6 J) from Figure 6.9, the fracture radius was estimated to be between 0.9 and 6.5 m. It can be seen from the

figure that the minimum complete detection magnitude is around $10^{3.6}$ J for the modelled microseismicity.

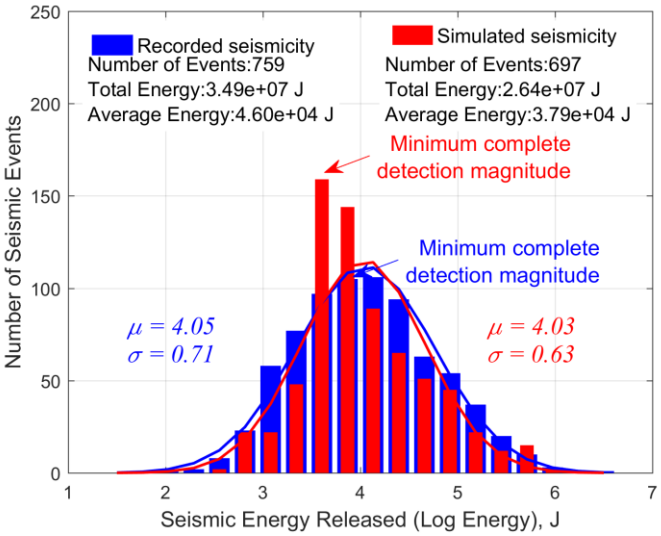


Figure 6.9. Estimation of the range of fracture sizes through the energy released from microseismic events during an eight-week coal production period from 23 May to 17 July 2011 around LTCC panel K.-50/C at Coal Mine Velenje.

It was found that a total fracture number of 45,000 and scaling exponent of 2.7 yielded a satisfactory match of the recorded event energy distribution (Figure 6.9). Figure 6.10 presents the implementation of DFN in the model domain.

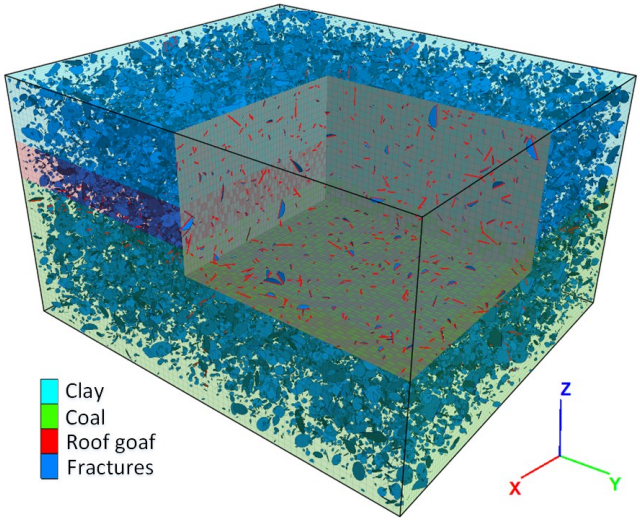


Figure 6.10. Spatial distribution of DFN following a power law relationship of fracture size in the model domain constructed.

6.3.2 Modelling of longwall top coal caving mining

The model run covered a period of eight weeks, starting on 23 May 2011, when the face was 81 m from the right-hand side model boundary (Figure 6.8b), and finished on 17 July 2011. In order to establish the initial stress conditions to account for the effects of previous mining activities, the two development headings driven around the panel were first extracted (Figure 6.8a). Next, a pre-modelling step, whereby a 12 m length (average weekly advance distance) of coal at the longwall behind the 23 May 2011 face-line was simulated. A total of eight longwall extraction steps were then modelled (from right to left in Figure 6.8b), each extraction step representing one production week during which 12 m of coal (4 elements in the x direction) was "removed" and then "backfilled" in the following week.

A subroutine, specially written to determine the failure state and the stress state of zone elements hosting the fractures, is invoked after an equilibrium state is reached at each excavation step, and whether the shear slip condition is met by each fracture to generate a microseismic event is ascertained. In order to account for the stochastic nature of the DFN, a total of five series of DFN realisations with different random seeds were generated and used in the model.

6.4 Model results and analysis

6.4.1 Stress and failure responses to mining activities

Figure 6.11 shows the induced failure zone during longwall coal extraction, which covers a region around 40 m ahead of the face-line at LTCC panel K.-50/C. In addition, the major and minor principal stress profiles in front of the longwall face during longwall face advance are plotted for four typical production weeks (Figure 6.12). It is observed that, for each production week, the major principle stress σ_1 first increases from 0.35 MPa (residual cohesion of coal matrix) to the peak value of over 15 MPa at the interface between elastic and plastic zones, and then decreases slowly to the *in situ* vertical stress level with the distance from the longwall face. The minor principle stress σ_3 also reaches a peak at the edge of the failed zone, and gradually converges to the *in situ* horizontal stress level.

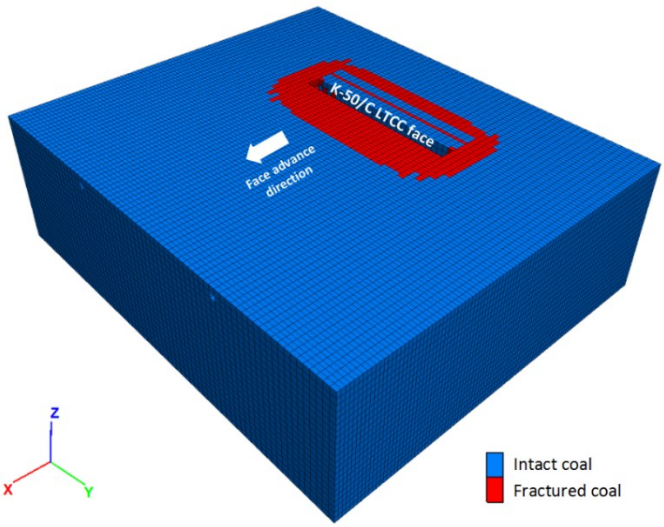


Figure 6.11. Mining-induced failure zone (in either shear or tensile mode) in the advancing LTCC panel K.-50/C during the period 30 May to 5 June, 2011.

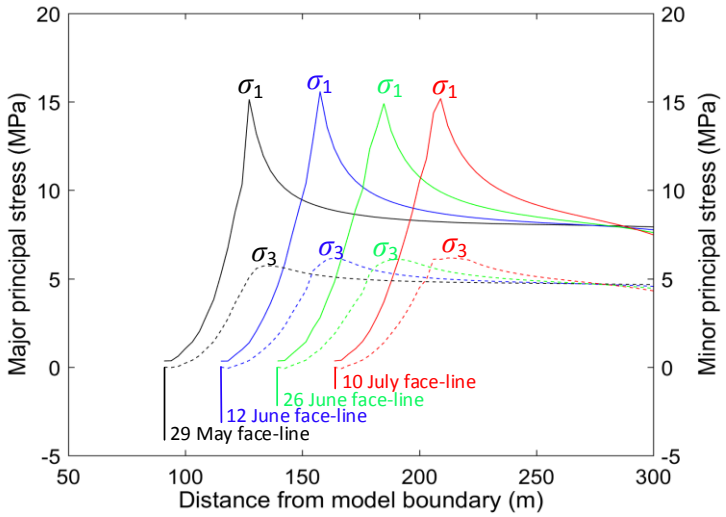


Figure 6.12. Major and minor principal stress profiles ahead of the LTCC panel K.-50/C face-line in the horizontal central cross-section of the LTCC face.

6.4.2 Spatial distributions of simulated microseismicity

Figure 6.13 shows a snapshot in time of simulated microseismicity around the longwall panel K.-50/C during one typical mining week, each microseismic event being represented by one point, with its colour representing the logarithmic magnitude of the released kinetic energy. It can be seen that, due to the relatively higher stresses in the floor compared to the roof, more microseismic events are generated in the floor coal.

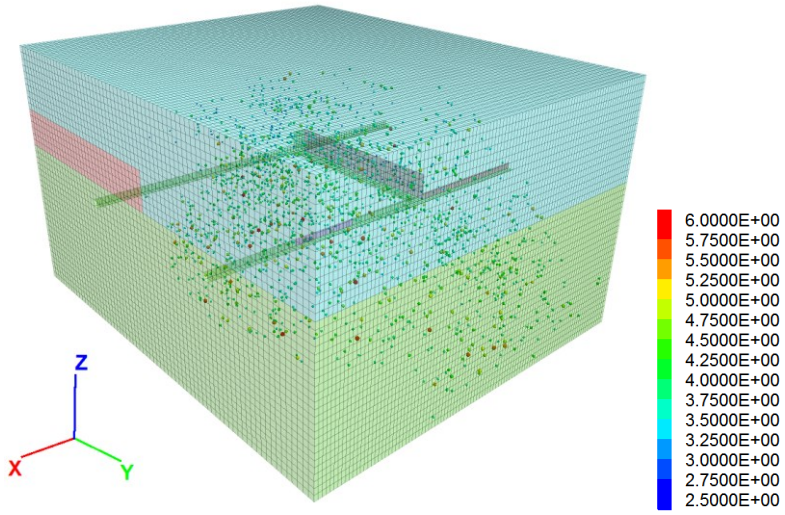
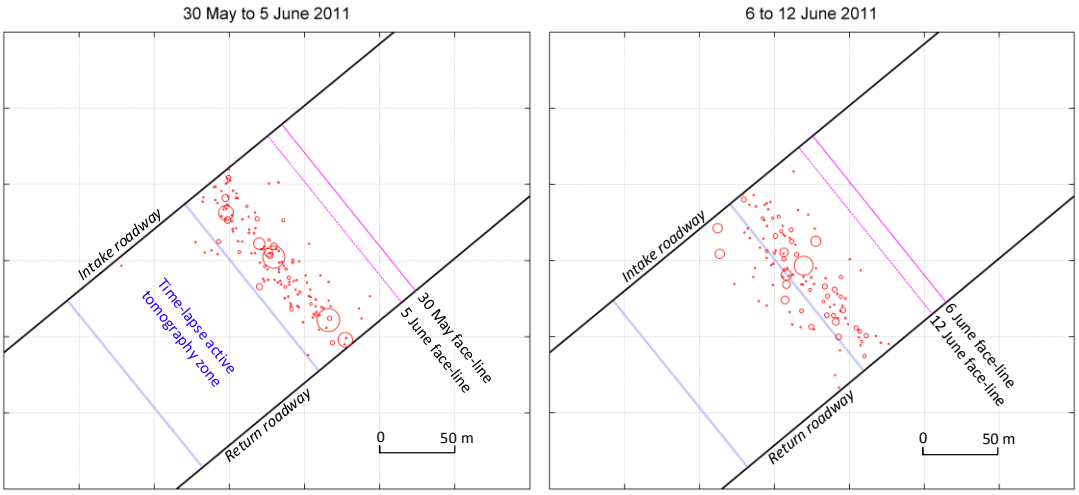


Figure 6.13. Three-dimensional distribution of mining-induced microseismicity and the released energy at LTCC panel K.-50/C during coal production from 6 to 12 June 2011 (the colour legend is in log scale).

In order to be comparable with the field monitored data available from Coal Mine Velenje (Figure 4.15), where microseismic events were recorded by geophones installed at the panel level [-330 m, -350 m], the simulated microseismic events located in the region 5 m above and below the longwall panel horizon [-325 m, -355 m] and in the zone more than100 m ahead of the face-line were filtered out. It was observed that the microseismic events concentrated in the area 40 m to 70 m ahead of the face-line (Figure 6.14), whereas the field recorded events were more evenly distributed over a much wider region (Figure 4.15). This relative discrepancy is believed to be caused by the omission of the presence of a small scale xylite rich heterogeneous zone in the coal panel, which will be further discussed in Section 6.5.

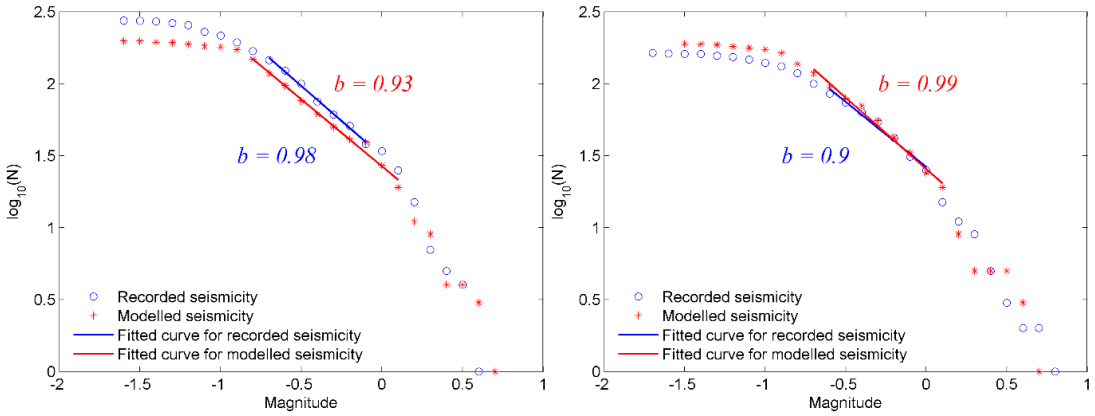


(a) 30 May to 5 June 2011 (b) 6 to 12 June 2011

Figure 6.14. Simulated weekly microseismic events ahead of the longwall face located within the depth interval [-325m, -355m], and up to 100 m ahead of the longwall face as the LTCC face at panel K.-50/C advances.

6.4.3 Frequency-magnitude distribution and released energy

Figure 6.15 presents the frequency-magnitude distribution of the recorded and modelled microseismic events. The event magnitude obtained from numerical modelling ranges between -2.0 and 1.0, which is in agreement with the field observations. In this work, both the monitored and modelled datasets were fitted to Equation (4.2), with the corresponding *b* values calculated and marked in the figure. The figure show that a relatively good agreement has been achieved between the model results and field observations. Frequency-magnitude distribution and associated *b* values for other production weeks are presented in Appendix 2. The *b* values for recorded seismicity fall within one standard deviation of those for the modelled seismicity, suggesting the robustness of applying DFN models in simulating microseismicity (Figure 6.16). In addition, *b* values for both field observations and model results only experience slight fluctuations during the modelling period, which means that the size scaling exponent for fractures in the extracted coal seam is quite consistent.



(a) 23 May to 5 June 2011 (b) 6 to 19 June 2011

Figure 6.15. Frequency-magnitude plots of the recorded and modelled seismic events for the LTCC panel K.-50/C at Coal Mine Velenje.

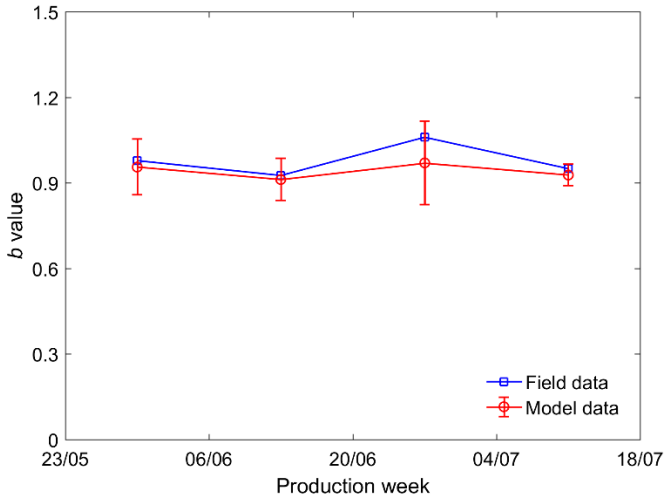
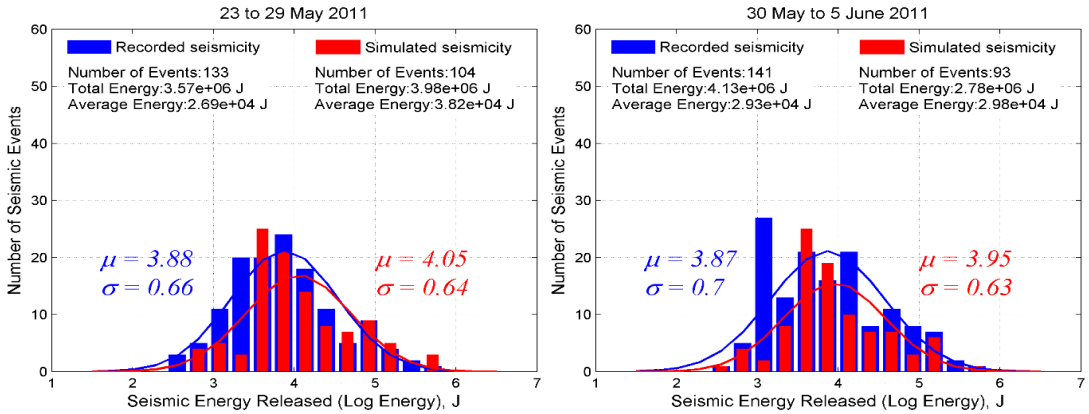


Figure 6.16. Bi-weekly variation of *b* values for recorded and modelled microseismic events.

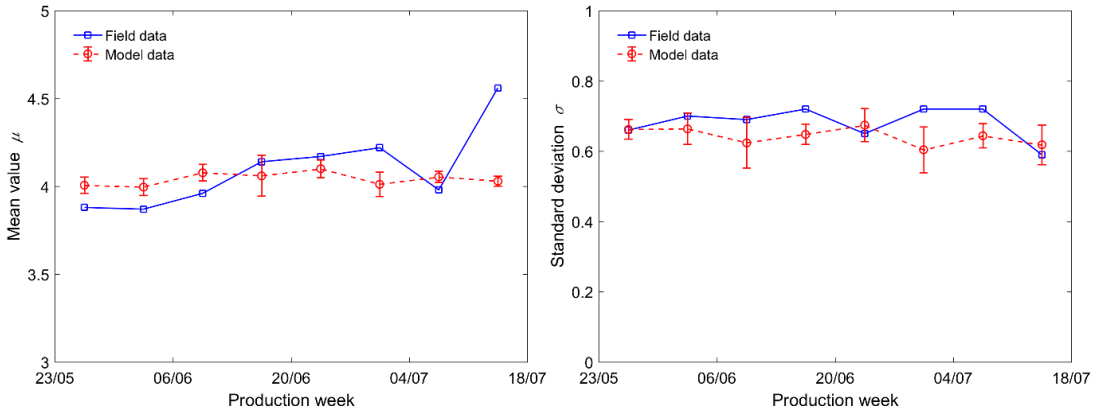
It has been shown earlier that the recorded weekly microseismic energy released around the K.-50/C LTCC panel at Coal Mine Velenje follows a Gaussian distribution. Curve fitting of a Gaussian distribution to the weekly histograms of the magnitude of microseismic energy predicted was also performed. Two examples of this are shown in Figure 6.17, with the remaining results being presented in Appendix 2. It can be seen that the goodness of fit for the modelled results to the Gaussian distribution is not as good as that obtained for the field monitored data. This is probably due to microseismic events generated from fractures smaller than the minimum fracture size (0.9 m) being ignored in the simulation, which were incompletely detected in field observations, leading to a discrepancy in the number of events falling into low energy ranges.



(a) Week 23 to 29 May 2011 (b) Week 30 May to 5 June 2011

Figure 6.17. Comparison of the recorded and modelled seismic energy released in the first two production weeks at LTCC panel K.-50/C.

As shown in Figure 6.18, the fitted mean value μ and standard deviation σ values during each week are fairly consistent over the eight production weeks. Moreover, the simulated values are compared favourably with the field observations over the same period.



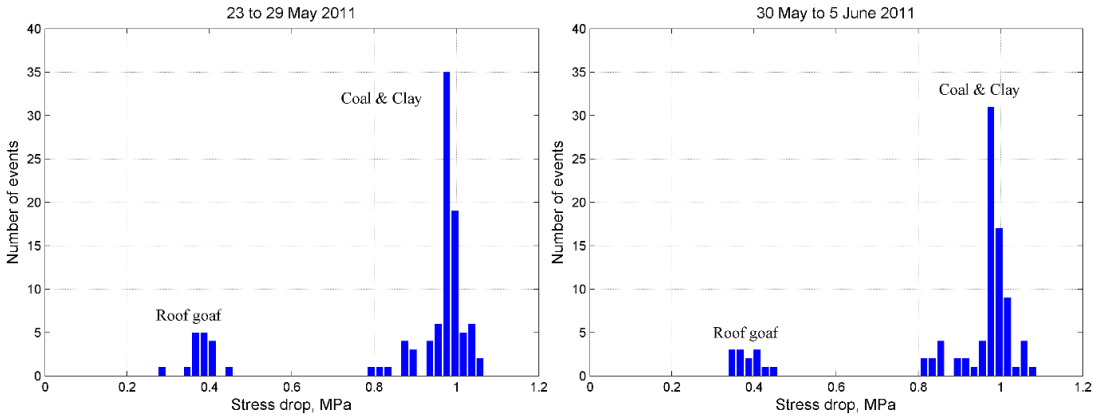
(a) (b)

Figure 6.18. Fitted weekly Gaussian parameters for recorded and modelled microseismic events: (a) mean value μ, and (b) standard deviation σ.

6.4.4 Stress drop frequency

As shown in Equation (6.13), the stress drop during rock failure is an important parameter influencing the released seismic energy. The histograms of modelled stress drops during the first two production weeks are plotted in Figure 6.19. It can be seen that two clusters are formed, with the right hand side one ranging from 0.78 to 1.10

MPa, and the left hand side one from 0.28 to 0.45 MPa. Most stress drops fall within the right hand side cluster.



(a) Week 23 to 29 May 2011 (b) Week 30 May to 5 June 2011

Figure 6.19. Histogram of stress drops for microseismic events during each production week at LTCC panel K.-50/C.

Stress drops are associated with the dynamic strength of the fracture surfaces, and thus with lithology as presented in Equation (6.9). Given that cohesion and friction coefficient values assigned to the detritic coal and clay roof are high and are not significantly different, stress drops occurring in these layers form the right hand side cluster in the histograms. In contrast, the left hand side cluster of stress drops represent the microseismic events occuring in the caved roof. In addition, it can be deduced that once failure has occurred in the xylite-rich heterogeneous zone, the associated stress drop, and thus seismic energy released would be much larger than that in the surrounding detritic coal matrix.

6.5 Discussion

Since the coal panel modelled was assumed to be homogeneous at element scale, the spatial distribution of small-scale heterogeneity was not considered in the model. Therefore, the plastic zones induced by coal extraction extends into the whole region approximately 40 m ahead of the working face, as shown in Figure 6.11. In the present methodology, only fractures located in elastic areas are evaluated for the occurrence of microseismicity, thus a few events occur in the immediate vicinity of the longwall face modelled. This is consistent with the monitoring results of Jackson (1984) and Yu *et al*. (2017).

However, small-scale heterogeneity in rock mechanical properties do exist in geological media. Regions with high rock strength in the vicinity of a working longwall face may remain intact, where microseismic events can still be generated. Therefore, the spatial distribution of recorded weekly microseismic events scattered over an extended area ahead of the working face at LTCC panel K.-50/C.

In addition, the xylite rich heterogeneous zone within the coal panel has a large influence on mining-induced microseismic characteristics, the influence of which will be investigated further in the next chapter.

The cumulative number of implemented fractures can be obtained by integrating Equation (4.4):

$$N(>l)=\frac{\alpha}{1-a}\cdot(l_{\max}^{1-a}-l^{1-a}) \tag{6.14}$$

Considering that there is no upper threshold for fracture size in natural geological media, Equation (6.14) can be reduced to:

$$N(>l)\approx\frac{\alpha}{a-1}\cdot l^{1-a} \tag{6.15}$$

This equation has a similar form to the Gutenberg-Richter relationship (Equation (4.2)), which is a power law relationship in linear scale. The scaling exponent for cumulative fracture number is $1–a$, compared to $–b$ for the Gutenberg-Richter relationship. This further confirms that microseismic events and related energy release are closely associated with the fracture systems in the coal seam. It is noteworthy that, due to the limited sensitivity of monitoring equipment, a considerable number of low energy events emitted by the initiation of small-scale fractures are overlooked. Therefore, the histogram of recorded microseismic energy follows a Gaussian distribution, rather than the power law distribution.

Given the complete detection range of released energy, the fracture size range in the geological media can be estimated. In previous studies, Board (1994) used fracture sizes ranging from less than 1 m to approximately 50 m. The mean fracture size used by Salamon (1993) reached up to 100 m. In the model described here, the average fracture spacing was around 7.76 m, and the fracture size ranged from 0.9 m to 6.5 m. Following the power law distribution, most fracture sizes tended to be close to the

lower fracture size limit. For example, the scaling exponent *a* used in the current model was 2.7, indicating that 90% of embedded fracture sizes are less than 5.94 m. In addition, a smaller *a* value indicates a larger proportion of large fractures over small ones, and thus a larger fitted mean value μ for the weekly histogram of released energy.

6.6 Conclusions

In this chapter, a methodology developed by the author to simulate longwall mining-induced microseismicity based upon the widely accepted fracture slip seismicity-generation mechanism was presented. Using the built-in DFN facility in FLAC^{3D}, discrete fractures following a power law size distribution were distributed throughout the 3D continuum model of a LTCC panel in a probabilistic way to account for the stochastic nature of microseismicity occurrence. A geomechanical model was constructed using FLAC^{3D} to model the progressive advance of the panel K.-50/C face during the first eight weeks in 2011, and the developed DFN-based modelling approach was applied to simulate LTCC mining-induced microseismicity. The model was homogeneous at the element scale, and only one set of fracture size distribution was implemented throughout the model domain. At each excavation step, global stress and failure analysis with reference to the strain-softening post-failure behaviour characteristic of coal, and fracture slip evaluation for microseismicity are conducted sequentially.

Model results have shown that a good match was achieved between recorded and modelled microseismic events in terms of spatial distribution, released energy, and frequency-magnitude distribution. The energy released from a microseismic event is shown to be proportional to the cube of fracture size. This suggests that the resulting microseismic energy distribution is expected to be strongly correlated with the fracture size distribution implemented in the model. The energy released from a microseismic event is also affected by the rock strength (through stress drop) and its mechanical properties. The model findings indicate that the power law fracture size distribution can be used to model microseismic generation around the longwall coal face. This modelling approach provides a new alternative to interpret and predict longwall coal mining-induced microseismicity in field applications.

Chapter 7 Microseismic anomaly influenced by lithological heterogeneity in longwall coal mining

7.1 Introduction

As reported in Section 4.4, the deviations in microseismic characteristics (including event counts, average energy release, the *b* value, and fitted Gaussian distribution parameters μ and σ) when approaching the xylite-rich zone suggest that except for rock strength, the fractures within the xylite-rich zone differ from those in the detrite dominated coal seam (Figure 4.29). It was reported that rock with lower fracture intensity has higher rock strength and elastic modulus, and that rock with lower fracture size distribution exponent *a* tends to have greater rock strength (Harthong *et al*., 2012). In this respect, it is deduced that fractures within the xylite-rich zone have lower intensity and power law exponent *a* related to the size distribution.

This chapter presents the application of the modelling approach developed in Chapter 6 to further model seismic characteristics during longwall coal extraction towards the heterogeneous zone inferred from active time-lapse seismic tomography measurements. The rock strength of the elements and fracture attributes within the zone are varied, respectively. The induced microseismicity is investigated in terms of frequency-magnitude distribution and logarithmic energy of microseismic events. This model provides a tool to obtain a better understanding of factors influencing mining-induced microseismicity, and lays a foundation for the prediction of rock bursts or coal and gas outbursts using recorded microseismic data.

7.2 Numerical simulation of longwall coal mining-induced microseismicity

7.2.1 Numerical model description

The numerical model was established based on the model developed in Section 6.3, while the model geometry, geological structures, constitutive model, material properties and boundary conditions remained the same. The geometry of the xylite-rich zone inferred from the active seismic tomography measurements was digitalised from Figure 4.14 and implemented into the FLAC^{3D} model, assuming full penetration within the coal panel (Figure 6.8a). The elastic properties (bulk modulus and shear modulus) of the xylite-rich coal were set to be the same as those of detritic coal, but the strength properties (compressive and tensile strength) of xylite-rich coal were set to be one to two times those of detritic coal.

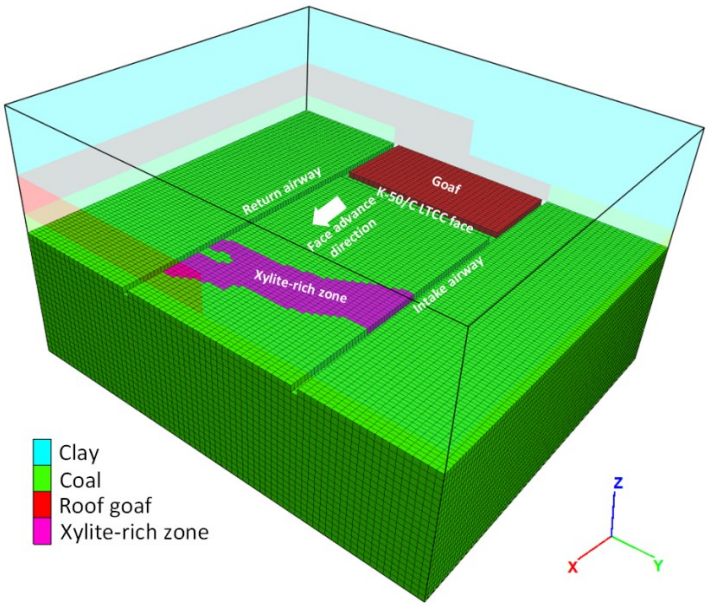
After construction of the model, fractures were embedded into the model domain. Two groups of fractures were employed: one group for the xylite-rich zone (DFN 1), and the other for the remaining zones (DFN 2). For both fracture groups, the fracture positions and orientations were set to be random, and the fracture radii ranged from 0.9 m to 6.5 m. A fracture number of 44,707 and scaling exponent $a = 2.7$ were applied for the DFN 2 to calibrate the synthetic microseismic intensity and size distribution to the recorded ones. The fracture number and scaling exponent for the DFN 1 were varied during modelling, and will be introduced in Section 7.2.2.

7.2.2 Modelling scenarios

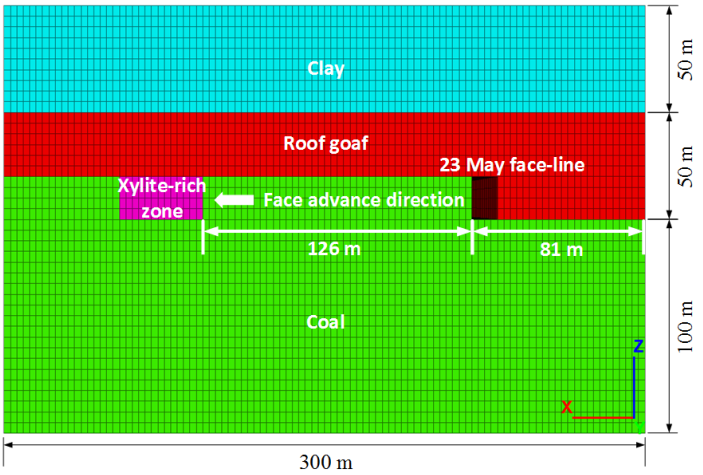
Following the procedures described in Section 6.2, a total of twelve extraction steps were simulated (from right to left in Figure 6.8b), from 23th May to 28th August, with an interruption of a two-week holiday period starting from 16th July. Each excavation step represented coal extraction for one week. Multiple runs were carried out with various rock strengths for xylite-rich coal and fracture attributes within the xylite-rich zone, respectively:

(1) The geometry parameters for fractures in the heterogeneous zone remained the same as those in the detrite dominated coal seam, and four scenarios were considered by varying compressive and tensile rock strength of elements within the heterogeneous zone: (a) $\sigma_{ch} = \sigma_{cc}$, $\sigma_{th} = \sigma_{tc}$; (b) $\sigma_{ch} = 1.5\sigma_{cc}$, $\sigma_{th} = 1.5\sigma_{tc}$; (c) $\sigma_{ch} = 2\sigma_{cc}$, $\sigma_{th} = 2\sigma_{tc}$, and (d) $\sigma_{ch} = 2.5\sigma_{cc}$, $\sigma_{th} = 2.5\sigma_{tc}$.

where σ_{cc} and σ_{tc} are respectively the compressive and tensile strengths of the detritic coal seam, and σ_{ch} and σ_{th} are those of the heterogeneous zone.



(a)



(b)

Figure 7.1. Mining geometry and geological implementation of the xylite-rich zone: (a) 3D model geometry, and (b) the central cross-section of the model along the face advance direction.

(2) The rock strength of the heterogeneous zone remained the same as that of the detrite dominated coal seam, and four scenarios were considered by varying the fracture intensity term and size distribution exponent of fractures hosted by the

heterogeneous zone: (a) $a_h = 2.7$, $\alpha_h = \alpha_c$; (b) $a_h = 2.4$, $\alpha_h = 0.9\alpha_c$; (c) $a_h = 2.1$, $\alpha_h = 0.8\alpha_c$, and (d) $a_h = 1.8$, $\alpha_h = 0.7\alpha_c$.

where a_h is the power law distribution exponent for the heterogeneous zone, and α_c and α_h are the fracture intensity terms for the detritic coal seam and heterogeneous zone, respectively. Since the fracture density term α is proportional to the fracture number in a certain volume, α_h is controlled by changing the total number of fractures assigned to the heterogeneous zone. The fracture distribution for the scenario (d) is presented in Figure 7.2.

In order to account for the stochastic nature of DFNs, a total of five series of DFN realisations were generated for each modelling scenario. The model results and analysis are presented in Section 7.3 and 7.4.

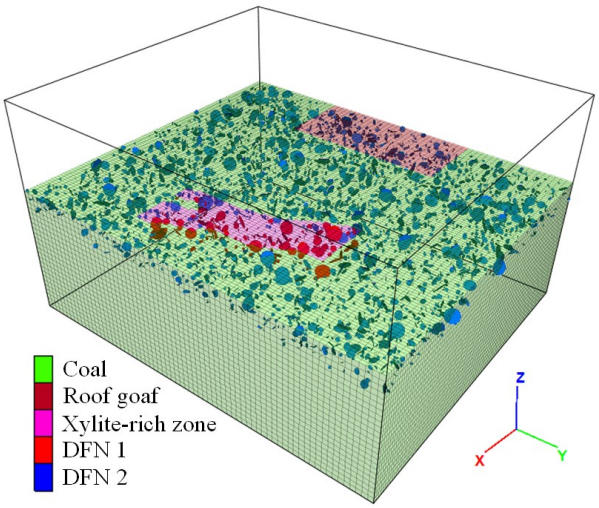
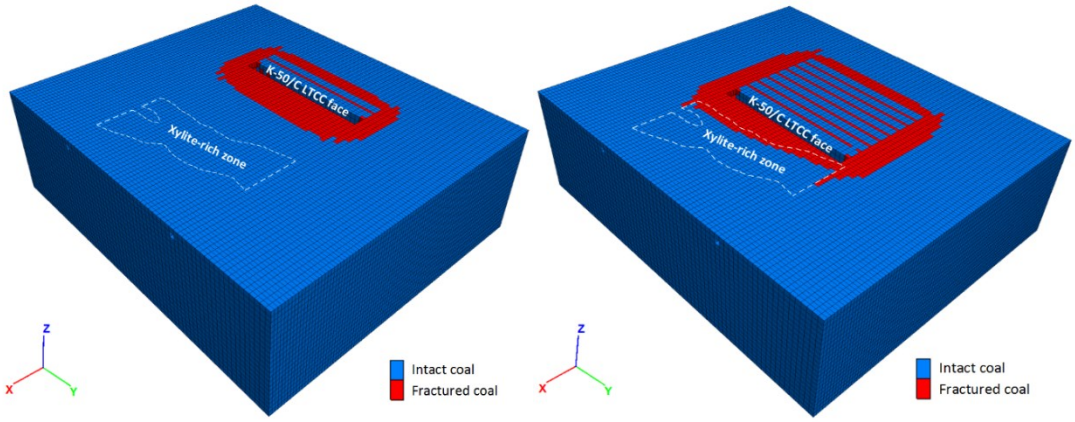


Figure 7.2. Distribution of DFNs located at the panel level [-330 m, -350 m] following power law relationship with $a_c = 2.7$, $a_h = 1.8$, $\alpha_h = 0.7\alpha_c$.

7.3 Results: Effect of rock strength on seismic response

7.3.1 Stress and failure zone distribution

The distribution of failed zones in response to coal production is shown in Figure 7.3. It can be observed that during 30 May to 5 June, when the face-line is far away from the xylite-rich zone, the failed zone extends to around 40 m ahead of the longwall face. When the xylite-rich zone is encountered during 11 to 17 July, the failed zone propagation is heavily confined by the boundaries of the xylite-rich zone.



(a) (b)

Figure 7.3. Failure zone distribution around the working longwall face for the scenario $\sigma_{ch} = 2\sigma_{cc}$, $\sigma_{lh} = 2\sigma_{lc}$: (a) during Week 30 May to 5 June, and (b) during Week 11 to 17 July.

The stress distribution ahead of the face-line as mining progresses are plotted for four typical production weeks in Figure 7.4. It is shown that the major principal stresses peak at the failed zone edge. In the first two production weeks, the abutment stress concentration is as far as 40 m ahead of the longwall face. As the longwall face approaches the xylite-rich zone during 11 to 17 July, the abutment stress concentration region is limited to be in front of the xylite-rich zone, suggesting an apparent stress disturbance resulting from the material heterogeneity.

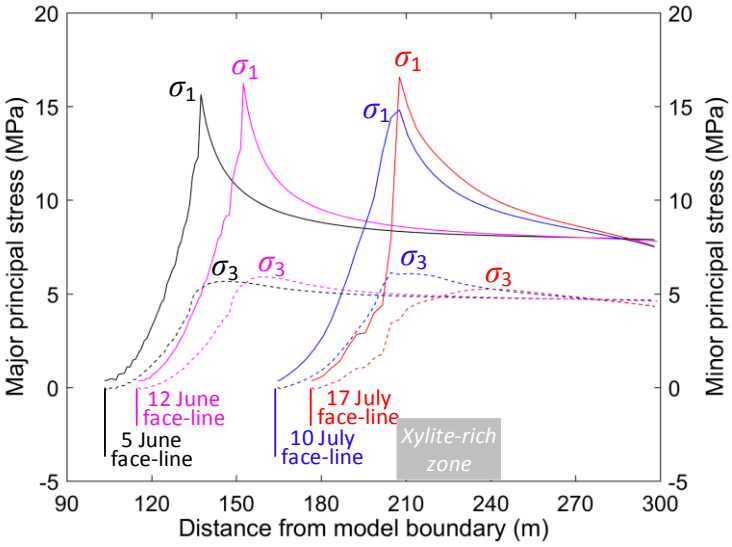


Figure 7.4. Major and minor principal stress profiles ahead of the longwall face in the central cross-section of the model domain for the scenario $\sigma_{ch} = 2\sigma_{cc}$, $\sigma_{lh} = 2\sigma_{lc}$.

7.3.2 Frequency-magnitude distribution

Figure 7.5 presents the variation of fitted *b* values from frequency-magnitude distribution of recorded and simulated microseismicity over the monitoring period. When the rock strength of elements within the xylite-rich zone is the same as that of detritic coal, *b* values of microseismicity are quite consistent over the whole period. When the rock strength of elements within the xylite-rich zone is stronger than that of detritic coal matrix, there is a notable reduction in *b* values several weeks before reaching the xylite-rich zone. The reduction in *b* values has a positive correlation with the increase in rock strength of elements within the xylite-rich zone. An average *b* value as low as 0.67 can be fitted when approaching the xylite-rich zone for the modelling scenario $\sigma_{ch} = 2.5\sigma_{cc}$, $\sigma_{th} = 2.5\sigma_{tc}$.

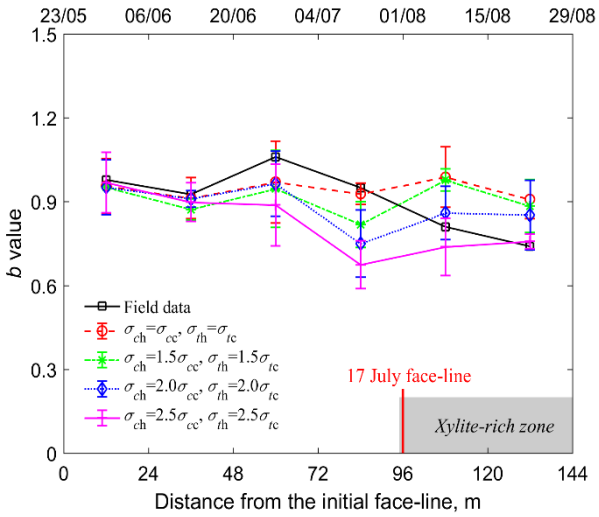


Figure 7.5. The bi-weekly *b* values for frequency-magnitude distribution of the recorded and simulated microseismic events over the monitoring period.

Figure 7.6 shows an example of the frequency-magnitude distribution of recorded and simulated microseismicity during a two-week period after reaching the xylite-rich zone. The frequency-magnitude distribution for different modelling scenarios approximately follows a power law relationship, but the fitted curve becomes less steep with increasing rock strength of elements within the xylite-rich zone, i.e. the *b* value decreases. When the rock strength of elements within the xylite-rich zone is 2.0-2.5 times of that of detritic coal, the fitted *b* values match well with that of recorded microseismicity.

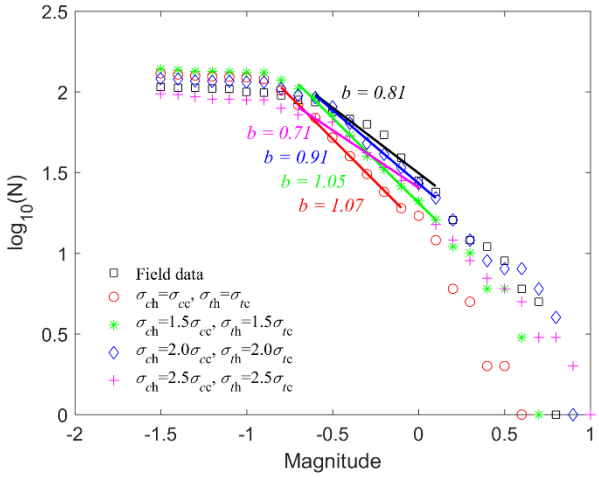


Figure 7.6. Examples of *b* values obtained through regression fitting for the recorded and simulated microseismic events during 1 to 14 August 2011.

7.3.3 Logarithmic released energy

Figure 7.7 presents examples of weekly histograms of the logarithmic event energy for the field data and modelling scenario $\sigma_{ch} = 2\sigma_{cc}$, $\sigma_{th} = 2\sigma_{tc}$ before and after reaching the xylite-rich zone, respectively. It can be observed that after reaching the xylite-rich zone, blue bars (the recorded microseismicity) have a notable shift to the right (higher energy levels), with a decrease in total number of microseismic events. The rightward shift can be modelled by increasing the rock strength of elements within the xylite-rich zone. In addition, the number of simulated microseismic events decreases due to a lower chance of slippage of fractures within the xylite-rich zone.

Figure 7.8 shows the fitted Gaussian distribution parameters to the logarithmic event energy for the recorded and simulated seismicity over the monitoring period. With the same rock strength for detritic coal and xylite-rich coal, both μ and σ of the logarithmic energy are fairly consistent during the twelve-week modelling period, fluctuating around 4.0 and 0.65, respectively. In contrast, strong rock strength for xylite-rich coal leads to a marked increase in both μ and σ when the xylite-rich zone is approached. μ and σ peak within one week before or after reaching the xylite-rich zone, and gradually decline until the end of the monitoring period. This is justified by the fact that more microseismic events releasing relatively large energy happen in the xylite-rich zone, shifting the domain of distribution to the right as well as stretching this domain.

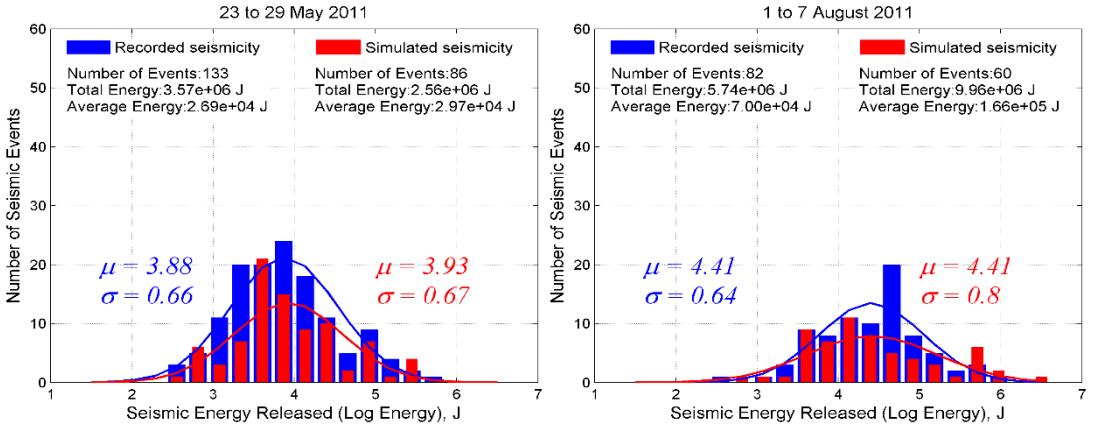


Figure 7.7. Example of weekly histograms of the logarithmic event energy for the recorded seismicity and simulated seismicity for the scenario $\sigma_{ch} = 2\sigma_{cc}$, $\sigma_{th} = 2\sigma_{tc}$: (a) during Week 23 to 29 May 2011, and (b) during Week 1 to 7 August 2011.

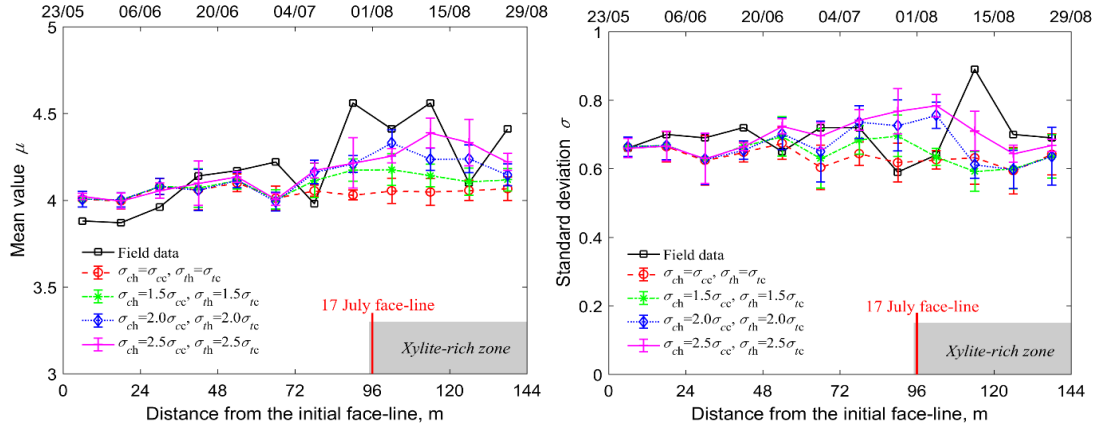


Figure 7.8. The fitted Gaussian distribution parameters to the logarithmic event energy for the recorded and simulated seismicity over the monitoring period: (a) mean value μ, and (b) standard deviation σ.

7.3.4 Average stress drop

Figure 7.9 presents the variation of simulated average resultant stress drop in each week during face advance towards the xylite-rich zone. It can be seen that for the scenario with strong xylite-rich coal, the resultant average stress drop remains quite consistent during the first few production weeks, increases up to three weeks before the xylite-rich zone is encountered and fluctuates till the end of the monitoring period.

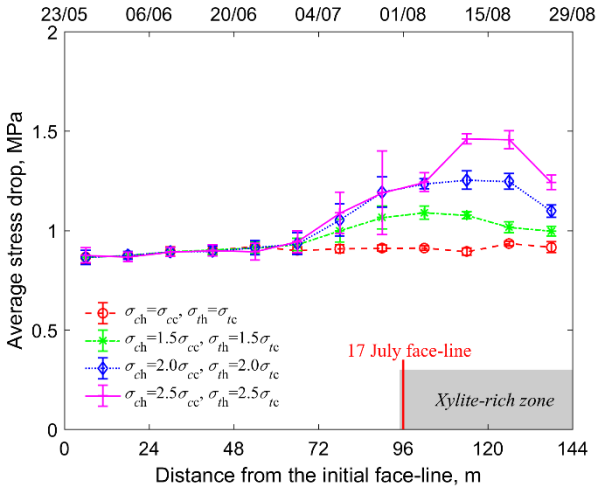


Figure 7.9. Simulated average stress drops over the twelve-week monitoring period.

In order to analyse the magnitude distribution of stress drops during coal extraction, the histograms of stress drops during two typical production weeks for the scenario $\sigma_{ch} = 2\sigma_{cc}$, $\sigma_{th} = 2\sigma_{tc}$ are plotted in Figure 7.10. It can be seen that stress drops form two clusters for the week 30 May to 5 June. Considering various rock strength properties for different geological structures, it is deduced that stress drops from events occurring in coal and clay range from 0.84 to 1.08 MPa, and that those from events taking place in roof goaf are between 0.25 and 0.42 MPa. In contrast, one more cluster ranging from 2.17 to 2.33 MPa, corresponding to microseismic events occurring in the xylite-rich zone, is observed during the week 1 to 7 August. The average stress drop in this cluster is more than twice that from events happening in detritic coal and clay. In addition, the number of events that occur in detritic coal and clay decreases remarkably. Therefore, the energy released from microseismic events is enhanced when the xylite-rich zone is reached.

7.4 Results: effect of fracture attributes on seismic response

7.4.1 Frequency-magnitude distribution

Figure 7.11 presents the variation of fitted *b* values from frequency-magnitude distribution of recorded and simulated microseismicity over the monitoring period. For modelling scenarios with lower power law length exponent *a* of embedded fractures within the xylite-rich zone, *b* values of mining-induced microseismicity begin to decrease during 20 June to 3 July and reach the bottom just before encountering the xylite-rich zone. The lower the length exponent a_h of embedded fractures within the

xylite-rich zone, the larger the reduction in fitted *b* values of simulated microseismicity. An average *b* value as low as 0.72 can be fitted when approaching the xylite-rich zone for the modelling scenario $a_h = 1.8$, $\alpha_h = 0.7\alpha_c$.

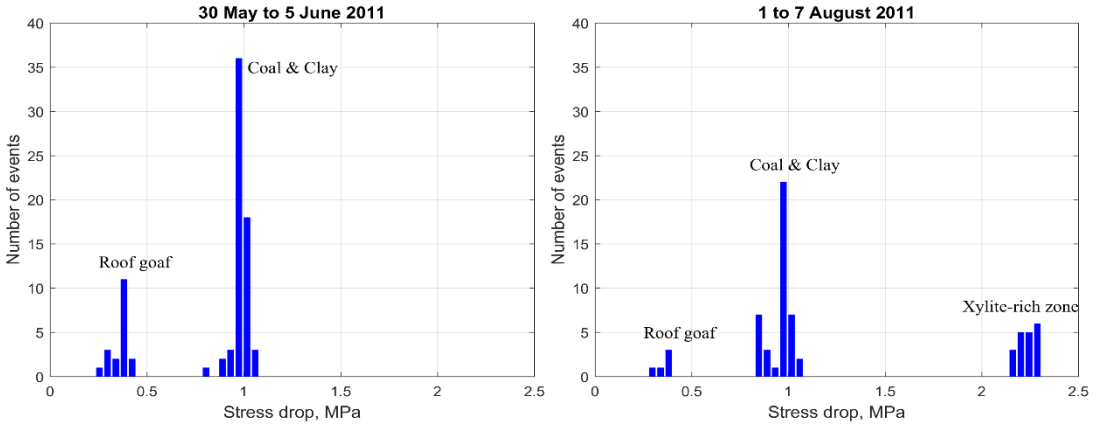


Figure 7.10. Histograms of stress drops for the scenario $\sigma_{ch} = 2\sigma_{cc}$, $\sigma_{th} = 2\sigma_{fc}$: (a) during Week 30 May to 5 June 2011, and (b) during Week 1 to 7 August 2011.

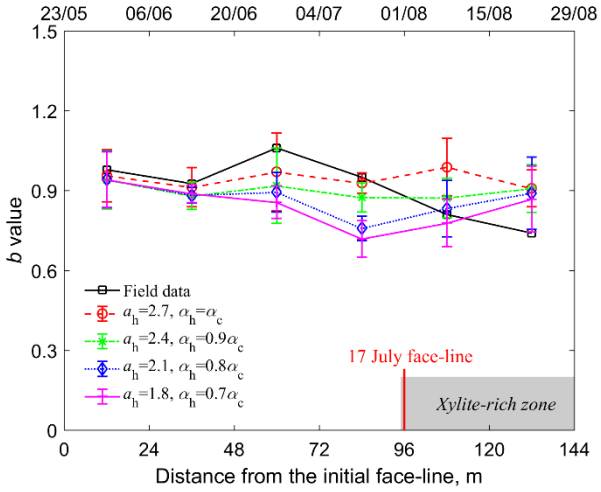


Figure 7.11. The bi-weekly *b* values for frequency-magnitude distribution of the recorded and simulated microseismic events over the monitoring period.

Figure 7.12 shows an example of the frequency-magnitude distribution of recorded and simulated microseismicity during a two-week period after reaching the xylite-rich zone. The frequency-magnitude distribution for different modelling scenarios remains a power law relationship, with the slope (*b* value) positively correlated with the length

exponent a_h of embedded fractures within the xylite-rich zone. When $a_h = 1.8$, $\alpha_h = 0.7\alpha_c$, the fitted b value is in good agreement with that of recorded microseismicity.

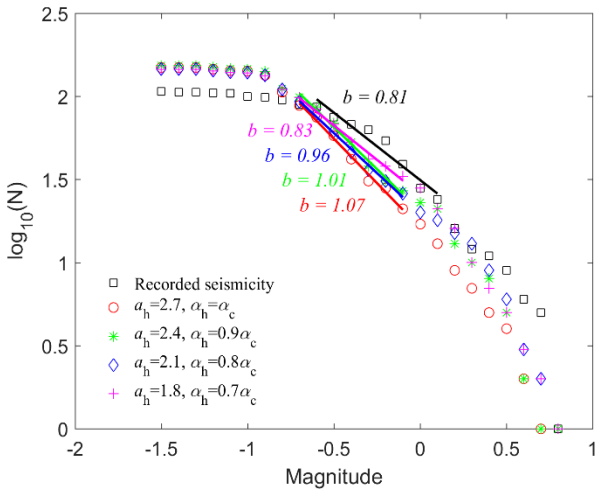


Figure 7.12. Examples of b values obtained through regression fitting for the recorded and simulated microseismic events during 1 to 14 August 2011.

7.4.2 Logarithmic released energy

Figure 7.13 presents examples of weekly histograms of the logarithmic event energy for the field data and modelling scenario $a_h = 1.8$, $\alpha_h = 0.7\alpha_c$ before and after reaching the xylite-rich zone, respectively. It can be observed that the rightward shift of bins to higher energy levels after encountering the xylite-rich zone can be simulated with lower a_h values. In addition, the number of simulated microseismic events decreases after reaching the xylite-rich zone, as observed in the recorded microseismicity.

Figure 7.14 shows fitted Gaussian distribution parameters to the logarithmic event energy for the recorded and simulated seismicity over the monitoring period. With the same fracture attributes for detritic coal and xylite-rich coal ($a_h = 2.7$, $\alpha_c = 2.7$), both μ and σ of the logarithmic energy are fairly consistent over the coal production period. In contrast, low length exponents a_h of embedded fractures within the xylite-rich zone lead to a slight increase in μ and a noticeable increase in σ when the xylite-rich zone is reached. This is the result of increased slippage chance of relatively large fractures within the xylite-rich zone given a lower a_h value. However, low a_h values alone, even as low as 1.8, cannot completely account for the remarkable increases in both μ and σ of the logarithmic energy of the recorded microseismicity.

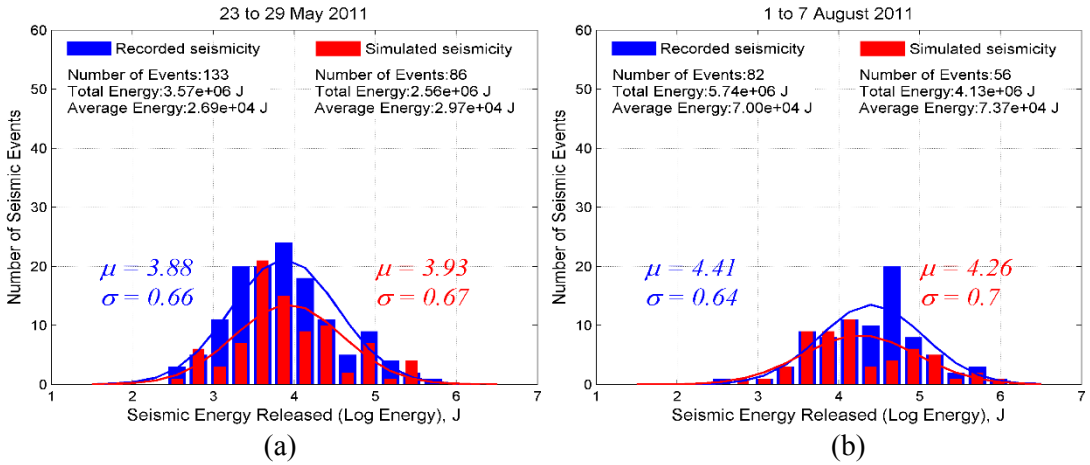


Figure 7.13. Examples of weekly histograms of the logarithmic event energy for the recorded seismicity and simulated seismicity for the scenario a_h = 1.8, $\alpha_h = 0.7\alpha_c$: (a) during Week 23 to 29 May 2011, and (b) during Week 1 to 7 August 2011.

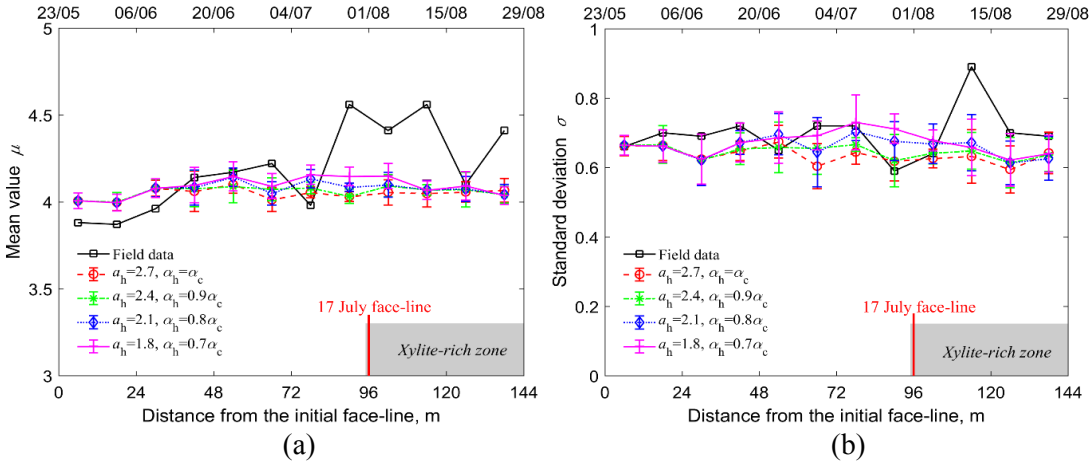


Figure 7.14. The fitted Gaussian distribution parameters to the logarithmic event energy for the recorded and simulated seismicity over the monitoring period: (a) mean value μ, and (b) standard deviation σ.

7.4.3 Average slipped fracture size

The slipped fracture size is closely associated with the seismic energy release. It can be observed from Figure 7.15 that the weekly average slipped fracture size is fairly steady over the monitoring period for the scenario a_h = 2.7, $\alpha_h = \alpha_c$, but experiences an increase when approaching the xylite-rich zone for modelling scenarios with lower a_h values. This is consistent with the variation trend of weekly fitted average value μ of the logarithmic energy. It is noted that, even for the same modelling scenario, there is a noticeable difference between the average slipped fracture sizes obtained from

different DFN realisations. This discrepancy can be attributed to the intrinsic stochastic nature in size distribution and spatial distribution of embedded fractures.

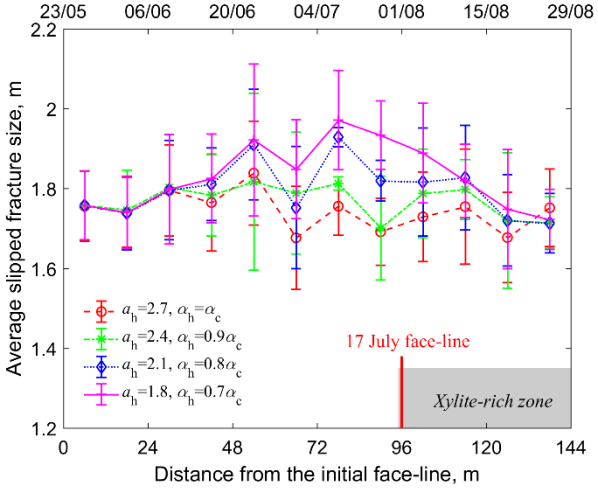


Figure 7.15. Average slipped fracture sizes over the monitoring period.

In order to analyse the distribution and variation of slipped fracture sizes, the weekly histograms for two production weeks for the scenario $a_h = 1.8$, $\alpha_h = 0.7\alpha_c$ are plotted in Figure 7.16. For both coal production weeks, the larger the slipped fracture sizes, the lesser the number of slipped fractures. During the week 1 to 7 August, however, there is a much smaller number of small slipped fracture sizes on the left of the histogram, followed by a longer tail comprising of relatively large slipped fracture sizes. The maximum slipped fracture size also increases from less than 5.5 m during the week 30 May to 5 June to over 6.0 m during 1 to 7 August. Therefore, the less dominance of small slipped fractures within the xylite-rich zone (lower a_h values) contributes to the increase in the average slipped fracture size when reaching the xylite-rich zone.

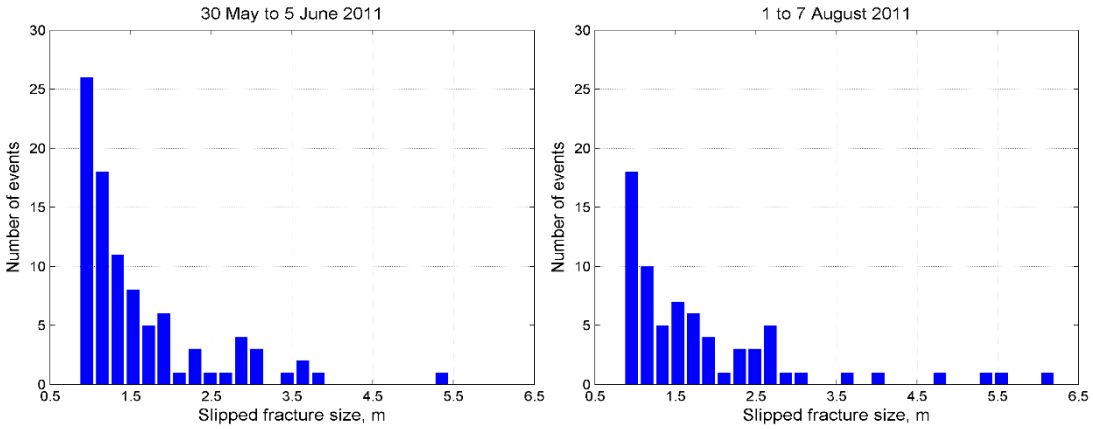


Figure 7.16. Histograms of average slipped fracture sizes for the scenario $a_h = 1.8$, $\alpha_h = 0.7\alpha_c$: (a) during Week 30 May to 5 June 2011, and (b) during Week 1 to 7 August 2011.

7.5 Discussion

As shown in Equation (6.13), the seismic energy released is proportional to the square of stress drop. Given that the strength of xylite-rich coal is higher than that of detritic coal, less fracturing would be expected to take place in xylite-rich coal, and thus less intensity in microseismicity, than in detritic coal under the same stress conditions. However, once failure has occurred in the xylite-rich zone, the associated stress drop, and thus seismic energy released, would be much larger than those in the surrounding detritic coal matrix.

Similarly, the seismic energy released is proportional to the cube of fracture size (Equation (6.13)). Given that less fractures are embedded within the xylite-rich zone, less microseismic events would occur in xylite-rich coal under the same stress conditions. In addition, a larger proportion of large fractures within the xylite-rich zone would lead to a larger slippage chance for large fractures, and thus increased seismic energy release under the same stress conditions.

It is noticed that the decrease in fitted *b* values from frequency-magnitude distribution (Figure 7.5 and Figure 7.11) and the increase in fitted Gaussian distribution parameters (Figure 7.8 and Figure 7.14) begin several weeks before reaching the xylite-rich zone in the models. Considering that mining-induced microseismic events can take place up to 80-100 m ahead of a longwall face-line, seismic characteristics of events from a heterogeneous zone can be detected before the zone is reached. In this respect, seismic

anomaly may be utilised as a precursory indicator for abnormal geological stratum or fracture attributes.

7.6 Conclusions

In this chapter, the microseismic occurrences and associated energy release associated with progressive advance of the K.-50/C panel towards a xylite-rich coal zone over a twelve-week period at Coal Mine Velenje were simulated utilising the developed microseismicity modelling approach in FLAC^{3D}. The heterogeneity of the xylite-rich zone was taken into account by varying rock strength of the xylite-rich coal and fracture attributes within the xylite-rich zone, respectively.

When the longwall face-line is far from the xylite-rich zone, the fitted *b* values from frequency-magnitude distribution and fitted Gaussian distribution parameters of microseismicity are fairly consistent during the coal extraction period, which is in agreement with the field observations. Once higher strength properties were assigned to the xylite-rich coal elements or fractures with lower fracture intensity and scaling exponent were embedded within the xylite-rich zone, a reduction in fitted *b* values and an increase in fitted Gaussian distribution parameters were observed as the longwall face approached the heterogeneous zone. Therefore, both the high rock strength of xylite-rich coal and low scaling exponent of fractures within the xylite-rich zone contribute to these deviations. These deviations are believed to result from the combined effects of increased stress drops and slipped fracture sizes when the xylite-rich zone is approached. The results of this work can provide implications for a precursory detection of abnormal geological strata and fracture attributes.

Chapter 8 Unloading induced dynamic stress perturbations contributing to rock bursts

8.1 Introduction

When underground extractions are conducted in a relatively short period of time, the load transferred from the removed rock/coal acts on surrounding rock/coal in a dynamic manner, introducing distinct excitation to adjacent underground structures and openings. Both rock burst and coal and gas outbursts are considered as problems of dynamic instability under excavation unloading conditions: rock bursts are a violent failure of highly-stressed rock triggered by dynamic stress perturbations, while coal and gas outbursts are attributed to excavation unloading followed by gas desorption-driven rapid propagation of fractures. This chapter focuses on the demonstration of excavation unloading induced dynamic stress perturbations as a source of vibration to trigger unstable rock failure, such as rock bursts, through two theoretical examples designed by the author.

The first example is the dynamic disturbance to adjacent pillars induced by dynamic pillar recovery, which is simplified to a problem of loading on a one-dimensional pre-stressed pillar. A mechanistic model based on structural dynamics is developed to evaluate the stress state and deformation of the pillar adjacent to the removed pillar, and a dynamic amplification coefficient is proposed to quantify the maximum vertical pillar load.

The second example is the dynamic disturbance to adjacent mine openings induced by dynamic excavation unloading, which is simplified to a problem of loading on a two-dimensional pre-stressed circular opening. Transient solutions of the response of the opening subjected to instantaneous and quasi-static unloading wave incidences are expressed as integrals of the steady-state solution using the wave function expansion

method. The dynamic stress concentration factor is further used to characterise dynamic perturbations around the existing circular opening.

8.2 Dynamic stress disturbance induced by pillar recovery

8.2.1 Problem definition

A flatly dipping coal seam extracted by the room-and-pillar method usually leaves a group of pillars acting as support for the overburden and surface structures. For the sake of increasing mine life and total return on investment, parts of residual pillars may be extracted after room-and-pillar mining, and vertical loads are redistributed and applied on adjacent pillars. Under higher stress levels, this may trigger the instability of neighbouring pillars, or even give rise to catastrophic progressive pillar collapses in large mined-out areas.

Figure 8.1 illustrates the recovery process of underground pre-stressed pillars. Only vertically designed pillar workings dominated by compressive stress are considered so as to minimise the impacts of shear loading on the behaviour of pillars (Suorineni *et al*., 2014, 2011). It is widely accepted that pillars adjacent to a removed pillar are prone to be damaged or even crushed by load transferred from the removed pillar. However, from the perspective of dynamics, the response of neighbouring pillars is caused by unloading disturbance emanating from the removed pillar. Specifically, loads acting on the top and bottom of an excavated pillar can be replaced by statically equivalent stresses. Instantaneous pillar recovery means sudden unloading of the equivalent stresses, initiating a dynamic unloading wave travelling away from the removed pillar. All rock/coal particles subjected to this wave tend to move towards the opposite direction of wave propagation. When the wave reaches adjacent pillars, the exerted force acts on both the top and bottom of pillars in the loading direction. Adjacent pillars, therefore, are subjected to the combined effects of the initial vertical stress (Figure 8.1a), and dynamic disturbance of rock masses (Figure 8.1b). The dynamic stress acting on adjacent pillars oscillates in a short time, and eventually converges to a fixed value equal to the redistributed overburden load.

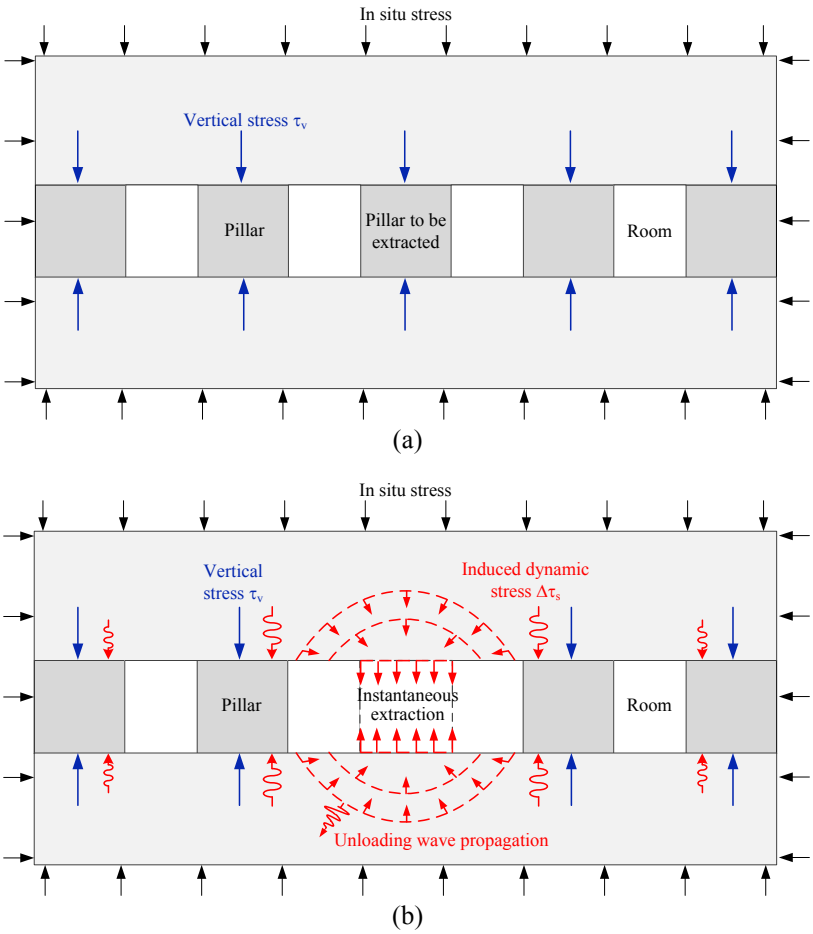


Figure 8.1. Schematic of instantaneous pillar recovery and induced dynamic response of adjacent pillar workings: (a) before pillar recovery, and (b) after pillar recovery.

With a large pillar spacing, the effect of incident wave's curvature is marginal, and the wave can be roughly treated as an elastic plane wave on adjacent pillars (Pao and Mow, 1973). In this respect, the dynamic response of pillar workings induced by pillar recovery can be simplified to a problem of loading on a one-dimensional pre-stressed pillar. The dynamic behaviour of adjacent pillars is primarily associated with the initial vertical stress, the transferred load, and the compressive strength of pillars. In the following sections, the pillars are assumed to be linearly elastic before failure and of regular shape. The instability criterion based on the coupled static and dynamic theory for pillar workings will first be introduced. The initial and transferred vertical pillar loads will then be calculated, and the dynamic pillar behaviour in response to neighbouring pillar recovery will be further assessed.

8.2.2 Dynamic instability criterion for pillar workings

In this work, rock/coal is considered to become unstable when the released energy exceeds the energy consumed in the failure process (Dou *et al*., 2015). The criterion can be given by:

$$\frac{dU}{dt} = \frac{dU_s}{dt} + \frac{dU_d}{dt} > \frac{dU_f}{dt} \tag{8.1}$$

where U is the total released energy in the extraction, U_s is the strain energy stored in the rock/coal to be extracted, U_d is the external energy from the dynamic disturbance, and U_f is the energy needed to be consumed in fracturing rock/coals. This criterion is applicable for rock/coal under both two- and three-dimensional stress states.

For pillar workings under uniaxial compressive stress state, the total released energy is:

$$U = \frac{(\sigma_s + \sigma_d)^2}{2E} \tag{8.2}$$

where E is the elastic modulus of the pillar, and σ_s and σ_d are static and dynamic pillar loads, respectively.

Similarly, U_f can be computed using the critical stress σ_{cri}, i.e., the pillar load under the critical equilibrium state:

$$U_f = \frac{\sigma_{cri}^2}{2E} \tag{8.3}$$

Substituting Equations (8.2)(8.3) to (8.1), the criterion becomes:

$$\sigma_s + \sigma_d \geq \sigma_{cri} \tag{8.4}$$

Combining Equations (8.4) and (8.12), the criterion for dynamic instability can be simplified to:

$$\sigma_v^{max} \geq \sigma_{cri} \tag{8.5}$$

8.2.3 Initial and transferred vertical pillar loads

Practical methods in estimation of vertical pillar loads have been a focus of research for many years. The tributary area method can be used to estimate the average pillar load for a reasonably uniform pattern of pillars by assuming that each pillar bears a

proportionate share of the total overburden load (Brady and Brown, 2013). After mining exploitation, the vertical load on any remnant pillar is related to the initial overburden loading and the near field extraction ratio. But this method does not account for interactions between adjacent pillars and between pillars and surrounding strata, possibly leading to a significant overestimation of vertical pillar loads (Roberts *et al*., 2002). Poulsen (2010) developed a pressure arch theory (PAT)-based method to calculate the average vertical stress acting on pillars of irregular geometries. Considering that pillars interact with adjacent pillars and surrounding strata within a lateral zone of influence, extraction ratios averaged over several pillars rather than the local extraction ratio for a single pillar are used in calculation. In this work, the PAT-based method was used to estimate initial vertical pillar loads and transferred loads after pillar recovery.

The load transfer distance (LTD) (unit: m) first introduced in the work of Abel (1988) represents the maximum distance that load can be transferred. Based on *in situ* measurements of 55 pillars within sedimentary deposits, the fitting quadratic function between the pillar depth H (unit: m) and the LTD can be written as:

$$\mathrm{LTD} = -1\times10^{-4}H^2 + 0.2701H \tag{8.6}$$

In the PAT-based method, the zone of influence (ZI) can be considered to be a circular area centred at the pillar with radius r, as illustrated in Figure 8.2. Both r and ZI are associated with the LTD, and can be computed respectively by (Poulsen, 2010):

$$r=2\mathrm{LTD}+\frac{w_\mathrm{e}}{2} \tag{8.7}$$

$$\mathrm{ZI}=\pi(2\mathrm{LTD}+\frac{w_\mathrm{e}}{2})^2 \tag{8.8}$$

where w_e is the effective width for non-square pillars, which is 4 times the ratio of pillar area to pillar circumference.

The vertical pillar load σ_v can be estimated by (Poulsen and Shen, 2013):

$$\sigma_\mathrm{v} = \frac{\rho g H}{1-e} \tag{8.9}$$

where e is the extraction ratio in the ZI of the pillar, and is given by:

$$e = \frac{\mathrm{EA}}{\mathrm{ZI}} \tag{8.10}$$

where EA denotes the excavated area in the ZI, as illustrated in Figure 8.2.

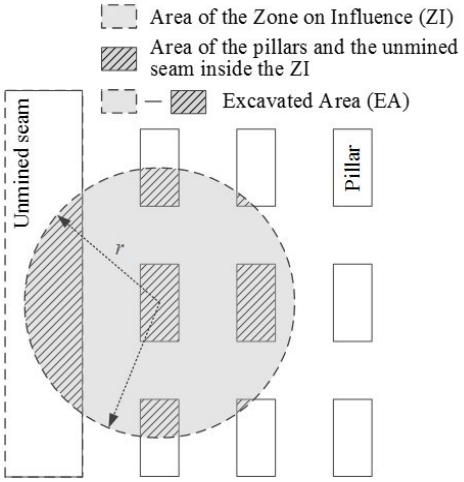


Figure 8.2. Pillar geometry and the zone of influence used in the PAT-based method.

After pillar recovery, the load previously carried by the removed pillar will be redistributed and act on neighbouring pillars or surrounding rock. For any pillar that remains unbroken, Equation (8.9) can be used to estimate the vertical pillar stresses σ_{v}^{0} and σ_{v}^{1} before and after adjacent pillar recovery. If the removed pillar locates within the ZI of any pillar, the vertical load on that pillar would increase with the increase in its EA after pillar recovery. The increment in the vertical pillar load, termed the transferred load, can be given by:

$$\Delta\sigma_{\mathrm{s}} = \sigma_{\mathrm{v}}^{1} - \sigma_{\mathrm{v}}^{0} \tag{8.11}$$

For any pillar to support the transferred load, $\Delta\sigma_{\mathrm{s}}$ depends on the percentage of the area of the removed pillar to that of the ZI. However, the transferred load acts on adjacent pillars in a dynamic manner, and can thus be much larger in practical mining activities. In this regard, the maximum induced vertical load will be computed from a dynamics viewpoint, which will be described in Section 8.2.4.

8.2.4 Pillar recovery-induced dynamic stress

Figure 8.3 illustrates the dynamic response of a pre-stressed pillar subjected to a suddenly applied load. The pillar is initially under compressional stress σ_{v}^{0}. When a transferred load is applied, the stress equilibrium is disturbed, and the pillar compression undergoes an acceleration stage until the vertical load reaches σ_{v}^{1}. At that moment, the vertical pillar stress is equal to the external load, indicating that it would be the equilibrium position for the pillar. Then the speed of pillar compression declines until reaching the maximum compressional position. The pillar would oscillate around and finally converge to the equilibrium position.

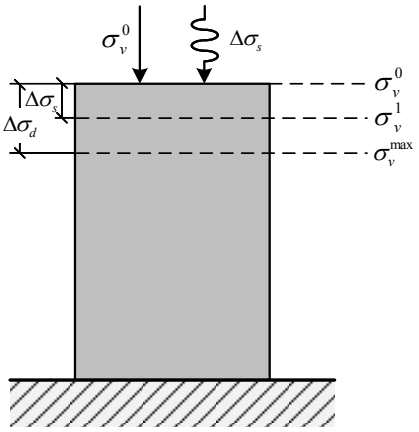


Figure 8.3 Dynamic response of a pre-stressed pillar subjected to a suddenly applied loading.

The induced disturbance to a pillar can be characterised by the dynamic amplification coefficient *R*, defined as the ratio of the dynamic increased vertical pillar load to the final transferred load. The maximum dynamic amplification coefficient $R_{\max}$ is achieved at the maximum compression position. The maximum vertical pillar load $\sigma_{\mathrm{v}}^{\max}$ can be expressed in terms of $R_{\max}$:

$$\sigma_{\mathrm{v}}^{\max}=\Delta\sigma_{\mathrm{d}}+\sigma_{\mathrm{v}}^{0}=R_{\max}\cdot\Delta\sigma_{\mathrm{s}}+\sigma_{\mathrm{v}}^{0} \tag{8.12}$$

When a pillar is extracted using the blasting method, the support to the roof is released in a very short time, and the overburden load is transferred to adjacent pillars. It is assumed that the load transfer duration is t_0. For any single neighbouring pillar, the time-dependent transferred load is considered to act as a single ramp loading followed

by constant loading, as illustrated in Figure 8.4. The loading history can be mathematically expressed as:

$$\sigma(t)=\begin{cases}\Delta\sigma_{\mathrm{s}}\dfrac{t}{t_0} & t<t_0\\ \Delta\sigma_{\mathrm{s}} & t\geq t_0\end{cases} \tag{8.13}$$

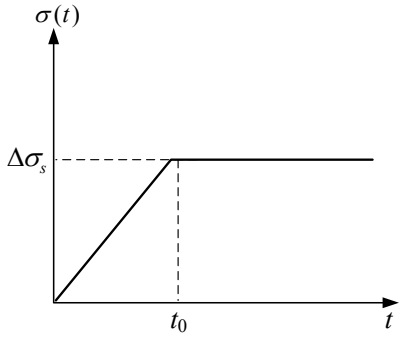


Figure 8.4. Loading history of a transferred pillar load.

The pillar response to dynamic loads can be analysed by means of structural dynamics. Consider a dynamic impulse $\sigma(\tau)$ acting on a static linearly elastic undamped system over time interval $d\tau$ at time τ, the resultant pillar response to the impulse at time t is:

$$y(t)=\frac{\sigma(\tau)d\tau}{m\omega}\sin\frac{2\pi}{T}(t-\tau),\ t\geq\tau \tag{8.14}$$

in which m and T are the mass and natural vibration period of the pillar, respectively. The mass and natural vibration period can be correlated by the elastic stiffness K of the pillar:

$$T=2\pi\sqrt{m/K} \tag{8.15}$$

Equation (8.14) is approximate for finite impulse duration, and it becomes accurate when the duration approaches zero. The entire loading history $\sigma(t)$ can be considered to consist of a succession of such short impulses, each giving rise to its own differential response. For the linearly elastic system, the total response can be obtained by integrating all differential responses over the loading time, which is known as the Duhamel integral equation (Clough and Penzien, 2003):

$$y(t)=\int_0^t \frac{\sigma(\tau)}{m\omega}\sin\frac{2\pi}{T}(t-\tau)d\tau=\frac{T}{2\pi\cdot m}\int_0^t \sigma(\tau)\sin\frac{2\pi}{T}(t-\tau)d\tau,\ t\geq\tau \qquad (8.16)$$

The pillar deformation in response to the time-dependent loading can be obtained by combining Equations (8.13)(8.15)and (8.16):

$$y(t)=\begin{cases}\dfrac{y_s}{t_0}\left(t-\dfrac{T}{2\pi}\sin\dfrac{2\pi}{T}t\right) & t<t_0\\ y_s\left[1-\dfrac{T}{\pi t_0}\cos\dfrac{2\pi}{T}(t-\dfrac{t_0}{2})\sin\dfrac{\pi t_0}{T}\right] & t\geq t_0\end{cases} \qquad (8.17)$$

where y_s is the pillar deformation increment given by $y_s=\Delta\sigma_s/K$. For the linearly elastic pillar, the deformation is proportional to the induced vertical stress, which can be written as:

$$\frac{y(t)_{\max}}{y_s}=\frac{\Delta\sigma_d}{\Delta\sigma_s}=R_{\max} \qquad (8.18)$$

Substituting Equations (8.17) to (8.18) gives the maximum dynamic amplification coefficient $R_{\max}$ in Equation (8.12):

$$R_{\max}=\max R(t)=\max\begin{bmatrix}\dfrac{1}{t_0}\left(t-\dfrac{T}{2\pi}\sin\dfrac{2\pi}{T}t\right) & t<t_0\\ 1-\dfrac{T}{\pi t_0}\cos\dfrac{2\pi}{T}(t-\dfrac{t_0}{2})\sin\dfrac{\pi t_0}{T} & t\geq t_0\end{bmatrix} \qquad (8.19)$$

It can be observed from Equation (8.19) that, given the natural vibration period T, $R_{\max}$ depends on the pillar recovery time t_0. To investigate the impact of pillar recovery time on dynamic response of adjacent pillars, the time-varying dynamic amplification coefficients for t_0 = 0, 0.01T, 0.5T, 1.0T and 2.0T respectively is presented in Figure 8.5. t_0 = 0 means instantaneous pillar recovery, which yields a $R_{\max}$ as much as 2. It can be seen that when t_0 is shorter than 0.01T, $R_{\max}$ approximates to that in the case of t_0 = 0. When the extraction time is longer than T, $R_{\max}$ becomes 1, suggesting no evidence of dynamic effect. When t_0 ranges from 0.01T to T, $R_{\max}$ falls in the range between 1 and 2.

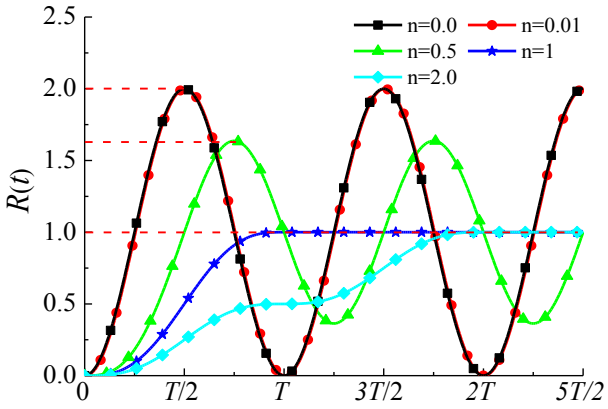


Figure 8.5. Dynamic amplification coefficients of a pillar for different extraction time ($n = t_0/T$).

Based on *in situ* microseismic measurements, the natural vibration period of rock masses is generally in a magnitude of 10^{-1} s (Pan *et al*., 2007). Using the blasting method, the fragmentation of rock/coal accompanied with the release of *in situ* stress takes places in several to tens milliseconds (10^{-3}-10^{-2} s) (Lu *et al*., 2012). Therefore, the induced dynamic amplification coefficient for a neighbouring pillar can exceed 1.5 or even approach 2, which brings about great threats to pillar stability according to Equation (8.5).

8.3 Dynamic stress disturbance induced by excavation unloading

8.3.1 Problem definition

This section focuses on the problem of underground excavation unloading impact on a neighbouring circular excavation. Stress analysis of excavation in elongated underground openings can be simplified as a plane strain problem for the sake of theoretical formulation (Jaeger *et al*., 2009). Figure 8.6 illustrates two circular excavations positioned at a certain distance in a hydrostatic stress state, where the one on the right is pre-existing and the one on the left to be excavated. The stress state of the rock/coal (Figure 8.6a) can be obtained via superposition of a static stress field (Figure 8.6b) and a tensile radial traction applied to excavation surfaces under unstressed conditions (Figure 8.6c) (Carter and Booker, 1990). More specifically, the stress state of the new excavation surface prior to excavation is the initial *in situ* stress P_0 as illustrated in Figure 8.6b. When excavation begins, a traction force that is equivalent to the unloaded stress force and that varies with time is applied to the internal boundary of the new excavation site (Figure 8.6c). Similarly, the stress state

of the existing excavation surface (Figure 8.6a) can be obtained by adding redistributed stress at the same point (Figure 8.6b) to the dynamic tensile stress disturbance from the new excavation (Figure 8.6c). In turn, the problem focuses on the dynamic response of a pressurised cavity subjected to tensile wave excitation. As no forms of deformation or displacement are shown in Figure 8.6b, the dynamic response can only be solved using the model shown in Figure 8.6c.

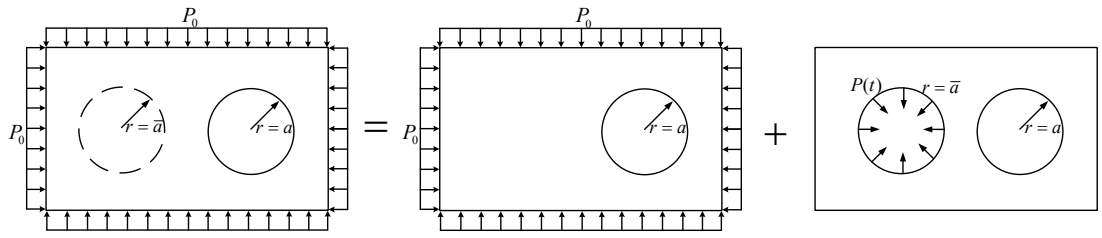


Figure 8.6. Schematic illustration showing the superposition principle applied to the stress analysis of a pre-stressed excavation opening subjected to dynamic disturbance.

It is noted that that an excavation is assumed to have no effect on stress redistribution processes in the vicinity of the new excavation explored in this model. This is attributed to the fact that the pre-mining stress field of only a limited domain would significantly differ from the virgin stress field after excavation (Brady and Brown, 2013). However, this may lead to significant errors owing to the narrow excavation spacing configurations used in this model, as the released radial stress is not exactly what is claimed in Figure 8.6b. In this work, both excavations examined have a radius a, and the minimum excavation spacing configuration considered is set as no less than $5a$ to accurately represent both static and dynamic stress forces around the excavations.

8.3.2 Dynamic responses of an existing excavation under transient wave incidence

The dynamic response of an existing excavation can be simplified as an analysis of circular holes under cylindrical wave forces. A cylindrical tensile stress pulse arising from the new excavation boundary travels in the positive x-direction and envelops the existing excavation symmetrically from $\theta = \pi$. Due to the presence of the circular excavation boundary, the propagation of this unloading wave is equivalent to that of a wave arising from a line source, i.e., the central axis of the new excavation.

This creates mathematical difficulties associated with analysing interactions between transient excitation forces and cavities. One solution is to represent the effect of transient wave excitation in terms of the superposition of harmonic wave excitation, based on the fact that waves of any form can be decomposed to harmonic waves having different frequencies. The response of a circular hole under harmonic wave excitation has been obtained using the wave function expansion method by Mow and Pao (1971). The geometry of the problem is illustrated in Figure 8.7, where r and $\bar{r}$ are distances from a point to the centres of the existing and new excavations, respectively; θ and $\bar{\theta}$ are the angles at the centres of the existing and new excavations, respectively; a and $\bar{a}$ are the radii of the existing and new excavations, respectively; and r_0 denotes excavation spacing.

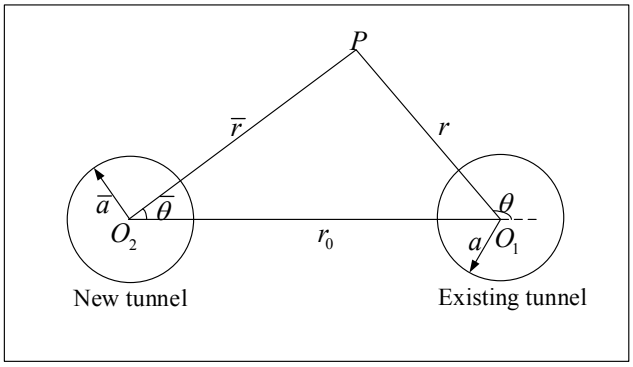


Figure 8.7. A schematic diagram showing the dynamic response of the existing excavation subjected to cylindrical wave excitation.

The dynamic stress concentration factor (DSCF), i.e., the steady-state dimensionless tangential stress defined as the ratio of the tangential stress at the excavation boundary subjected to an incident plane *P* wave over the radial stress at the same position without the circular excavation, was proposed to characterise dynamic perturbations at boundary of pre-existing excavations (Mow and Pao, 1971). DSCF can be expressed by:

$$\bar{\sigma}_{\theta\theta}\big|_{r=a} = \frac{4i}{\pi}\left[H_0^{(1)}(\alpha\bar{r}) - \frac{1}{\kappa^2-1}H_2^{(1)}(\alpha\bar{r})\right]^{-1}\sum_{n=0}^{\infty}(-1)^n\varepsilon_n H_n^{(1)}(\alpha r_0)S_n\cos n\theta e^{-i\omega t} \quad (8.20)$$

where κ is the ratio of P to S wave velocities, α and β are compressional and shear wave numbers, $H_n^{(1)}(x)$ is the first type of Hankel function, ω is the circular frequency, $\varepsilon_n = \begin{cases} 1, & n=0 \\ 2, & n \geq 1 \end{cases}$, and $S_n = \frac{N_n}{D_n}$, where

$$N_n = (n^2-1)\beta a H_{n-1}^{(1)}(\beta a) - (n^3 - n + \frac{1}{2}\beta^2 a^2) H_n^{(1)}(\beta a) \tag{8.21}$$

$$D_n = \alpha a H_{n-1}^{(1)}(\alpha a) N_n - H_n^{(1)}(\alpha a)\left[(n^3 - n + \frac{1}{2}\beta^2 a^2)\beta a H_{n-1}^{(1)}(\beta a) - (n^2 + n - \frac{1}{4}\beta^2 a^2)\beta^2 a^2 H_n^{(1)}(\beta a) \right] \tag{8.22}$$

The Fourier transform technique was applied to obtain the transient response of an existing excavation from the steady-state response. The transient dimensionless tangential stress around an existing excavation under any input function $f(\bar{\tau})$ is given by:

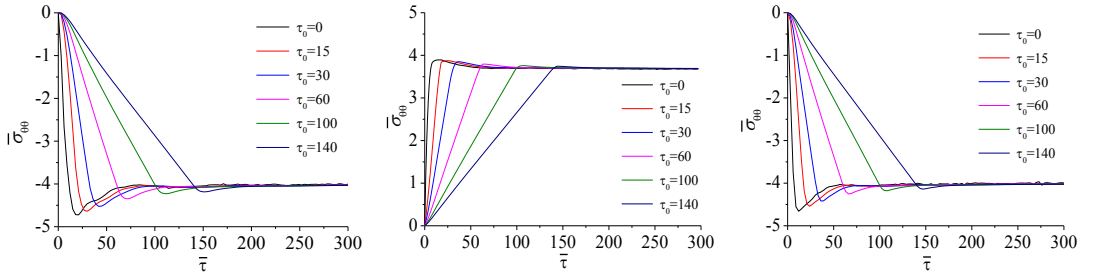
$$\sigma_{\theta\theta}(\bar{\tau})\big|_{r=a} = \frac{1}{\sqrt{2\pi}} \int_{-\infty}^{\infty} \bar{\sigma}_{\theta\theta}\big|_{r=a} \cdot F(\zeta) e^{-i\zeta\bar{\tau}} d\zeta \tag{8.23}$$

where $\bar{\tau}$ is the elapsed time normalised by the time required to travel through the length of the radius a, and $F(\zeta)$ is the transformed form of $f(\bar{\tau})$.

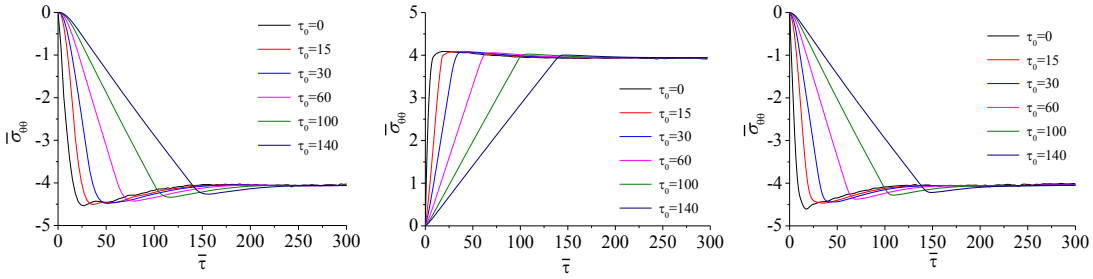
The theoretical formulation for stress released instantaneously or over a period of time can be obtained from Equation (8.23) by varying the input function $f(\bar{\tau})$. A numerical solution algorithm referred to as trapezoidal approximation (Stovel, 1967) was applied to obtain numerical transient wave excitation results for both dynamic and quasi-static unloading conditions.

8.3.3 Results and analysis

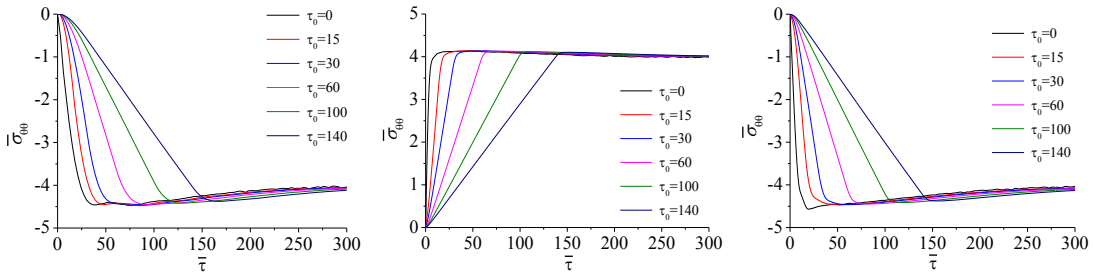
Calculations were conducted for the following set of parameters: a bulk modulus of K = 10.8 GPa, a shear modulus of G = 16.5 GPa, and a density of ρ = 2,520 kg/m^3. Figure 8.8 presents DSCF variations around the existing excavation over time when r_0/a is 5, 10 and 20. The dynamic response under plane wave excitation is also presented for comparison purposes (Mow and Pao, 1971). As vibrations vary in relation to observation locations, DSCF variations at θ = 0, $\pi/2$ and π are shown.



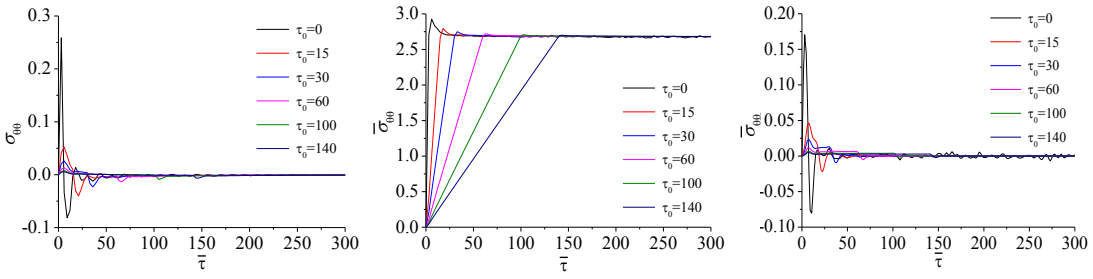
(a) $\frac{r_0}{a}=5,\ \theta=0$ (b) $\frac{r_0}{a}=5,\ \theta=\frac{\pi}{2}$ (c) $\frac{r_0}{a}=5,\ \theta=\pi$



(d) $\frac{r_0}{a}=10,\ \theta=0$ (e) $\frac{r_0}{a}=10,\ \theta=\frac{\pi}{2}$ (f) $\frac{r_0}{a}=10,\ \theta=\pi$



(g) $\frac{r_0}{a}=20,\ \theta=0$ (h) $\frac{r_0}{a}=20,\ \theta=\frac{\pi}{2}$ (i) $\frac{r_0}{a}=20,\ \theta=\pi$



(j) Plane wave, $\theta=0$ (k) Plane wave, $\theta=\frac{\pi}{2}$ (l) Plane wave, $\theta=\pi$

Figure 8.8. Numerical results of the DSCF at the pre-existing excavation boundary.

Figure 8.8 shows the correlation between DSCF and the normalised unloading period. DSCF at $\theta=0$ follows a similar trend as that when $\theta=\pi$, denoting that the dynamic unloading process has an effect on both locations. As shown in Figure 8.8a, b, c,

dynamic effects subjected to instantaneous unloading yield maximum values at $\theta = 0$, $\pi/2$ and π. During the incidence process, the DSCF roughly varies based on a linear path. When the normalised unloading time increases to $\tau_0 = 140$, the dynamic response becomes virtually unnoticeable. DSCF values at different locations converge to the static stress concentration factor after the passage of waves, which are given by

$$\sigma^*_{\theta\theta} = -4\left[1 - \frac{2\sin^2\theta}{1+(a/r_0)^2 + 2(a/r_0)\cos\theta}\right]$$

for cylindrical waves and by

$$\sigma^*_{\theta\theta} = \frac{2}{\kappa^2}[(\kappa^2 - 1) - 2\cos 2\theta]$$

for plane waves (Mow and Pao, 1971). The analogous static solution for plane waves is Kirsch's static solution for biaxial loadings, the far field stress (P_0) in one direction, and stress caused by the Poisson's effect ($P_0\upsilon/(1 - \upsilon)$) in the other direction (Mow and Pao, 1971).

It is also noted that the dynamic effect diminishes as excavation spacing increases. To facilitate the quantitative analysis, the dynamic effect coefficient η is defined as the ratio of the difference between the maximum DSCF and final value (SCF) over the final value. The dynamic effect coefficients for the above 12 scenarios are presented in Table 8.1. In regard to cylindrical wave incidence, maximum and final values at $\theta = \pi/2$ increase as excavation spacing increases, though the dynamic effect drops from 5.42% when $r_0/a = 5$ to 3.52% when $r_0/a = 20$. The final value at $\theta = 0$ and π remains at -4 while the maximum absolute value decreases with an increase in r_0/a, and dynamic effects also decrease with excavation spacing. It is worthwhile noting that the DSCF is much larger at $\theta = 0$ and π than when $\theta = \pi/2$. When r_0/a approaches infinity with increasing r_0 values, it can be deduced that both the maximum and final stress will tend toward zero, denoting no dynamic effects. However, in regard to plane wave excitation, the results are quite different: while the unloading wave induces lower maximum and final values at $\theta = \pi/2$, the dynamic effect can reach as high as 10.11%. In addition, the DSCF approaches zero at $\theta = 0$ and π. Thus, when a vibration source is adjacent to an excavation, dynamic responses differ from those at longer distances.

Furthermore, the critical point of stress concentration shifts from $\theta = \pi$ under a cylindrical wave to $\theta = \pi/2$ under a plane wave.

Table 8.1. Dynamic effects of the existing excavation subjected to instantaneous unloading disturbance.

	$\theta = 0$			$\theta = \pi/2$			$\theta = \pi$		
	DSCF	SCF	η	DSCF	SCF	η	DSCF	SCF	η
$r_0/a = 5$	-4.72	-4.00	18.0%	3.89	3.69	5.4%	-4.66	-4.00	16.5%
$r_0/a = 10$	-4.54	-4.00	13.5%	4.09	3.92	4.3%	-4.62	-4.00	15.5%
$r_0/a = 20$	-4.46	-4.00	11.5%	4.12	3.98	3.5%	-4.58	-4.00	14.5%
Plane wave	0.26	0	--	2.94	2.67	10.1%	0.17	0	--

8.4 Conclusions

In this chapter, theoretical models were presented to verify the physical plausibility of dynamic stress disturbances induced by underground excavation, including dynamic pillar recovery, and dynamic excavation unloading.

The dynamic stress acting on a pillar adjacent to pillar recovery was evaluated using a mechanistic model based on structural dynamics. The induced disturbance to the pillar can be characterised by the dynamic amplification coefficient R, the ratio of the increased vertical pillar load to the transferred load. The results have shown that R_{max} is associated with the extraction time and the natural vibration period of rock mass. During pillar recovery using blasting method, R_{max} can exceed 1.5 or even approach 2. The results have indicated that the maximum load carried by pillar workings would be largely underestimated if the dynamic effect resulting from pillar recovery is ignored in the design of pillar workings. Pillar workings designed to small safety factors can be considered as stable according to conventional methods, while in fact dynamic instability might be triggered in the event of dynamic disturbance.

The dynamic stress around an existing excavation subjected to unloading wave excitation was analysed based on the wave function expansion method. The dynamic perturbations can be characterised by the dynamic stress concentration factor (DSCF), the steady-state dimensionless tangential stress at excavation boundary. The findings indicate that dynamic stress becomes concentrated around the existing excavation subjected to unloading waves, with a DSCF up to 18 % for an excavation spacing 5

times of the excavation radius. Strong dynamic stress effect is attributed to short unloading period of the adjacent excavation, high levels of initial stress, and short excavation spacing. Therefore, dynamic unloading disturbances should be considered when designing and supporting adjacent underground openings in regions characterised by high levels of stress.

Chapter 9 Unloading induced gas-driven rapid fracture propagation in coal and gas outbursts

9.1 Introduction

It has been recognised that the coal and gas outbursts are triggered by excavation unloading followed by gas-driven rapid propagation of a system of pre-existing or mining-induced fractures. Based upon this understanding, this chapter presents a coal and gas outburst model based on fracture mechanics and gas dynamics, where gas-containing fractures parallel to a working face experience opening first, then expansion and rapid propagation stages under unloading conditions.

The model is numerically implemented to simulate the occurrence of coal and gas outbursts when development headings approach towards an outburst prone zone. The simulated temporal evolution of coal and gas outbursts in terms of ejected volume of coal, stress and gas pressure, and fracture growth are presented, and key parameters (coal properties and geological conditions) contributing to coal and gas outbursts in terms of both burst potential and intensity are identified and discussed.

9.2 A coal and gas outburst model based on fracture mechanics and gas dynamics

9.2.1 Conceptual model

Figure 9.1 illustrates a schematic of a coal seam with a working face and an induced failure zone ahead of the face, and the resulting stress redistribution. In addition, fractures oriented parallel to the advancing face are also created near the face. Here, the focus is on a newly formed penny-shaped fracture (which is initially closed), and its subsequent opening and propagation as the face advances. The fracture is subjected to an internal gas pressure p as well as the external stress (the minor principal stress σ_{min}). The dynamic fracture behaviour is controlled by the effective stress ($\sigma_{eff} = p$-

σ_{min}). The intra-fracture gas pressure is affected by the fracture opening (aperture) and inward gas migration. The latter tends to offset the pressure reduction caused by fracture volume increase. In this work, it is assumed that the gas inflow is predominantly the result of gas desorption from the surrounding coal matrix.

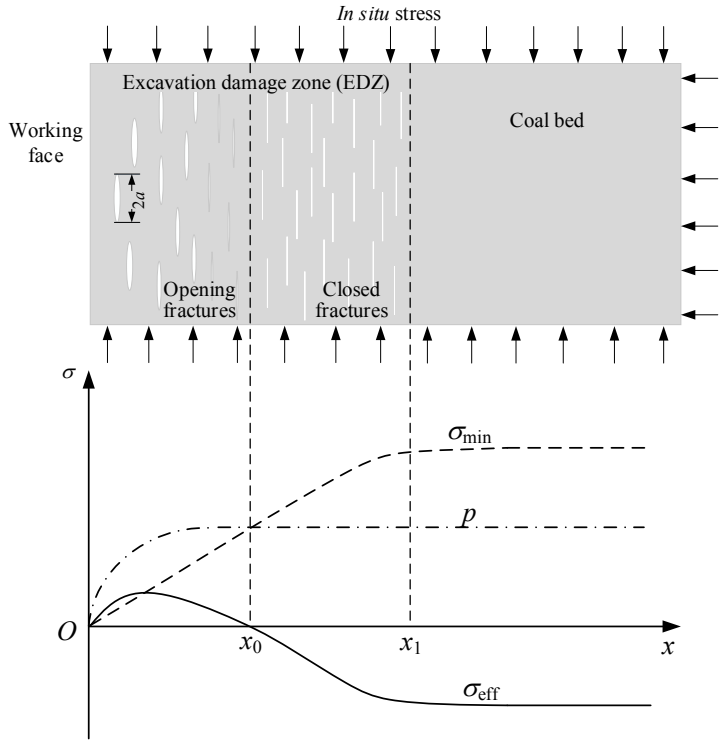


Figure 9.1. Schematic representation of fracture opening in relation to effective stress changes ahead of a working face (modified after Feldman *et al.*, 2017).

This model does not take into account the gas pressure variation caused by gas flow. This is because gas flow in coal occurs at a time scale of tens of hours or days under *in situ* stress conditions, whilst a coal and gas outburst lasts a very short time from several to tens of minutes, during which process only a tiny amount of gas flows from the coal seam towards the opening. The in-seam gas pressure, or the initial gas pressure saturated in micro-pores in the pristine coalbed, can thus be considered as constant during the coal and gas outbursts.

9.2.2 Fracture behaviour subjected to intra-fracture effective stress

As shown in Figure 9.1, the minor principal stress acting on a fracture decreases as the face advances towards it. Therefore, the effective stress increases correspondingly,

becoming positive eventually. Considering that there is a time-lag in the seam gas pressure response to face advance, the model developed assumes that the initial fracture pressure is equal to the initial seam gas pressure. As the working face advances, the fracture is likely to experience opening first, then expansion and rapid propagation under the interplay of gas pressure and stress. Subscripts for relevant parameters such as fracture radius, fracture volume, intra-fracture gas pressure, etc., are assigned according to evolutional stages, where 0 stands for initial values, 1 for values at the opening and expansion stages, and 2 for values in the propagation stage.

(1) Fracture opening triggered by excavation unloading.

The volume of the induced penny-shaped fracture of radius a and thickness d is given by:

$$V_c = \pi a^2 d \tag{9.1}$$

The fracture volume as a function of the prevailing effective stress can be obtained by considering the work done by the prevailing effective stress. The total work W done to form a disk-shaped fracture in solid under three-dimensional (3D) stress conditions is given by (Sneddon, 1946):

$$W = \frac{8(1-\upsilon^2)\sigma_{\text{eff}}^2 a^3}{3E} \tag{9.2}$$

where υ and E are the Poison's ratio and the Young's modulus of coal, respectively.

The work done is equal to half the integral of the product of the traction over the whole fracture surface and the displacement (Sack, 1946):

$$W = \pi a^2 \sigma_{\text{eff}} d / 2 \tag{9.3}$$

Combining Equations (9.1), (9.2) and (9.3), the volume of an isolated fracture embedded in a coal seam can be written as (Odintsev, 1997):

$$V_c = \frac{16(1-\upsilon^2)a_0^3 \sigma_{\text{eff, 0}}}{3E} \tag{9.4}$$

The saturation gas pressure in the virgin coal seam is usually much lower than the *in situ* stress, which suggests that the fracture in the virgin coal seam remains closed according to Equation (9.4). When the advancing face reaches a distance less than x_0

to the fracture in Figure 9.1, the change of stress conditions results in the opening of the fracture (Equation (9.4)).

(2) Gas desorption and its migration into the fracture.

Fracture opening results in an initial decrease in the intra-fracture gas pressure, which prompts the desorption of gas from the coal surrounding the fracture and its subsequent migration to the fracture. Considering the short duration of a coal and gas outburst, the surrounding coal contributing to gas desorption is assumed to be two loosened surficial microlayers with gas-containing micro-pores on both sides of the fracture. The volume of the two microlayers is given by (Odintsev, 1997):

$$V_{\text{coal}}=2\pi a_1^2 h \tag{9.5}$$

where h is the thickness of the loosened surficial microlayer.

The initial volume of adsorbed gas at pressure P is:

$$V_{\text{total}}=\rho V_{\text{coal}} V \tag{9.6}$$

where ρ is the density of coal, and V is the adsorbed gas volume per unit mass of coal at pressure P.

According to gas adsorption kinetics, the volume of desorbed gas V_{g} following a sudden drop in the gas pressure from p to atmospheric pressure p_{atm} is written as (Crank, 1979):

$$\frac{V_{\text{g}}}{V_{\text{total}}}=1-\frac{6}{\pi^2}\sum_{n=1}^{\infty}\frac{e^{-n^2\pi^2\kappa t}}{n^2} \tag{9.7}$$

where t is the gas desorption time, and κ is the diffusivity of coal which is associated with diffusion coefficient and coal particle radius. For a small gas desorption time, which is the case in the context of this research, the equation has an asymptotic approximation (Smith and Williams, 1984):

$$\frac{V_{\text{g}}}{V_{\text{total}}}=6\sqrt{\frac{\kappa t}{\pi}} \tag{9.8}$$

The total volume of gas that can be desorbed due to the change in gas pressure is limited by the Langmuir isotherm (Equation (2.1)).

The resulting gas pressure p_1 in the fracture with volume V_c is related to V_g by the ideal gas law:

$$V_c p_1 = V_g p_{atm} \tag{9.9}$$

Meanwhile, V_c is also a function of the gas pressure following Equation (9.4):

$$V_c = \frac{16(1-\upsilon^2)a_1^3(p_1-\sigma_{min})}{3E} \tag{9.10}$$

Substituting Equations (9.8) and (9.10) to (9.9) yields the gas pressure p_1 in the fracture.

The fracture radius remains constant ($a_0 = a_1$) at this stage, but the fracture volume continuously increases as gas pressure builds up. If the accumulated gas pressure is not sufficient to drive fracture propagation, gas release into the fracture would proceed until the desorbed gas maintains a certain intra-fracture pressure p_{equ} at which gas adsorption and desorption reach an equilibrium, according to the methane adsorption isotherm. p_{equ} can be obtained by combining Equations (2.1) and (9.9). It is noted that the intra-fracture gas pressure p_1 is in the range of (σ_{min}, p_{equ}), and that p_{equ} ranges in (σ_{min}, p_0).

(3) Fracture propagation.

Given a certain *in situ* stress, fracture expansion is only dominated by kinetic gas desorption lasting up to tens or hundreds of hours. However, once intra-fracture gas pressure reaches a certain limit, the fracture would begin to propagate immediately. Based on linear elastic fracture mechanics (LEFM), the material is deemed to fail when the stress intensity factor at a fracture tip, either for mode I (opening mode, K_I) or mode II (sliding mode, K_{II}), reaches a critical value K_{Ic} or K_{IIc}. K_{II} would be zero when there are no free surfaces; otherwise, the interaction between the fracture and the free surface gives rise to a finite K_{II}. However, the stress intensity factor for the mode II (K_{II}) at the tip of a fracture adjacent to a free surface, which is the case in this work, is considerably smaller than that for the mode I (K_I) (Dyskin and Germanovich, 1993). This allows using the stress intensity factor criterion only for the mode I in the evaluation of fracture propagation:

$$K_I \geq K_{Ic} \tag{9.11}$$

where K_{Ic} is the fracture toughness of coal.

The stress intensity factor K_I for a fracture embedded in an infinite domain can be expressed in terms of effective stress and fracture radius as:

$$K_I = 2\sigma_{eff}(a/\pi)^{1/2} \tag{9.12}$$

During fracture propagation, the following equation holds for an isothermal process according to the ideal gas equation of state:

$$p_1 V_{c1} = p_2 V_{c2} = znRT = \text{constant} \tag{9.13}$$

Fracture propagation propelled by a certain volume of desorbed gas results in an increase in fracture radius and a drop in gas pressure as governed by Equations (9.4) and (9.13). Substituting Equations (9.4) and (9.13) in Equation (9.12), it can be found that K_I monotonically decreases as the gas pressure decreases when $p \geq \sigma_{min}$, which suggests that the propagation would cease at a state where the following equation is satisfied:

$$K_{I2} = 2(p_2 - \sigma_{min})(a_2/\pi)^{1/2} = K_{Ic} \tag{9.14}$$

It is noted that gas continues to desorb and flow into the fracture due to the decreased intra-fracture gas pressure after the fracture propagates. On the other hand, as Equation (9.14) suggests, the increase in fracture radius aggravates the vulnerability of the fracture by lowering the critical intra-fracture gas pressure that is needed for further propagation. This suggests that, once a fracture begins to propagate, it would keep on propagating, rather than reaching a state of equilibrium under continuous gas desorption conditions.

From then on, gas desorption and fracture propagation occur simultaneously. The intra-fracture gas pressure p_2 decreases towards σ_{min}, and the fracture radius increases until a coal fragment is separated from the coal seam and extruded by the residual gas pressure. Given the same fracture radius, fracture toughness and gas desorption conditions, the fracture closest to the free surface is the least loaded and can reach the fracture propagation criterion the most readily. The coal failure induced by this fracture would then turn the next fracture closest to it to one as the most susceptible to failure. In this way, a relatively small spacing between multiple parallel fractures would lead to successive propagation of fractures and coal expulsion from the coal seam, i.e., a coal and gas outburst.

9.2.3 Estimation of outburst threshold limits

The threshold limits of coal and gas outbursts can be estimated according to Equations (9.11) and (9.12) using practical ranges of parameters. Figure 9.2 presents critical stress intensity factor K_I for fractures associated with different values of fracture toughness K_{Ic}, fracture radius a_0, and effective stress p-σ_{min}. As can be seen, large fracture radius, high effective stress and low fracture toughness have a favourable effect on the potential for coal and gas outbursts. For typical coal properties and effective stresses faced in coal mining, the minimum fracture radius that can trigger unstable failure spans from below 10^{-4} to over 10^{-3} m.

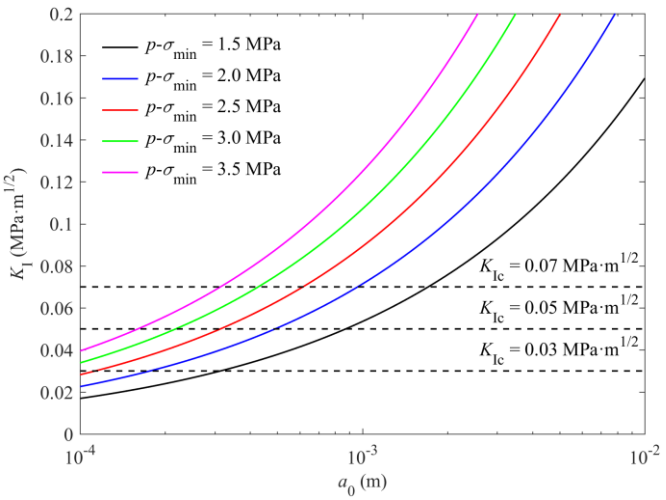


Figure 9.2. Stress intensity factors K_I as a function of fracture radius a_0 and effective stress p-σ_{min}. Fractures are deemed to propagate if $K_I \geq K_{Ic}$.

The criterion for coal and gas outbursts can equally be expressed in terms of intra-fracture gas pressure, that is, a fracture with continuous inflow of desorbed gas is deemed to propagate if the critical intra-fracture gas pressure p_{lim} to drive fracture propagation is lower than that at adsorption/desorption equilibrium p_{equ}. As coal and gas outbursts initiate from the working face, it is essential to examine the criterion for fracture propagation at this specific location where the minor principal stress can be approximated as 0. As illustrated in Figure 9.3, the intra-fracture gas pressure threshold p_{lim} associated with different values of fracture toughness K_{Ic}, fracture radius a_0 and initial gas pressure p_0 for fractures located close to a working face were calculated using coal seam properties from Pniowek Colliery in the Upper Silesian Coal Basin in Poland (later presented in Section 9.4). Because p_{equ} is dominated by p_0, and is

independent of strength properties of coal such as fracture toughness K_I or fracture radius a_0, this alternative criterion isolates the impact of initial gas pressure on the potential for coal and gas outbursts.

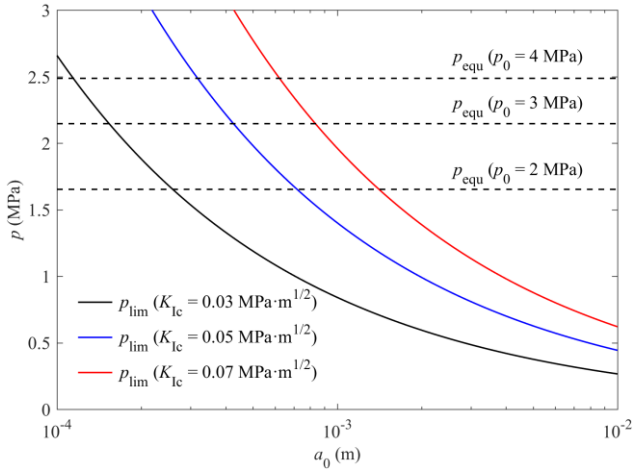


Figure 9.3. Intra-fracture gas pressure p_{lim} as a function of fracture toughness K_{Ic} and fracture radius a_0 for fractures located close to a working face. Fractures are deemed to propagate if $p_{lim} \leq p_{equ}$.

9.3 Numerical implementation of the outburst model

Based upon the preceding analyses, a methodology incorporating stress changes, gas desorption and fracture propagation was developed to model the initiation and temporal evolution of a coal and gas outburst triggered by coal extraction. Because it is computationally intensive to perform explicit simulation of fracture propagation in field-scale models, each element of coal seam in the model is assumed to host a gas-containing micro-fracture of the same length, and the failure of model elements is governed by the propagated lengths of embedded fractures. The outburst modelling procedure developed involves three main steps as detailed below.

The *model set-up and initialisation* start with the construction of a 3D model representing the coal seam extracted and the surrounding strata in FLAC^{3D}. Each coal seam model element is assumed to contain a pre-set fracture perpendicular to the minor principal stress. The elastic model is used as the constitutive model, and mechanical properties are assigned to the grid blocks representing different rock formations. The boundary and initial conditions are then applied to the model so as to reach an initial equilibrium state.

Next, the *simulation of stress redistribution* step is performed. Progressive coal extraction is simulated by a series of coal excavation steps, each of which typically reflects face advance in one or a few working days. In each step, coal extraction activities are mimicked by "removing" grid elements representing the coal to be extracted or ejected. This is achieved by assigning null mechanical properties to these elements. In this way, the loads previously withstood by the "removed" cells are redistributed to the surrounding cells and a new stress equilibrium is established. The stress equilibrium is considered to be achieved instantly after the removal of elements.

In the final modelling step, *fracture behaviour evaluation and associated failure analysis* is performed. At the end of each time step, a subroutine specially-written for this purpose is invoked to check whether the embedded fracture has been triggered to expand, and even grow, for each model element based upon the prevailing stress states. When the outburst criterion induced by coal extraction is met in a host element, this element is ejected from the coal seam. This process is described in Section 9.3.1.

Steps 2 and 3 described above are repeated in each coal extraction step until the end of the physical time to be modelled. A flow chart of the modelling procedure is presented in Figure 9.4.

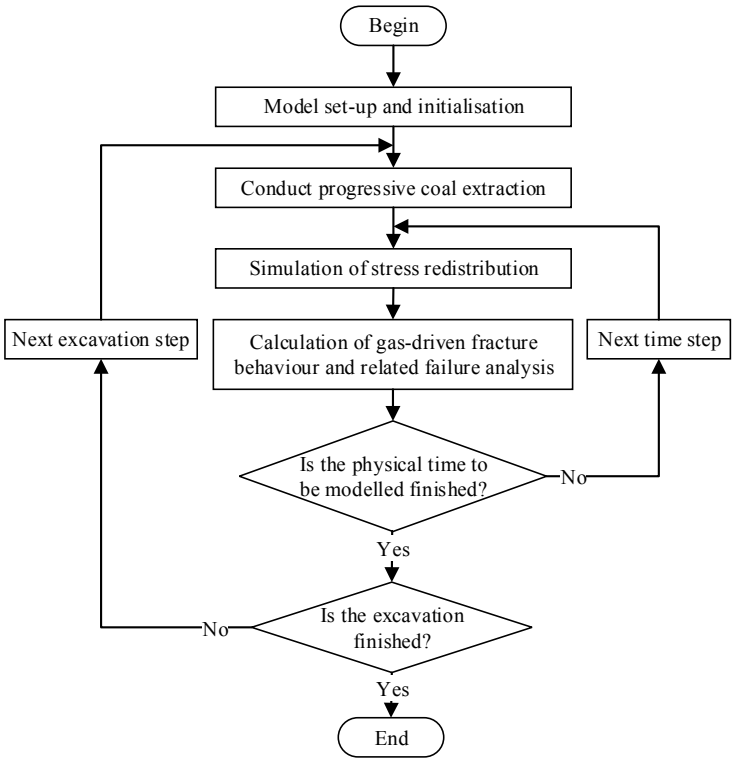


Figure 9.4. Flow chart for the modelling procedure.

9.3.1 Evaluation of fracture behaviour

A pre-set closed fracture, when later on is involved in a coal and gas outburst, is deemed to subsequently undergo opening, expansion and propagation until causing failure. Accordingly, each host element is assigned with a flag indicating its state, i.e., 0 for the undisturbed state (the hosting fracture remains closed), 1 for the disturbed state (the hosting fracture begins expansion and propagation), and 2 for the post-failure state (the hosting fracture runs through the model element). Model elements are traversed to evaluate the change of model state and update fracture attributes and intra-fracture gas pressure at each time step.

For an undisturbed model element (state_flag = 0), the onset of gas desorption is examined based on the intra-fracture effective stress, i.e., the difference between initial in-seam gas pressure and the minor principal stress of its host element. Once the intra-fracture effective stress becomes positive, the host element turns to the disturbed state (state_flag = 1); otherwise this model element remains undisturbed and the cycle moves on to the next model element.

For a disturbed model element (state_flag = 1), gas continuously desorbs and migrates into the embedded fracture, contributing to the build-up of intra-fracture gas pressure, regardless of whether the fracture has propagated or not. The intra-fracture gas pressure at the current time step p_t is first updated according to the time since the onset of gas desorption into the fracture (Equations (9.8) and (9.9)). Two types of assessments are then performed sequentially, examining whether the stress intensity factor criterion is met for fracture propagation, followed by checking whether the intra-fracture gas pressure reaches the gas pressure p_{equ} at equilibrium. Three potential conditions may exist depending on the assessments:

(1) $K_{\mathrm{I},t} \geq K_{\mathrm{Ic}}$: the fracture begins to propagate before reaching the gas adsorption/desorption equilibrium. The increased fracture radius and the associated intra-fracture gas pressure after propagation at the current time step are updated according to Equations (9.13) and (9.14). The fracture propagation velocity can be computed by dividing the increment in fracture radius by the timestep Δt. The fracture propagation is denoted as dynamic if the fracture propagation velocity monotonically increases over time and quasi-static if not.

The host element is considered to enter the post-failure state (state_flag = 2) and be extruded from the coal seam when the fracture length exceeds the element dimension. This failure criterion based on fracture length has been previously applied in numerical analysis at laboratory scale and verified to realistically mimic the failure zone in loaded rock samples (Li and Konietzky, 2015, 2014). Gas-related calculations for this model element will be skipped in subsequent time steps.

(2) $K_{I,t} < K_{Ic}$, $p_t \geq p_{equ}$: gas adsorption and desorption reach equilibrium inside the fracture in the model element so that the gas pressure will be set to p_{equ} in subsequent calculations.

(3) $K_{I,t} < K_{Ic}$, $p_t < p_{equ}$: the cycle will proceed to the next model element. Intra-fracture gas pressure in this model element will further accumulate in subsequent time steps until either the condition (1) or (2) is achieved.

The flow diagram for the implementation of the theoretical model into the geomechanical model is presented in Figure 9.5.

9.4 Model set-up for unloading-induced coal and gas outbursts

The roadway development used as an example to demonstrate the methodology developed in this work utilises the field data and layout from an outburst prone coal seam at Pniowek Colliery, which is located in the Upper Silesian Coal Basin in Poland. The mine is one of the four deep underground coal mines operated by Jastrzebska Spolka Weglowa SA (JSW), the largest hard coking coal producer in Poland and in European Union. The coal resource at the Pniowek Colliery field site contains multiple stratigraphic layers such as mudstone, sandstone, and aleurolite, etc. Pniowek Colliery is exploiting a multi-seam deposit using highly efficient longwall mining. The coal seam used for the modelling and assessment of coal and gas outbursts in this research lies at 720 m depth below sea level. A longwall panel measuring around 800 m long and 250 m wide is being developed in the coal seam modelled.

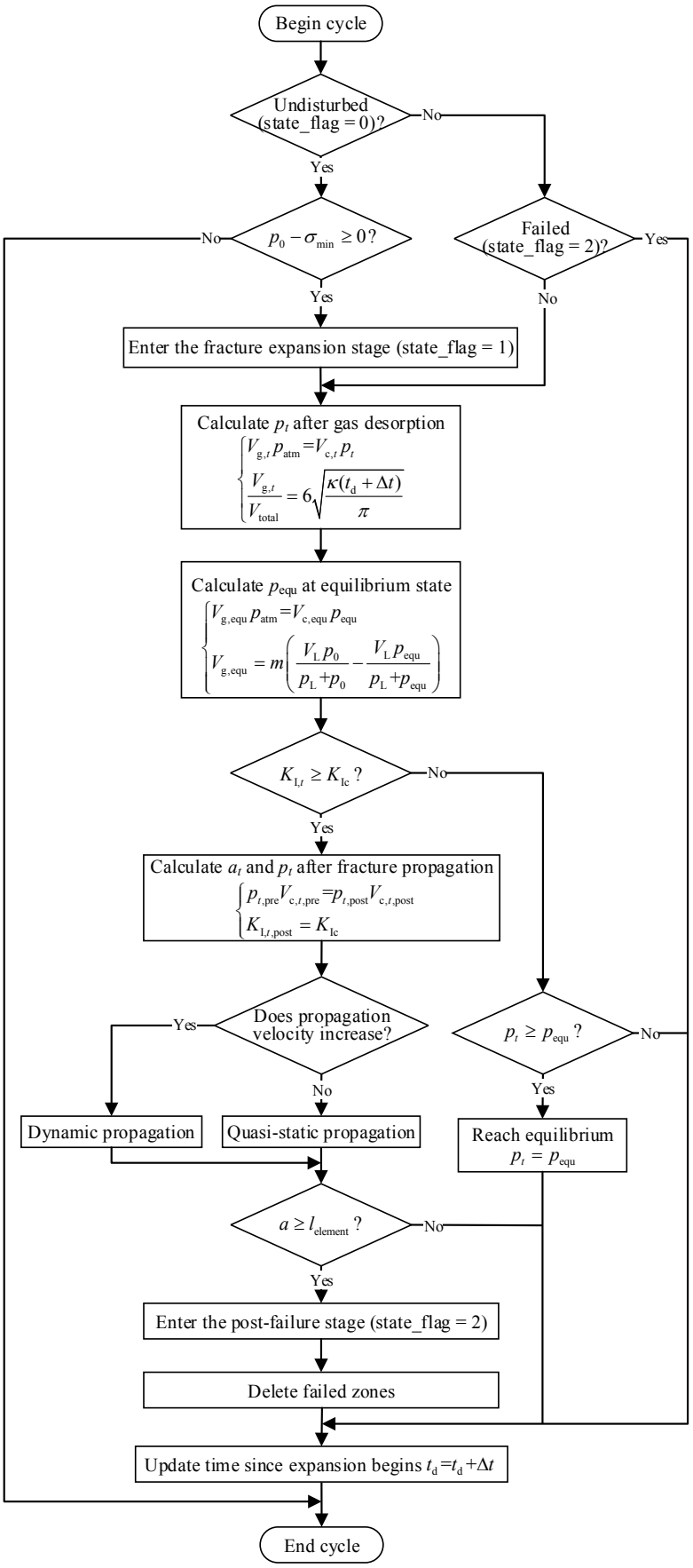


Figure 9.5. Flow diagram for the calculation of the fracture expansion and propagation in a model element at time *t*.

A three-dimensional geomechanical model measuring 30 m × 30 m × 35 m in x, y and z directions respectively was constructed using FLAC^{3D} to simulate the roadway development and the assessment of coal and gas outburst potential at each stage of roadway development. As illustrated in Figure 9.6, the model included the coal layer and surrounding strata around a developing roadway without covering the whole longwall panel in the coal seam. The model depth varied from -1,030 to -940 m levels. The coal seam modelled was located at 1,000 m depth below ground level with a thickness of 3 m. This seam was overlain by a 6 m thick sandstone roof, and underlain by a 16 m thick mudstone floor. The sandstone layer was further underlain by a mudstone layer of 10 m in thickness. A 6 m × 11 m × 3 m outburst prone zone, represented by a much lower coal fracture toughness in the model, was placed in the coal seam 10 m ahead of the roadway, which is developed by progressive excavation steps. The dimension of the elements in the model is 1 m. The elements in the outburst prone zone were refined down to 0.1 m in each direction to better represent the gas pressure evolution and mechanical behaviour in response to roadway development.

Elastic constitutive model was used for all geological structures. The failure of mudstone and sandstone is not considered in the model, and fracture toughness was only assigned to coal formations. Langmuir volume and Langmuir pressure for the coal seam were obtained from the 45°C high pressure adsorption isotherms measured using coal samples collected from the same coal seam. The thickness h of desorption zones around fractures was taken as a/100. The outburst prone zone had the same physical, elastic and reservoir properties as the coal seam and a fracture toughness of a quarter of that of the coal seam (fracture toughness of 0.05 MPa·m$^{1/2}$). Physical, rock mechanical and reservoir properties used for geological structures in the model are summarised in Table 9.1.

The *in situ* vertical stress in the model was induced by the overburden weight (using a density of 2,360 kg/m^3), and the horizontal stresses were estimated by the Poisson's effect under gravity loading of the overburden. The vertical and horizontal stresses at 1,000 m depth were σ_v = 23.13 MPa, and σ_H = σ_h = 9.45 MPa, respectively. The boundary conditions of the model were such that it was laterally confined and fixed at the base. The saturation gas pressure in the virgin coal seam was taken as 3 MPa.

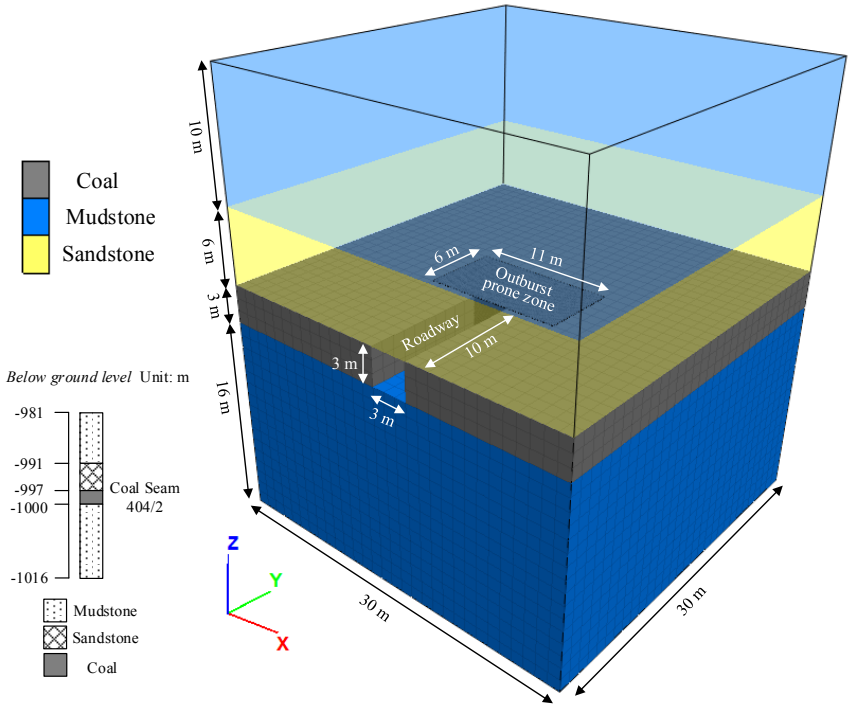


Figure 9.6. General stratigraphy and model geometry of roadway development in the modelled coal seam.

Table 9.1. Model parameters used in the baseline model.

Model parameters	Unit	Coal	Mudstone	Sandstone
Physical properties				
Density	kg/m^3	1290	2360	2360
Rock mechanical properties				
Bulk modulus K	GPa	1.26	6.04	8.00
Shear modulus G	GPa	0.60	3.45	3.70
Fracture toughness K_{Ic}	MPa·m$^{1/2}$	0.20	-	-
Adsorption properties				
Langmuir volume V_L	m^3/kg	0.015	-	-
Langmuir pressure p_L	MPa	1.7	-	-
Diffusivity κ	min^{-1}	7.51×10^{-4}	-	-
Fracture attributes				
Radius a_0	m	0.001	-	-

During geomechanical modelling, a total of five roadway development steps, each representing the removal of a 2 m length of the roadway, were modelled until the roadway reached the outburst prone zone. The timestep for mechanical calculation was automatically determined based on the minimum eigenperiod of model elements, while the timestep for the calculation of gas-driven fracture behaviour was set to 1 s. The physical time to be modelled after each roadway development step was 360 s in the model.

The preceding theoretical analyses in Section 9.2 suggest that the potential and intensity of gas-driven coal outbursts depend on stress and gas pressure conditions as well as coal properties. In order to quantify their roles in evolution of coal and gas outbursts, parametric investigations were further performed by varying four influencing factors, namely fracture toughness of coal, fracture radius, initial gas pressure, and *in situ* stress, while keeping other properties the same as those in the baseline model. The change in i*n situ* stress was achieved by varying the overburden thickness over the coal seam. The model parameters used in the parametric investigations are presented in Table 9.2.

Table 9.2. Parameter magnitude ranges used in the parametric investigations.

Model parameters	Unit	Magnitude range
Coal properties in the outburst prone zone		
Fracture toughness K_{Ic}	MPa·m$^{1/2}$	0.03, 0.04, 0.05*, 0.06, 0.07
Fracture radius a_0	m	0.0005, 0.0007, 0.001*,0.002, 0.005
Stress and gas pressure conditions of the coal seam		
Initial gas pressure p_0	MPa	2.0, 2.5, 3.0*, 3.5, 4.0
Overburden thickness H	m	400, 600, 800, 1000*, 1200

The values denoted with an * are used as default values unless otherwise noted.

9.5 Results and analysis

9.5.1 Coal outburst behaviour of the baseline model

Figure 9.7 presents a plan view of the evolution of intra-fracture gas pressure distribution 360 s after each roadway development step. As can be seen, the intra-fracture gas pressure is relieved within a 2 m wide zone ahead of the development face due to mining-induced stresses, but no coal failure is induced during this first four roadway development steps. As the development heading reaches the outburst prone zone in the fifth step, a coal and gas outburst, which spreads within the outburst prone zone, is initiated, whereby the coal elements are expelled from the seam and a steep gas pressure gradient forms at the outburst front (Figure 9.7e).

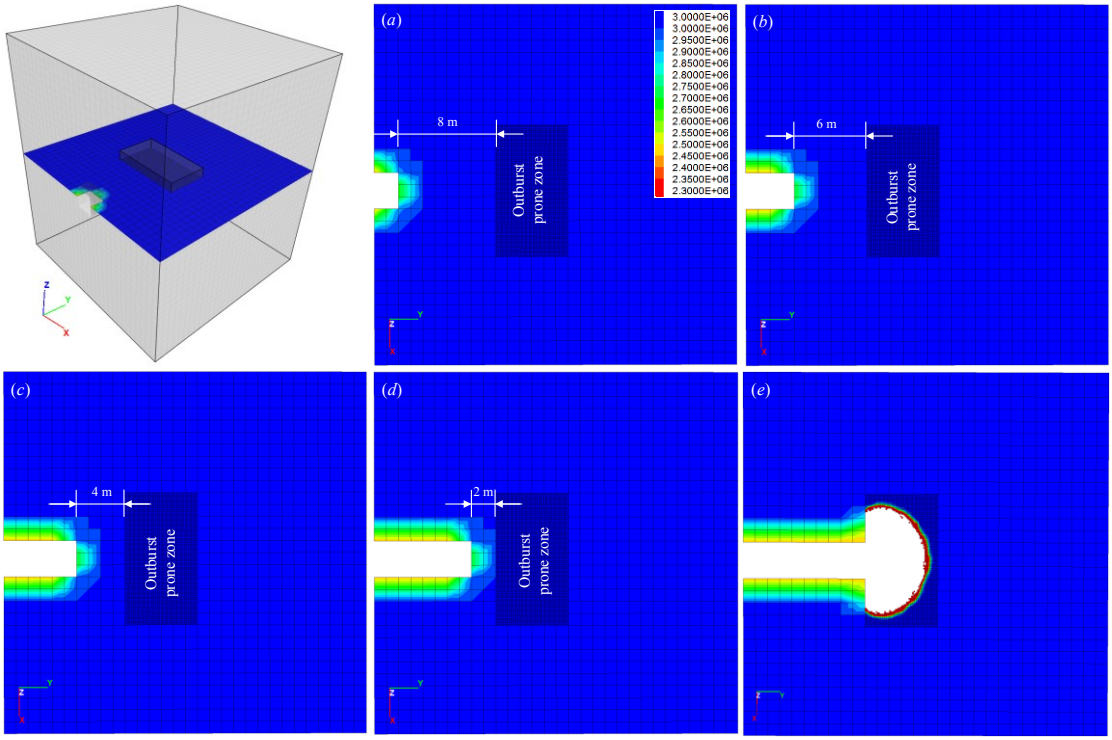


Figure 9.7. Intra-fracture gas pressure distribution caused by gas desorption after each roadway development step (Unit: Pa).

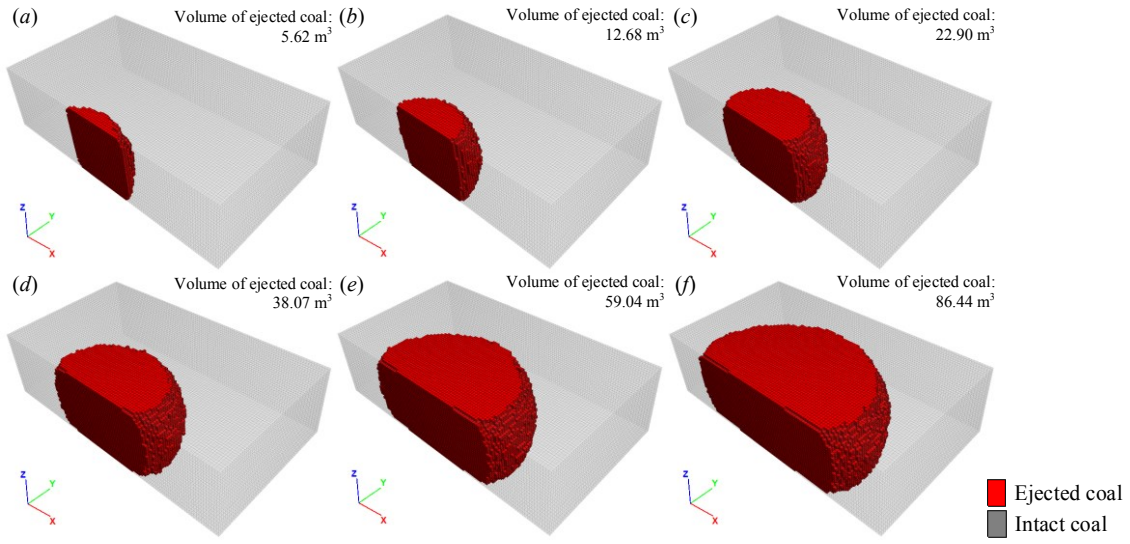


Figure 9.8. Extension of the coal outburst zone over time: (a) 60 s, (b) 120 s, (c) 180 s, (d) 240 s, (e) 300 s and (f) 360 s after reaching the outburst prone zone.

Figure 9.8 illustrates how the coal outburst progresses from the exposed working face into the outburst prone zone. It can be seen that the coal outburst modelled forms a dome-shaped cavity, which is quite common in field observations (Shepherd *et al.*, 1981). Expulsion of coal at the working face causes the subsequent ejection of

neighbouring coal elements by aggravating the release of *in situ* stress and facilitating gas desorption-driven fracture opening and propagation. This results in an accelerated growth of the ejected volume of coal over time. In this perspective, a coal and gas outburst represents a domino effect-type failure, which would proceed continuously given that coal properties, stress conditions and gas pressure remain the same. As illustrated in Figure 9.9, the expansion of the outburst zone follows the same pattern as that represented by the onset of gas desorption from the coal elements.

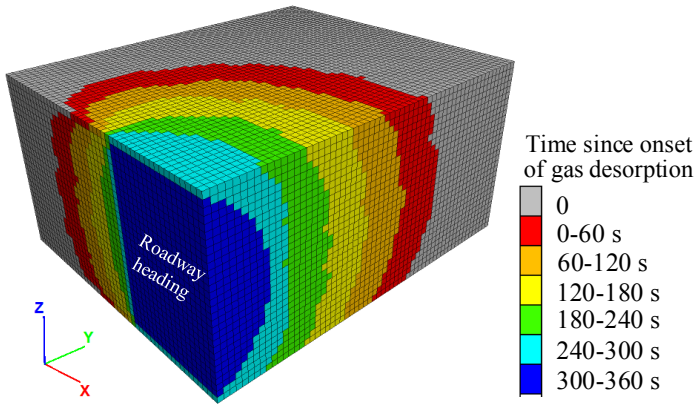


Figure 9.9. Time since fracture expansion begins and gas desorption from coal elements is initiated (only the left half of the outburst prone zone is shown).

Figure 9.10 illustrates the distribution of minor principal stress ahead of the development heading when the outburst is initiated. In order to monitor the evolution of minor principal stress and intra-fracture gas pressure, a trace line was drawn from the centroid of the working face in the direction of roadway development, and five monitoring points with a spacing of 1 m were assigned along the trace line (Figure 9.10). Figure 9.11 illustrates the gas pressure variation associated with fracture behaviour in the proximity of the development face during the initiation stage of the outburst. Intra-fracture gas pressure first drops drastically to a value not lower than σ_{min}, and then experiences a gentle increase, followed by a gradual decline, corresponding to three stages of the fracture behaviour, namely fracture opening, expansion and propagation. The initial sudden gas pressure drop arises from the generation of intra-fracture space during the fracture opening stage. It is noted that, even for coal and gas outburst prone areas, a certain amount of time delay is needed for the intra-fracture gas pressure to build up before it reaches a threshold value to

initiate fracture propagation. In this model, fractures located closest to the development face begin to propagate at 11 s and lead to the failure of the host element at 20 s after exposure of the outburst prone zone. This provides an explanation for the short time delay observed before coal and gas outbursts occur in the field, which ranges from several to tens of minutes after exposure to an outburst prone zone, or being initiated by a dynamic disturbance, such as shotfiring (Hargraves, 1980). The time delay relative to the build-up time of intra-fracture gas pressure will be discussed in Section 9.5.2.

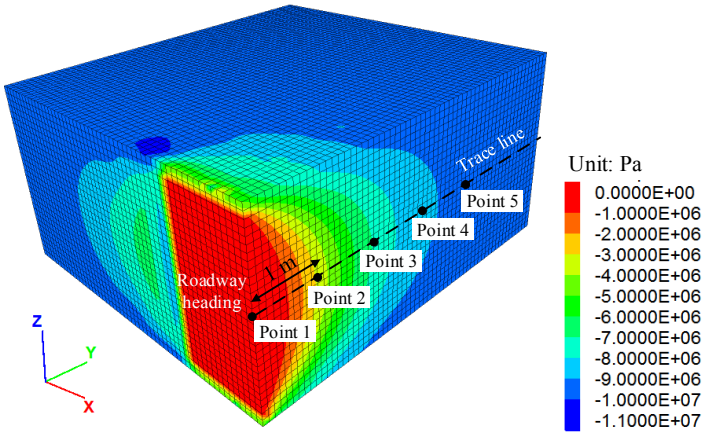


Figure 9.10. Minor principal stress contours as the development face reaches the outburst prone zone (only the left half of the outburst prone zone is shown).

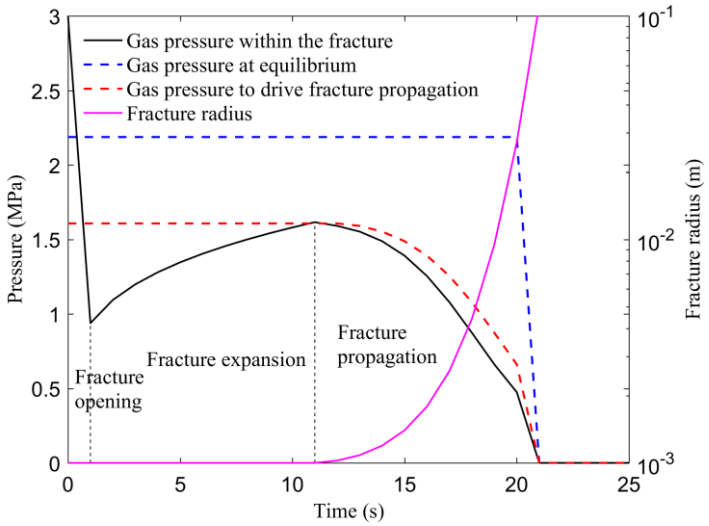


Figure 9.11. Evolution of intra-fracture gas pressure and associated fracture behaviour at monitoring point 1.

Figure 9.12 illustrates minor principal stress, intra-fracture gas pressure and effective stress profiles in the outburst prone zone during the development of the outburst. Although the initial gas pressure is much lower than the *in situ* minor principal stress, positive effective stress exists in a localised thin layer at the outburst front, which ensures that the outburst propagates steadily into the outburst prone zone. Figure 9.13 plots minor principal stress and intra-fracture gas pressure variations over time at different monitoring points. It can be seen that minor principal stresses gradually decrease as the development face approaches. When it drops below the initial gas pressure, the intra-fracture effective stress becomes positive, which leads to fracture expansion and in turn influences the intra-fracture gas pressure. It should be noted that intra-fracture gas pressure is always larger than the minor principal stress of the host element so as to sustain the fracture volume after the fracture opens.

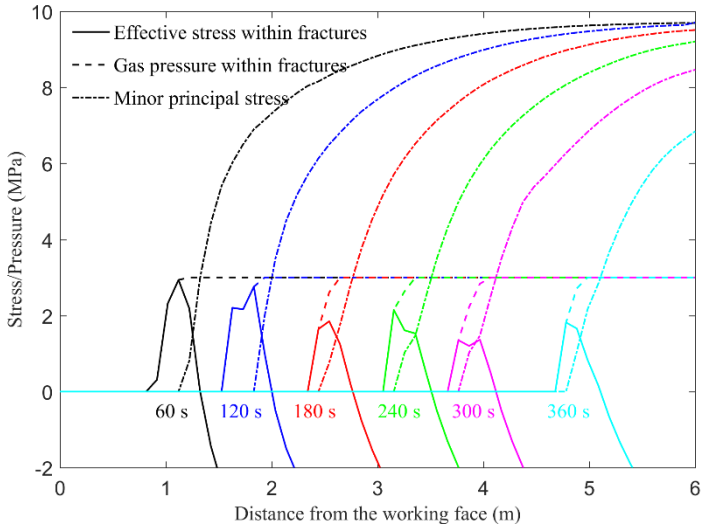


Figure 9.12. Minor principal stress, intra-fracture gas pressure and effective stress profiles along the central trace line at different times after the onset of the outburst.

Figure 9.14 presents the fracture radius profile during the developing stage of the coal and gas outburst. It can be seen that propagated fractures concentrate only in a limited layer at the outburst front, which confirms that failure occurs in a layer-by-layer manner when extending into the outburst prone zone. Figure 9.15 plots the time-varying fracture radii at different monitoring points as the coal and gas outburst develops. Fractures in this model usually fail coal elements in less than 10 s from the onset of fracture propagation.

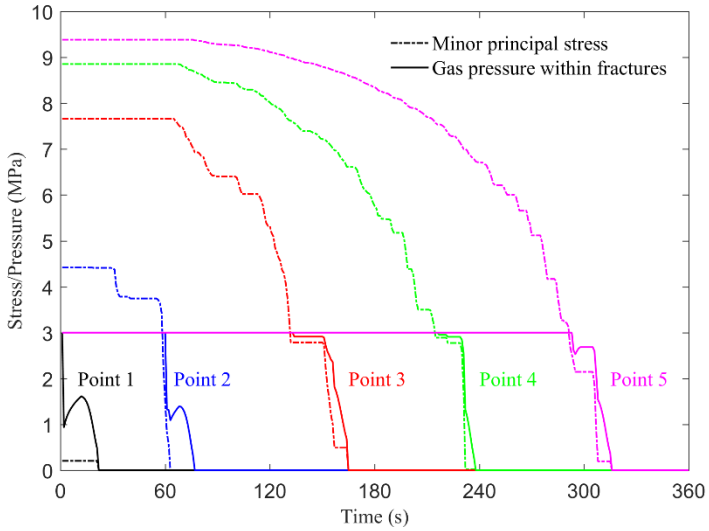


Figure 9.13. Minor principal stresses and intra-fracture gas pressures over time at different monitoring points after the onset of the outburst.

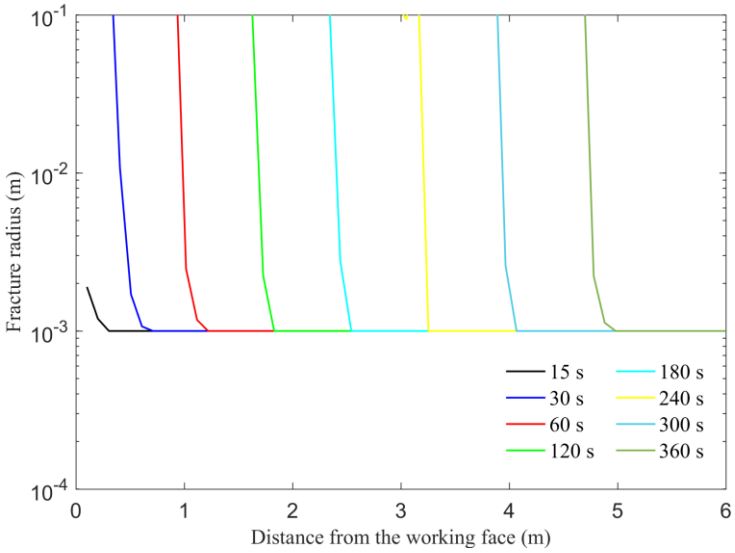


Figure 9.14. Fracture radius profile along the central trace line in the outburst prone zone.

The fracture propagation velocities at different monitoring points were further calculated by dividing the increments in fracture length by the timestep. As shown in Figure 9.16, fracture propagation velocities from the onset to the end of the outburst increase by three orders of magnitude. This suggests that a coal and gas outburst as a succession of ejection of coal fragments resulting from gas-driven rapid fracture propagation, can be consequently considered as dynamic unstable failure of coal.

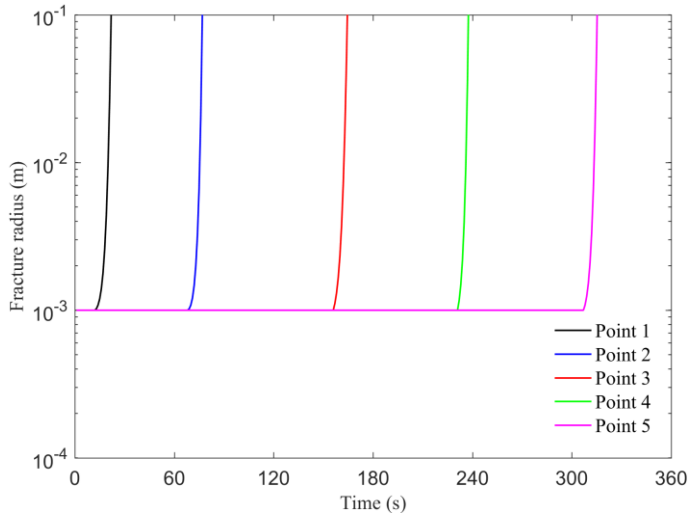


Figure 9.15. Fracture radius growth at different monitoring points over time.

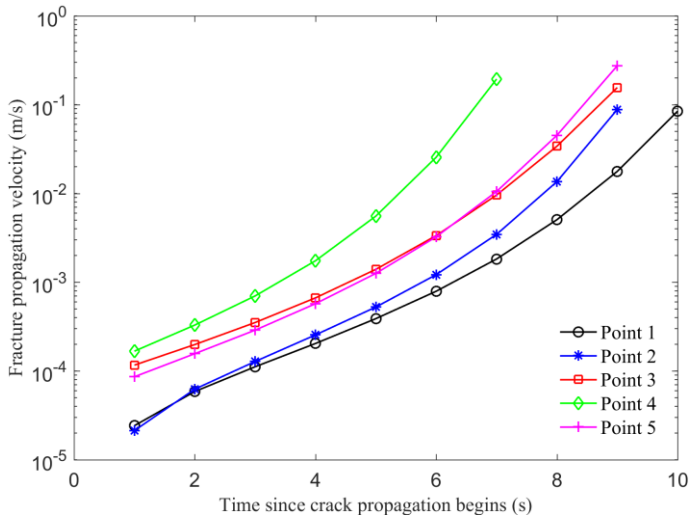


Figure 9.16. Fracture propagation velocity variation over time.

9.5.2 Parametric investigations on coal outburst behaviour

Figure 9.17 presents the effects of different influencing factors on the intra-fracture gas pressure variation and associated fracture propagation in the vicinity of a development face. It is seen that the time delay before a coal and gas outburst is dominated by the fracture expansion stage, the duration of which equals the time for intra-fracture gas pressure to reach p_{lim}. Fracture toughness K_{Ic} and fracture radius a_0 largely influence the duration of the fracture expansion stage near the development face, whilst initial gas pressure p_0 and *in situ* vertical stress σ_{v} have minimal effects. This is because p_{lim} is positively correlated with K_{Ic} and negatively related to a_0, but is

independent of p_0 and σ_v for fractures near the development face, according to Equations (9.11) and (9.12). However, this does not mean that initial gas pressure and *in situ* stress state do not influence fracture propagation some distance away from the development face. As illustrated in Section 9.5.1, rapid fracture propagation only occurs at the outburst front, which is a localised thin layer where the outburst threshold limit is satisfied. High initial gas pressure and low *in situ* stress state contribute to the outburst intensity by thickening this layer at the outburst front.

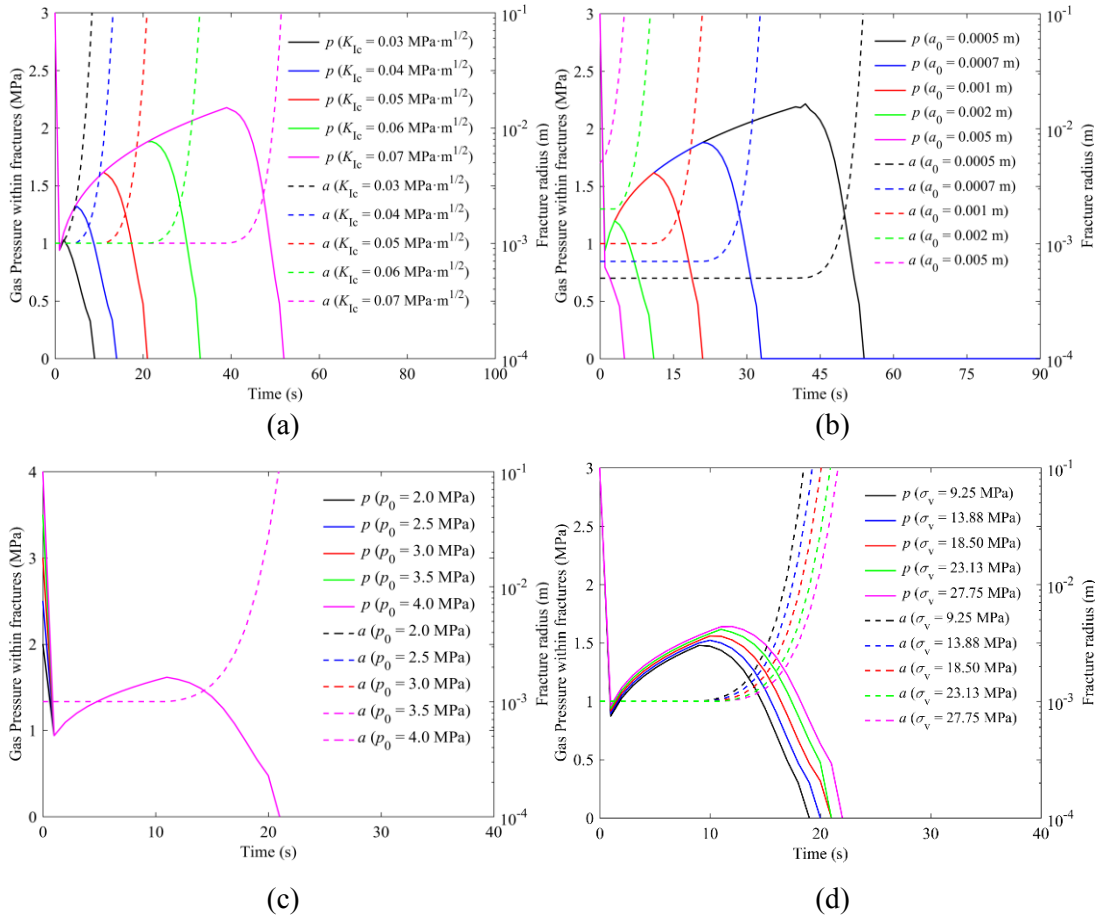


Figure 9.17. Influences of (a) K_{Ic}, (b) a_0, (c) p_0, and (d) σ_v on variations in intra-fracture gas pressure and fracture radius close to a development face.

Figure 9.18 illustrates effects of different influencing factors on the intensity of coal and gas outbursts, represented by ejected volume of coal over time. The time delay before the onset of a coal and gas outburst is dominated by fracture toughness K_{Ic} and fracture radius a_0, which is consistent with Figure 9.17. Large fracture toughness, fracture radius and initial gas pressure and low minor principal stress have favourable

effects on the intensity of coal and gas outbursts. It can be seen that the outburst intensity is very sensitive to fracture toughness and fracture length.

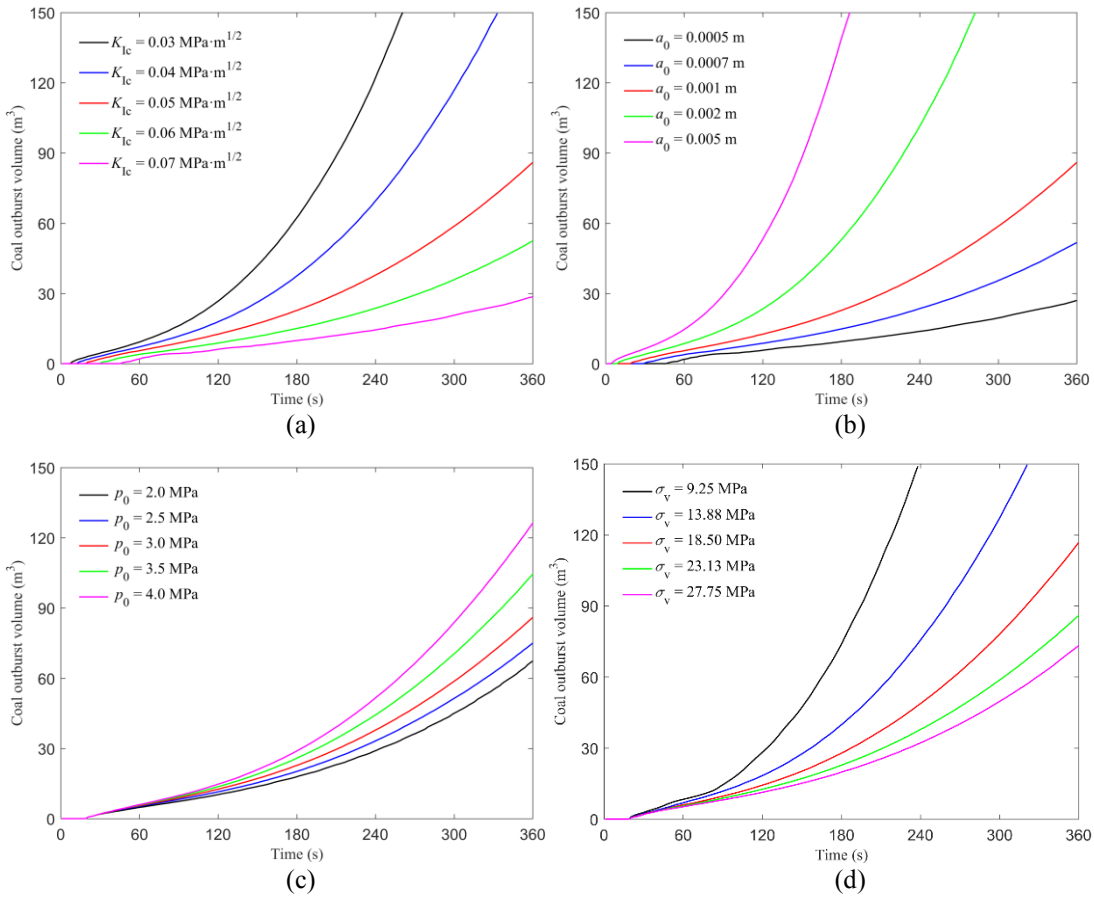


Figure 9.18. Influences of (a) K_{Ic}, (b) a_0, (c) p_0, and (d) σ_v on the ejected volume of coal over time.

9.6 Discussion

The outburst model developed is capable of explaining several characteristics of coal and gas outbursts. First, coal and gas outbursts often happen not immediately but a period of time after the exposure of an outburst prone zone or being initiated by a dynamic perturbation. This is due to the gradual build-up of intra-fracture gas pressure resulting from coal extraction-triggered gas adsorption. Second, a coal and gas outburst usually initiates from a working face and manifests itself as surface stripping of coal slices. This is because given the same fracture toughness and fracture length, the minimum critical intra-fracture gas pressure p_{lim} is achieved near the working face, which indicates that fractures near the working face have the shortest time delay before

the onset of fracture propagation, as suggested by Equations (9.11) and (9.12). In addition, the tensile fracture mode allows for easy formation of layer-by-layer breakage. Third, a coal and gas outburst is continuous and dynamic failure of coal. This can be explained by the fact that the expulsion of coal fragments accelerates the persistent failure by not only reducing the resistance for subsequent coal fragments to be ejected, but also increasing the intra-fracture gas pressure in subsequent fragments, as suggested by Equations (9.9) and (9.10).

The model findings confirmed that low strength of coal adds to its proneness to coal and gas outbursts. It is reported that outburst-prone coal yields strength values much lower than those of normal coal (Cao *et al*., 2001; Shepherd *et al*., 1981). A large number of outbursts were reported as being associated with soft coal, such as those in Metropolitan Colliery (Hargraves, 1965), Cynheidre/Pentremawr Colliery (Marshall, 1971), and Bowen No. 2 mine (Gray, 1980). Those soft coal materials are usually tectonically disturbed or sheared and with a sugary texture and soil-approaching structure (Gray, 1980). In view of the excellent correlation between fracture toughness and strength of coal (Bhagat, 1985), those soft coals would usually have low fracture toughnesses.

The model findings also confirmed that coal and gas outbursts tend to occur in highly fractured sites subjected to geological disturbance or intense mining-induced fracturing. In longwall coal mining, a fractured zone could be found extending several tens of meters ahead of the longwall face. Outburst prone coal at geologically active sites has far more number of fractures and less average spacing of fractures (Shepherd *et al*., 1981). Because fractured coal does not bear much load, it is usually subjected to a higher effective stress when unloaded. Fracturing of coal is also conducive to rapid gas release considering that gas adsorbed on to small coal particles only needs to travel a short distance before it reaches a free surface (Shepherd *et al*., 1981). Furthermore, the dominant orientation of fractures should be emphasised considering that fractures parallel to the working face are the most effective for the initiation of coal and gas outbursts. In this perspective, the model developed justifies the effectiveness of protective mining methods which first mine upper or lower level coal seams (Khristianovich and Salganik, 1983). Apart from gas pressure relief and stress redistribution, protective mining methods cause a system of oriented fractures to

develop parallel to the roof and floor, which impedes the fracture propagation near the working face and, in turn, the onset of coal and gas outbursts.

9.7 Conclusions

Coal and gas outbursts are characterised by a succession of ejection of coal fragments as a result of rapid fracture propagation. In this chapter, a theoretical model based on fracture mechanics and adsorption kinetics was presented to describe the behaviour of gas-containing fractures parallel to a working face, which involves opening first, then expansion and finally the rapid propagation stages under excavation unloading conditions. The fracture opening is driven by the effective minor principal stress inside the fracture, while the fracture expansion and rapid propagation is propelled by the pressure build-up of desorbed gas in the vicinity of the fracture.

The theoretical model developed was implemented in FLAC^{3D} to simulate coal and gas outbursts. A 3D continuum geomechanical model was constructed to model roadway development towards an outburst prone zone in a coal seam sandwiched between rock layers using a layout similar to that at Pniowek Colliery. A system of gas-containing fractures oriented parallel to the development face was distributed uniformly throughout the model domain of the coal formation. The numerically implemented model was applied to simulate a coal and gas outburst when the outburst prone zone was reached. Fracture behaviour in response to variations in gas pressure and stress state, and associated failure of host elements with reference to the stress intensity factor of embedded fractures were analysed sequentially at each roadway development step. Parametric investigations were subsequently carried out to identify the key factors contributing to the initiation and temporal evolution of coal and gas outbursts.

The model results have shown that coal and gas outbursts can be considered as a domino effect-type failure triggered by excavation unloading and propelled by gas desorption-driven fracture propagation. The coal ejection manifests itself as layer-by-layer breakage, eventually leading to a domed-shape erupted zone. The potential for coal and gas outbursts is governed by the threshold for fracture propagation, while the intensity, represented by the volume of coal to be ejected over a certain period of time, is highly dependent on the gas desorption into fractures. Both the potential and intensity of coal and gas outbursts are dominated by four factors, namely fracture

toughness of coal, pre-existing fracture radius, initial gas pressure and *in situ* stress state. Furthermore, the delay in the occurrence of coal and gas outbursts, especially after sudden exposure of soft coal or after excitations due to dynamic disturbances, may be associated with the gas desorption behaviour.

Chapter 10 Conclusions and recommendations for future research

10.1 Summary of the present research

This thesis presented a systematic investigation into the mechanisms, monitoring, modelling and forecasting of microseismicity associated with rock burst and coal and gas outburst hazards in coal mines. Knowledge gaps in terms of short-term forecasting of underground seismic hazards, mechanisms of rock bursts and coal and gas outbursts and modelling of microseismicity associated with longwall top coal caving mining were investigated.

The first step in this research was to conduct experimental investigations into the seismic response and fracturing behaviour of coal to stress and fracturing (Chapter 3). In the experiments, fluid was injected into naturally fractured coal blocks under true triaxial stress states to create hydraulic fractures, and the temporal and spatial evolution of fractures was analysed in integration with the associated seismic response. The understanding gained from the experiments laid the foundation for the analysis and interpretation of field recorded microseismicity in coal mines.

Next, field microseismic monitoring during coal production periods at Coal Mine Velenje was carried out, with the data obtained being analysed in combination with concurrent face advance records (Chapter 4). Based on the monitoring results and the fracture-slip seismic-generation mechanism, a conceptual model of mining-induced microseismicity was developed to shed light into the causes of anomalous microseismicity and statistical estimation of microseismicity to be triggered.

Two forecasting methodologies for rock bursts and coal and gas outbursts were then developed based upon the conceptual model developed. One is a field microseismic monitoring-based statistical short-term forecasting methodology, which estimates the

probability of hazardous microseismicity during longwall coal mining using the most recent microseismic and face advance records (Chapter 5). The other is a DFN-based microseismic modelling methodology, which could simulate microseismicity occurrence in a probabilistic way through the combination of deterministic stress and failure analysis and stochastic fracture slip evaluation (Chapter 6). Both methodologies were applied to forecast burst hazards associated with LTCC mining at Coal Mine Velenje, and the results were compared against recorded data. The latter methodology was further employed to investigate the impact of heterogeneity (coal strength and fracture attributes) on microseismic characteristics (Chapter 7).

As the last step, the mechanisms controlling rock bursts and coal and gas outbursts were investigated. Both underground hazards are considered as problems of dynamic instability under excavation unloading conditions: rock bursts are a violent failure of highly-stressed rock triggered by dynamic stress perturbations, while coal and gas outbursts are attributed to excavation unloading followed by gas desorption-driven rapid propagation of fractures. The role of excavation unloading (pillar recovery and mine opening excavation) as a source of dynamic stress perturbations in contributing to rock bursts was examined by quantifying the induced dynamic stress concentration around underground openings and structures (Chapter 8). As for coal and gas outbursts, a theoretical model based on fracture mechanics and gas dynamics was introduced, and numerically implemented to simulate coal and gas outbursts during roadway developments (Chapter 9). Key factors affecting outburst initiation and its temporal evolution were also identified.

10.2 Main conclusions

The main conclusions of this research are summarised as follows:

- The active acoustic monitoring technique is helpful to reflect the fracturing behaviour in coal. During the fluid injection process, seismograms of S waves of straight transmission (stS) and oblique transmission (otS) raypaths could only capture the initiation of induced fracture, whilst those of diffraction (dS) raypath could reflect both the fracture initiation and subsequent interactions with the natural fracture system in coal. In addition, the seismic velocity tomography based on first arrival time of S waves before and after hydraulic fracturing could approximately locate pre-existing fractures and injection-disturbed regions. The active acoustic

monitoring technique, in combination with seismogram processing, active seismic tomography and X-ray CT techniques, provides a new alternative to detect and analyse the initiation of hydraulic fracture and its subsequent interaction with the complex natural fracture system within coal.

- The frequency-magnitude distribution of recorded microseismic events follows the Gutenberg-Richter relationship, with the b value reflecting the scaling of microseismic event magnitude. In addition, the histogram of the released seismic energy follows a Gaussian distribution, which is characterised by the mean of the distribution μ, and the standard deviation σ, which are associated with the fracture sizes and size distribution, respectively.
- Microseismicity is mostly concentrated around extracted regions and stress concentrated regions, although some events can occur at a fair distance away from the closest longwall face. The microseismic intensity and energy range vary from panel to panel even at the same mine, but both seismic count and energy intensive regions associated with coal mining in different panels are spatially connected. Microseismic event counts frequency is moderately correlated with mining intensity, while seismic energy magnitude and spatial distribution are poorly related with mining intensity.
- A conceptual model has been developed to explain field observations by interpreting mining-induced microseismicity as slippages of natural fractures in response to progressive longwall coal mining. The triggered microseismicity and associated energy release can be analysed in terms of three mechanisms: fracture abundance, fracture slip criterion, and the resulting stress drop. Although microseismicity is induced by the longwall coal mining production, its energy and spatial distribution are controlled by the attributes of natural fractures throughout the coal seam.
- Based on the conceptual model developed, a statistical short-term forecasting methodology was developed, where the probability that at least one hazardous microseismic event occurs is considered as the joint probability considering the event counts frequency, energy magnitude distribution and spatial distribution with respect to the closest longwall face. The methodology was applied to forecast hazardous microseismicity associated with LTCC mining, and results in terms of forecasted daily event counts, and forecasted probabilities for microseismicity

having large magnitude and close to face-lines were in good accordance with field observations. Forecasting results also suggest that the energy magnitude distribution of microseismicity plays a dominant role in the potential of hazardous microseismicity.

- Based on the conceptual model developed, this research developed a DFN-based microseismic modelling methodology which could reflect the stochastic nature and magnitude characteristics of microseismicity. The modelling methodology was applied to simulate LTCC mining-induced microseismicity, and model results have shown that a good match was achieved between recorded and modelled microseismic events in terms of spatial distribution, released energy, and frequency-magnitude distribution. The energy released from a microseismic event is shown to be proportional to the cube of fracture size. The energy released from a microseismic event is also affected by the rock strength (through stress drop) and its mechanical properties. The model findings indicate that the power law fracture size distribution can be used to model microseismic generation around the longwall coal face.
- The microseismic modelling methodology developed was further implemented to model microseismicity associated with the progressive advance of a longwall face towards a xylite-rich heterogeneous zone with higher mechanical strength. Model results have shown a reduction in fitted *b* values and an increase in fitted Gaussian distribution parameters as the longwall face approached the heterogeneous zone. Both the high rock strength of xylite and low scaling exponent of fractures within the xylite-rich zone contribute to these deviations. The deviations in microseismic characteristics are believed to result from the combined effects of increased stress drops and slipped fracture sizes when the xylite-rich zone is approached.
- Dynamic stress disturbances induced by underground excavations, including pillar recovery and large mine openings contribute significantly to unstable rock failure such as rock bursts. The dynamic stress effect is closely associated with the extraction time. The maximum dynamic amplification coefficient R_{max} on a pillar can exceed 1.5 or even approach 2 subjected to instantaneous recovery of an adjacent pillar, while the dynamic stress concentration factor (DSCF) around a mine opening can reach up to 18 % subjected to instantaneous excavation of an adjacent mine opening. The findings indicate that dynamic unloading disturbances should

be considered when designing and supporting adjacent underground structures and openings in regions characterised by high levels of stress.

- Coal and gas outbursts can be considered as a domino effect-type failure triggered by excavation unloading and propelled by gas desorption driven fracture propagation. The coal ejection manifests itself as layer-by-layer breakage, eventually leading to a domed-shape erupted zone. The potential of coal and gas outbursts is governed by the threshold for fracture propagation, while the intensity is highly dependent on the gas desorption into fractures. Both the potential and intensity of coal and gas outbursts are dominated by four factors, namely fracture toughness of coal, fracture radius, initial gas pressure and *in situ* stress state. Furthermore, the delayed occurrence of coal and gas outbursts reported by many researchers, especially after sudden exposure of soft coal materials or after excitations due to dynamic disturbances, may be associated with the gas desorption behaviour.

10.3 Recommendations for future research

Based upon the main findings of this research, further research can advance the understanding in regard to the mechanism and control of underground hazards associated with coal mining. Several topics worthy of investigation are recommended under the following categories.

Mining-induced microseismicity indicative of attributes of underlying fractures

One urgent task is the forecast of the most probable spatial location of potential hazards. Considering underlying fractures as hypocentres of microseismicity, microseismicity concentration is indicative of intensive population of underlying fractures, where rock masses or coal seams are susceptible to underground hazards. As such, cluster analysis appears to be a promising tool for this suppose. The analysis could be greatly enhanced with the knowledge of the local fracture field.

Another challenging task is the characterisation of heterogeneity of the coal seam being mined using recorded microseismic signals. Passive seismic velocity tomography can be performed using first arrival times of P and S seismic waves. The velocity tomograms obtained can be compared against the spatial distribution of recorded microseismicity, in an effort to improve understanding of the relationship between fracture abundance (microseismicity concentration) and seismic wave

velocity, as well as verify the accuracy and efficiency of the algorithm used. The velocities are also expected to be comparable with those obtained from experiments to monitor seismic response of naturally fractured coal to stress and fracturing.

One more critical issue is the application of microseismic monitoring as a means of fracture mapping. While locations and sizes of slipped fractures are well constrained by those of corresponding seismic events, orientations of slipped fractures are largely unknown. Source mechanism analysis making use of recorded seismograms can be conducted to supplement this information. As such, a set of deterministic fracture pattern throughout active mining regions can be mapped, which is imperative for subsequent numerical analysis of geomechanical and hydraulic behaviour of rock or coal.

Dynamic excavation unloading in fractured rock masses

The dynamic stress effect induced by excavation unloading in this research is based on a continuum medium assumption. However, natural fractures such as joints and faults are ubiquitous in rock masses and coal deposits. An extension to the current research of dynamic stress effect is to simulate the response of fractured rock masses subjected to dynamic unloading perturbances. This will help advance the understanding regarding how the dynamic rock failure (in terms of failure mode, failed area, fracture propagation and energy release) can be influenced by attributes of natural fractures.

A coupled hydromechanical model for coal and gas outbursts

The explicit simulation of the fracturing and fragmentation of coal after outburst initiation has not been well achieved. A coupled DEM-fluid flow modelling algorithm can be developed for simulating the outburst initiation process as well as the fracture and fragmentation of coal ahead of the working face. This can be realised through supplementing the gas desorption from coal following the Langmuir isotherm equation to the fracture network fluid flow scheme, and formulating the gas migration in coal to follow the Darcy's law for compressive fluids.

The coupled hydromechanical model proposed can be further applied to investigate coal and gas outbursts resulting from geological structures, such as pre-existing faults and bedding shear zones. Faults can be represented by the built-in smooth-joint contact model (SJM) in PFC, where particles located on opposite sides of the fault are allowed

to overlap and slide past each other. Results are expected to confirm the indispensable role of geological structures in contributing to coal and gas outbursts.

Hydraulic fracturing performance in naturally fractured coal seams

To mitigate against rock burst and coal and gas outburst hazards, a planned research is the assessment of hydraulic fracturing performance in realistic naturally fractured coal seams, which could be realised through both numerical analysis and field trials.

A coupled DEM-fluid flow modelling scheme can be applied to model the hydraulic fracturing behaviour in the model domain of coal embedded with a DFN. All contacts between particles that lie on opposite sides of fractures will be assigned with the smooth-joint contact model (SJM) having low strength and high permeability. Deterministic fractures, whether being mapped fracture traces from coalfields or back-calculated fracture patterns from microseismic monitoring, are planned to be used first to model the interaction between hydraulic and natural fractures. Parametric investigations can be further conducted using stochastically generated fracture patterns to investigate how the hydraulic connectivity is controlled by attributes of fractures.

In *in situ* hydraulic fracture tests, the effectiveness of hydraulic fracturing with large diameter boreholes can be carried out and monitored through the microseismic monitoring network set up underground. The logistically located monitoring boreholes can be employed to monitor stress and gas pressure around the large diameter boreholes used for stress and gas pressure relief as well.

References

Abdul-Wahed, M.K., Al Heib, M., Senfaute, G., 2006. Mining-induced seismicity: Seismic measurement using multiplet approach and numerical modeling. Int. J. Coal Geol. 66(1), 137–147.

Abel, J.F., 1988. Soft rock pillars. Int. J. Min. Geol. Eng. 6, 215–248. doi:10.1007/BF00880975

Abolfazlzadeh, Y., Hudyma, M., 2016. Identifying and Describing a Seismogenic Zone in a Sublevel Caving Mine. Rock Mech. Rock Eng. 49, 3735–3751. doi:10.1007/s00603-016-1017-x

Afshari Moein, M.J., Tormann, T., Valley, B., Wiemer, S., 2018. Maximum magnitude forecast in hydraulic stimulation based on clustering and size distribution of early microseismicity. Geophys. Res. Lett. doi:10.1029/2018GL077609

Aguado, M.B.D., Nicieza, C.G., 2007. Control and prevention of gas outbursts in coal mines, Riosa–Olloniego coalfield, Spain. Int. J. Coal Geol. 69, 253–266.

Airey, E.M., 1968. Gas emission from broken coal. An experimental and theoretical investigation, in: International Journal of Rock Mechanics and Mining Sciences & Geomechanics Abstracts. Elsevier, pp. 475–494.

Alcott, J.M., Kaiser, P.K., Simser, B.P., 1998. Use of microseismic source parameters for rockburst hazard assessment, in: Seismicity Caused by Mines, Fluid Injections, Reservoirs, and Oil Extraction. Springer, pp. 41–65.

Alekseev, A.D., Nedodsev, N.V., Starikov, G.P., 1980. Fracture of gas-saturated coal under volumetric state of stress in the course of unloading: modelling of outbursts of coal and gas, in: Moscow: Institute for Problems in Mechanics of the Russian Academy of Sciences. p. 139. (in Russian).

Alexeev, A.D., Revva, V.N., Alyshev, N.A., Zhitlyonok, D.M., 2004. True triaxial loading apparatus and its application to coal outburst prediction. Int. J. Coal Geol. 58, 245–250. doi:10.1016/j.coal.2003.09.007

An, F.H., Cheng, Y.P., 2014. An explanation of large-scale coal and gas outbursts in underground coal mines: The effect of low-permeability zones on abnormally abundant gas. Nat. Hazards Earth Syst. Sci. 14, 2125–2132. doi:10.5194/nhess-14-2125-2014

Barron, K., Kullmann, D., 1990. Modelling of outbursts at# 26 Colliery, Glace Bay, Nova Scotia. Part 2: Proposed outburst mechanism and model. Min. Sci. Technol. 11, 261–268.

Barton, N., Lien, R., Lunde, J., 1974. Engineering classification of rock masses for the design of tunnel support. Rock Mech. 6, 189–236.

Beamish, B.B., Crosdale, P.J., 1998. Instantaneous outbursts in underground coal mines: an overview and association with coal type. Int. J. Coal Geol. 35, 27–55.

Bhagat, R., 1985. Mode I fracture toughness of coal. Geotech. Geol. Eng. 229–236.

Bishop, I., Styles, P., Allen, M., 1993. Mining-induced seismicity in the Nottinghamshire Coalfield. Q. J. Eng. Geol. Hydrogeol. 26, 253–279. doi:10.1144/GSL.QJEGH.1993.026.004.03

Board, M., 1994. Numerical examination of mining-induced seismicity. (Doctoral dissertation, University of Minnesota).

Board, M., Rorke, T., Williams, G., Gay, N., 1992. Fluid injection for rockburst control in deep mining, in: The 33th US Symposium on Rock Mechanics (USRMS). American Rock Mechanics Association.

Boltz, M.S., 2014. Mining-induced seismicity and FLAC3D modeling at the Trail Mountain Mine. (Master dissertation, The University of Utah).

Bonnet, E., Bour, O., Odling, N.E., Davy, P., Main, I., Cowie, P., Berkowitz, B., 2001. Scaling of fracture systems in geological media. Rev. Geophys. 39, 347–383. doi:10.1029/1999RG000074

Brady, B., Brown, E., 2013. Rock mechanics: for underground mining. Springer Science & Business Media.

Brady, B.T., 1977. Anomalous seismicity prior to rock bursts: Implications for earthquake prediction. Stress Earth 357–374.

Briggs, H., 1921. Characteristics of outbursts of gas in mines. Trans. Inst. Min. Eng. 61, 119–146.

Cai, M., Kaiser, I.P.K., Martini, C.D., 1998. A Tensile Model for the Interpretation of Microseismic Events near Underground Openings. Pure Appl. Geophys. 153, 67–92. doi:10.1007/s000240050185

Cai, M., Kaiser, P.K., Morioka, H., Minami, M., Maejima, T., Tasaka, Y., Kurose, H., 2007. FLAC/PFC coupled numerical simulation of AE in large-scale underground excavations. Int. J. Rock Mech. Min. Sci. 44(4), 550–564.

Cai, W., Dou, L., Cao, A., Gong, S., Li, Z., 2014a. Application of seismic velocity tomography in underground coal mines: A case study of Yima mining area, Henan, China. J. Appl. Geophys. 109, 140–149. doi:10.1016/j.jappgeo.2014.07.021

Cai, W., Dou, L., Li, Z., Liu, J., Gong, S., He, J., 2014b. Microseismic multidimensional information identification and spatio-temporal forecasting of rock burst: a case study of Yima Yuejin coal mine, Henan, China. Chinese J. Geophys. Ed. 57, 2687–2700.

Cai, W., Dou, L., Zhang, M., Cao, W., Shi, J.Q., Feng, L., 2018. A fuzzy comprehensive evaluation methodology for rock burst forecasting using microseismic monitoring. Tunn. Undergr. Sp. Technol. 80, 232–245. doi:10.1016/j.tust.2018.06.029

Cao, W., Li, X., Tao, M., Zhou, Z., 2016. Vibrations induced by high initial stress release during underground excavations. Tunn. Undergr. Sp. Technol. 53, 78–95. doi:10.1016/j.tust.2016.01.017

Cao, Y., He, D., Glick, D.C., 2001. Coal and gas outbursts in footwalls of reverse faults. Int. J. Coal Geol. 48, 47–63. doi:10.1016/S0166-5162(01)00037-4

Carter, J.P., Booker, J.R., 1990. Sudden excavation of a long circular tunnel in elastic ground. Intl J Rock Mech Min. Sci Geomech. Abs 27.

Castro, L.A.M., Bewick, R.P., Carter, T.G., 2012. An overview of numerical modelling applied to deep mining. Innov. Numer. Model. Geomech. 393–414.

Chen, B.-R., Feng, X.-T., Li, Q.-P., Luo, R.-Z., Li, S., 2015. Rock burst intensity classification based on the radiated energy with damage intensity at Jinping II hydropower station, China. Rock Mech. Rock Eng. 48, 289–303.

Chen, K.P., 2011. A new mechanistic model for prediction of instantaneous coal outbursts - Dedicated to the memory of Prof. Daniel D. Joseph. Int. J. Coal Geol. 87, 72–79. doi:10.1016/j.coal.2011.04.012

Chen, L., Wang, E., Feng, J., Kong, X., Li, X., Zhang, Z., 2016. A dynamic gas emission prediction model at the heading face and its engineering application. J. Nat. Gas Sci. Eng. 30, 228–236.

Choi, S.K., Wold, M.B., 2004. A coupled geomechanical-reservoir model for the modelling of coal and gas outbursts, in: Elsevier Geo-Engineering Book Series. Elsevier, pp. 629–634.

Choi, S.K., Wold, M.B., 2001. A mechanistic study of coal and gas outbursts, in: DC Rocks 2001, The 38th US Symposium on Rock Mechanics (USRMS). American Rock Mechanics Association.

Choi, X.S.K., 2012. Application of a numerical model for outburst prediction , control and management, in: 12th Coal Operators' Conference & The Australasian Institute of Mining and Metallurgy. pp. 286–293.

Close, J.C., 1993. Natural Fractures in Coal: Chapter 5.

Clough, R., Penzien, J., 2003. Dynamics of structures. Computers & Structures, Inc.

Connell, L.D., 2009. Coupled flow and geomechanical processes during gas production from coal seams. Int. J. Coal Geol. 79, 18–28.

Connell, L.D., Detournay, C., 2009. Coupled flow and geomechanical processes during enhanced coal seam methane recovery through CO2 sequestration. Int. J. Coal Geol. 77, 222–233.

Cook, N.G.W., 1965. A note on rockbursts considered as a problem of stability. J. South. African Inst. Min. Metall. 65, 437–446.

Cook, N.G.W., 1964. The application of seismic techniques to problems in rock mechanics, in: International Journal of Rock Mechanics and Mining Sciences & Geomechanics Abstracts. Elsevier, pp. 169–179.

Cook, N.G.W., 1963. The seismic location of rock bursts, in: In Proceedings of the Fifth Rock Mechanics Symposium (Vol. 493). Pergamon Press.

Cook, N.G.W., Hoek, E., Pretorius, J.P., Ortlepp, W.D., Salamon, M.D.G., 1966. Rock mechanics applied to study of rockbursts. J. South. AFRICAN Inst. Min. Metall. 66, 436–528.

Crank, J., 1979. The mathematics of diffusion. Oxford University press.

Curl, S., 1978. Methane prediction in coal mines. London IEA Coal Res.

Dou, L., He, J., Cao, A., Gong, S., Cai, W., 2015. Rock burst prevention methods based on theory of dynamic and static combined load induced in coal mine. J. China Coal Soc. 40, 1469–1476 (in Chinese).

Dubiński, J., Mutke, G., 1996. Characteristics of mining tremors within the near-wave field zone, in: Induced Seismic Events. Springer, pp. 249–261.

Durrheim, R.J., Anderson, R.L., Cichowicz, A., Ebrahim-Trollope, R., Hubert, G., Kijko, A., McGarr, A., Ortlepp, W.D., Van der Merwe, N., 2011. Risks posed by large seismic events in the gold mining districts of South Africa. Daya Publishing House.

Durrheim, R.J., Roberts, M.K.C., Haile, A.T., Hagan, T.O., Jager, A.J., Handley, M.F., Spottiswoode, S.M., Ortlepp, W.D., 1998. Factors influencing the severity of rockburst damage in South African gold mines. JOURNAL-SOUTH AFRICAN Inst. Min. Metall. 98, 53–58.

Durucan, S., 1981. An investigation into the stress-permeability relationship of coals and flow patterns around working longwall faces. (Doctoral dissertation, University of Nottingham).

Durucan, S., Edwards, J.S., 1986. The effects of stress and fracturing on permeability of coal. Min. Sci. Technol. 3, 205–216. doi:10.1016/S0167-9031(86)90357-9

Dyskin, A. V., Germanovich, L.N., 1993. Model of rockburst caused by cracks growing near free surface, in: Rockbursts and Seismicity in Mines. pp. 169–175.

Ettinger, I.L., 1952. Index for susceptibility of coal to gas and coal outbursts. Ugol 10, 31–34.

Ewy, R.T., Cook, N.G.W., 1990. Deformation and fracture around cylindrical openings in rock- I. Observations and analysis of deformations. Int J Rock Mech Min Sci Geomech Abstr 27, 387–407.

Fairhurst, C., Cook, N., 1966. The phenomenon of rock splitting parallel to the direction of maximum compression in the neighborhood of a surface. Proc. First Congr. Int. Soc. Rock Mech. 1, 687–692.

Fakhimi, A., Hosseini, O., Theodore, R., 2016. Physical and numerical study of strain burst of mine pillars. Comput. Geotech. 74, 36–44.

Fan, T. gang, Zhang, G. qing, 2014. Laboratory investigation of hydraulic fracture networks in formations with continuous orthogonal fractures. Energy 74, 164–173. doi:10.1016/j.energy.2014.05.037

Fang, Z., Harrison, J.P., 2002. Application of a local degradation model to the analysis of brittle fracture of laboratory scale rock specimens under triaxial conditions. Int. J. Rock Mech. Min. Sci. 39(4), 459–476.

Farmer, I.W., Pooley, F.D., 1967. A hypothesis to explain the occurrence of outbursts in coal, based on a study of west wales outburst coal. Int. J. Rock Mech. Min. Sci. Geomech. Abstr. 4, 189–193. doi:10.1016/0148-9062(67)90043-5

Feldman, E.P., Kalugina, N.A., Meln'ik, T.N., 2017. Role of unloading and filtration of gas in the development of main cracks in coal seams. J. Appl. Mech. Tech. Phys. 58, 155–164. doi:10.1134/S0021894417010175

Feng, G.L., Feng, X.T., Chen, B. rui, Xiao, Y.X., Yu, Y., 2015. A Microseismic Method for Dynamic Warning of Rockburst Development Processes in Tunnels. Rock Mech. Rock Eng. 48, 2061–2076. doi:10.1007/s00603-014-0689-3

Fritschen, R., 2010. Mining-induced seismicity in the Saarland, Germany. Pure Appl. Geophys. 167, 77–89. doi:10.1007/s00024-009-0002-7

Fujii, Y., Ishijima, Y., Deguchi, G., 1997. Prediction of coal face rockbursts and microseismicity in deep longwall coal mining. Int. J. Rock Mech. Min. Sci. 34, 85–96. doi:10.1016/S1365-1609(97)80035-4

Gawor, M., Litwiniszyn, J., Rysz, J., Smolarski, A.Z., 2000. Rock and gas outbursts. Arch. Min. Sci. 45, 347–361.

Gibowicz, S.J., Kijko, A., 2013. An introduction to mining seismology. Elsevier.

Gil, H., Swidzinski, A., 1988. Wyrzuty gazow I skal Politechnika Slaska, in: Skrypty Uczelnaine, No. 1366, Wyd. II Gliwice. p. 492 (in Polish).

Gilbert, P., 1972. Iterative methods for the three-dimensional reconstruction of an object from projections. J. Theor. Biol. 36, 105–117.

Głowacka, E., 1992. Application of the extracted volume of a deposit as a measure of deformation for seismic hazard evaluation in mines. Tectonophysics 202, 285–290. doi:10.1016/0040-1951(92)90114-L

Goodman, R.E., 1989. Introduction to rock mechanics. Wiley New York.

Grasso, J.-R., Sornette, D., 1998. Testing self-organized criticality by induced seismicity. J. Geophys. Res. Solid Earth 103, 29965–29987. doi:10.1029/97JB01344

Gray, I., 1987. Reservoir engineering in coal seams: Part 1-The physical process of gas storage and movement in coal seams. SPE Reserv. Eng. 2, 28–34.

Gray, I., 1980. The mechanism of, and energy release associated with outbursts, in: The Occurrence, Prediction and Control of Outbursts in Coal Mines Symposium. The Aus. I.M.M. Southern Queensland Branch, pp. 111–125.

Groenenboom, J., 1998. Acoustic monitoring of hydraulic fracture growth. Doctoral dissertation, Delft University of Technology.

Guan, P., Wang, H., Zhang, Y., 2009. Mechanism of instantaneous coal outbursts. Geology 37, 915–918. doi:10.1130/G25470A.1

Guo, H., Aziz, N.I., L.C, S., 1993. Rock fracture toughness determination by the Brazilian test. Eng. Geol. 33, 177–181.

Hanes, J., Shepherd, J., 1981. Mining induced cleavage, cleat and instantaneous outbursts in the Gemini Seam at Leichhardt Colliery, Blackwater, Queesland, in: Proc. Australas. Inst. Min. Metall. pp. 17–26.

Hargraves, A.J., 1980. A review of instantaneous outburst data, in: Proceedings of the Occurrence, Prediction and Control of Outbursts in Coal Mines. The Australian Institute of Mining and Metallurgy. Melbourne, pp. 1–8.

Hargraves, A.J., 1965. Instantaneous outbursts of coal and gas in Australia., in: Proc. 8th Commonwealth Mining and Metallurgy Conor. Aust. & N.Z. pp. 871–885.

Harris, R.A., 1998. Introduction to Special Section: Stress Triggers, Stress Shadows, and Implications for Seismic Hazard. J. Geophys. Res. Solid Earth 103, 24347–24358. doi:10.1029/98JB01576

Harthong, B., Scholtes, L., Donze, F.-V., 2012. Strength characterization of rock masses, using a coupled DEM–DFN model. Geophys. J. Int. 191, 467–480. doi:10.1111/j.1365-246X.2012.05642.x

Hassani, H., Hloušek, F., Alexandrakis, C., Buske, S., 2018. Migration-based microseismic event location in the Schlema-Alberoda mining area. Int. J. Rock Mech. Min. Sci. 110, 161–167. doi:10.1016/j.ijrmms.2018.08.002

Hazzard, J.F., Young, R.P., 2004. Dynamic modelling of induced seismicity. Int. J. Rock Mech. Min. Sci. 41(8), 1365–1376.

Hazzard, J.F., Young, R.P., 2000. Simulating acoustic emissions in bonded-particle models of rock. Int. J. Rock Mech. Min. Sci. 37(5), 867–872.

He, M., Jia, X., Coli, M., Livi, E., Sousa, L., 2012a. Experimental study of rockbursts in underground quarrying of Carrara marble. Int. J. Rock Mech. Min. Sci. 1–8.

He, M., Xia, H., Jia, X., Gong, W., Zhao, F., Liang, K., 2012b. Studies on classification, criteria and control of rockbursts. J. Rock Mech. Geotech. Eng. 4, 97–114.

He, M.C., Miao, J.L., Feng, J.L., 2010. Rock burst process of limestone and its acoustic emission characteristics under true-triaxial unloading conditions. Int. J. Rock Mech. Min. Sci. 47, 286–298.

He, M.C., Zhao, F., Cai, M., Du, S., 2015. A novel experimental technique to simulate pillar burst in laboratory. Rock Mech. Rock Eng. 48, 1833–1848.

Hildenbrand, A., Schlömer, S., Krooss, B.M., 2002. Gas breakthrough experiments on fine-grained sedimentary rocks. Geofluids 2, 3–23. doi:10.1046/j.1468-8123.2002.00031.x

Hodgson, K., Joughin, N.C., 1966. The relationship between energy release rate, damage, and seismicity in deep mines, in: The 8th US Symposium on Rock Mechanics (USRMS). American Rock Mechanics Association.

Hoek, E., Brown, E.T., 1980. Underground excavations in rock. CRC Press.

Hou, P., Gao, F., Ju, Y., Liang, X., Zhang, Z., Cheng, H., Gao, Y., 2016. Experimental investigation on the failure and acoustic emission characteristics of shale, sandstone and coal under gas fracturing. J. Nat. Gas Sci. Eng. 35, 211–223. doi:10.1016/j.jngse.2016.08.048

Hua, A.-Z., You, M.-Q., 2001. Rock failure due to energy release during unloading and application to underground rock burst control. Tunn. Undergr. Sp. Technol. Inc. Trenchless Technol. Res. 3, 241–246.

Huang, D., Li, Y., 2014. Conversion of strain energy in triaxial unloading tests on marble. Int. J. Rock Mech. Min. Sci. 66, 160–168.

Huang, R.Q., Huang, D., 2014. Evolution of rock cracks under unloading condition. Rock Mech. rock Eng. 47, 453–466.

Huang, R.Q., Wang, X.N., Chan, L.S., 2001. Triaxial unloading test of rocks and its implication for rock burst. Bull. Eng. Geol. Environ. 60, 37–41.

Huang, S., Liu, D., Yao, Y., Gan, Q., Cai, Y., Xu, L., 2017. Natural fractures initiation and fracture type prediction in coal reservoir under different in-situ stresses during hydraulic fracturing. J. Nat. Gas Sci. Eng. 43, 69–80. doi:10.1016/j.jngse.2017.03.022

Hucka, V., Das, B., 1974. Brittleness determination of rocks by different methods, in: International Journal of Rock Mechanics and Mining Sciences & Geomechanics Abstracts. Pergamon, pp. 389–392.

Hudyma, M., Potvin, Y.H., 2010. An engineering approach to seismic risk management in hardrock mines. Rock Mech. rock Eng. 43, 891–906.

Hyman, D.M., 1987. A review of the mechanisms of gas outbursts in coal. US Department of the Interior, Bureau of Mines.

Jackson, L.J., 1984. Outbursts in coal mines. IEA Coal Res.

Jaeger, J.C., Cook, N.G.W., Zimmerman, R., 2009. Fundamentals of rock mechanics. John Wiley & Sons.

Jeromel, G., Medved, M., Likar, J., 2010. An analysis of the geomechanical processes in coal mining using the velenje mining method. Acta Geotech. Slov. 7(1), 31–45.

Jeu, S.J., Logan, T.L., McBane, R.A., 1988. Exploitation of deeply buried coalbed methane using different hydraulic fracturing techniques in the Piceance Basin, Colorado and San Juan Basin New Mexico, in: SPE Annual Technical Conference and Exhibition. Society of Petroleum Engineers.

Jiang, Q., Feng, X.-T., Xiang, T.-B., Su, G.-S., 2010. Rockburst characteristics and numerical simulation based on a new energy index: a case study of a tunnel at 2,500 m depth. Bull. Eng. Geol. Environ. 69, 381–388.

Jin, H., Hu, Q., Liu, Y., 2011. Failure mechanism of coal and gas outburst initiation. Procedia Eng. 26, 1352–1360.

Jin, K., Cheng, Y., Ren, T., Zhao, W., Tu, Q., Dong, J., Wang, Z., Hu, B., 2018. Experimental investigation on the formation and transport mechanism of outburst coal-gas flow: Implications for the role of gas desorption in the development stage of outburst. Int. J. Coal Geol. 194, 45–58. doi:10.1016/j.coal.2018.05.012

Journel, A., Huijbregts, C., 1978. Mining geostatistics. Academic Press, London.

Kaiser, P.K., Cai, M., 2012. Design of rock support system under rockburst condition. J. Rock Mech. Geotech. Eng. 4, 215–227. doi:10.3724/SP.J.1235.2012.00215

Khristianovich, S.A., Salganik, R.L., 1983. Several basic aspects of the forming of sudden outbursts of coal (rock) and gas, in: 5th ISRM Congress. International Society for Rock Mechanics.

Kidybiński, A., 1981. Bursting liability indices of coal, in: International Journal of Rock Mechanics and Mining Sciences & Geomechanics Abstracts. Elsevier, pp. 295–304.

Kijko, A., Funk, C.W., Brink, A.V.Z., 1993. Identification of anomalous patterns in time-dependent mine seismicity, in: In Proceedings of the 3rd International Symposium on Rockbursts and Seismicity in Mines. pp. 205–210.

Kozłowska, M., Orlecka-Sikora, B., Rudziński, Ł., Cielesta, S., Mutke, G., 2016. Atypical evolution of seismicity patterns resulting from the coupled natural, human-induced and coseismic stresses in a longwall coal mining environment. Int. J. Rock Mech. Min. Sci. 86, 5–15. doi:10.1016/j.ijrmms.2016.03.024

Lama, R.D., Bodziony, J., 1998. Management of outburst in underground coal mines. Int. J. Coal Geol. 35, 83–115.

Langmuir, I., 1918. The adsorption of gases on plane surfaces of glass, mica and platinum. J. Am. Chem. Soc. 40, 1361–1403. doi:10.1021/ja02242a004

Lasocki, S., 1993a. Statistical short-term prediction in mining induced seismicity, in: Rockbursts and Seismicity in Mines. pp. 211–216.

Lasocki, S., 1993b. Weibull distribution as a model for sequence of seismic events induced by mining. Acta Geophys. Pol 41(2), 101–111.

Lasocki, S., 1992. Truncated Pareto distribution used in the statistical analysis of rockburst hazard. Acta Mont. A 2, 121–131.

Lasocki, S., Orlecka-Sikora, B., 2008. Seismic hazard assessment under complex source size distribution of mining-induced seismicity. Tectonophysics 456, 28–37. doi:10.1016/j.tecto.2006.08.013

Lei, Q., Latham, J., Tsang, C., 2017. The use of discrete fracture networks for modelling coupled geomechanical and hydrological behaviour of fractured rocks. Comput. Geotech. 85, 151–176. doi:10.1016/j.compgeo.2016.12.024

Lei, X., Masuda, K., Nishizawa, O., Jouniaux, L., Liu, L., Ma, W., Kusunose, K., 2004. Detailed analysis of acoustic emission activity during catastrophic fracture of faults in rock. J. Struct. Geol. 26(2), 247–258.

Leśniak, A., Isakow, Z., 2009. Space–time clustering of seismic events and hazard assessment in the Zabrze-Bielszowice coal mine, Poland. Int. J. Rock Mech. Min. Sci. 46, 918–928.

Li, D., Wong, L.N.Y., 2013. The brazilian disc test for rock mechanics applications: Review and new insights. Rock Mech. Rock Eng. 46, 269–287. doi:10.1007/s00603-012-0257-7

Li, H., 2001. Major and minor structural features of a bedding shear zone along a coal seam and related gas outburst, Pingdingshan coalfield, northern China. Int. J. Coal Geol. 47, 101–113.

Li, M., Cao, J., Li, W., 2016. Stress and Damage Induced Gas Flow Pattern and Permeability Variation of Coal from Songzao. doi:10.3390/en9050351

Li, X., Cao, W., Tao, M., Zhou, Z., Chen, Z., 2016. Influence of unloading disturbance on adjacent tunnels. Int. J. Rock Mech. Min. Sci. 84, 10–24. doi:10.1016/j.ijrmms.2016.01.014

Li, X., Cao, W., Zhou, Z., Zou, Y., 2014. Influence of stress path on excavation unloading

response. Tunn. Undergr. Sp. Technol. 42, 237–246. doi:10.1016/j.tust.2014.03.002

Li, X., Du, K., Li, D., 2015. True triaxial strength and failure modes of cubic rock specimens with unloading the minor principal stress. Rock Mech. Rock Eng. 48, 2185–2196.

Li, X., Konietzky, H., 2015. Numerical simulation schemes for time-dependent crack growth in hard brittle rock. Acta Geotech. 10, 513–531. doi:10.1007/s11440-014-0337-9

Li, X., Konietzky, H., 2014. Time to failure prediction scheme for rocks. Rock Mech. Rock Eng. 47, 1493–1503. doi:10.1007/s00603-013-0447-y

Li, X., Nie, B., He, X., Zhang, X., Yang, T., 2012. Influence of gas adsorption on coal body. J. China Coal Soc. 36, 2035–2038.

Li, X., Zhou, Z., Lok, T.-S., Hong, L., Yin, T., 2008a. Innovative testing technique of rock subjected to coupled static and dynamic loads. Int. J. Rock Mech. Min. Sci. 45, 739–748.

Li, X., Zhou, Z., YE, Z., MA, C., ZHAO, F., ZUO, Y., HONG, L., 2008b. Study of rock mechanical characteristics under coupled static and dynamic loads [J]. Chinese J. Rock Mech. Eng. 7, 13.

Li, X., Zuo, Y., Ma, C., 2005. Failure criterion of strain energy density and catastrophe theory analysis of rock subjected to static-dynamic coupling loading. Chinese J. Rock Mech. Eng. 24, 2814–2824 (in Chinese).

Li, Y., Rui, Z., Zhao, W., Bo, Y., Fu, C., Chen, G., Patil, S., 2018. Study on the mechanism of rupture and propagation of T-type fractures in coal fracturing. J. Nat. Gas Sci. Eng. 52, 379–389. doi:10.1016/j.jngse.2018.01.010

Li, Y., Yang, T.H., Liu, H.L., Wang, H., Hou, X.G., Zhang, P.H., Wang, P.T., 2016. Real-time microseismic monitoring and its characteristic analysis in working face with high-intensity mining. J. Appl. Geophys. 132, 152–163. doi:10.1016/j.jappgeo.2016.07.010

Li, Z., Dou, L., Cai, W., Wang, G., He, J., Gong, S., Ding, Y., 2014. Investigation and analysis of the rock burst mechanism induced within fault–pillars. Int. J. Rock Mech. Min. Sci. 70, 192–200.

Liang, Y., Cheng, Y., Zou, Q., Wang, W., Ma, Y., Li, Q., 2017. Response characteristics of coal subjected to hydraulic fracturing: An evaluation based on real-time monitoring of borehole strain and acoustic emission. J. Nat. Gas Sci. Eng. 38, 402–411. doi:10.1016/j.jngse.2017.01.001

Linkov, A.M., 1997. Key-note address: New geomechanical approaches to develop quantitative seismicity, in: In Proceedings of the 4th International Symposium on Rockbursts and Seismicity in Mines. Rotterdam: Balkema.

Linkov, A.M., 1996. Rockbursts and the instability of rock masses. Int. J. rock Mech. Min. Sci. Geomech. Abstr. 33, 727–732.

Lisjak, A., Liu, Q., Zhao, Q., Mahabadi, O.K., Grasselli, G., 2013. Numerical simulation of acoustic emission in brittle rocks by two-dimensional finite-discrete element analysis. Geophys. J. Int. 195, 423–443. doi:10.1093/gji/ggt221

Litwiniszyn, J., 1985. Model for the initiation of coal-gas outbursts. Int. J. Rock Mech. Min. Sci. Geomech. Abstr.;(United States) 22.

Liu, J., Xu, S., Li, Y., Lei, G., 2018. Analysis of Rock Mass Stability Based on Mining-Induced Seismicity: A Case Study at the Hongtoushan Copper Mine in China. Rock Mech. Rock Eng. 0, 0. doi:10.1007/s00603-018-1541-y

Liu, J., Yao, Y., Liu, D., Xu, L., Elsworth, D., Huang, S., Luo, W., 2018. Experimental simulation of the hydraulic fracture propagation in an anthracite coal reservoir in the southern Qinshui basin, China. J. Pet. Sci. Eng. 168, 400–408. doi:10.1016/j.petrol.2018.05.035

Liu, P., Ju, Y., Gao, F., Ranjith, P.G., Zhang, Q., 2018. CT Identification and Fractal Characterization of 3-D Propagation and Distribution of Hydrofracturing Cracks in Low-Permeability Heterogeneous Rocks. J. Geophys. Res. Solid Earth 1–18. doi:10.1002/2017JB015048

Lockner, D., 1993. The role of acoustic emission in the study of rock fracture, in: International Journal of Rock Mechanics and Mining Sciences & Geomechanics Abstracts. Elsevier, pp. 883–899.

Lockner, D.A., Byerlee, J.D., Kuksenko, V., Ponomarev, A., Sidorin, A., 1991. Quasi-static fault growth and shear fracture energy in granite. Nature 350, 39–42. doi:10.1038/350039a0

Lu, W., Yang, J., Yan, P., Chen, M., Zhou, C., Luo, Y., Jin, L., 2012. Dynamic response of rock mass induced by the transient release of in-situ stress. Int. J. Rock Mech. Min. Sci. 53, 129–141. doi:10.1016/j.ijrmms.2012.05.001

Ma, C.S., Chen, W.Z., Tan, X.J., Tian, H.M., Yang, J.P., Yu, J.X., 2018. Novel rockburst criterion based on the TBM tunnel construction of the Neelum–Jhelum (NJ) hydroelectric project in Pakistan. Tunn. Undergr. Sp. Technol. 81, 391–402. doi:10.1016/j.tust.2018.06.032

Ma, T., Tang, C., Tang, S., Kuang, L., Yu, Q., Kong, D., Zhu, X., 2018. Rockburst mechanism and prediction based on microseismic monitoring. Int. J. Rock Mech. Min. Sci. 110, 177–188. doi:10.1016/j.ijrmms.2018.07.016

Ma, X., Westman, E., Slaker, B., Thibodeau, D., Counter, D., 2018. The b-value evolution of mining-induced seismicity and mainshock occurrences at hard-rock mines. Int. J. Rock Mech. Min. Sci. 104, 64–70. doi:10.1016/j.ijrmms.2018.02.003

Malovichko, D., Basson, G., 2014. Simulation of mining induced seismicity using Salamon-Linkov method Method, in: In Int. Conference on Deep and High Stress Mining. Sudbury: Australian Centre for Geomechanics, pp. 667–680.

Manouchehrian, A., Cai, M., 2015. Simulation of unstable rock failure under unloading conditions. Can. Geotech. J. 53, 22–34.

Marcak, H., 1993. The use of pattern recognition methods for prediction of the rockbursts, in: Proc. 3rd Int. Symp. on Rockbursts and Seismicity in Mines. pp. 223–226.

Marcak, H., Mutke, G., 2013. Seismic activation of tectonic stresses by mining. J. Seismol. 17, 1139–1148. doi:10.1007/s10950-013-9382-3

Markič, M., Sachsenhofer, R.F., 2010. The Velenje lignite: its petrology and genesis. Geological Survey of Slovenia, Ljubljana.

Marshall, J.S., 1971. Outburst of coal and firedamp at Cynheidre/Pentremawr Colliery, Carmarthenshire. HMSO Command Rep. 4804, 21.

Martino, J.B., Chandler, N.A., 2004. Excavation-induced damage studies at the Underground Research Laboratory. Int. J. Rock Mech. Min. Sci. 41, 1413–1426. doi:10.1016/j.ijrmms.2004.09.010

Maxwell, S.C., Young, R.P., 1993. Associations between temporal velocity changes and induced seismicity. Geophys. Res. Lett. 20, 2929–2932.

Mazaira, A., Konicek, P., 2015. Intense rockburst impacts in deep underground construction and their prevention. Can. Geotech. J. 52, 1426–1439. doi:10.1139/cgj-2014-0359

McElhiney, J.E., 1993. Reservoir engineering aspects of coalbed methane. Hydrocarb. from Coal, AAPG Stud. Geol. 38, 361–372.

McGarr, A., 1976. Seismic moments and volume changes. J. Geophys. Res. 81, 1487–1494.

McKavanagh, B.M., Enever, J.R., 1980. Developing a microseismic outburst warning system, in: In Proceedings of the Second Conference on Acoustic Emission/Microseismic Activity in Geologic Structures and Materials. pp. 211–225.

McKee, C.R., Bumb, A.C., Koenig, R.A., 1988. Stress-dependent permeability and porosity of coal, in: In International Coalbed Methane Symposium, University of Alabama, Tuscaloosa, Alabama. Rocky Mountain Association of Geologists, pp. 183–193.

Melnikov, N.N., Kozyrev, A.A., Panin, V.I., 1996. Induced seismicity in large-scale mining in the kola peninsula and monitoring to reveal informative precursors. Pure Appl. Geophys. PAGEOPH 147, 263–276. doi:10.1007/BF00877482

Mendecki, A.J., 1996. Seismic monitoring in mines. Springer Science & Business Media.

Meng, C., 2010. Interaction between Hydraulic Fracturing Process and Pre-existing Natural Fractures. Doctoral dissertation. Doctoral dissertation, Delft University of Technology.

Mengtao, Z., Zenghe, X., Yishan, P., Yangsheng, Z., 1991. A united instability theory on coal (rock) burst and outburst. Journl China Coal Soc. 4, 5.

Miao, S.-J., Cai, M.-F., Guo, Q.-F., Huang, Z.-J., 2016. Rock burst prediction based on in-situ stress and energy accumulation theory. Int. J. Rock Mech. Min. Sci. 86–94.

Mitri, H.S., Tang, B., Simon, R., 1999. FE modelling of mining-induced energy release and storage rates. Journal-South African Inst. Min. Metall. 99, 103–110.

Mow, C.-C., Pao, Y.-H., 1971. The diffraction of elastic waves and dynamic stress concentrations. RAND CORP SANTA MONICA CALIF.

Mutke, G., 2008. Stability of the underground mine workings in the near field zone of seismic events, in: 21st World Mining Congress: Underground Mine Environment. The Fundation for the AGH, Kraków, Poland, pp. 89–97.

Nakagawa, S., Kneafsey, T.J., Borglin, S.E., 2015. Laboratory Visualization of Hydraulic Fracture Propagation and Interaction with a Network of Preexisting Fractures, in: AGU Fall Meeting Abstracts.

Nakajima, I., Watanabe, Y., Fukai, T., 1984. Acoustic emission during advance boring associated with the prevention of coal and gas outbursts. Hokkaido Univ., Sapporo, Japan.

Naoi, M., Chen, Y., Nishihara, K., Yamamoto, K., Yano, S., Watanabe, S., Morishige, Y., Kawakata, H., Akai, T., Kurosawa, I., Ishida, T., 2018. Monitoring hydraulically-induced fractures in the laboratory using acoustic emissions and the fluorescent method. Int. J. Rock Mech. Min. Sci. 104, 53–63. doi:10.1016/j.ijrmms.2018.02.015

Nazimko, V. V., Babenko, K. V., 2011. Use of FLAC3D for mining induced seismicity prediction, in: Conference: Continuum and Distinct Element Numerical Modeling in Geomechanics. Sainsbury, Hart, Detournay & Nelson (eds.), pp. 1–8.

Nemat-Nasser, S., Horii, H., 1982. Compression-induced nonplanar crack extension with application to splitting, exfoliation, and rockburst. J. Geophys. Res. Solid Earth 87, 6805–6821.

Neyman, B., Szecowka, Z., Zuberek, W., 1972. Effective methods for fighting rock burst in Polish collieries, in: Proceedings of the 5th International Strata Control Conference. pp. 1–9.

Nie, B., Li, X., 2012. Mechanism research on coal and gas outburst during vibration blasting. Saf. Sci. 50, 741–744.

Odintsev, V.. N., 1997. Sudden outburst of coal and gas—failure of natural coal as a solution of methane in a solid substance. J. Min. Sci. 33, 508–516.

Olson, J.E., Bahorich, B., Holder, J., 2012. Examining Hydraulic Fracture: Natural Fracture

Interaction in Hydrostone Block Experiments. SPE Hydraul. Fract. Technol. Conf. doi:10.2118/152618-MS

Orlecka-Sikora, B., 2010. The role of static stress transfer in mining induced seismic events occurrence, a case study of the Rudna mine in the Legnica-Glogow Copper District in Poland. Geophys. J. Int. 182, 1087–1095. doi:10.1111/j.1365-246X.2010.04672.x

Orlecka-Sikora, B., Lasocki, S., Lizurek, G., Rudziński, Ł., 2012. Response of seismic activity in mines to the stress changes due to mining induced strong seismic events. Int. J. Rock Mech. Min. Sci. 53, 151–158. doi:10.1016/j.ijrmms.2012.05.010

Ortlepp, W.D., 1983. The mechanism and control of rockbursts. Rock Mech. Min. Pract. 257–281.

Ortlepp, W.D., Stacey, T.R., 1998. Performance of tunnel support under large deformation static and dynamic loading. Tunn. Undergr. Sp. Technol. 13, 15–21.

Ortlepp, W.D., Stacey, T.R., 1994. Rockburst mechanisms in tunnels and shafts. Tunn. Undergr. Sp. Technol. 9, 59–65.

Otuonye, F., Sheng, J., 1994. A numerical simulation of gas flow during coal/gas outbursts. Geotech. Geol. Eng. 12, 15–34.

Palmer, I., Mansoori, J., 1996. How Permeability Depends on Stress and Pore Pressure in Coalbeds: A New Model. SPE Reserv. Eval. Eng. 1, 539–544. doi:10.2118/52607-PA

Pan, Y., Zhao, Y., Guan, F., Li, G., Ma, Z., 2007. Study on rockburst monitoring and orientation system and its application. Chinese J. Rock Mech. Eng. 26, 1002–1011 (in Chinese).

Pao, Y., Mow, C., 1973. Diffraction of Elastic Waves and Dynamics Stress Concentrations. New York.

Paterson, L., 1986. A model for outbursts in coal, in: International Journal of Rock Mechanics and Mining Sciences & Geomechanics Abstracts. Pergamon, pp. 327–332.

Petukhov, I.M., Linkov, A.M., 1979. The theory of post-failure deformations and the problem of stability in rock mechanics. Int. J. Rock Mech. Min. Sci. 16, 57–76. doi:10.1016/0148-9062(79)91444-X

Poulsen, B.A., 2010. Coal pillar load calculation by pressure arch theory and near field extraction ratio. Int. J. Rock Mech. Min. Sci. 47, 1158–1165. doi:10.1016/j.ijrmms.2010.06.011

Poulsen, B.A., Shen, B., 2013. Subsidence risk assessment of decommissioned bord-and-pillar collieries. Int. J. Rock Mech. Min. Sci. 60, 312–320. doi:10.1016/j.ijrmms.2013.01.014

Read, R.S., 2004. 20 years of excavation response studies at AECL's Underground Research Laboratory. Int. J. Rock Mech. Min. Sci. 41(8), 1251–1275.

Reiss, L.H., 1980. The reservoir engineering aspects of fractured formations. Editions Technip.

Richter, C.F., 1958. Elementary Seismology. WH. Freeman and Company, San Francisco.

Richter, C.F., 1935. An instrumental earthquake magnitude scale. Bull. Seismol. Soc. Am. 25, 1–32.

Roberts, D.P., van der Merwe, J.N., Canbulat, I., Sellers, E.J., Coetzer, S., 2002. Development of a method to estimate coal pillar loading. Safety in Mines Research Advisory Committee.

Rorke, A.J., Roering, C., 1984. Source mechanism studies of mining-induced seismic events in a deep level gold mine, in: Proceedings Symposium on Rockbursts and Seismicity in Mines. Johannesburg. The South African Institute of Mining and Metallurgy, pp. 51–56.

Rudajev, V., Teisseyre, R., Kozak, J., Sileny, J., 1986. Possible Mechanism of Rockbursts in Coal-Mines. Pure Appl. Geophys. Pageoph 124, 841.

Russenes, B.F., 1974. Analysis of rock spalling for tunnels in steep valley sides. Nor. Inst. Technol. Deptartment Geol. Trondheim Google Sch.

Rutqvist, J., Rinaldi, A.P., Cappa, F., Jeanne, P., Mazzoldi, A., Urpi, L., Guglielmi, Y., Vilarrasa, V., 2016. Fault activation and induced seismicity in geological carbon storage – Lessons learned from recent modeling studies. J. Rock Mech. Geotech. Eng. 8, 789–804. doi:10.1016/j.jrmge.2016.09.001

RWTH Aachen, 2016. MapROC project internal reports.

Ryder, J.A., 1988. Excess shear stress in the assessment of geologically hazardous situations. J. South African Inst. Min. Metall. 88, 27–39.

Sack, R.A., 1946. Extension of Griffith's theory of rupture to three dimensions. Proc. Phys. Soc. 58, 729–736. doi:10.1088/0959-5309/58/6/312

Sainoki, A., Mitri, H.S., 2014. Methodology for the interpretation of fault-slip seismicity in a weak shear zone. J. Appl. Geophys. 110, 126–134. doi:10.1016/j.jappgeo.2014.09.007

Salamon, M.D.G., 1993. Keynote address: Some applications of geomechanical modelling in rockburst and related research, in: In Proceedings of the 3rd International Symposium on Rockbursts and Seismicity in Mines. Rotterdam: AA Balkema, pp. 297–309.

Salamon, M.D.G., 1984. Energy considerations in rock mechanics: fundamental results. J. South. African Inst. Min. Metall. 84, 233–246.

Salamon, M.D.G., 1983. Rockburst hazard and the fight for its alleviation in South African gold mines, in: Proceedings of the Conference on Rockbursts, Prediction and Control. Institute of Mining and Metallurgy London, pp. 11–52.

Salamon, M.D.G., 1970. Stability, instability and design of pillar workings. Int. J. Rock Mech. Min. Sci. 7, 613–631. doi:10.1016/0148-9062(70)90022-7

Sato, K., Fujii, Y., 1988. Induced seismicity associated with longwall coal mining. Int. J. Rock Mech. Min. Sci. 25, 253–262. doi:10.1016/0148-9062(88)90002-2

Savic, M., 1995. Ultrasonic scattering from a hydraulic fracture: theory, computation and experiment. Doctoral dissertation, Delft University of Technology.

Scholz, C.H., 2002. The Mechanics of Earthquakes and Faulting. Cambridge University Press.

Segger, D. von, 1980. A random stress model for seismicity statistics and earthquake prediction. Geophys. J. R. Astron. Soc. 7, 637–640.

Seidle, J., 2011. Fundamentals of coalbed methane reservoir engineering. PennWell Books.

Seidle, J.P., Jeansonne, M.W., Erickson, D.J., 1992. Application of matchstick geometry to stress dependent permeability in coals, in: SPE Rocky Mountain Regional Meeting. Society of Petroleum Engineers.

Seidle, J.R., Huitt, L.G., 1995. Experimental Measurement of Coal Matrix Shrinkage Due to Gas Desorption and Implications for Cleat Permeability Increases. Int. Meet. Pet. Eng. doi:10.2118/30010-MS

Senfaute, G., Al Heib, M., Josien, J.P., Noirel, J.F., 2001. Detection and monitoring of high stress concentration zones induced by coal mining using numerical and microseismic method, in: In 5. International Symposium on" Rockbursts and Seismicity in Mines".

Shah, A.K., Keller, G.R., 2017. Geologic influence on induced seismicity: Constraints from potential field data in Oklahoma. Geophys. Res. Lett. 44, 152–161. doi:10.1002/2016GL071808

Shearer, P.M., 1975. Introduction to Seismology, Geophysical Journal of the Royal Astronomical Society. doi:10.1111/j.1365-246X.1975.tb01612.x

Shen, B., King, A., Guo, H., 2008. Displacement, stress and seismicity in roadway roofs during mining-induced failure. Int. J. Rock Mech. Min. Sci. 45, 672–688. doi:10.1016/j.ijrmms.2007.08.011

Shepherd, J., Rixon, L.K., Griffiths, L., 1981. Outbursts and geological structures in coal mines: A review. Int. J. Rock Mech. Min. Sci. 18, 267–283. doi:10.1016/0148-9062(81)91192-X

Shi, J.Q., Durucan, S., 2004. Drawdown induced changes in permeability of coalbeds: A new interpretation of the reservoir response to primary recovery. Transp. Porous Media 56, 1–16. doi:10.1023/B:TIPM.0000018398.19928.5a

Shnorhokian, S., Mitri, H. S., Moreau-Verlaan, L., 2014. Analysis of microseismic cluster locations based on the evolution of mining-induced stresses, in: Conference: 7th International Conference on Deep and High Stress Mining - Deep Mining. Sudbury, Canada, pp. 709–722.

Si, G., 2015. An investigation into gas emission and outburst control in thick seam coal mining. (Doctoral dissertation, Imperial College London).

Si, G., Durucan, S., Jamnikar, S., Lazar, J., Abraham, K., Korre, A., Shi, J.Q., Zavšek, S., Mutke, G., Lurka, A., 2015a. Seismic monitoring and analysis of excessive gas emissions in heterogeneous coal seams. Int. J. Coal Geol. 149, 41–54. doi:10.1016/j.coal.2015.06.016

Si, G., Jamnikar, S., Lazar, J., Shi, J.Q., Durucan, S., Korre, A., Zavšek, S., 2015b. Monitoring and modelling of gas dynamics in multi-level longwall top coal caving of ultra-thick coal seams, part I: Borehole measurements and a conceptual model for gas emission zones. Int. J. Coal Geol. 144–145, 98–110. doi:10.1016/j.coal.2015.04.008

Si, G., Shi, J.Q., Durucan, S., Korre, A., Lazar, J., Jamnikar, S., Zavšek, S., 2015c. Monitoring and modelling of gas dynamics in multi-level longwall top coal caving of ultra-thick coal seams, Part II: Numerical modelling. Int. J. Coal Geol. 144–145, 58–70. doi:10.1016/j.coal.2015.04.009

Singh, J.G., 1984. Mechanism of outbursts of coal and gas. MIN. SCI. TECH. 1, 269–274.

Sirait, B., Wattimena, R.K., Widodo, N.P., 2013. Rockburst prediction of a cut and fill mine by using energy balance and induced stress. Procedia Earth Planet. Sci. 6, 426–434.

Smith, D., Williams, F., 1984. Diffusional effects in the recovery of methane from coalbeds. SPEJ, Soc. Pet. Eng. J.;(United States) 529–535. doi:10.2118/10821-PA

Sneddon, I.N., 1946. The distribution of stress in the neighbourhood of a flat elliptical crack in an elastic solid. Proc. R. Soc. London A-187, 229–260. doi:10.1017/S0305004100025585

Spottiswoode, S.M., 1984. Source mechanisms of mine tremors at Blyvooruitzicht gold mine, in: Rockbursts and Seismicity in Mines. pp. 29–37.

Srinivasan, C., Arora, S.K., Yaji, R.K., 1997. Use of mining and seismological parameters as premonitors of rockbursts. Int. J. Rock Mech. Min. Sci. 34, 1001–1008. doi:10.1016/S1365-1609(97)80009-3

Staszek, M., Orlecka-Sikora, B., Leptokaropoulos, K., Kwiatek, G., Martínez-Garzón, P., 2017. Temporal static stress drop variations due to injection activity at The Geysers geothermal field, California. Geophys. Res. Lett. 44, 7168–7176. doi:10.1002/2017GL073929

Stewart, R.D., Spottiswoode, S.M., 1993. A technique for determining the seismic risk in deep-

level mining, in: Proc. 3rd Int. Symp. on Rockbursts and Seismicity in Mines. pp. 123–128.

Stiller, H., Hustig, E., Grosser, H., Knoll, P., 1983. On the nature of mining tremors. J. Earthq. Predict. Res. 2, 61.

Stovel, R.T., 1967. Approximate techniques for determining transient solutions. Cornell University.

Styles, P., 1993. Implications of harmonic-tremor precursory events for the mechanism of coal and gas outbursts, in: Proc. 3rd Int. Symp. on Rockbursts and Seismicity in Mines. pp. 415–421.

Styles, P., Emsley, S.J., Jowitt, T., 1988. Microseismic monitoring for the prediction of outbursts at Cynheidre Colliery, Dyfed, S. Wales. Geol. Soc. London, Eng. Geol. Spec. Publ. 5, 423–433. doi:10.1144/GSL.ENG.1988.005.01.47

Suorineni, F.T., Kaiser, P.K., Mgumbwa, J.J., Thibodeau, D., 2011. Mining of orebodies under shear loading Part 1 – case histories. Min. Technol. 120, 137–147. doi:10.1179/1743286311Y.0000000012

Suorineni, F.T., Mgumbwa, J.J., Kaiser, P.K., Thibodeau, D., 2014. Mining of orebodies under shear loading Part 2 – failure modes and mechanisms. Min. Technol. 123, 240–249. doi:10.1179/1743286314Y.0000000072

Swanson, P., Koontz, W., Abshire, J.I.M., 2009. Seismic network operations at a deep underground coal mining district in western Colorado (USA). Control. Seism. Hazard Sustain. Dev. Deep Mines (Volume 2).

Swanson, P.L., 1992. Mining-induced seismicity in faulted geologic structures: An analysis of seismicity-induced slip potential. Pure Appl. Geophys. 139, 657–676.

Talebi, S., Corbett, G.R., Mottahed, P., 1995. Outburst monitoring using microseismic techniques in the Phalen colliery, Sydney, Nova Scotia, Canada. CANMET Library of Technical Reports, Coal Mine Seismicity.

Tang, C., 1997. Numerical simulation of progressive rock failure and associated seismicity. Int. J. rock Mech. Min. Sci. Geomech. Abstr. 34, 249–261. doi:10.1016/S0148-9062(96)00039-3

Tang, Z., Liu, X., Xu, Q., Li, C., Qin, P., 2018. Stability evaluation of deep-buried TBM construction tunnel based on microseismic monitoring technology. Tunn. Undergr. Sp. Technol. 81, 512–524. doi:10.1016/j.tust.2018.08.028

Tao, M., Li, X., Wu, C., 2012. Characteristics of the unloading process of rocks under high initial stress. Comput. Geotech. 45, 83–92. doi:10.1016/j.compgeo.2012.05.002

Tarokh, A., Kao, C.-S., Fakhimi, A., Labuz, J.F., 2015. Spalling and brittleness in surface instability failure of rock. Géotechnique 66, 161–166.

Turchaninov, I.A., Markov, G.A., Gzovsky, M. V, Kazikayev, D.M., Frenze, U.K., Batugin, S.A., Chabdarova, U.I., 1972. State of stress in the upper part of the earth's crust based on direct measurements in mines and on tectonophysical and seismological studies. Phys. Earth Planet. Inter. 6, 229–234.

Valliappan, S., Wohua, Z., 1999. Role of gas energy during coal outbursts. Int. J. Numer. Methods Eng. 44, 875–895.

Van Aswegen, G., Butler, A.G., 1993. Applications of quantitative seismology in South African gold mines. Rockbursts Seism. Mines 93, 261–266.

Van de Ketterij, R.G., 2001. Optimisation of the near-wellbore geometry of hydraulic fractures propagating from cased perforated completions. Doctoral dissertation, Delft University of Technology.

Vasak, P., Dasys, A., 2009. Research to reality: Application of mining-induced seismic hazard maps, in: ROCKENG09: Proceedings of the 3rd CANUS Rock Mechanics Symposium, Toronto, 10p.

Vatcher, J., 2014. Mine-scale numerical modelling, seismicity and stresses at Kiirunavaara Mine, Sweden, in: Conference: 7th International Conference on Deep and High Stress Mining - Deep Mining. Sudbury, Canada, pp. 363–376.

Wang, G., Gong, S., Li, Z., Dou, L., Cai, W., Mao, Y., 2016. Evolution of stress concentration and energy release before rock bursts: two case studies from Xingan coal mine, Hegang, China. Rock Mech. Rock Eng. 49, 3393–3401.

Wang, J.-A., Park, H.D., 2001. Comprehensive prediction of rockburst based on analysis of strain energy in rocks. Tunn. Undergr. Sp. Technol. 16, 49–57.

Wang, S., Elsworth, D., Liu, J., 2013. Permeability evolution during progressive deformation of intact coal and implications for instability in underground coal seams. Int. J. Rock Mech. Min. Sci. 58, 34–45. doi:10.1016/j.ijrmms.2012.09.005

Wang, X., Cai, M., 2015. Influence of wavelength-to-excavation span ratio on ground motion around deep underground excavations. Tunn. Undergr. Sp. Technol. 49, 438–453.

Wawersik, W.R., Fairhurst, C., 1970. A study of brittle rock fracture in laboratory compression experiments, in: International Journal of Rock Mechanics and Mining Sciences & Geomechanics Abstracts. Elsevier, pp. 561–575.

Weijers, L., 1995. The near-wellbore geometry of hydraulic fractures initiated from horizontal and deviated wells. Doctoral dissertation, Delft University of Technology.

Wiles, T.D., Lachenicht, R., van Aswegen, G., 2000. Integration of deterministic modelling with seismic monitoring for the assessment of rock mass response to mining: Part I theory, in: In the Fifth International Symposium on Rockburst and Seismicity in Mines. South African Institute of Mining and Metallurgy, pp. 379–387.

Williams, R.J., Weissmann, J.J., 1995. Gas emission and outburst assessment in mixed CO2 and CH4 environments. Proc. ACIRL Undergr. Min. Sem. Aust. Coal Ind. Res. Lab., North Ryde 12, 20.

Woessner, J., Wiemer, S., 2005. Assessing the quality of earthquake catalogues: Estimating the magnitude of completeness and its uncertainty. Bull. Seismol. Soc. Am. 95, 684–698. doi:10.1785/0120040007

Wold, M.B., Connell, L.D., Choi, S.K., 2008. The role of spatial variability in coal seam parameters on gas outburst behaviour during coal mining. Int. J. Coal Geol. 75, 1–14.

Wong, G.I., McGarr, A., 1990. Implosional failure in mining-induced seismicity: a critical review, in: In Proceedings of the 2nd International Symposium on Rockbursts and Seismicity in Mines. Rotterdam: AA Balkema, pp. 45–51.

Xu, D.P., Feng, X.T., Cui, Y.J., Jiang, Q., 2015. Use of the equivalent continuum approach to model the behavior of a rock mass containing an interlayer shear weakness zone in an underground cavern excavation. Tunn. Undergr. Sp. Technol. 47, 35–51. doi:10.1016/j.tust.2014.12.006

Xu, T., Tang, C.A., Yang, T.H., Zhu, W.C., Liu, J., 2006. Numerical investigation of coal and gas outbursts in underground collieries. Int. J. Rock Mech. Min. Sci. 43, 905–919.

Xue, S., Wang, Y., Xie, J., Wang, G., 2011. A coupled approach to simulate initiation of outbursts of coal and gas—model development. Int. J. Coal Geol. 86, 222–230.

Xue, S., Yuan, L., Wang, J., Wang, Y., Xie, J., 2015. A coupled DEM and LBM model for simulation of outbursts of coal and gas. Int. J. Coal Sci. Technol. 2, 22–29.

Yin, G., Li, M., Wang, J.G., Xu, J., Li, W., 2015. Mechanical behavior and permeability

evolution of gas infiltrated coals during protective layer mining. Int. J. Rock Mech. Min. Sci. 80, 292–301. doi:10.1016/j.ijrmms.2015.08.022

Youan, W., Sijing, Y., 1980. Some characteristics of coal seams with hazard of outburst. Journl China Coal Soc. 1, 6.

Young, R.P., Collins, D.S., Hazzard, J., Heath, A., P., W.S., B., C., …, Lebon, P., 2005. Seismic validation of 3-D thermo-mechanical models for the prediction of rock damage around radioactive waste packages in geological repositories.

Yu, B., Zhao, J., Xiao, H., 2017. Case Study on Overburden Fracturing during Longwall Top Coal Caving Using Microseismic Monitoring. Rock Mech. Rock Eng. 50, 507–511. doi:10.1007/s00603-016-1096-8

Završek, S., 1993. Stabilnost jamskih progc: Stability of mine roadways. MSc thesis (in Slovene), Ljubljana.

Zhai, G., Shirzaei, M., 2018. Fluid Injection and Time-Dependent Seismic Hazard in the Barnett Shale, Texas. Geophys. Res. Lett. 45, 4743–4753. doi:10.1029/2018GL077696

Zhang, J.J., Fu, B.J., Li, Z.K., Song, S.W., Shang, Y.J., 2011. Criterion and classification for strain mode rockbursts based on five-factor comprehensive method, in: 12th ISRM Congress. International Society for Rock Mechanics.

Zhang, M., Shimada, H., Sasaoka, T., Matsui, K., Dou, L., 2013. Seismic energy distribution and hazard assessment in underground coal mines using statistical energy analysis. Int. J. Rock Mech. Min. Sci. 64, 192–200. doi:10.1016/j.ijrmms.2013.09.001

Zhang, Z.Y., 1992. Introduction to coal seam gas-geology map. China Coal Ind. Publ. House, Beijing 178.

Zhao, K., Janutolo, M., Barla, G., Chen, G., 2014. 3D simulation of TBM excavation in brittle rock associated with fault zones: The Brenner Exploratory Tunnel case. Eng. Geol. 181, 93–111. doi:10.1016/j.enggeo.2014.07.002

Zhao, W., Cheng, Y., Jiang, H., Jin, K., Wang, H., Wang, L., 2016. Role of the rapid gas desorption of coal powders in the development stage of outbursts. J. Nat. Gas Sci. Eng. 28, 491–501. doi:10.1016/j.jngse.2015.12.025

Zhao, X., Huang, B., Wang, Z., 2018. Experimental Investigation on the Basic Law of Directional Hydraulic Fracturing Controlled by Dense Linear Multi-Hole Drilling. Rock Mech. Rock Eng. doi:10.1007/s00603-018-1439-8

Zhao, X.G., Wang, J., Cai, M., Cheng, C., Ma, L.K., Su, R., Zhao, F., Li, D.J., 2014. Influence of unloading rate on the strainburst characteristics of Beishan granite under true-triaxial unloading conditions. Rock Mech. Rock Eng. 47, 467–483.

Zhou, J., Li, X., Mitri, H.S., 2018. Evaluation method of rockburst: State-of-the-art literature review. Tunn. Undergr. Sp. Technol. 81, 632–659. doi:10.1016/j.tust.2018.08.029

Zhu, W.C., Li, Z.H., Zhu, L., Tang, C.A., 2010. Numerical simulation on rockburst of underground opening triggered by dynamic disturbance. Tunn. Undergr. Sp. Technol. 25, 587–599.

Zimmerman, R., Main, I., 2003. Hydromechanical Behavior of Fractured Rocks, in: Mechanics of Fluid-Saturated Rocks. pp. 363–421. doi:10.1016/S0074-6142(03)80023-2

Zubelewicz, A., Mroz, Z., 1983. Numerical simulation of rock burst processes treated as problems of dynamic instability. Rock Mech. Rock Eng. 16, 253–274. doi:10.1007/BF01042360

Zuo, Y., Li, X., Ma, C., Zhang, Y., Wang, W., 2005. Catastrophic model and testing study on failure of static loading rock system under dynamic loading. Chinese J. Rock Mech. Eng.

24, 741–746 (in Chinese).

Appendices

Appendix 1 Analysis of recorded microseismicity at Coal Mine Velenje in 2016-2018

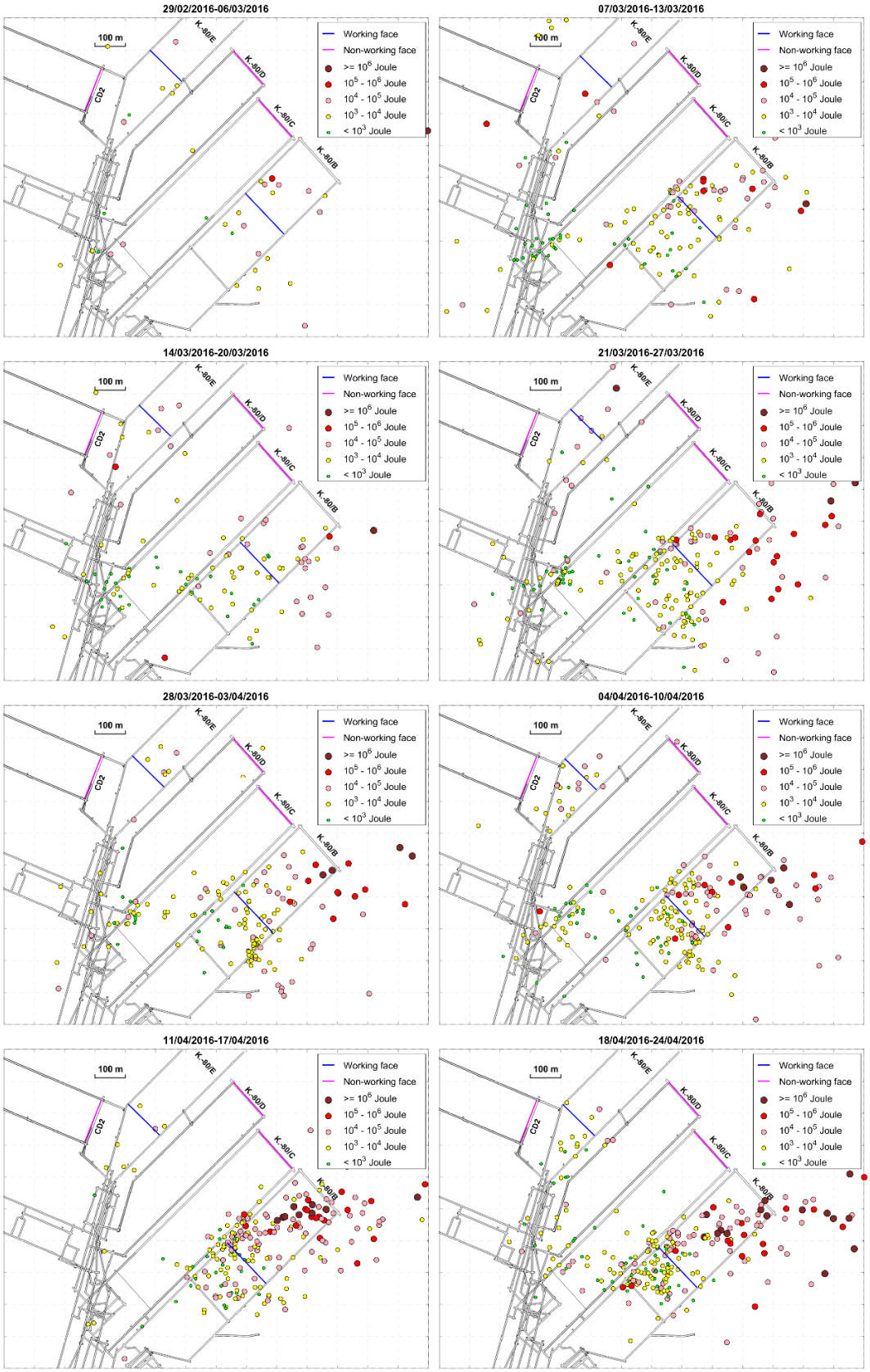


Figure A1.1. Spatial distribution of recorded microseismicity at Coal Mine Velenje in 2016-2018 (analysed for each week).

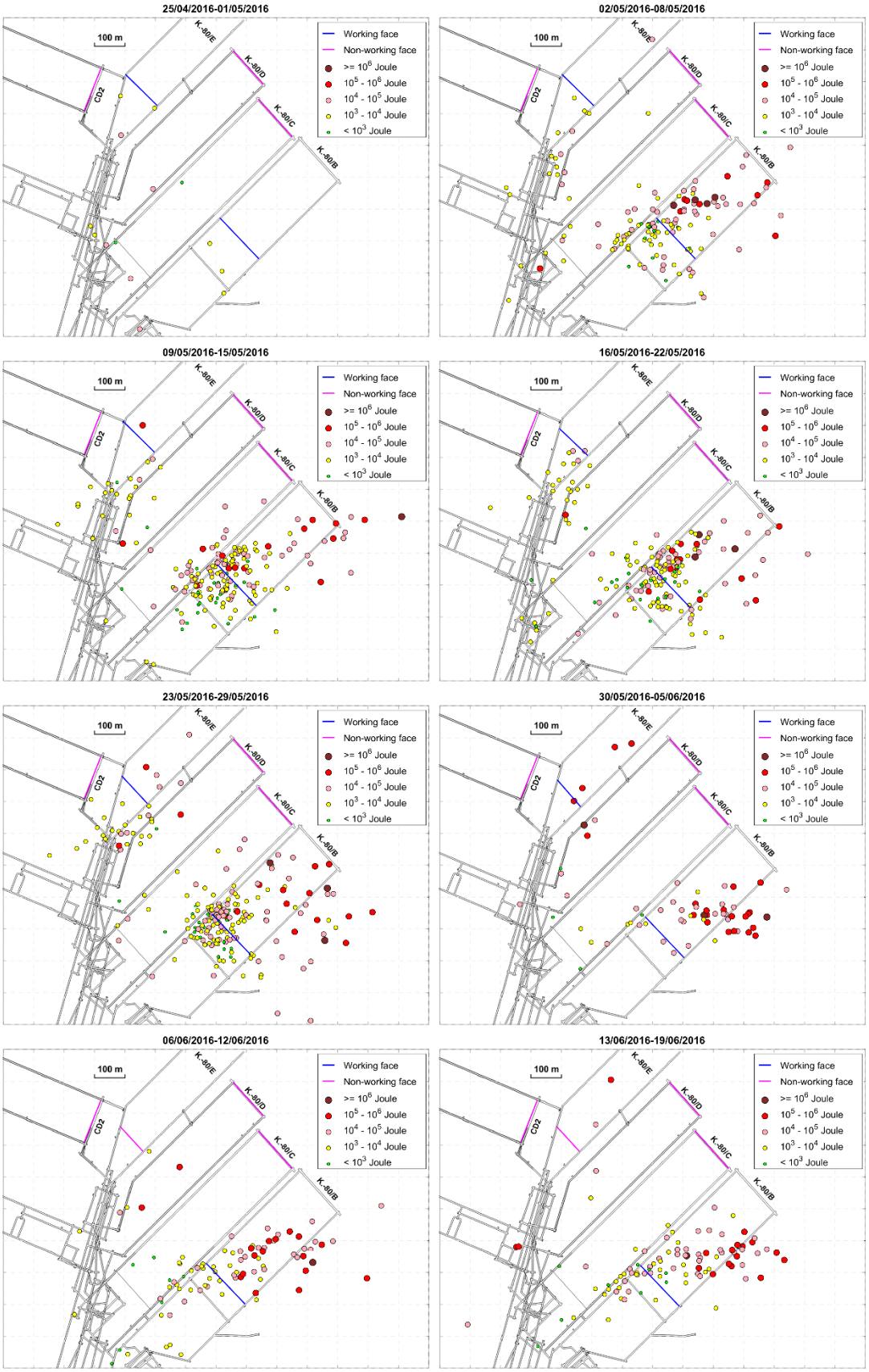


Figure A1.1.(Continued). Spatial distribution of recorded microseismicity at Coal Mine Velenje in 2016-2018 (analysed for each week).

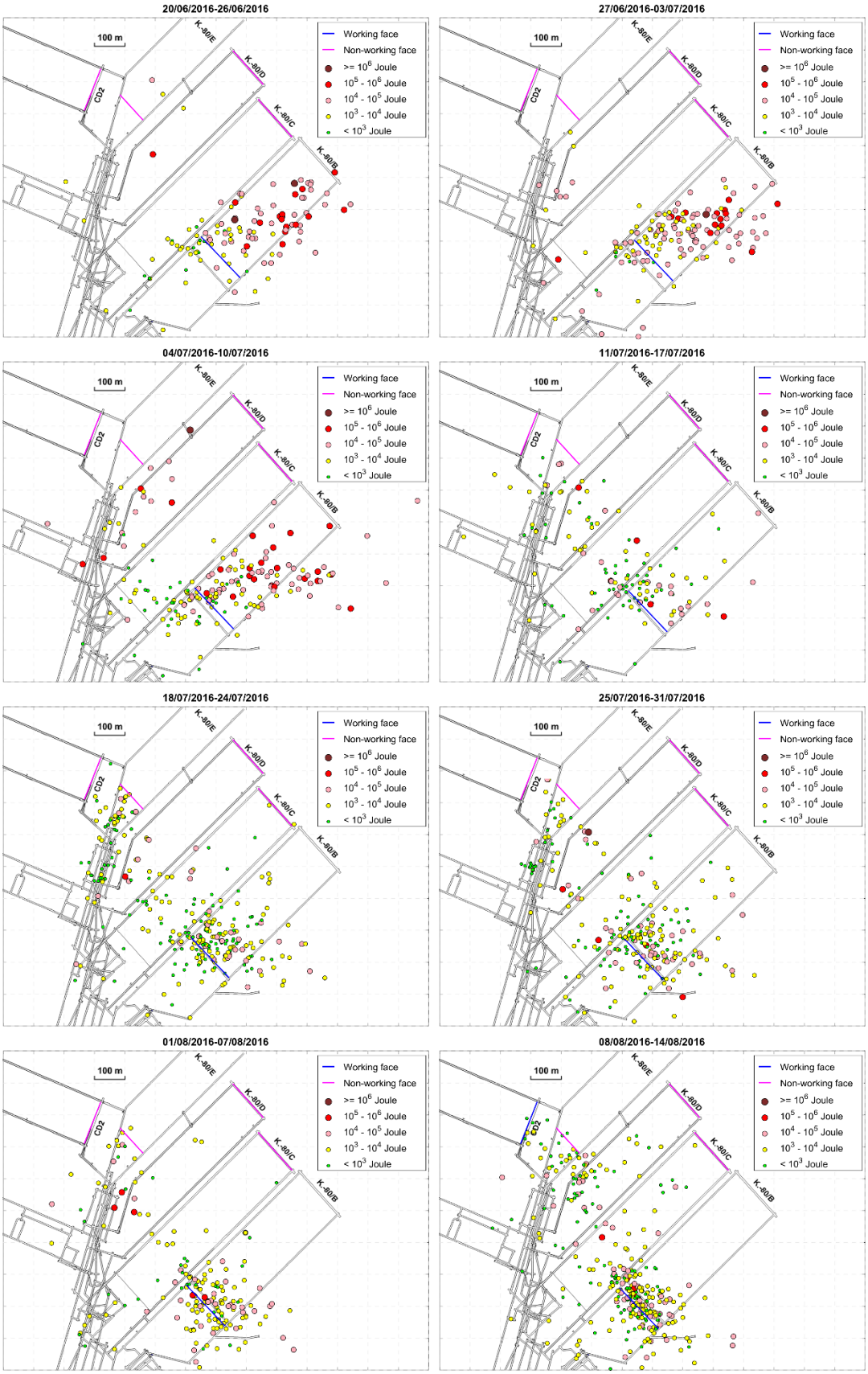


Figure A1.1. (Continued). Spatial distribution of recorded microseismicity at Coal Mine Velenje in 2016-2018 (analysed for each week).

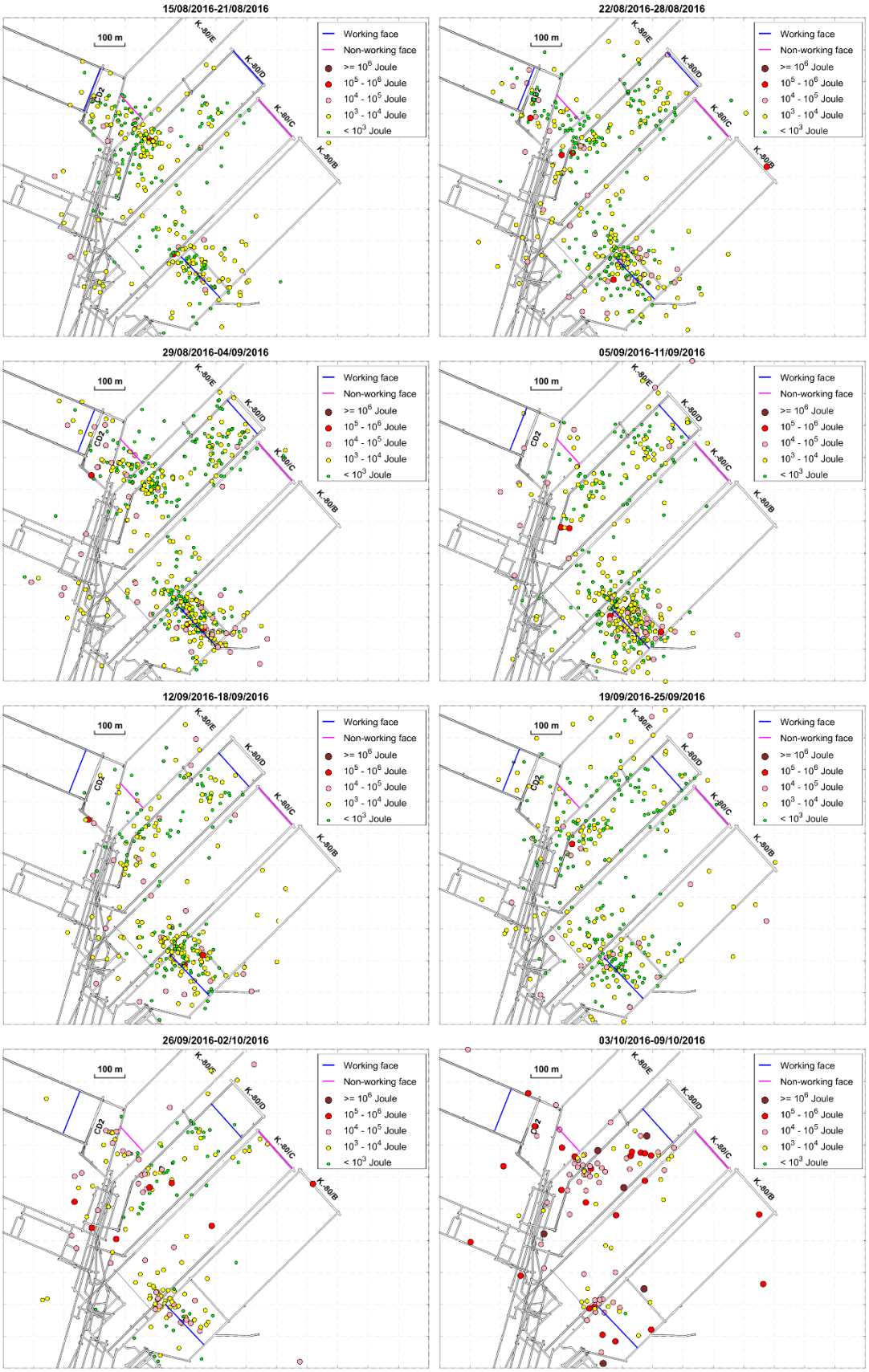


Figure A1.1. (Continued). Spatial distribution of recorded microseismicity at Coal Mine Velenje in 2016-2018 (analysed for each week).

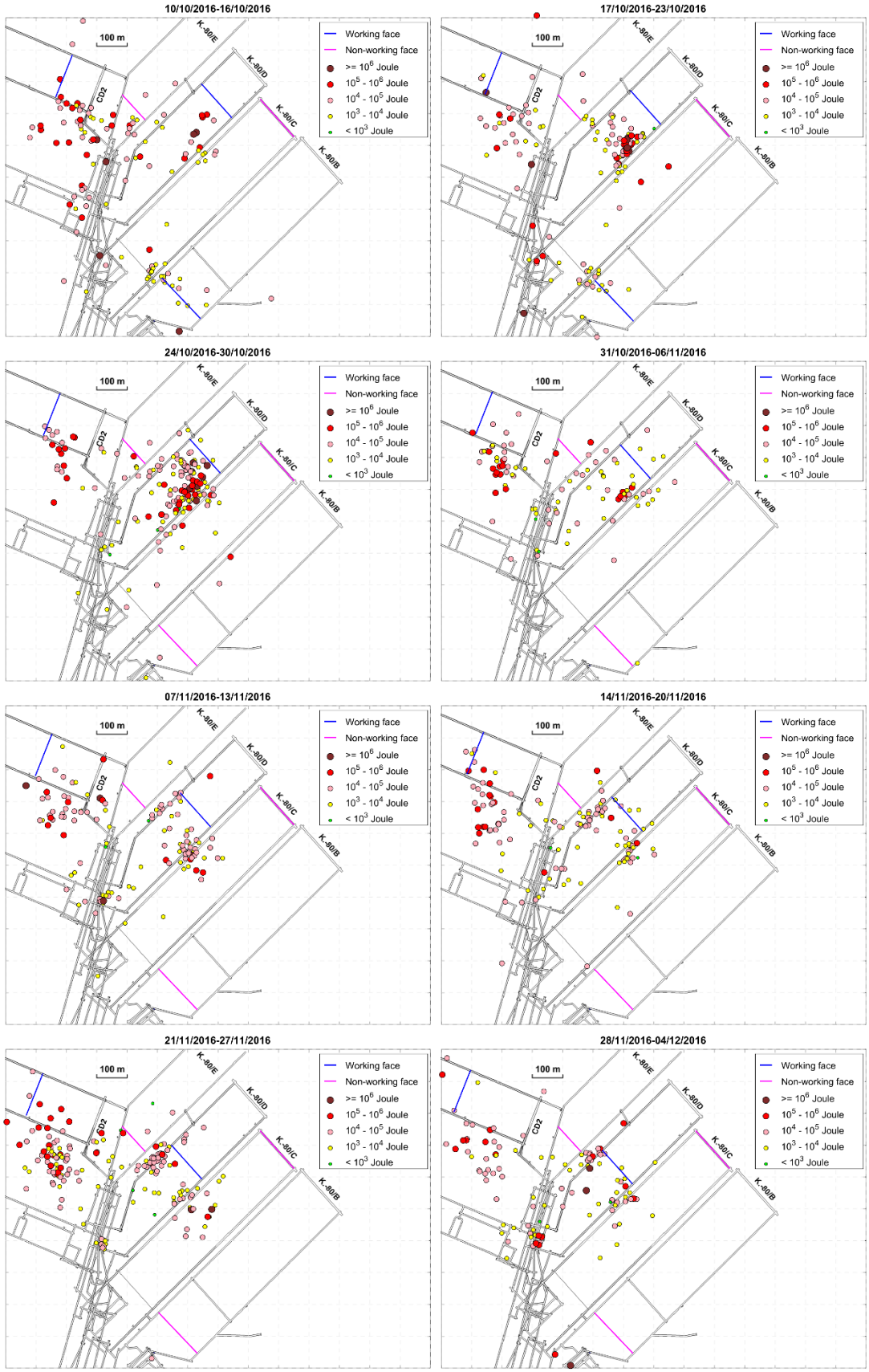


Figure A1.1. (Continued). Spatial distribution of recorded microseismicity at Coal Mine Velenje in 2016-2018 (analysed for each week).

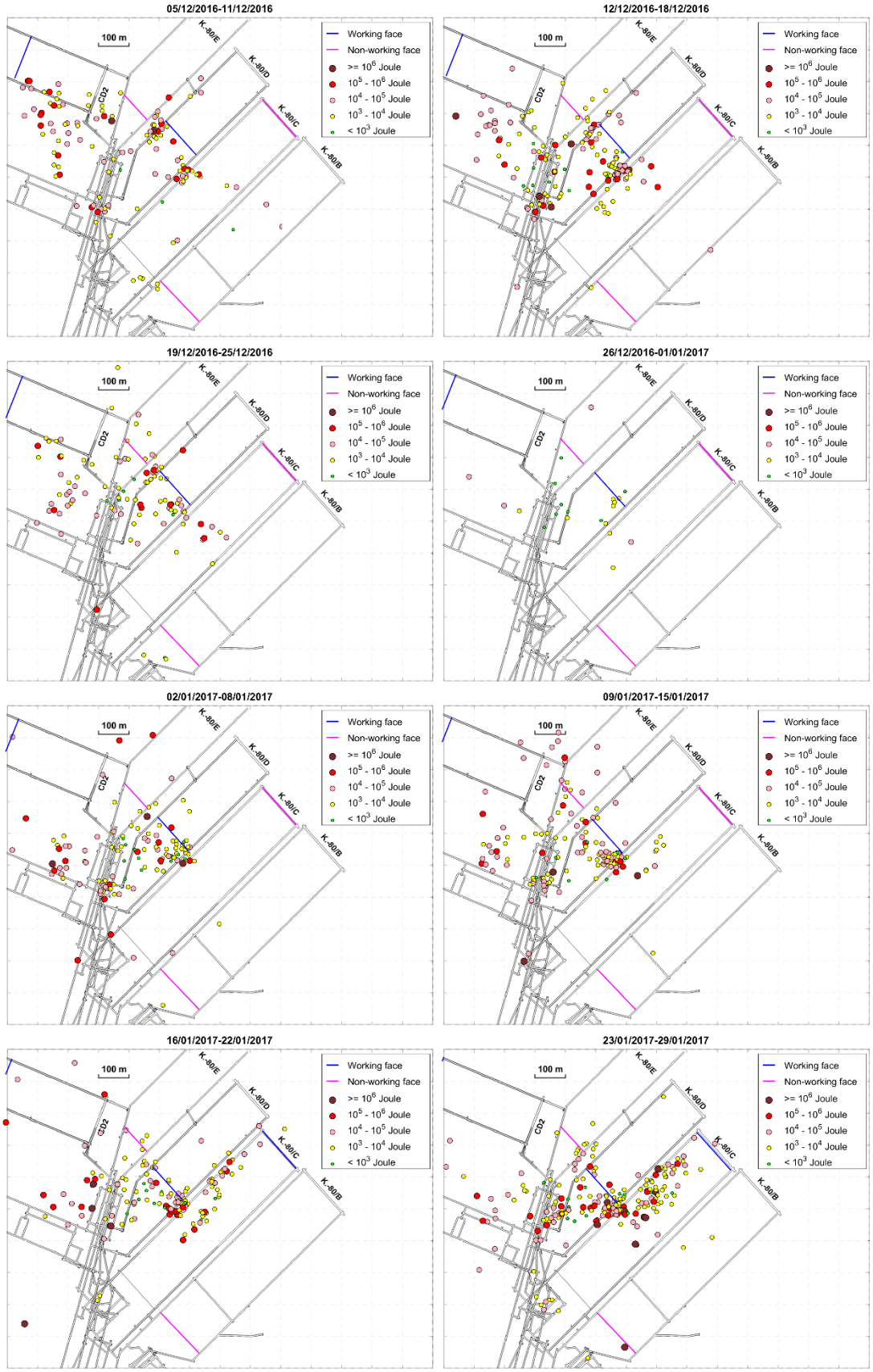


Figure A1.1. (Continued). Spatial distribution of recorded microseismicity at Coal Mine Velenje in 2016-2018 (analysed for each week).

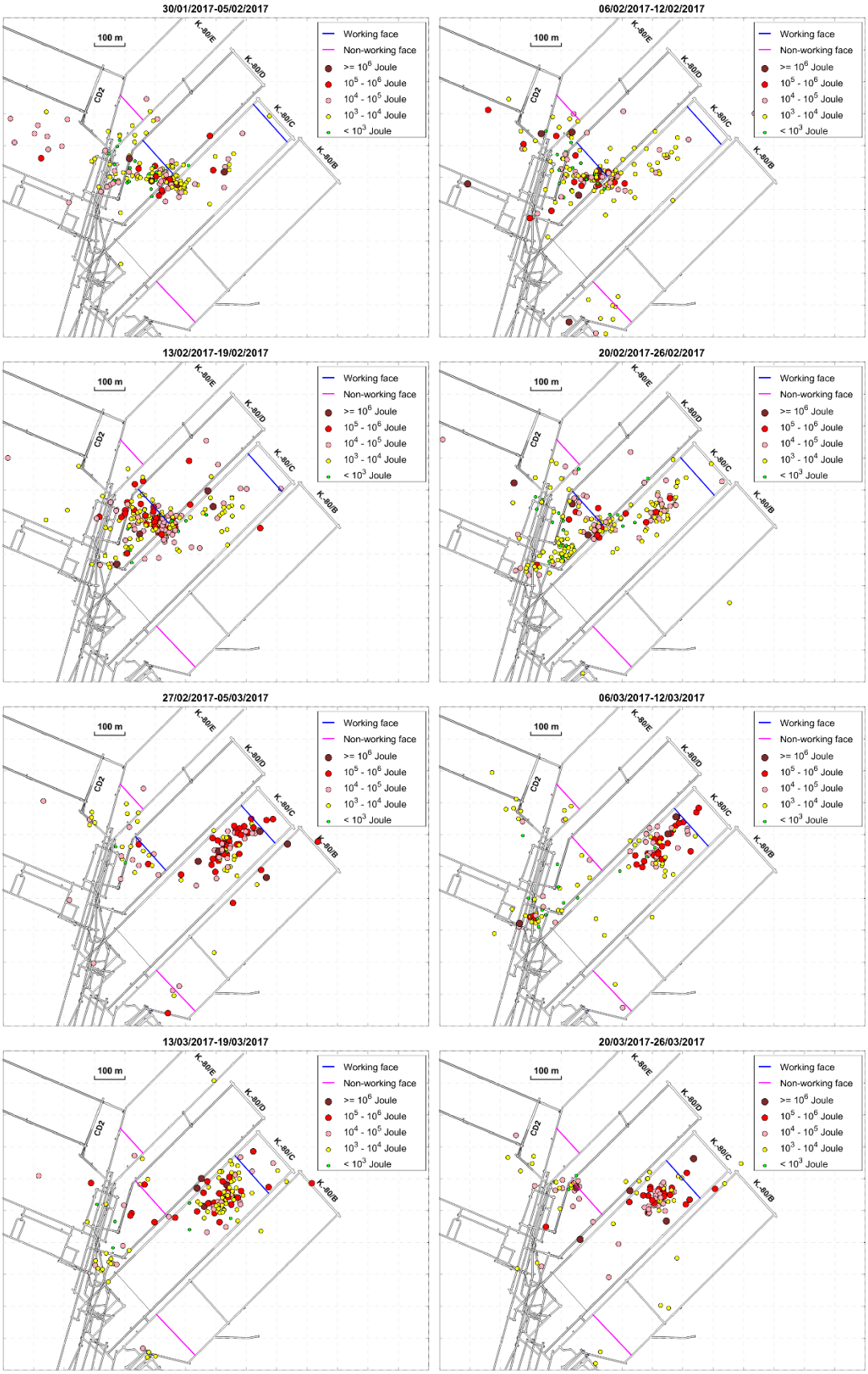


Figure A1.1. (Continued). Spatial distribution of recorded microseismicity at Coal Mine Velenje in 2016-2018 (analysed for each week).

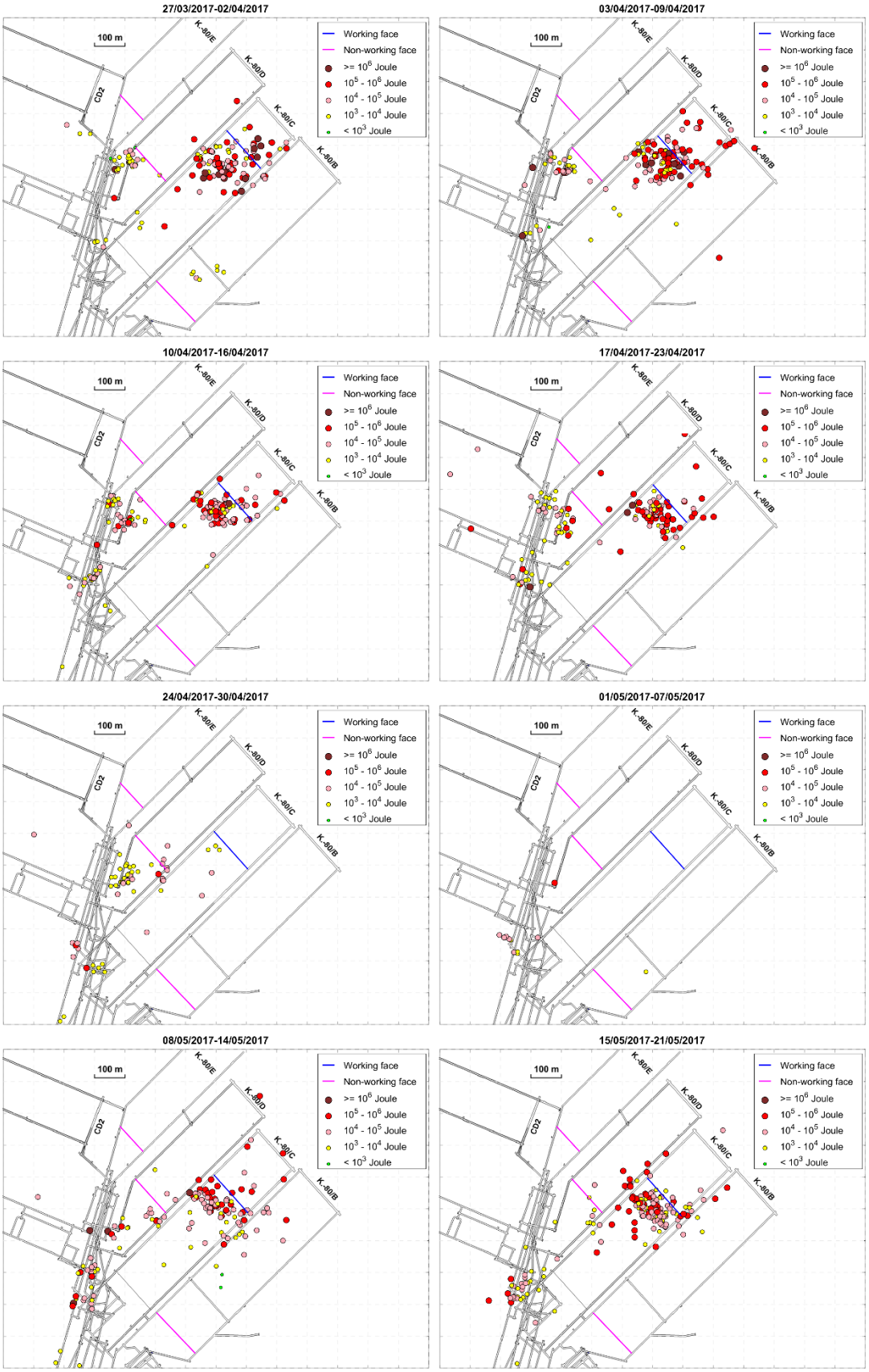


Figure A1.1. (Continued). Spatial distribution of recorded microseismicity at Coal Mine Velenje in 2016-2018 (analysed for each week).

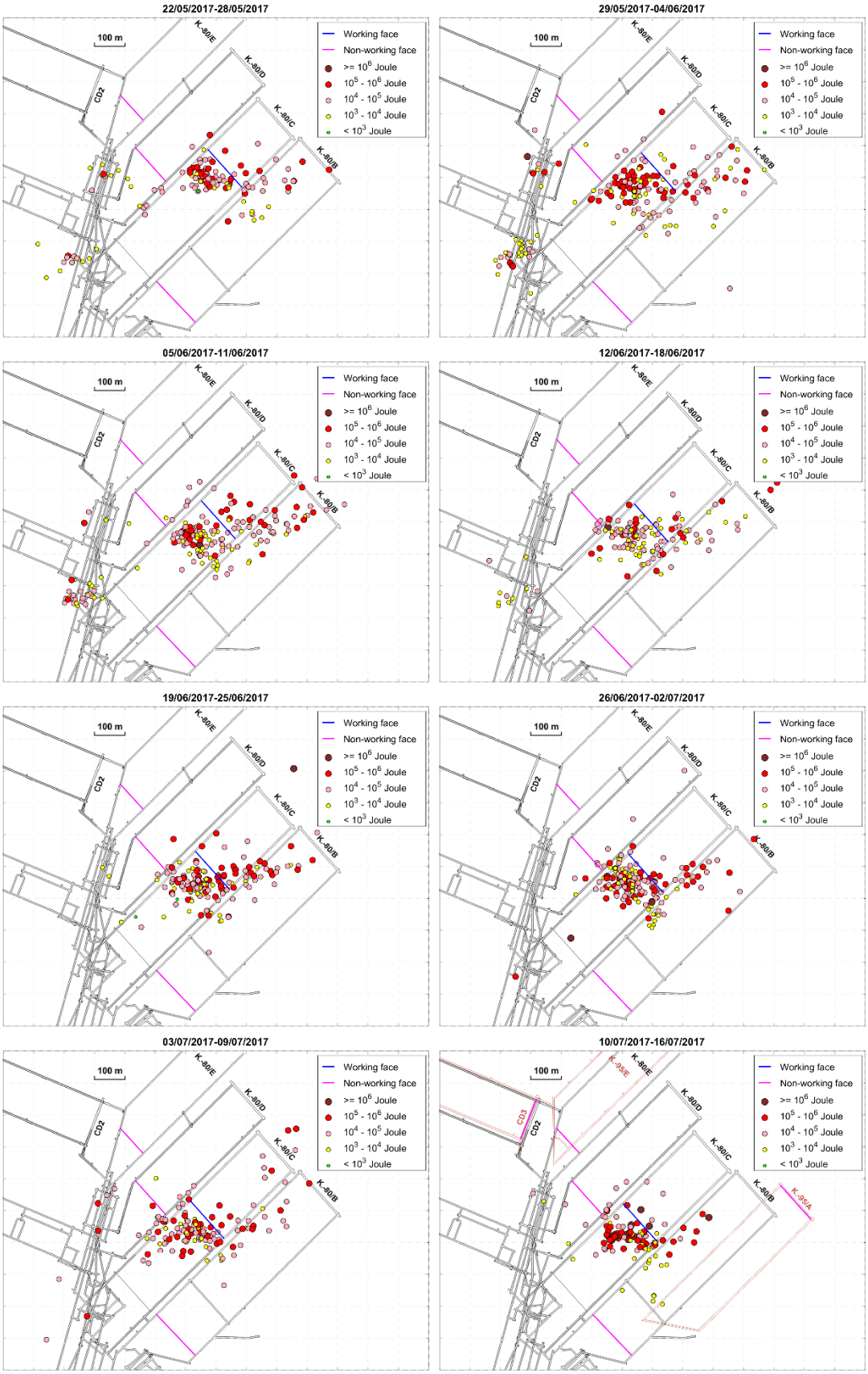


Figure A1.1. (Continued). Spatial distribution of recorded microseismicity at Coal Mine Velenje in 2016-2018 (analysed for each week).

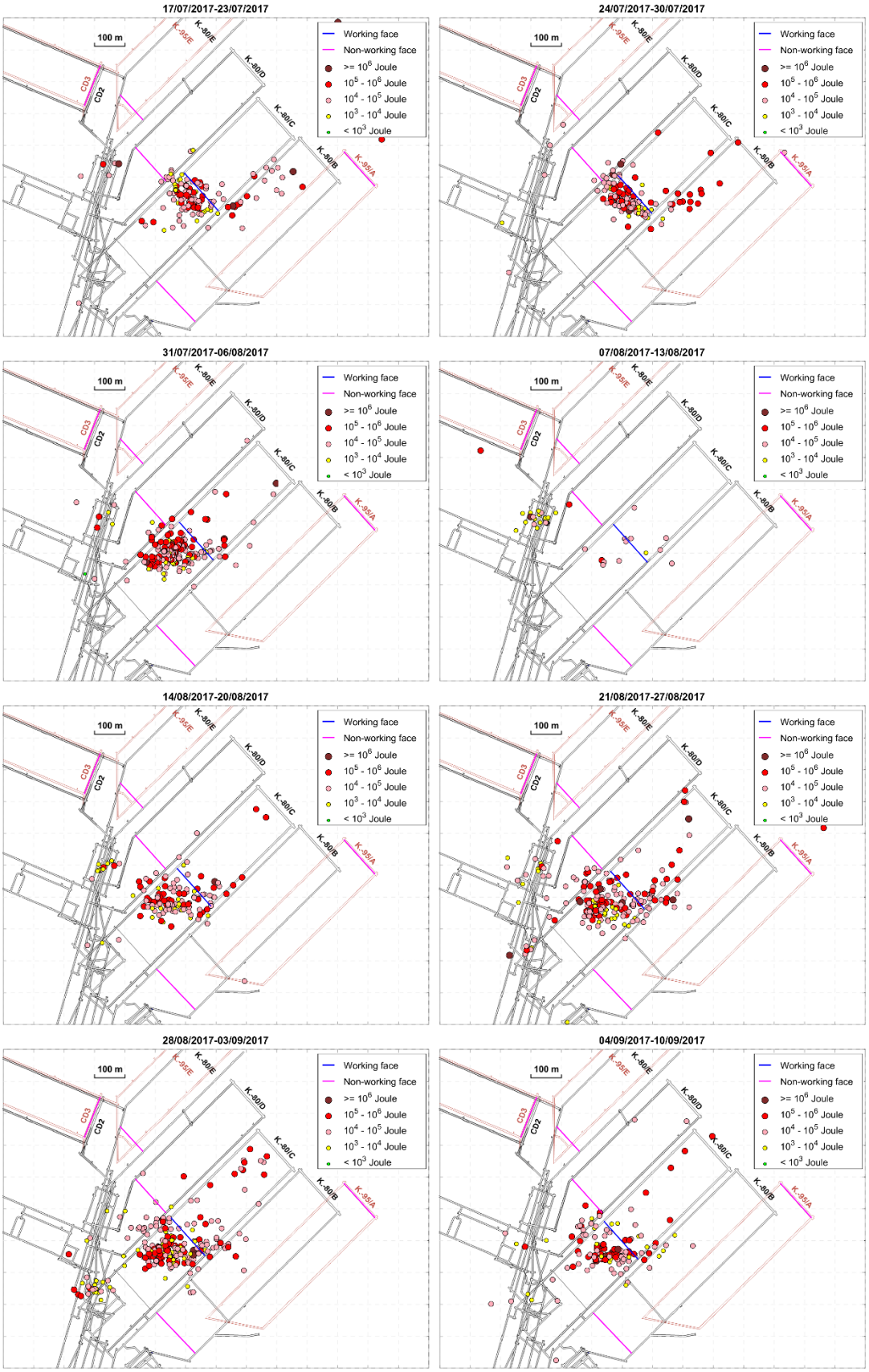


Figure A1.1. (Continued). Spatial distribution of recorded microseismicity at Coal Mine Velenje in 2016-2018 (analysed for each week).

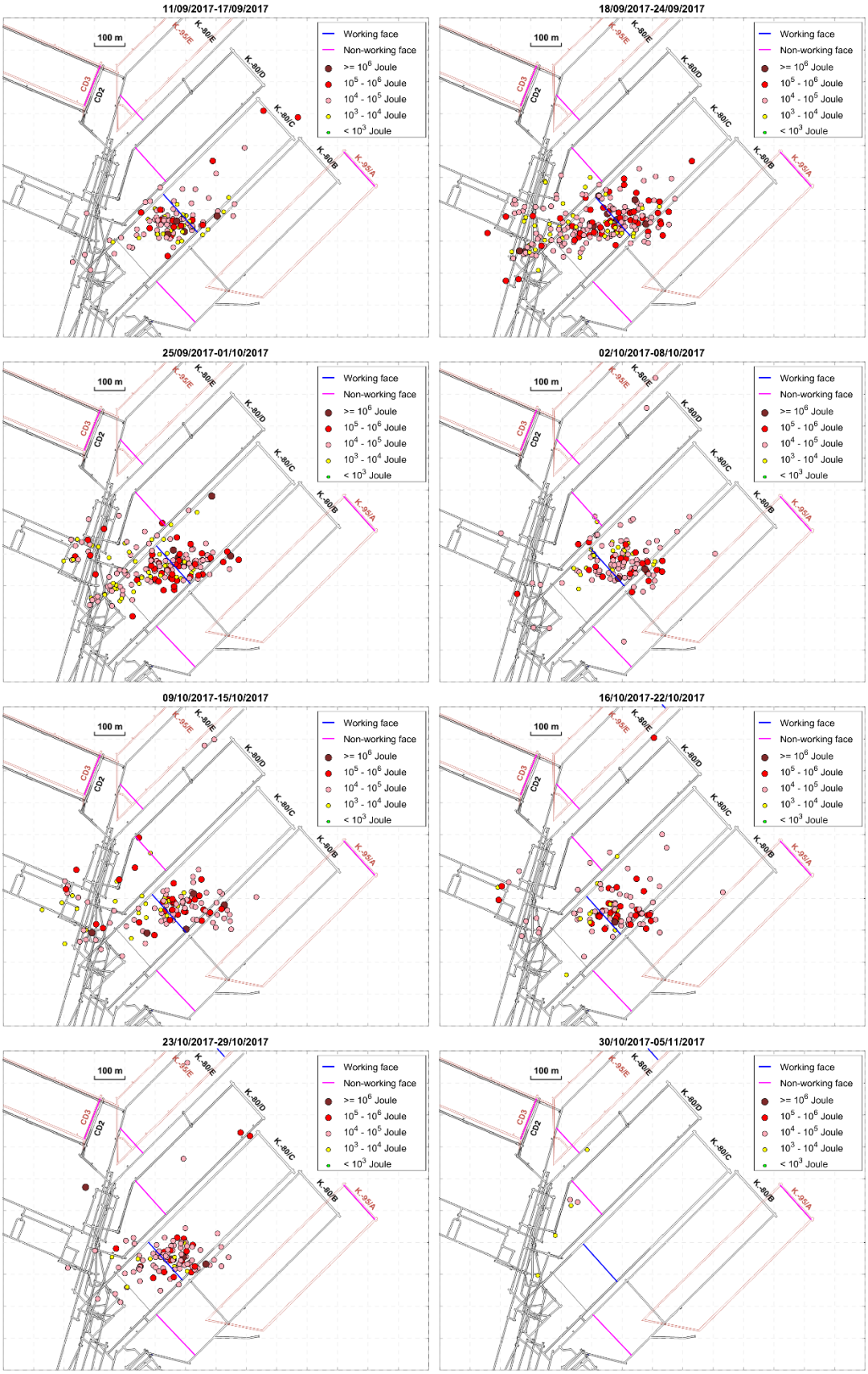


Figure A1.1.(Continued). Spatial distribution of recorded microseismicity at Coal Mine Velenje in 2016-2018 (analysed for each week).

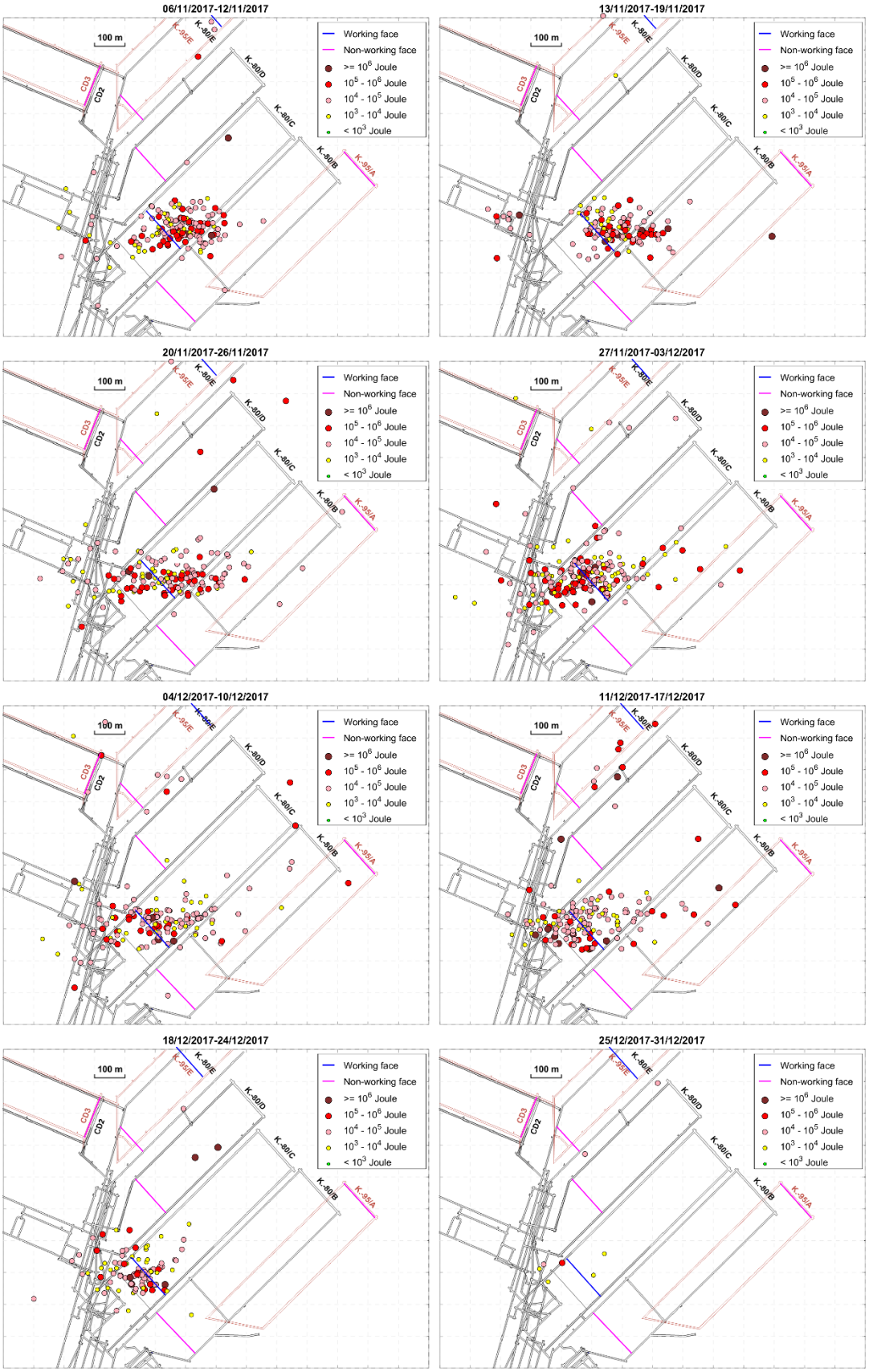


Figure A1.1. (Continued). Spatial distribution of recorded microseismicity at Coal Mine Velenje in 2016-2018 (analysed for each week).

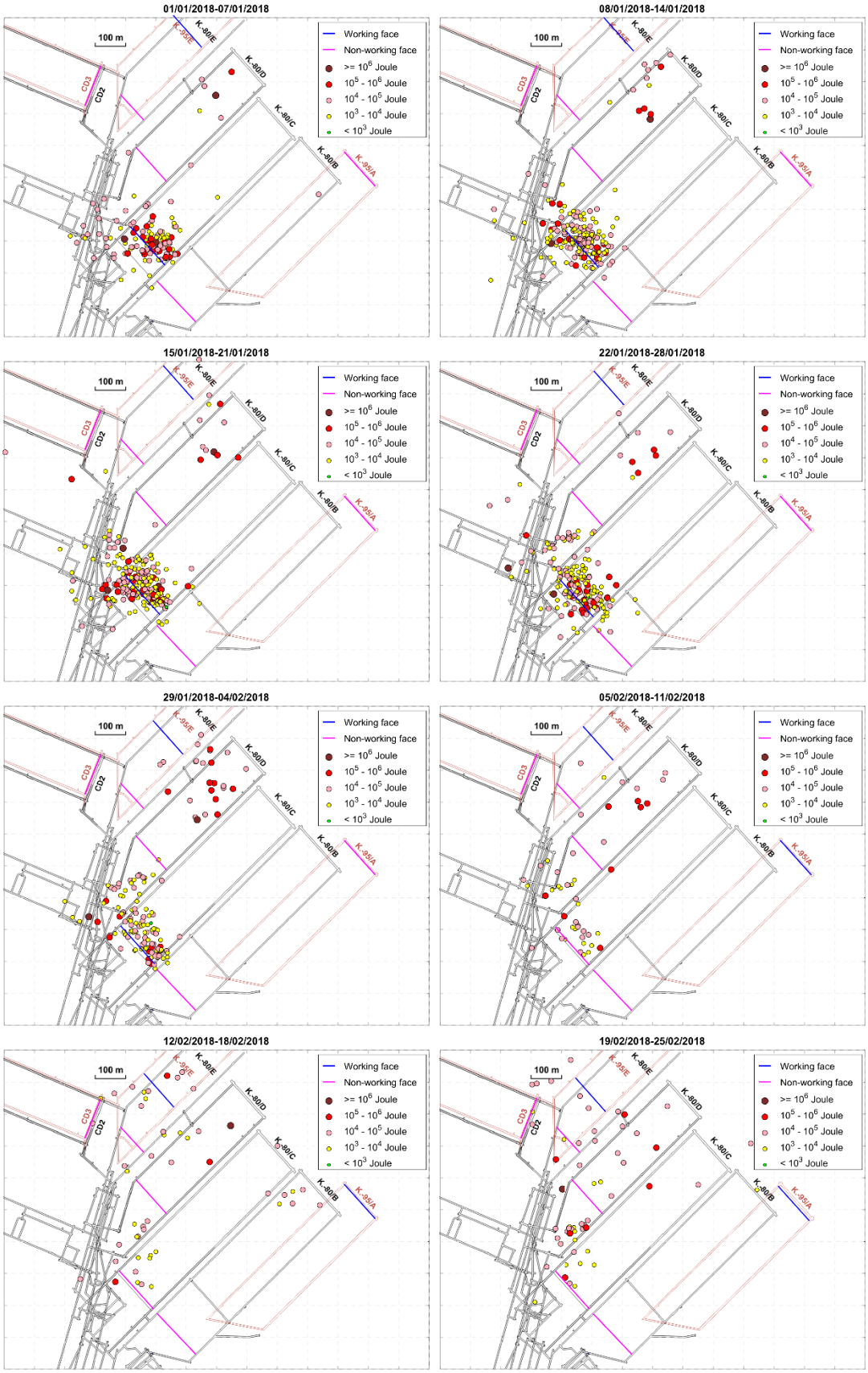


Figure A1.1.(Continued). Spatial distribution of recorded microseismicity at Coal Mine Velenje in 2016-2018 (analysed for each week).

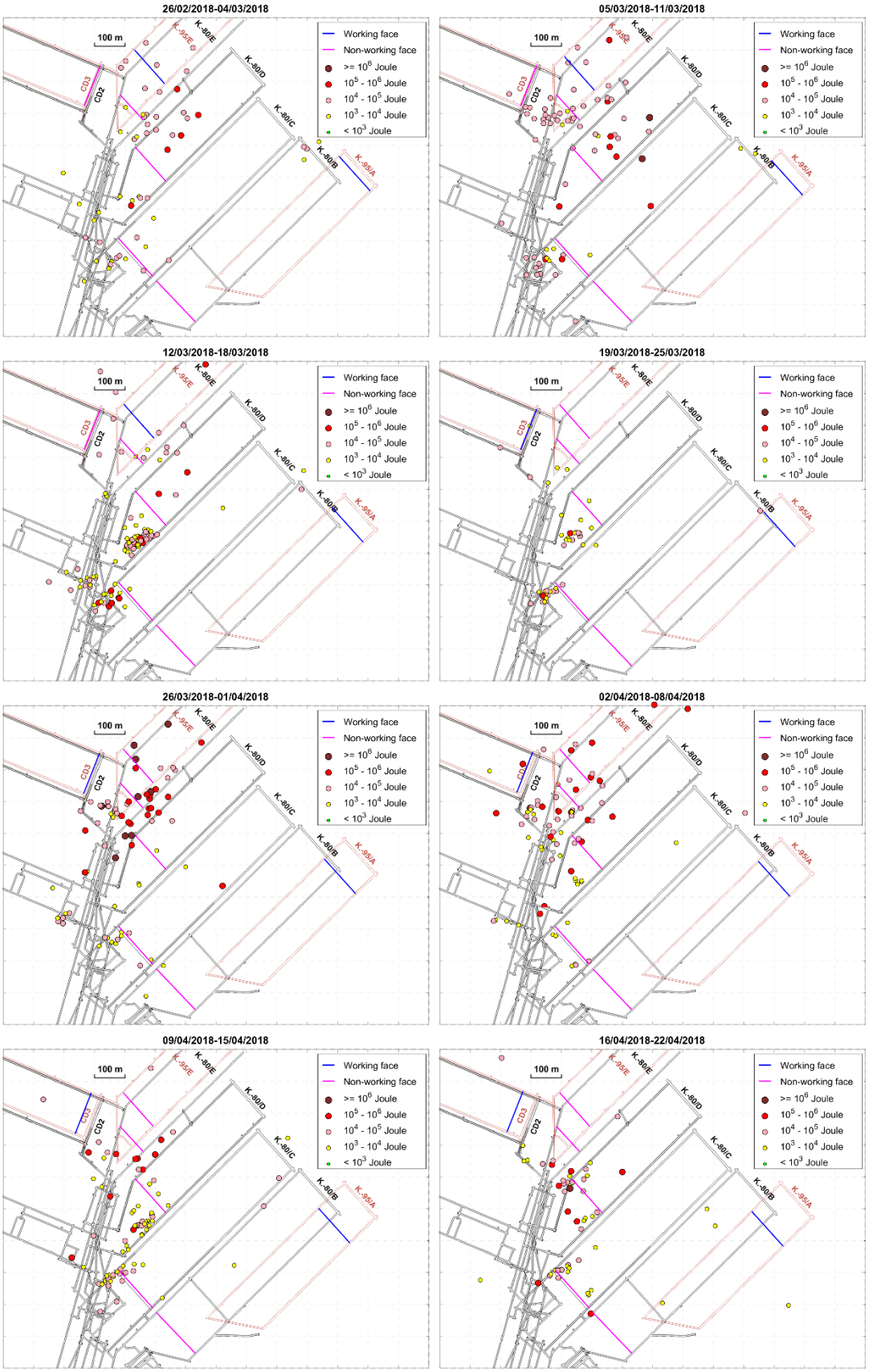


Figure A1.1.(Continued). Spatial distribution of recorded microseismicity at Coal Mine Velenje in 2016-2018 (analysed for each week).

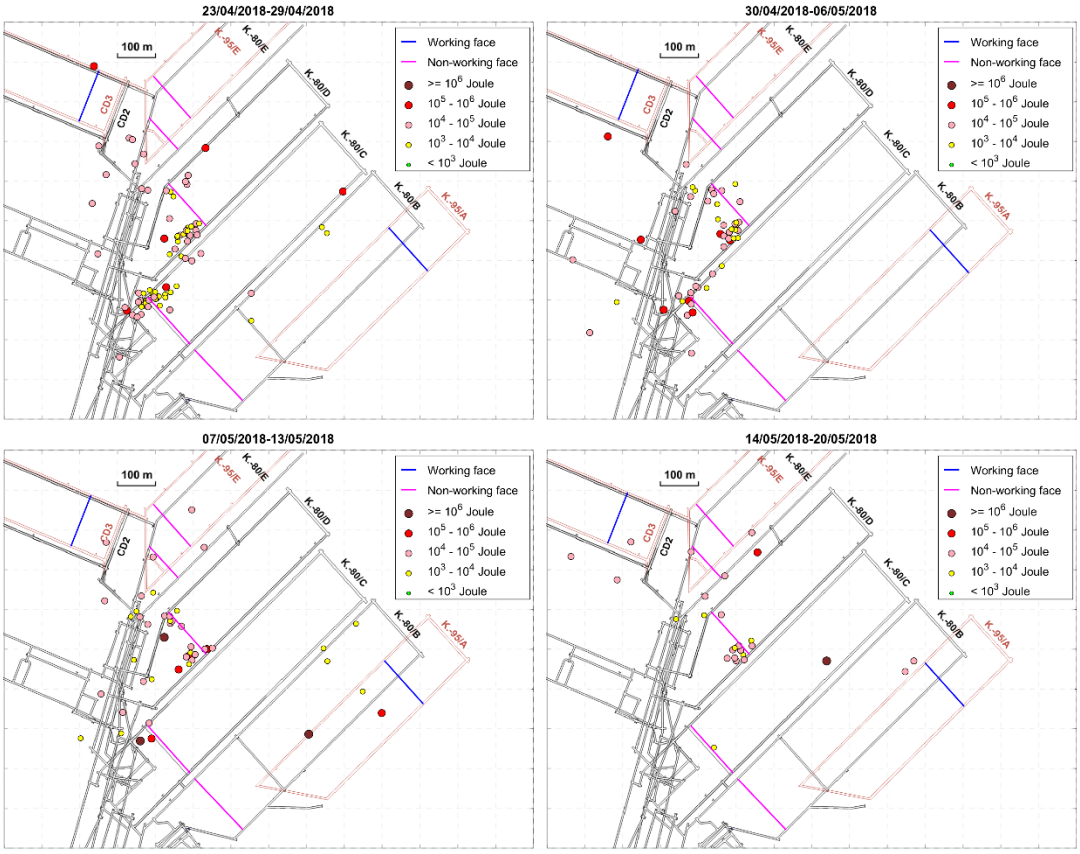


Figure A1.1.(Continued). Spatial distribution of recorded microseismicity at Coal Mine Velenje in 2016-2018 (analysed for each week).

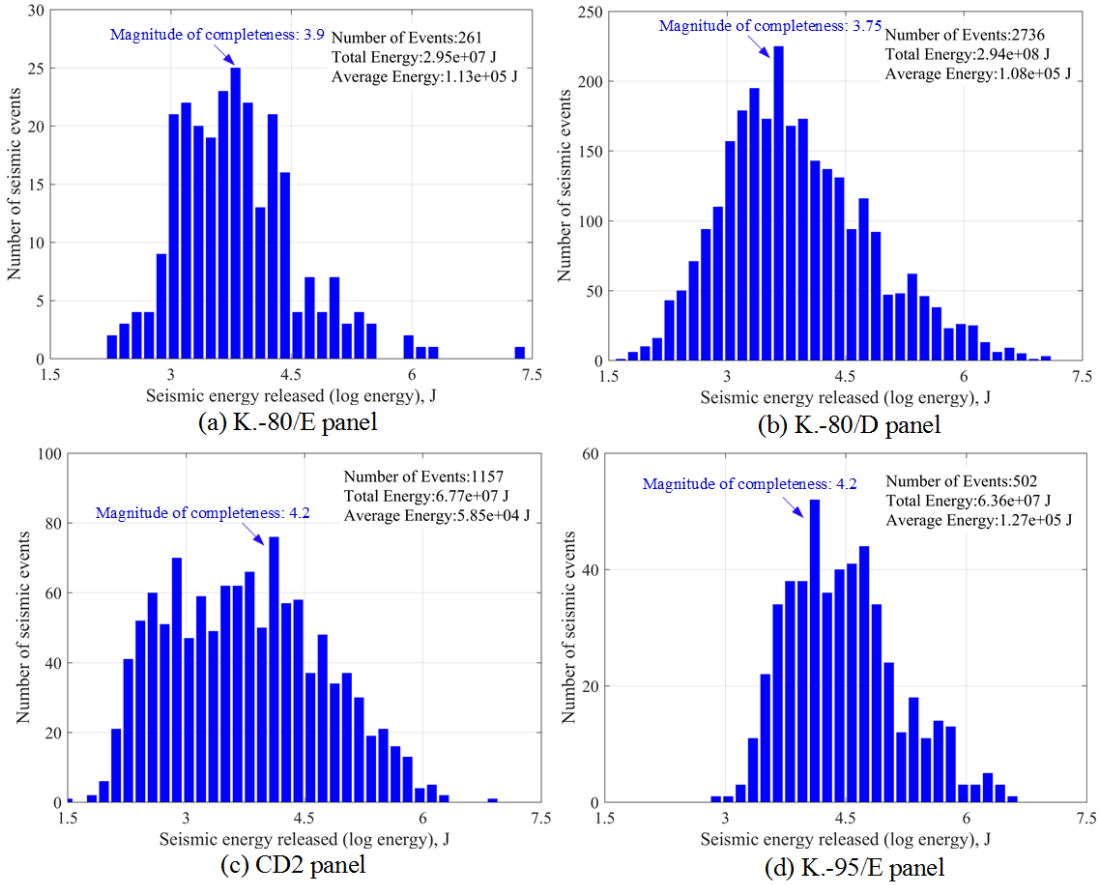
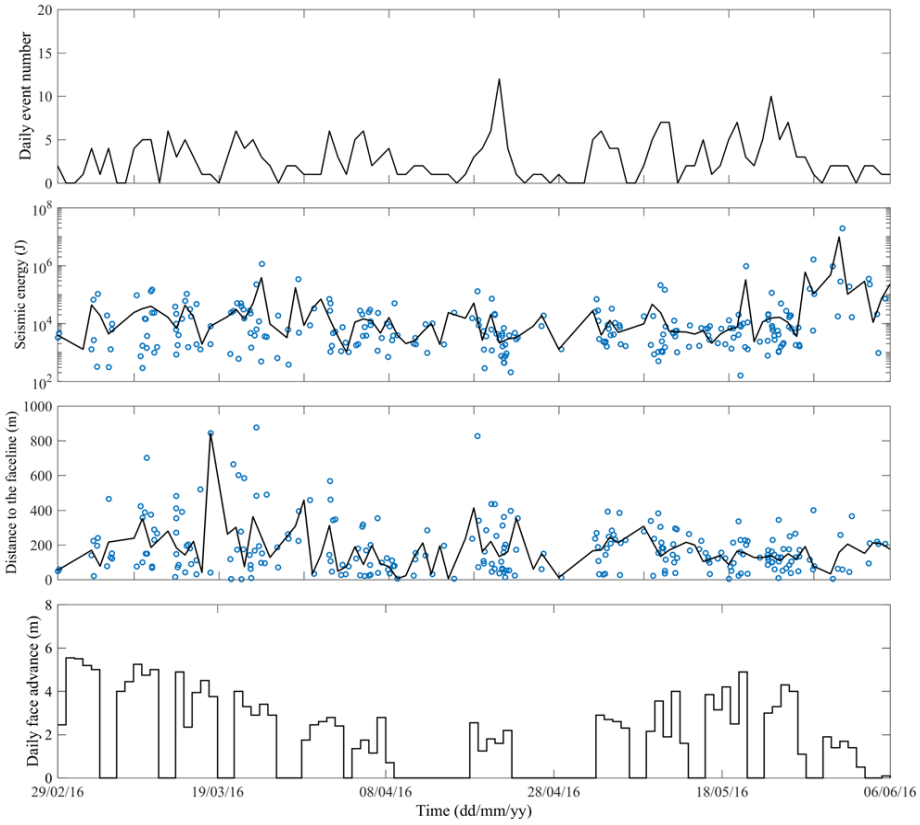
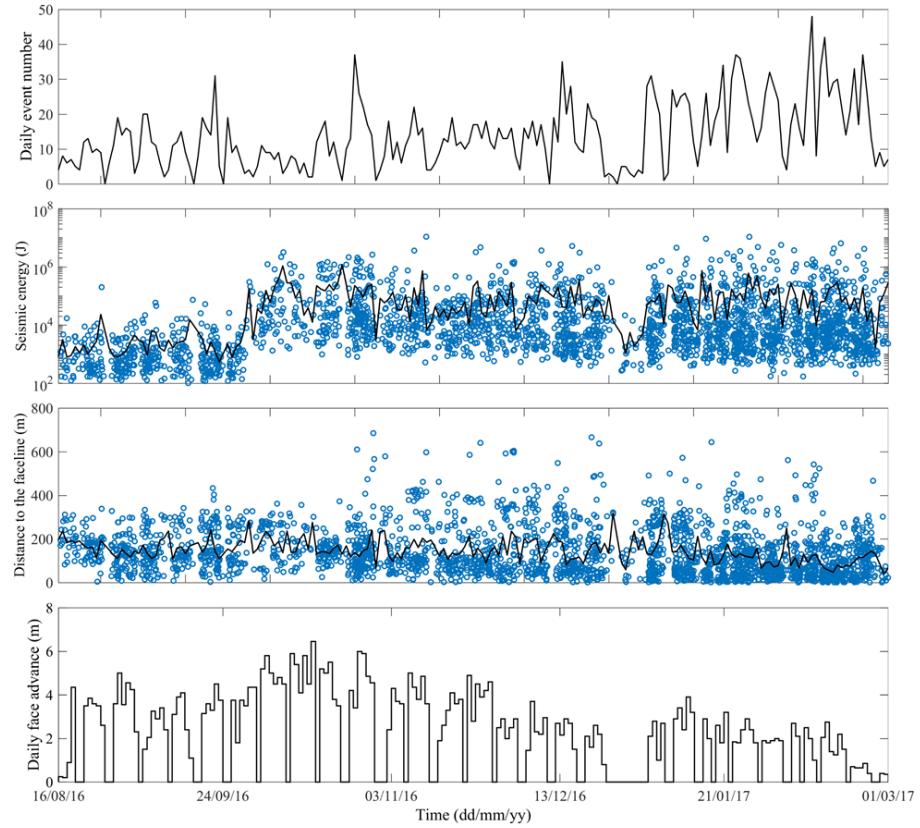


Figure A1.2. Histograms of the recorded microseismicity at Coal Mine Velenje in 2016-2018.

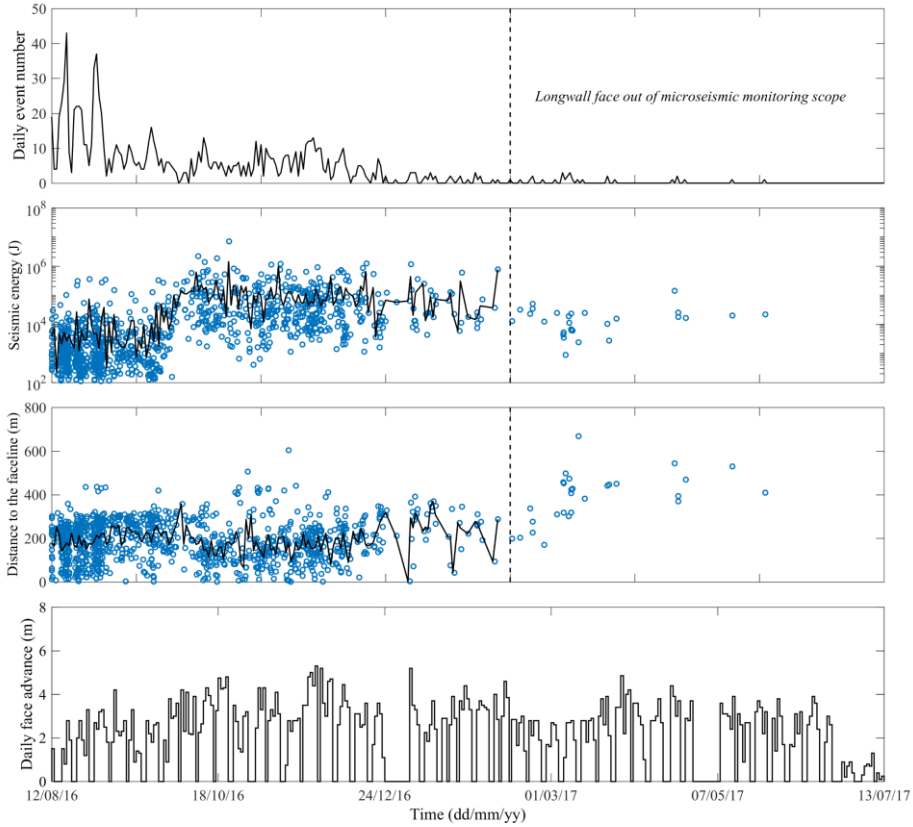


(a) panel E.-80/E

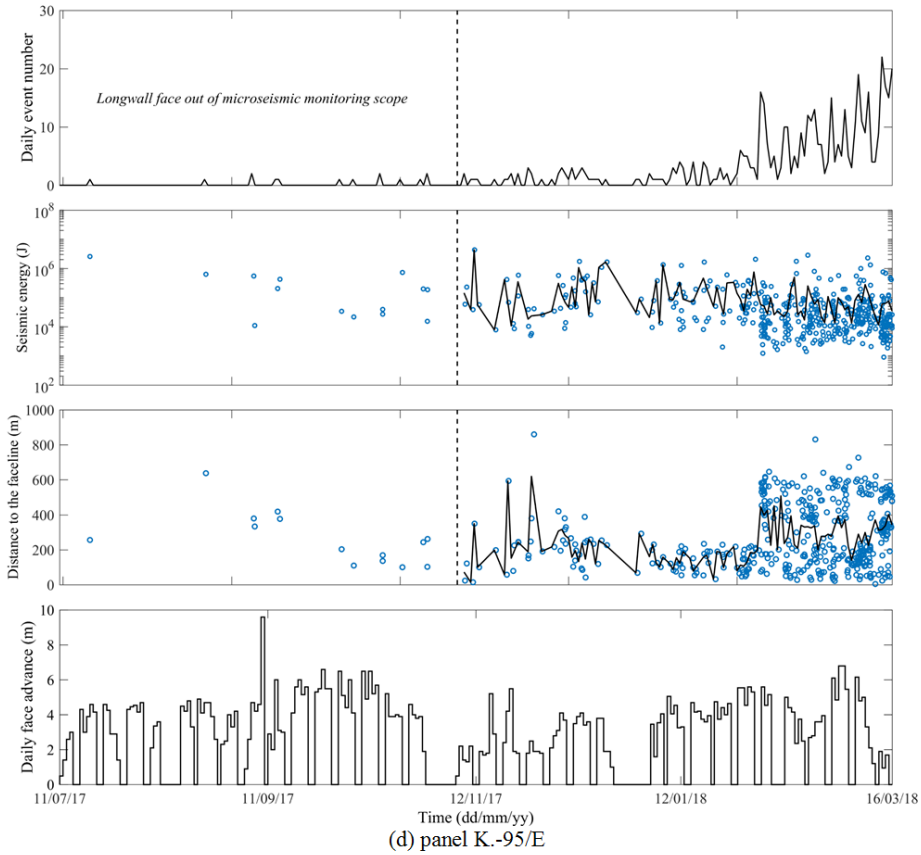


(b) panel E.-80/D

Figure A1.3.Evolutional characteristics of recorded microseismicity at Coal Mine Velenje in 2016-2018 on a daily basis.

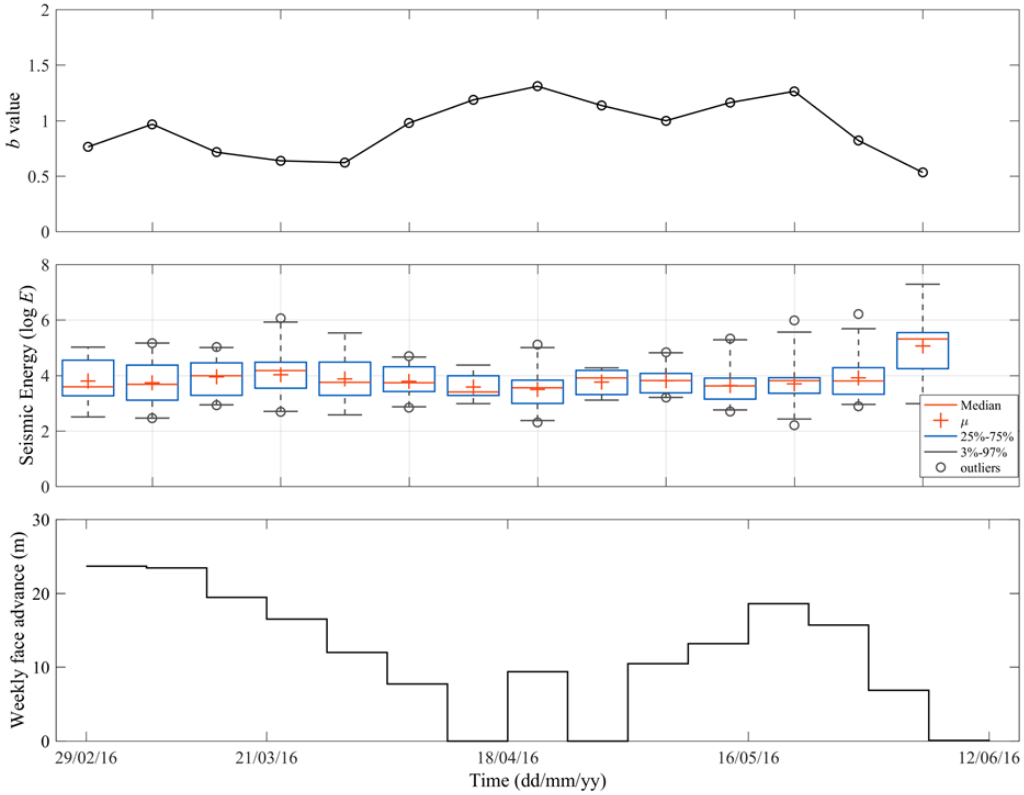


(c) panel CD2

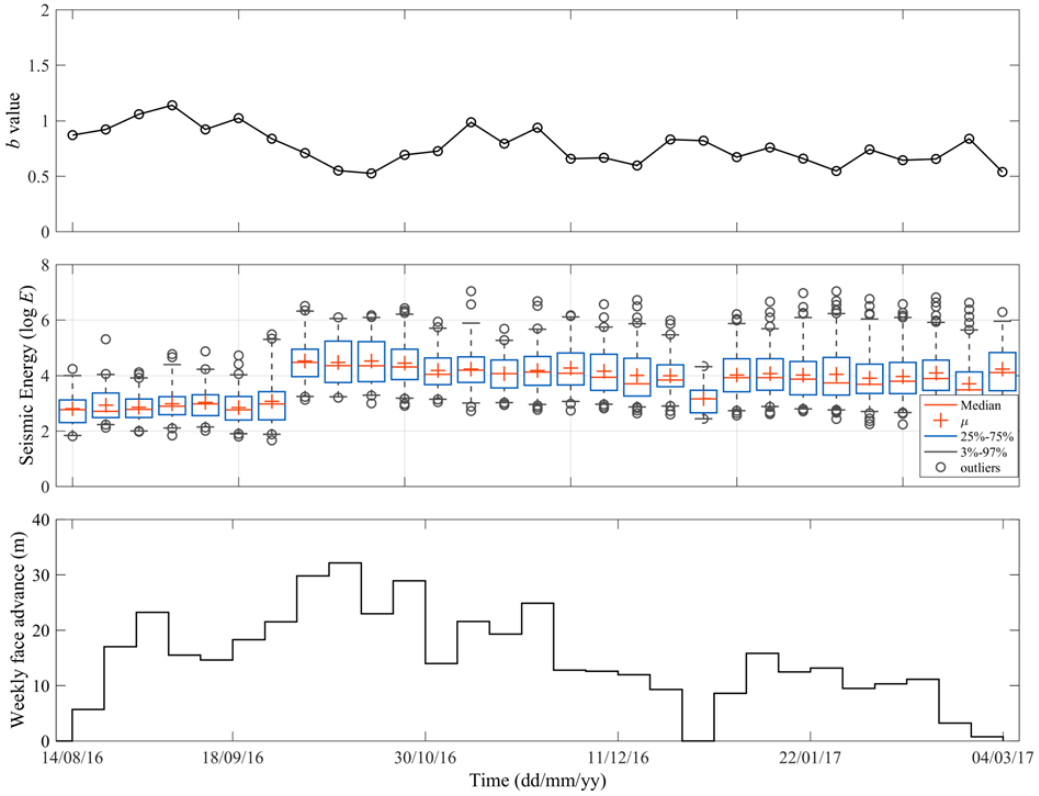


(d) panel K.-95/E

Figure A1.3.(Continued). Evolutional characteristics of recorded microseismicity at Coal Mine Velenje in 2016-2018 on a daily basis.

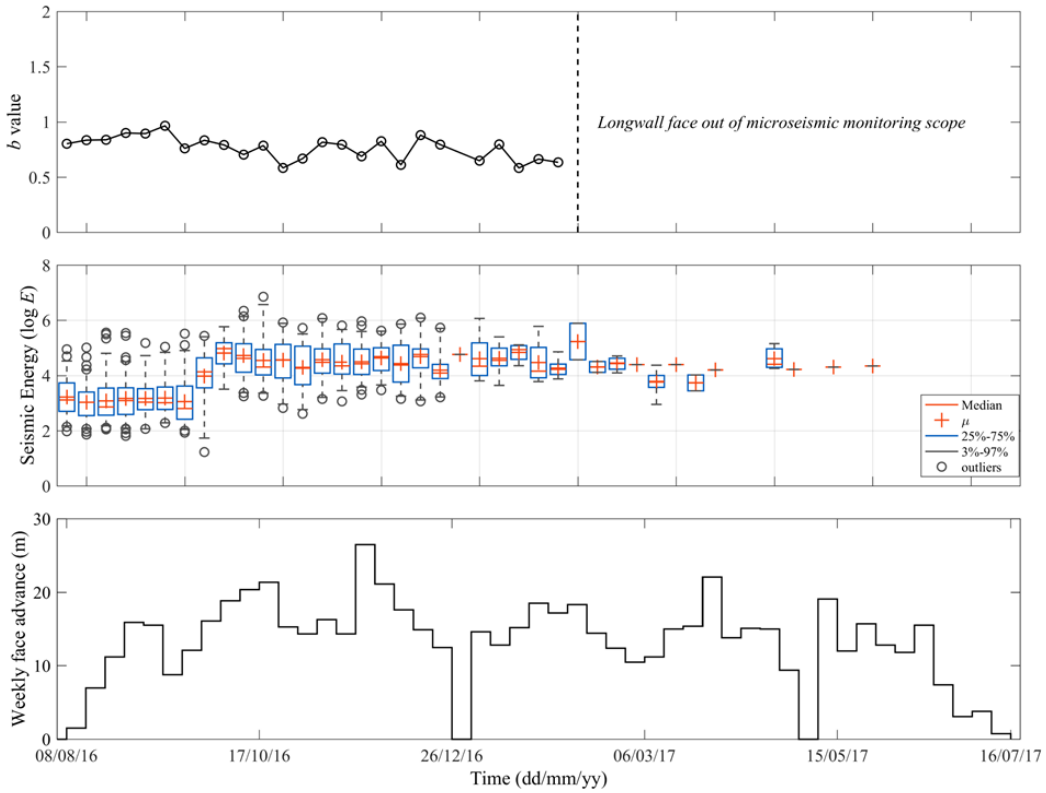


(a) panel E.-80/E

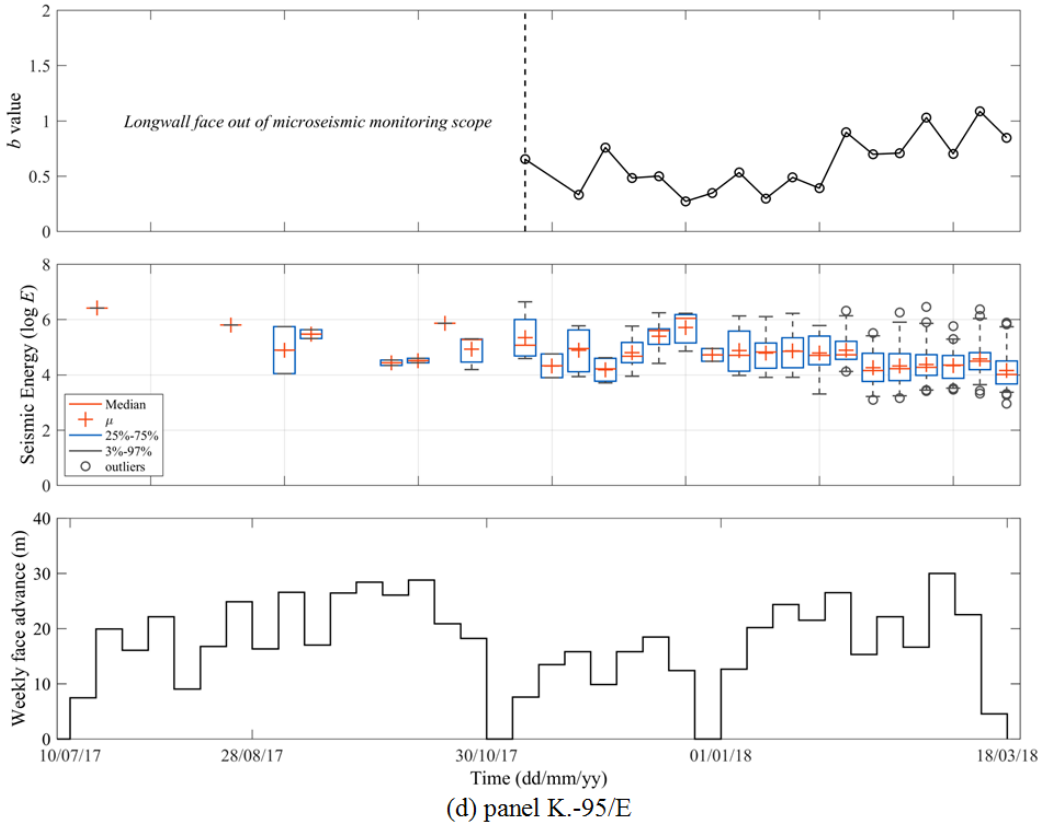


(b) panel E.-80/D

Figure A1.4.Evolutional characteristics of recorded microseismicity at Coal Mine Velenje in 2016-2018 on a weekly basis.



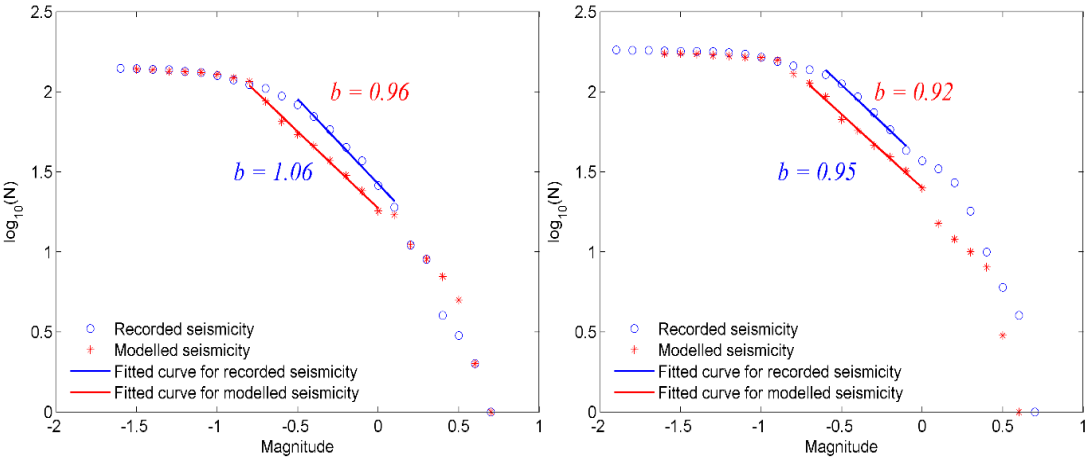
(c) panel CD2



(d) panel K.-95/E

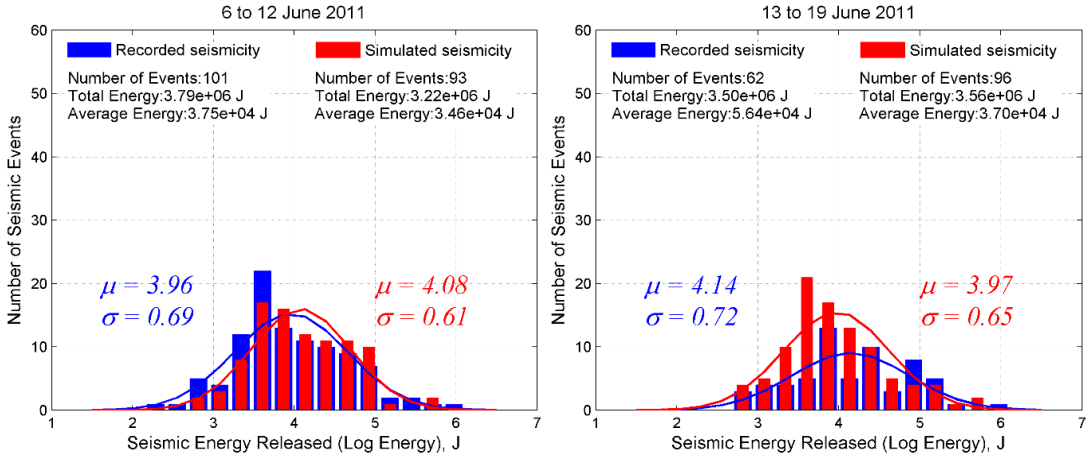
Figure A1.4.(Continued). Evolutional characteristics of recorded microseismicity at Coal Mine Velenje in 2016-2018 on a weekly basis.

Appendix 2 Modelled against recorded microseismicity at Coal Mine Velenje in 2011



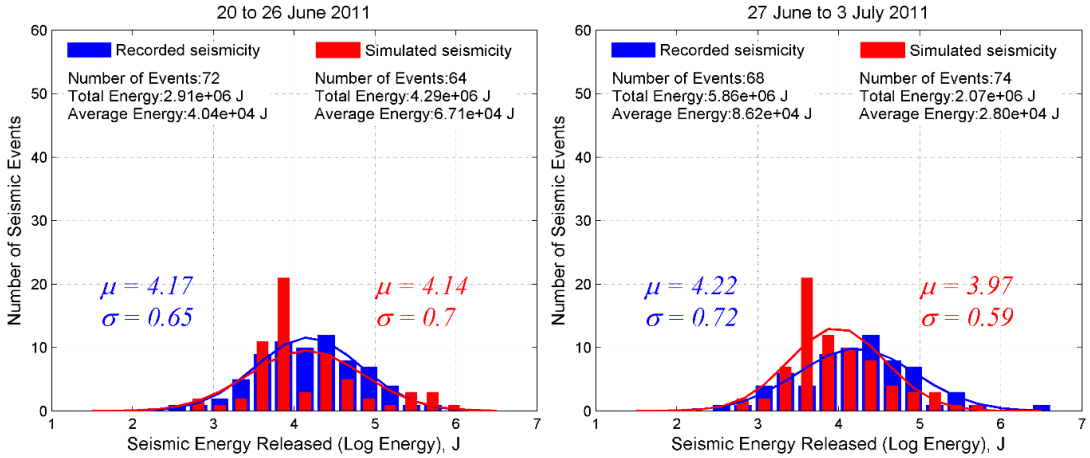
(a) 20 June to 3 July 2011 (b) 4 to 17 July 2011

Figure A2.1. Frequency-magnitude plots of the recorded and modelled seismic events.



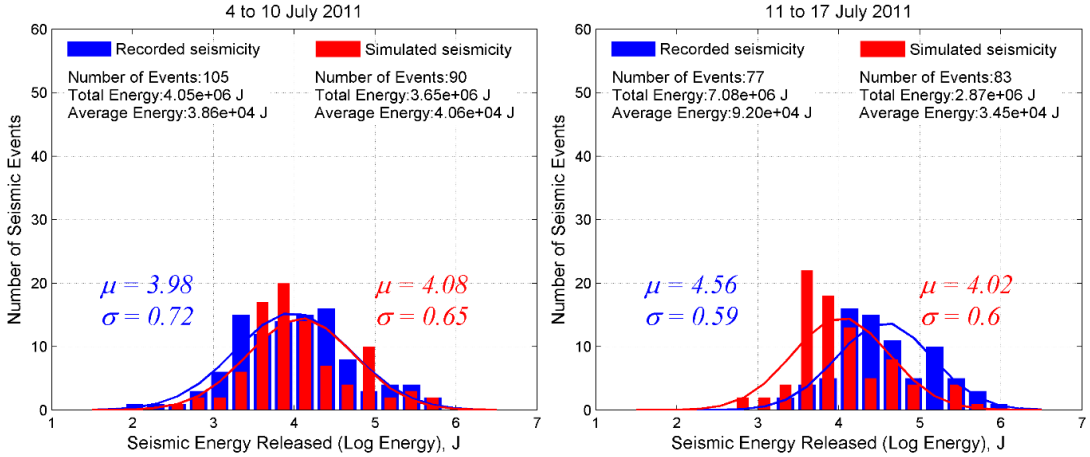
(a) Week 6 to12 June 2011

(b) Week 13 to 19 June 2011



(c) Week 20 to 26 June 2011

(d) Week 27 June to 3 July 2011



(e) Week 4 to 10 July 2011

(f) Week 11 to 17 July 2011

Figure A2.2. Histograms of the recorded and modelled released seismic energy.